HEINRICH HEINE
UNIVERSITÄT
DÜSSELDORF

On the ultrafast kinetics of the energy and electron transfer reactions in Photosystem I

Inaugural-Dissertation

zur Erlangung des Doktorgrades
der Mathematisch-Naturwissenschaftlichen Fakultät
der Heinrich-Heine-Universität Düsseldorf

vorgelegt von

Chavdar Lyubomirov Slavov
aus Kyustendil, Bulgarien

Düsseldorf/Mülheim an der Ruhr, August 2009

aus dem Max-Planck-Institut für Bioanorganische Chemie, Mülheim an der Ruhr

Gedruckt mit der Genehmigung der
Mathematisch-Naturwissenschaftlichen Fakultät der
Heinrich-Heine-Universität Düsseldorf

Referent: Prof. Dr. Alfred R. Holzwarth
Koreferent: Prof. Dr. Peter Westhoff

Tag der mündlichen Prüfung: 9 Juli 2009

If you have an apple and I have an apple and we exchange apples then each of us will still have one apple. But if you have an idea and I have an idea and we exchange ideas then each of us will have two ideas.

George Bernard Shaw

Abbreviations

A_0	primary electron acceptor chlorophyll(s) in Photosystem I
ADP	Adenosine diphosphate
A. thaliana	*Arabidopsis thaliana*
ATP	Adenosine triphosphate
β(α)-DM	n-dodecyl-β(α)-D-maltoside
C. reinhardtii	*Chlamydomonas reinhardtii*
Car	Carotenoid
CFD	constant-fraction discriminator
Chl	Chlorophyll
CS	charge separation
Cyt	cytochrome
DAS	decay-associated spectrum
DCM	4-(dicyanomethylene)-2-methyl-6-(p-dimethylaminostyryl)-4H-pyran
Phe or F	phenylalanine
ET	energy transfer
EPR	electron paramagnetic resonance
Fd	ferredoxin
FNR	ferredoxin-$NADPH^+$ reductase
FWHM	full-width at half-maximum
IRF	instrument response function (=PR)
LHC I	light-harvesting complex I of green plants
LHC II	light-harvesting complex II of green plants
Lut	lutein
MCP	microchannel plate
MES	2-(N-morpholino)ethanesulfonic acid
Met or M	methionine
MO	molecular orbital
NADPH	nicotinamide adenine dinucleotide phosphate
OD	optical density
OEC	oxygen-evolving complex
OPA	optical parametric amplifier
OPO	optical parametric oscillator
PC	plastocyanin
PD	photodiode
PMS	phenazine methosulphate
Phe or F	phenylalanine
PQ	plastoquinone
PS I	Photosystem I
PS II	Photosystem II
PR	prompt response (= IRF)
RC	reaction center
RP	radical pair
SAES	species-associated emission spectrum
SADS	species-associated absorption difference spectrum
SC	streak camera
SPT	single photon timing
TA	transient absorption
TAC	time-to-amplitude converter
TCSPC	time-correlated single photon counting
SPT	single photon timing
T. elongatus	*Thermosynechococcus elongatus*
TMH	transmembrane helix
Tyr or Y	tyrosine
Vio	Violaxanthin
WT	wild type

Chapter 1

Introduction

Photosynthesis is the primary process by which energy is fed into the biological world. In its course complex machinery performs highly effective transformation of light energy. Quite generally, the process consists of two parts: *light-dependent*, including the reactions necessary for the conversion of light into chemical energy (ATP) and reducing power (NADPH), and *carbon-fixation*, where the latter compounds are used to incorporate CO_2 into simple sugars. Additionally, the products of the light-dependent reactions are used for the synthesis of different carbon derivatives and for the incorporation of the inorganic forms of sulfur and nitrogen into organic molecules. Even tough some photosynthetic organisms use as an electron source compounds like H_2, H_2S, Fe^{2+}, NO_2^-, AsO_3^{3-}, and sometimes even organic molecules, the majority utilize the most abundant for the living organisms substrate, water. Since the oxidation of the latter leads to oxygen evolution, this type of photosynthesis is called *oxygenic*. Oxygenic photosynthesis is conducted by cyanobacteria, algae, and higher plants and appears to be the dominant type of photosynthesis.

The significance and complexity of photosynthesis have been a matter of systematic research from the pure molecular mechanisms up to the physiological and even ecological aspects. The results from these studies find extensive application in fields like agronomy and environmental protection. Moreover, in the light of the global warming and the energy crisis faced by humanity, the detailed understanding of photosynthesis becomes crucial not only for the preservation of the vulnerable ecosystems, but also for the prevention of the world economy collapse. In this respect, a large field related to photosynthesis research deals with the design and development of eco-friendly light energy conversion systems mimicking the photosynthetic apparatus.

In order to precisely understand Nature's engineering approaches the working mechanism of each part of the photosynthetic apparatus has to be studied in detail. In this regard, the subject of the current work is one of the main participants in the light-dependent phase of oxygenic photosynthesis, Photosystem I (PS I). This complex carries an immense number of cofactors: chlorophylls (Chl), carotenoids (Car), quinones, *etc*, which together with the protein entity exhibit several exceptional properties. First, PS I has an ultrafast light energy trapping kinetics with a nearly 100% quantum efficiency. Secondly, both of the electron transfer branches in the reaction center are suggested to be active. Thirdly, there are some so called *'red'* Chls in the antenna system of PS I, absorbing light with longer wavelengths than the reaction center. These 'red' Chls significantly modify the trapping kinetics of PS I.

The purpose of this thesis is to obtain better understanding of the above-mentioned, specific features of PS I. This will not merely cast more light on the mechanisms of energy and electron transfer in the complex, but also will contribute to the future developments of optimized artificial light-harvesting systems. In the current work, a number of PS I complexes isolated from different organisms (*Thermosynechococcus elongatus*, *Chlamydomonas reinhardtii*, *Arabidopsis thaliana*) and possessing distinctive features (different macroorganisation – monomers, trimers, monomers with a semibelt of peripheral antenna attached; presence of *'red'* Chls) is investigated. The studies are primarily focused on the electron transfer kinetics in each of the cofactor branches in the PS I reaction center, as well as on the effect of the antenna size and the presence of *'red'* Chls on the trapping kinetics of PS I. These aspects are explored with the help of several ultrafast optical spectroscopy methods: *i)* time-resolved fluorescence – single photon counting and synchroscan streak camera and *ii)* ultrafast transient absorption. Physically meaningful information about the molecular mechanisms of the energy trapping in PS I is gained with the help of kinetic modeling.

1.1 Light-dependent phase of oxygenic photosynthesis

The process of photosynthesis is initiated with the absorption of light by some of the versatile pigment molecules of the photosynthetic complexes. This act leads to transformation of the energy of the quantum into energy of the excited state of the pigment. However, the lifetime of such an excited state is very short and the energy cannot be used in the slow chemical processes; therefore, the energy has to be converted into a more stable form. The conversion occurs in a series of reactions, beginning with the migration of the excitation from the extensive antenna system of the photosynthetic complex to a specific site, called *reaction center* (RC). There the excitation is used for generation of a charge-separated state. The latter is further stabilized in a cascade of subsequent electron transfer reactions, during which the free energy of the ejected electron decreases, preventing the recombination reaction. In addition, the protein matrix in which the cofactors are embedded also relaxes making the energy barrier for charge recombination even higher (1). In effect, a long-lived charge-separated state, which can drive other processes, is created. These early reactions of light conversion induce a flow of electrons in the photosynthetic apparatus, which on the one hand is used indirectly for the synthesis of ATP, and on the other hand for the accumulation of NADPH.

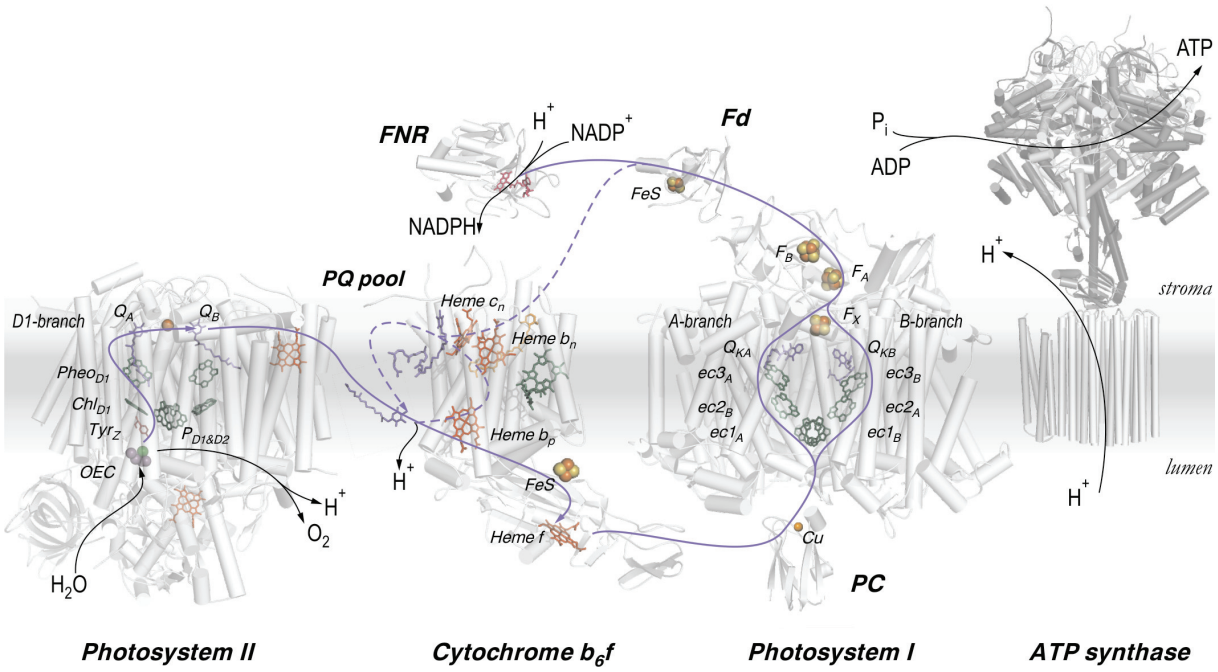

Figure 1.1
Schematic representation of the photosynthetic electron transfer chain and the ATP synthase operating in the thylakoid membrane (see text for abbreviations). The electrons are transferred in vectorial manner from the OEC in PS II through the PQ pool, Cyt b_6f and PC to PS I, and finally delivered to Fd and FNR (violet solid lines). Apart from this direct pathway, which is ultimately used for the reduction of $NADP^+$, there are several cyclic electron transfer pathways (violet dashed lines) – between PS I and Cyt b_6f (2), in Cyt b_6f (2) and in PS II (not shown) (3). The black solid lines show the positions of the transmembrane H^+ gradient generation and the consumption of H^+ in ATP synthase.

1.1.1 The photosynthetic electron transfer chain

In oxygenic photosynthesis, the components carrying out the above-mentioned reactions are embedded in a special membrane system, called *thylakoid*. This membrane is either a part of the chloroplast as in the algal and higher plant cell, or exists as a separate membrane compartment as in the cyanobacterial cell. In either case, it represents a continuous membrane system enclosing aqueous space called *lumen*. Figure 1.1 illustrates schematically the membrane organization of the components

performing the light-dependent phase of oxygenic photosynthesis. The utilization of light energy begins with the excitation of a light-harvesting pigment in the photosynthetic units. Then, through a series of energy transfer (ET) steps, the excitation is equilibrated over the antenna and the RC. This excitation is finally captured by the RC in the form of a charge-separated state. At present, it is widely accepted that the primary charge separation (CS), both in PS I and PS II, occurs from the accessory Chls (Chl_{acc}) (4-6). The real breakthrough in the understanding of the electron transfer reactions occurring in the thylakoid membrane has been made by Hill and Bendall (7). They have proposed that the two photosystems work in tandem, so that two photons act sequentially to drive electrons from the very poor electron donor H_2O to the weak electron acceptor $NADP^+$. In this regard, the cofactors of the photosynthetic electron transfer chain can be ordered according to their reduction potential in a Z-like manner (Figure 1.2).

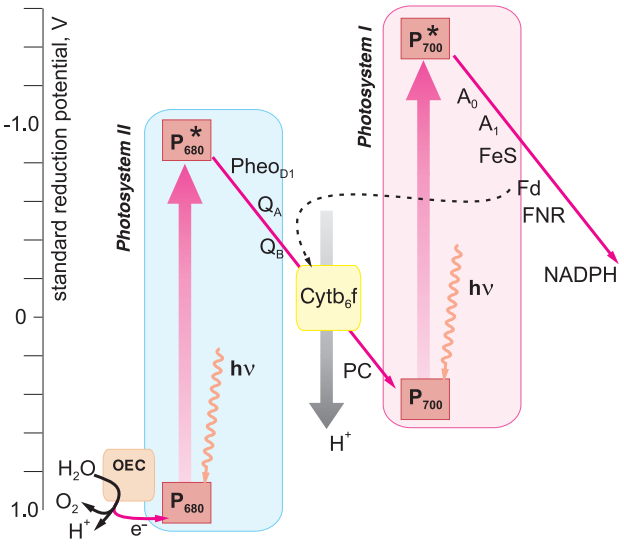

Figure 1.2
Z-scheme of the photosynthetic electron transfer reactions (7) (see text for abbreviations). The scheme shows the redox reactions necessary to transfer one electron from H_2O to NADPH, and to pump H^+ across the thylakoid membrane. Two photons (one in each photosystem) are necessary to raise the energy of an electron in order to traverse the whole path. The dashed arrow represents the cyclic electron transfer pathway between Cyt b_6f and PS I. (For historical reasons the labels of the different components are preserved. However, in the light of the new evidences for Chl_{acc} as the primary electron donor in both photosystems (4-6) the labeling of P_{680} and P_{700} should be reconsidered. In addition, new labels should be used also for the electron transfer cofactors of PS I (2).)

1.1.2 Electron transfer reactions in PS II

Following Figure 1.1, the electrons ejected from the primary donor in PS II (Chl_{D1}) are transferred further towards the outer side of the thylakoid membrane where they are eventually delivered to a plastoquinone molecule (PQ). The PQ accepts for complete reduction also H^+ from the stroma (higher plants and algae) or the cytoplasm (cyanobacteria). After two such reduction cycles the mobile electron carrier, plastoquinol (PQH_2), leaves the PQ binding pocket of PS II. The electron deficit generated in PS II after the CS is compensated by water oxidation. As depicted in Figure 1.1, after the primary CS the cation radical created on Chl_{D1} moves promptly to the 'special Chl pair', P_{680} ($P_{D1\&D2}$). This newly generated, highly oxidizing species, P_{680}^+, is neutralized by an electron transfer from a proximate Tyr residue (Tyr_Z). Tyr_Z is in fact the molecule which, in its radical form, triggers water oxidation in the metal cluster (Mn_4Ca) of PS II oxygen-evolving complex (OEC) (2,8). The oxidation of each H_2O molecule leads to release of $2H^+$ in the lumen of the thylakoids.

1.1.3 Electron transfer between PS II and PS I

After leaving the binding pocket in PS II, the hydrophobic PQH_2 molecules diffuse inside the membrane towards the inner side of the thylakoid, where they interact with another electron transfer complex – Cytochrome b_6f (Cyt b_6f) (9,10). The electrons carried by PQH_2 are transferred through

Cyt b_6f to a water-soluble, mobile electron carrier, while the H^+ are ejected into the lumen of the thylakoids. The copper containing protein, plastocyanin (PC) is the exclusive luminal electron carrier in higher plants, whereas in cyanobacteria and some algae both PC and a Cyt c_6 carry out this function (11,12).

1.1.4 Electron transfer reactions in PS I

Analogous to PS II, after the excitation reaches the RC of PS I the CS reaction occurs from one of the accessory Chls ($ec2_B$ or $ec2_A$). As the electron travels towards the outer side of the thylakoid membrane along one of the electron transfer branches of PS I, on the lumenal side of this complex the cation radical P_{700}^+ ($ec1_A/1_B^+$) is formed. The electrons from PS I are transferred to a water-soluble protein, called ferredoxin (Fd), which contains a [2Fe2S] cluster as a redox-active cofactor (13). Fd finally delivers the electrons to the flavoprotein, Fd:$NADP^+$ oxidoreductase (FNR), where $NADP^+$ is reduced to NADPH (14,15). There exists an alternative pathway, operating at low $NADP^+$ concentrations, where the electrons on the Fd are delivered to the Cyt b_6f and then to a PQ to create a cyclic electron transport chain between the Cyt b_6f complex and PS I (Figure 1.1). The purpose of this cyclic electron transport is additional proton gradient generation. PS I can perform another electron donation cycle only after P_{700}^+ is reduced. This is done by the mobile electron carrier PC (and/or Cyt c_6), which diffuses freely in the lumen of the thylakoids from Cyt b_6f complex to PS I (16).

1.1.5 ATP synthesis

Apart from the NADPH, there is another major product of the light-dependent part of photosynthesis – ATP. As illustrated in Figure 1.1, there are three positions which contribute to the generation of H^+ gradient across the thylakoid membrane: *i)* H^+ release in the lumen of the thylakoid during water oxidation in PS II; *ii)* H^+ transfer by PQH_2 from the outer side of the thylakoid membrane to the lumen; *iii)* H^+ consumption by $NADP^+$ reduction in the FNR on the outer side of the thylakoid. The accumulated H^+ gradient is then used by a highly specialized membrane protein complex, ATP synthase, for the formation of a ′macroenergetic′ bond between ADP and an orthophosphate group (17,18), in accordance with the chemiosmotic model proposed by Mitchell (19).

1.2 Light-harvesting pigments of PS I

Pigments are the elements of the photosynthetic complexes that directly interact with light. Apart from their light-harvesting function, they are also involved in the primary CS and electron transfer reactions. Additionally, they play photoprotective and structural role.

1.2.1 Chlorophylls

Chlorophylls (Chls) are the main light-absorbing pigments in photosynthesis. They are planar molecules composed of a chlorin ring that coordinates a Mg^{2+}, and a long phytol side chain (Figure 1.3). Both chlorins and porphyrins are tetrapyrrole derivatives; however, in chlorins one of the pyrrole rings is reduced, leading to shortening of the π-conjugated electron system and reduction of the symmetry of the molecule. In addition to the four pyrroles, a fifth isocyclic ring is present in the Chl structure. By convention, the Y molecular axis of all Chls is defined as passing through the N

atoms of the first and the third pyrrole rings, while the X one – through the N atoms of the second and the fourth.

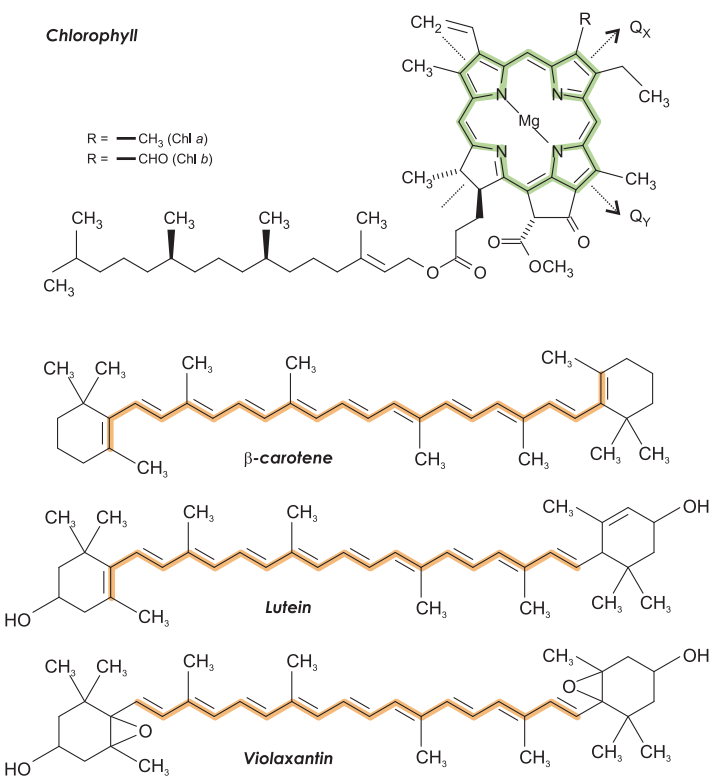

Figure 1.3
Pigments found in PS I. The colored shaded areas represent the conjugated double bond system in the corresponding pigment.

The spectroscopic properties of the Chls (Figure 1.4) are due to their extended π-conjugated electron system. Their spectra can be well described by the *four orbital* model proposed by (20), although the picture appears to be a bit more complex (21,22). In the simplified view, the four π molecular orbitals (MO) involved in the electronic transitions are the two highest occupied (HOMO) and the two lowest unoccupied (LUMO). In contrast to porphyrins, where these MO are degenerate, in Chls the reduction of the fourth tetrapyrrole ring (*cf.* Figure 1.3)) leads to certain destabilization of the π –system and thus destruction of the degeneracy; in effect, electronic transitions with different energies can be observed. These transitions are characterized with different orientation and strength of their transition dipole moment. The lower energy transitions form the so-called Q-bands of the Chl absorption spectrum: *i)* Q_Y (S1) transition is polarized along the Y-axis of the molecule; *ii)* Q_X (S_2) – along the X-axis. Q_Y is the stronger of the two transitions, being oriented along the more asymmetric axis. The higher energy transitions have mixed polarization and form the so-called B- or Soret bands. Both Soret and Q_Y bands have very high molar extinction coefficients (in the order of 70000-80000 $M^{-1}cm^{-1}$).

Chlorophyll fluorescence originates from the lowest excited state (S_1) and therefore is polarized along the Y molecular axis. In diethyl ether the quantum yield of fluorescence and the Q_Y excited state lifetimes are, respectively, ~0.35 and 6 ns for Chl *a* and 0.15 and ~4 ns for Chl *b*.

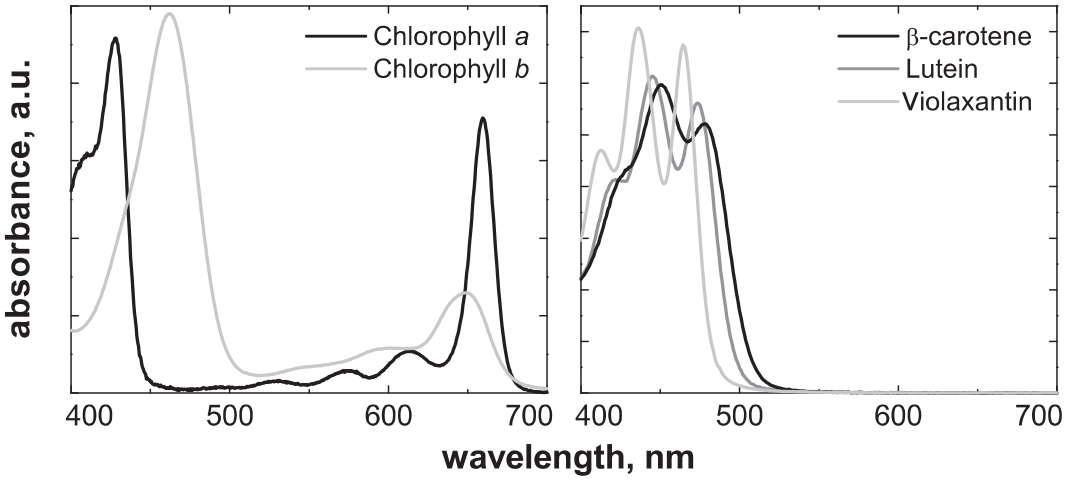

Figure 1.4
Absorption spectra of the pigments found in PS I.

1.2.2 Carotenoids

Carotenoids (Cars) have several essential functions in photosynthesis. First, they are efficient light-harvesting pigments, transferring the collected energy to the Chls (23,24). Second, Cars are irreplaceable for their photoprotective role of quenching harmful Chl triplet and oxygen singlet states, preventing the photooxidative damage of the pigment-protein complexes (25,26). Third, Cars have important structural role in stabilizing the photosynthetic proteins (27,28).

Structurally Cars belong to the group of the polyisoprenoid derivatives. They differ by the number of the alternating single and double bonds in the polyene chain and by the presence and the type of the terminal ring structures (Figure 1.3). The spectroscopic properties of the Cars are mainly determined by their extended π-conjugated electron system, and can also be modified by the presence of some substituents (25). Cars exhibit major absorption in the 400-600 nm range (Figure 1.4), with extremely high molar extinction coefficients (~150000 $M^{-1}cm^{-1}$). This absorption is related to a strongly allowed transition from the ground state (S_0) to the second excited state (S_2). The one photon transition to the first excited state (S_1) is optically forbidden for symmetry reasons. The fluorescence quantum yield of Cars appears to be very low. This is caused by the ultrafast internal conversion from the S_2 to the S_1 state, which efficiently quenches the fluorescence. Moreover, the transition from the S_1 to the S_0 is optically forbidden, making the non-radiative relaxation pathway dominant.

1.2.3 Influence of the environment

The spectral properties of the different pigments are strongly modified by their interaction with the environment (29). Chls and Cars are involved in versatile interaction with the protein in the photosynthetic complexes. These include *i)* H-bonding and *ii)* coordination of the central Mg atom in Chl (30), *iii)* electrostatic interactions; *iv)* mutual polarizabilities; *v)* distortion of the π-conjugated electron system; *vi)* coupling to the vibrational motions of the protein (29). In addition to these, the dense packing of the pigments in the protein scaffold reduces the distances between them allowing multiple pigment-pigment interactions (29). Depending on its immediate surrounding each pigment molecule exhibits different spectroscopic properties as compared to the rest of the pigments or to

pigments in solution. This kind of heterogeneity usually leads to spectral shifts and/or appearance of new peaks or shoulders in their spectra.

1.3 Fate of the pigment excited state

Once a pigment molecule is excited by absorption of a photon, it can return to the ground state through several competing de-excitation pathways. These are well summarized by the famous Perrin-Jabłoński diagram (Figure 1.5). Some of the relaxation pathways are intrinsic for the molecule, *e.g.* fluorescence, internal conversion (IC), intersystem crossing (ISC), *etc*, while others involve intermolecular interactions – energy transfer (ET), electron transfer, *etc*. It is important to understand at this point, that by simply monitoring one of the mutually dependent de-excitation channels, a wealth of information can be obtained about the different reactions that an excited molecule undergoes.

Particularly important for the understanding of the early reactions in photosynthesis are the energy and electron transfer de-excitation pathways.

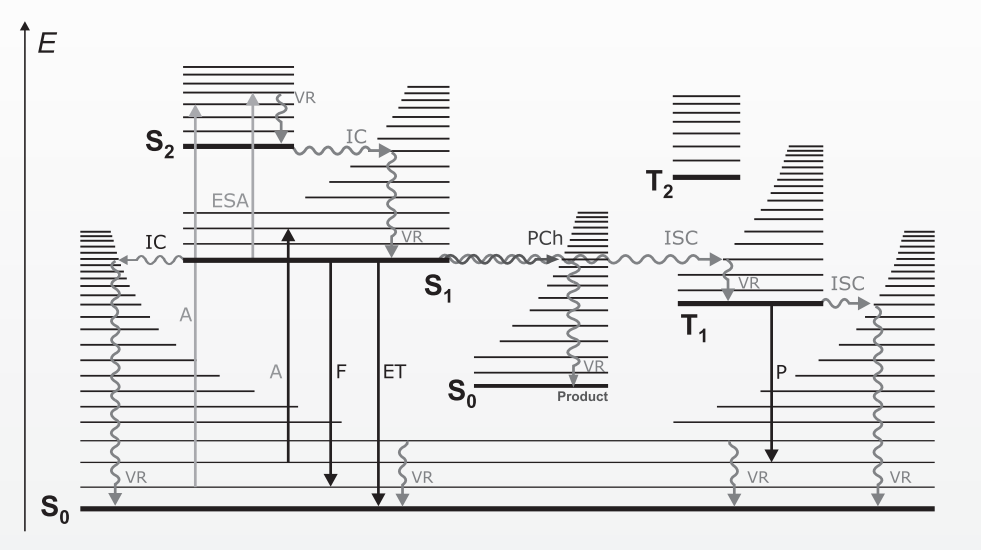

Figure 1.5
Perrin-Jabłoński diagram. The diagram demonstrates in a simple, straightforward manner the major photophysical and photochemical de-excitation pathways that can be used by an excited molecule. The horizontal bold lines represent different electronic states – singlet (S) or triplet (T), while the thin ones – different vibrational states. The straight arrows represent absorption (A), emission (fluorescence (F) and phosphorescence (P)) and energy transfer (ET). The radiationless transitions are shown as wavy arrows – internal conversion (IC), intersystem crossing (ISC), vibrational relaxation (VR), and photochemistry (PCh).

1.3.1 Excitation energy transfer

The process of ET can occur when the fluorescence spectrum of the donor (D) molecule overlaps at least partially with the absorption spectrum of the acceptor (A) molecule. In the case when the ET process occurs repeatedly over several molecules, it should rather be called *energy transport* or *energy migration*. Distinction should be made between the radiative and the non-radiative ET. Radiative ET is realized through absorption by the A molecule of a photon, which was previously emitted by the D molecule. This type of ET is typical for systems with large intermolecular distance. However, in systems like the pigment-protein complexes, where these distances are extremely short, the radiationless ET mechanism is dominant. Due to the spectral overlap between the A and the D molecules, several of their vibronic levels have the same energy and therefore this mechanism is also

called *resonance* ET. Resonance ET occurs without emission of photons and results from short- and long-range interaction between the molecules. The total interaction energy is a sum of two terms: *Coulombic* and *exchange*. The Coulombic term described by Förster (31) is relevant when the ET occurs through relaxation of the excited electron to the ground state in the D and simultaneous promotion of an electron to an excited state in the A. The exchange term (32), on the other hand, is related to ET processes occurring with exchange of electrons between the D and the A. Allowed transitions (singlet-singlet) occur mainly via Coulombic interaction, while the forbidden ones (involving triplet states) via the exchange mechanism.

Very weak Coulombic interactions (Förster's ET mechanism). The changes in the spectral and dynamic properties of interacting pigment molecules can be described by the dipole-dipole term of the multipole expansion of the Coulombic interaction (point-dipole approximation) (33):

$$V_{mn} = \frac{1}{4\pi\varepsilon_0\varepsilon_r}\left(\frac{(\vec{\mu}_m\vec{\mu}_n)}{\left|\vec{R}_{mn}\right|^3} - \frac{3(\vec{\mu}_m\vec{R}_{mn})(\vec{\mu}_n\vec{R}_{mn})}{\left|\vec{R}_{mn}\right|^5}\right) \tag{1.1}$$

where μ is the transition dipole moment of the corresponding pigment, R is the center-to-center spatial vector between the pigments, ε is the dielectric constant for vacuum (0) and the protein environment (r).

When the interaction term in Eq. (1.1) is small, the coupling between the pigments is weak and the excitation is essentially localized on the individual pigments; however, the interaction is still sufficient to facilitate the ET. Förster has derived the following equation for the rate constant of the ET occurring in the weak interaction limit (31):

$$k_{m\to n} = \frac{\kappa_{mn}^2}{R_{mn}^6}\cdot\frac{9c^4\ ln(10)}{128\pi^5 n^4 N_A \tau_m}\int_0^\infty I_m(\nu)\varepsilon_n(\nu)\frac{d\nu}{\nu^4} \tag{1.2}$$

where: k_{mn} is the rate constant for ET between D and A; c is the velocity of light; n is the refractive index of the medium; N_A is the Avogadro's number; κ is an orientational factor; τ_m is the radiative lifetime of D; R is the distance between D and A; ε is the molar extinction coefficient of A; I_D is the area normalized D emission spectrum.

Strong Coulombic interaction. This coupling is present when the intermolecular interaction is stronger than the interaction between the electronic and nuclear motions within the molecule. In this case, the Coulombic term is larger than the width of the individual transitions of the pigments and all the vibronic subtransitions are in resonance. The excitation energy is now delocalized over the interacting pigments and oscillates coherently between the D and the A. This situation is described in the frame of the exciton concept (29,33). The energy levels of the strongly interacting molecules merge into new excitonic bands, whose energy is a weighted combination of the energy levels of the individual molecules.

In photosynthesis, the part of the ET between the pigments which is related to light harvesting (unlike photoprotection, *vide infra*) occurs via singlet-singlet ET and thus relies on the above-described weak and strong interactions between the molecules. However, due to the relatively short distances and the specific orientations of the pigments neither of the two types of intermolecular interactions can be strictly applied; sophisticated techniques are used for the theoretical description of these ET processes (33).

Exchange interaction (Dexter's ET mechanism). This mechanism occurs only when there is overlap of the wave functions of the D and the A. Dexter's mechanism is dominant in the triplet-triplet ET and hence plays an important function in photosynthesis (the photoprotective role of Cars

is realized through ^{3}Chl → ^{3}Cars ET). Contrary to the Förster's mechanism, the ET rate constant is independent from the oscillator strength of both transitions (this is evident from the normalization conditions) (32).

1.3.2 Electron transfer

The photoinduced electron transfer has central role in photosynthesis. The primary photochemical reactions of light energy utilization, which occur after the excitation energy is transferred from the extended antenna system to the RC of the photosynthetic complexes, are essentially electron transfer events between a D and A molecule. The electron transfer reactions are described in the frame of Marcus theory (34). This theory predicts quadratic dependence (unlike ET) of the activation free energy of the electron transfer, ΔG, on the standard free energy, ΔG^0. The electron transfer rate can be expressed in the following way:

$$k_{et} = \frac{2\pi}{\hbar} V_e^2 FC \tag{1.3}$$

where V_e^2 is the electronic coupling between the molecules and FC is the Franck-Condon factor:

$$FC = \frac{1}{\sqrt{4\pi\lambda kT}} exp\left[-\left(-\Delta G^0 - \lambda\right)^2 / 4\lambda kT\right] \tag{1.4}$$

where λ is the total reorganization energy, k is the Boltzmann constant and T is the absolute temperature.

According to this relation, three different regimes for the electron transfer rate can be realized (*cf.* (35) for clear graphical representation):

i) 'activationless' regime ($-\Delta G^0 = \lambda$). This is the situation with highest k_{et} value. The forward electron transfer reactions in the photosynthetic RCs occur in this regime (16).

ii) normal region ($-\Delta G^0 < \lambda$). The electron transfer exhibits thermally activated behavior and k_{et} is lower than in the previous regime.

iii) Marcus' inverted region ($-\Delta G^0 > \lambda$) (extremely exergonic reactions). In this region, the FC factor and therefore the k_{et} decrease again. This regime has been used to explain the relatively low charge recombination probability in the photosynthetic RCs (16).

A comfortable, simplified formula for the electron transfer rate in the 'activationless' regime has also been derived (36-38):

$$log_{10}\ k_{et} = 15 - 0.6(R - 3.6) \tag{1.5}$$

where k_{et} is in s^{-1}, R is the edge-to-edge distance between the redox cofactors, 3.6 is the van der Waals contact.

In this case, k_{et} is primarily dependent on the distance between the D and the A molecules (*cf.* the latter references for simplified formulas describing the electron transfer in the other two regimes).

1.4 Structure of Photosystem I

PS I is a multi-subunit pigment-protein complex, which catalyzes the second part of the light-induced electron transfer reactions in oxygenic photosynthesis (Figure 1.1 & Figure 1.2). Apart from its nearly 100% quantum efficiency, PS I generates one of the most negative reduction potentials (~ -1.2 V) in Nature. Such a negative reduction potential is necessary to boost the energy of the transferred electron so that it can be finally delivered to the relatively poor electron acceptor NADP.

This is in contrast to PS II where the evolution has been concentrated on generating a state, which has more positive reduction potential than H_2O, so that it can drive electron extraction from this very stable molecule (Figure 1.2).

Both structurally and functionally, PS I can be viewed as composed of two parts: *i)* an extensive antenna system, which harvests light quanta and *ii)* a RC part, where the primary CS and the rest of the redox reactions occur.

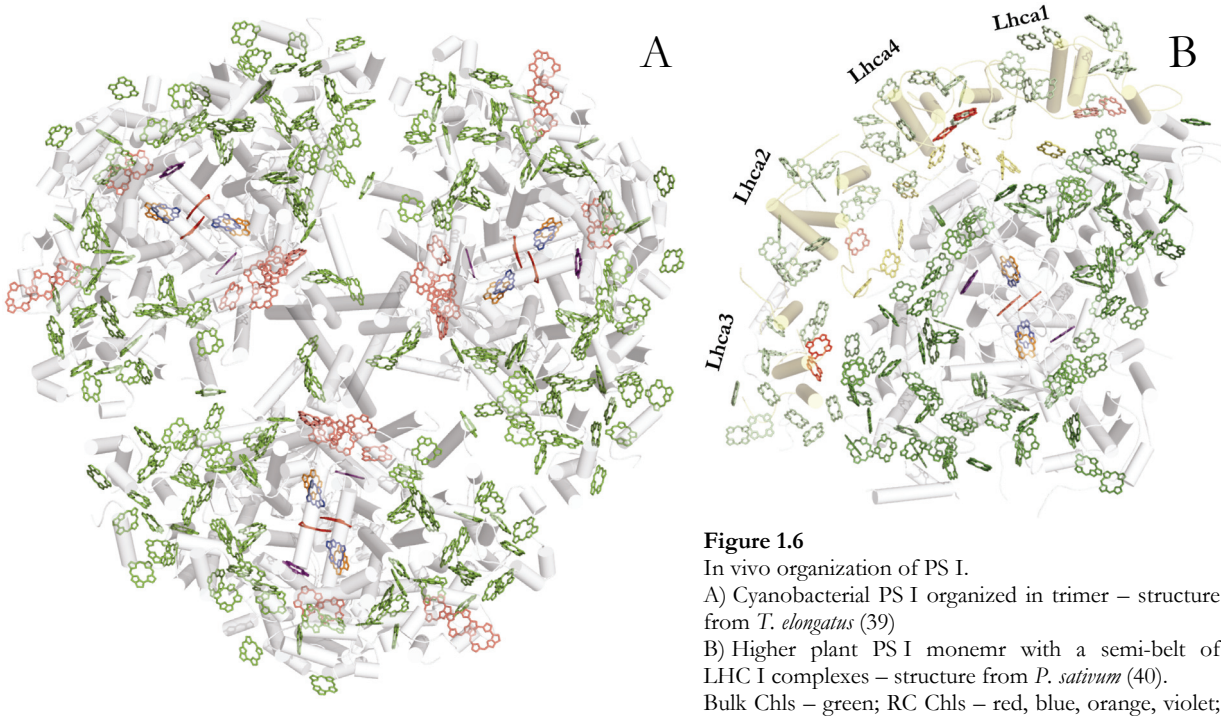

Figure 1.6
In vivo organization of PS I.
A) Cyanobacterial PS I organized in trimer – structure from *T. elongatus* (39)
B) Higher plant PS I monemr with a semi-belt of LHC I complexes – structure from *P. sativum* (40).
Bulk Chls – green; RC Chls – red, blue, orange, violet; LHC I Chls – light green; ′red′ Chls – light or dark red

1.4.1 Structure of cyanobacterial Photosystem I

The structure of PS I from the cyanobacterium *Thermosynechococcus elongatus* is resolved to 2.5 Å (41). *In vivo,* cyanobacterial PS I is predominantly organized in trimers (42,43) (Figure 1.6 A); each monomeric unit of the trimer is composed of 12 protein subunits, which harbour 128 cofactors – 96 Chls *a*, 22 Cars, 4 lipids, 2 phylloquinone (Q_K) molecules, 3 [4Fe4S] clusters, and a Ca^{2+} ion. The core of PS I is formed by two large protein subunits PsaA and PsaB (each with 11 transmembrane helices (TMH)). All of the membrane intrinsic redox-active cofactors and 79 of the antenna Chls of PS I are located in the scaffold formed by these two subunits. The first five TMHs from the C-terminal part of PsaA and PsaB form a pseudo-symmetric structure similar to the D1 and D2 subunits of PS II (2), which surrounds the electron transfer cofactors and isolates them from the antenna Chls at distance >16 Å. The remaining six N-terminal TMHs are organized in pairs and show certain homology to the CP43 and CP47 subunits of PS II. PsaA and PsaB play an important role in the interaction with the soluble electron carriers both on the lumenal and on the stromal side of the thylakoid membrane: *i)* the lumenal loops of PsaA and PsaB have hydrophobic regions which are involved in formation of a docking site for the soluble electron carriers, PC and Cyt b_6f (44); *ii)* the stroma-exposed parts of PsaA and PsaB are in contact with the three membrane extrinsic subunits of PS I – PsaC, PsaD and PsaE, which form a specific ridge for attachment of Fd (2). The electron transfer to Fd is facilitated by the two terminal [4Fe4S] clusters, F_A and F_B, which are bound to PsaC. The structure of cyanobacterial PS I is completed by seven small transmembrane subunits, which carry the rest of the

antenna Chls. These subunits are involved in different interactions, like *e.g.* with the other PS I monomers during the trimer formation (PsaL, Figure 1.8) (2) or with the peripheral antenna formed by the iron stress induced protein IsiA (PsaF, PsaJ, PsaK) (45).

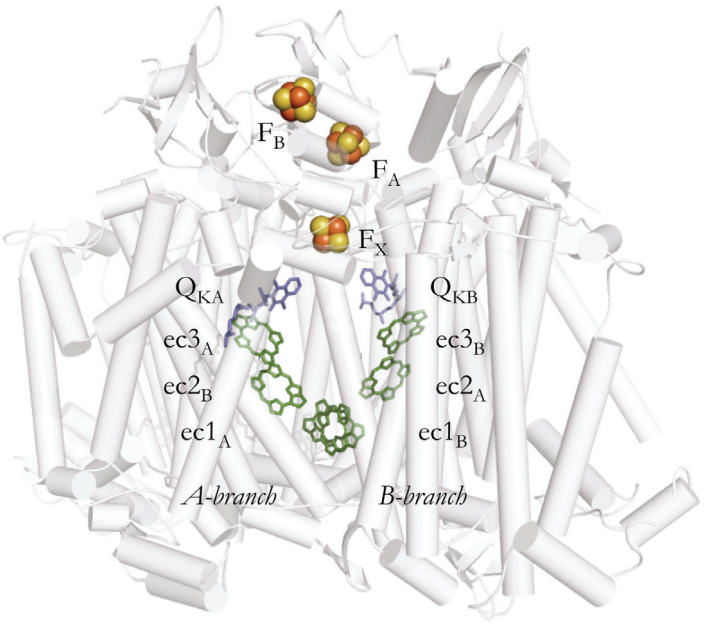

Figure 1.7
Structural organization of the electron transfer cofactors in the RC of PS I (41)

Organization and properties of the cofactors in the PS I RC. Similar to all other known RCs, the cofactors in the RC of PS I form two quasi-symmetric branches (Figure 1.7), diverging from a Chl *a*′/Chl *a* pair ($ec1_A$, $ec1_B$), traditionally called P_{700} (41). The chlorin rings of the P_{700} Chls are oriented parallel to each other at distance of ~3.6 Å, and perpendicular to the membrane plane. Interestingly, Chl *a*′ forms three H-bonds to the protein, while Chl *a* - none. This difference leads to enhancement of the electronic asymmetry of the P_{700} heterodimer and is most probably the reason for the shift of the spin density of $P700^{+\bullet}$ to the $ec1_B$ Chl (46). The next cofactors in each branch are two Chl *a* couples, $ec2_A/ec2_B$ (sometimes called accessory Chls) and $ec3_A/ec3_B$ (assigned to the spectroscopically identified primary electron acceptor, A_0). These Chls have relatively unusual ligands – H_2O is the axial ligand to ec2, while Met to ec3 (41). It has been suggested that the low reduction potential of $ec3/ec3^-$ pair is due to the Met ligation (47). In each cofactor branch, the ec2 and the ec3 Chls are parallel to each other with plane-to-plane distance of ~3.86 Å. The six Chls of the RC are strongly coupled (6,48-54), which leads to a ′red′ shift (~700 nm) of their absorption spectrum in comparison to the bulk antenna Chls (680 nm), and broadening of the covered light energy range. This change in the properties of the RC Chls has high importance for the effective energy transfer from the different antenna compartments (55). The last cofactors in the two branches of PS I are two phylloquinone molecules (Q_{KA} and Q_{KB}, spectroscopically identified as the secondary electron acceptor, A_1). Both of the Q_Ks are involved in specific interactions with the protein environment; on the one hand, they form only by one H-bond to the protein (in contrast to Q_A in PS II forms two H-bonds) and on the other hand, the Q_Ks are in π-stacking contact with Trp residues. It has been suggested (56,57) that these interactions are the reason for the extremely low reduction potential of the Q_K/Q_K^- couple in PS I, which is the most negative amongst the quinones found in Nature (58). Finally, the two cofactor branches join at the F_X [4Fe4S] cluster. Four conserved Cys residues (by two

from PsaA and PsaB) are the ligands to this cluster. The environment of the two Q_Ks and the F_X shows significant asymmetry between the two branches (2,41), which may play an important role in the electron transfer reactions.

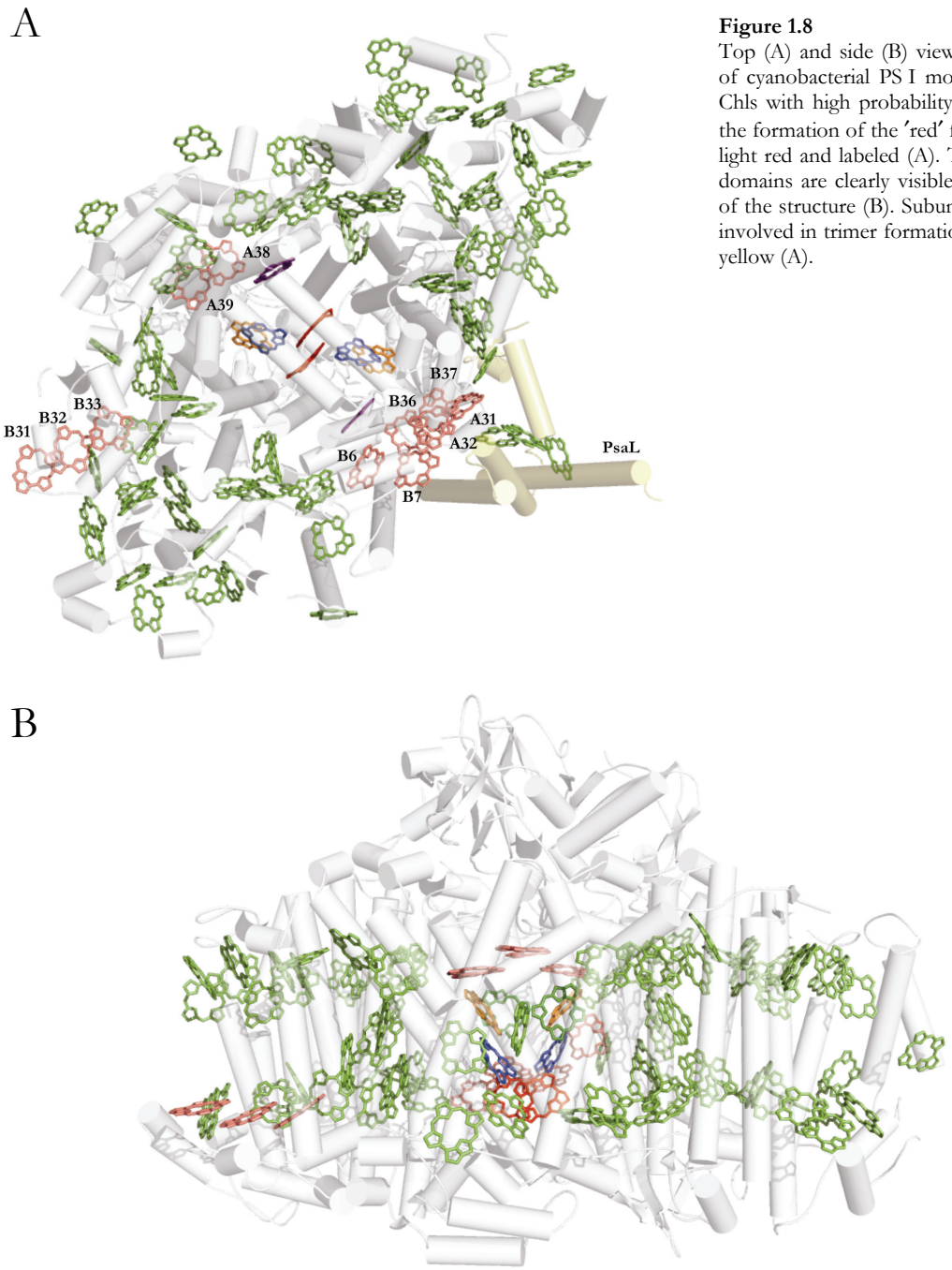

Figure 1.8
Top (A) and side (B) view of the structure of cyanobacterial PS I monomer (41). The Chls with high probability to participate in the formation of the ′red′ forms are painted light red and labeled (A). The bulk antenna domains are clearly visible in the side view of the structure (B). Subunit PsaL, which is involved in trimer formation is painted pale yellow (A).

The core antenna system of PS I. The core antenna of PS I is densely packed with 90 Chls *a* and 22 Cars which efficiently transfer the absorbed light energy to the RC, where the primary photochemical reaction occurs. Structurally, the Chls of the core antenna of PS I are organized in three domains (41) (Figure 1.8): *i)* central domain, which surrounds the cofactors in the RC (at distance of ~16 Å) and spreads from the lumenal to the stromal side of the complex; and *ii)* two peripheral domains (one on each side of the central domain) organized in two separate layers – stromal and lumenal. The presence of the central domain is a notable difference between PS I and PS II (8), which may contribute to the difference in their quantum efficiency. The organization of the

Chls in the cyanobacterial PS I is such that it facilitates efficient excitation energy transfer inside the core antenna and between the monomers in a PS I trimer (59,60). The majority of the antenna Chls (so-called bulk antenna Chls) has similar spectroscopic properties and forms an absorption band with a maximum at ~680 nm.

'Red' Chlorophylls. In the core antenna of some cyanobacterial PS I complexes exist the so-called 'red' Chls (61,61,62). These Chls have very broad, 'red'-shifted spectra and absorb light with significantly lower energy than the bulk antenna Chls and, more surprisingly, than the six coupled Chls of the RC. The peculiar properties of the 'red' Chls are explained by a strong excitonic interaction between neighboring Chls (63,64) and high electron-phonon coupling (64-68), likely combined with energetic shifts induced by the protein (69). In addition, mixing with a charge transfer state was also proposed (64,66,68,70-72).

The precise location of these Chls in the core antenna system is not identified yet. Amongst the proposed positions are the monomer-monomer interaction region of the trimer (41), in the vicinity of the RC (73), or more to the periphery of the complex (66,71,74-76). At present, few pools of Chl molecules (the trimer B31/B32/B33, and the dimers - A38/A39, A32/B7 and B37/B38) have some experimental basis (41,77) to be the most likely candidates for the formation of the 'red' Chls in cyanobacteria, in particular in *T. elongatus* (Figure 1.8). However, several other Chl groups (the tetramer A31/A32/B7/B6, the trimers A2/A3/A4, A19/A20/A21 and the dimers A12/A14, A26/A27, A24/A35, A33/A34, B24/B25, B22/B34) were also proposed to contribute to the peculiar 'red' forms (59,69,71,78,79). It is apparent that the uncertainty in the assignment of the 'red' pigments is fairly large, since the different proposals involve over 20% of the Chls of PS I.

1.4.2 Structure of higher plant Photosystem I

Currently, the structure of higher plant PS I (from *Pisum sativum*) is resolved to 3.4 Å resolution (40). Unlike cyanobacterial PS I, which forms trimers (Figure 1.6), higher plant PS I exists as a monomer (80) with a semi-belt of four LHC I proteins, attached on one side of the PS I complex (40) (Figure 1.9). It is worth noting that although the composition of the PS I core complex is the same in higher plants and algae (81), their macroorganization differ significantly. This is mainly due to the higher number of LHC I complexes attached to the PS I core complex in algae (82,83).

PS I core complex. The core complex of higher plant PS I is composed of 14 protein subunits, which harbor approximately 100 Chls, as well as the redox-active cofactors of the RC (*vide supra*). At present, the resolution of the higher plant PS I structure is not high enough to allow assignment of the expected ~30 Cars. The structural comparison between cyanobacterial and higher plant PS I shows that the structure of the core complex is well preserved (84), thus here we will only discuss the major differences between the two complexes.

From all the subunits of cyanobacterial PS I only two are not present in the higher plant core complex – PsaX and PsaM. However, there are four new subunits in higher plant PS I – PsaG, PsaH, PsaN and PsaO, of which only PsaO is not resolved in the structure (40). While subunit PsaH is located close to the subunit PsaL and is suggested to play role in the docking of LHC II during state transitions (85), subunit PsaG is positioned on the opposite side of the core complex and provides most of the contact area for LHC I (Figure 1.9). The major changes in the preserved subunits can be found in PsaF, which in higher plants has larger lumenal region that enables more efficient PC binding (86). Additionally, certain changes can be observed in subunit PsaL (40), which together with the close association of PsaH prevent trimer formation (*vide supra*) in higher plants (Figure 1.9).

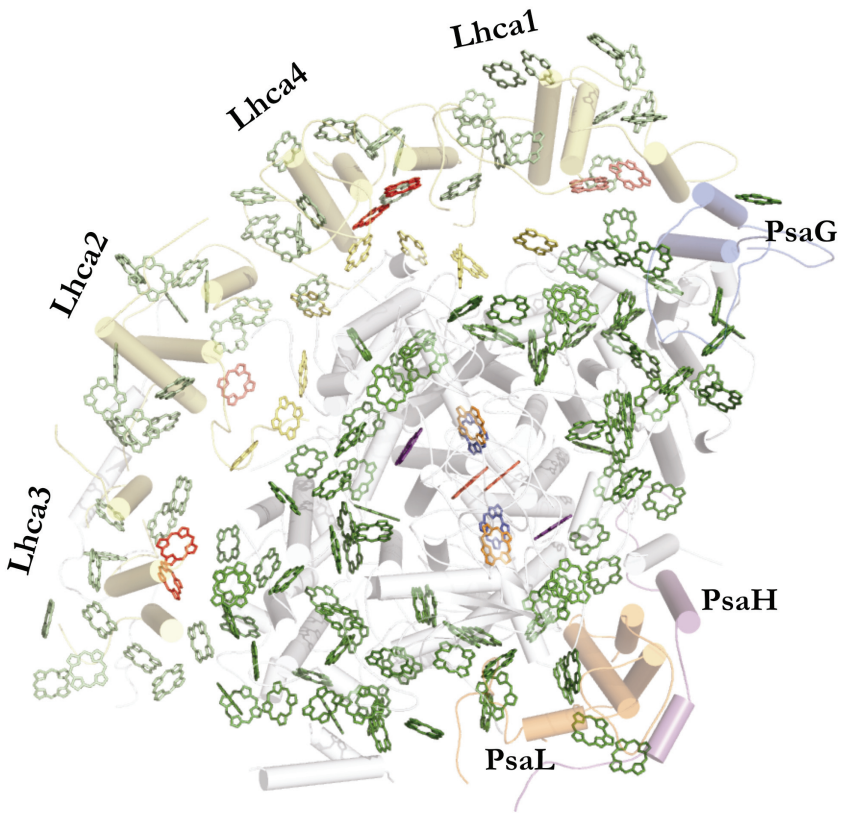

Figure 1.9
Structure of higher plant PS I. ′red′ Chls – dark or light red; bulk Chls of the core antenna – dark green; bulk Chls of the LHC I – light green; RC Chls – red, blue, orange.

Light-harvesting complex I (LHC I). The antenna system of PS I in higher plants is extended by four Chl *a* and *b* binding light-harvesting proteins, Lhca 1, Lhca 2, Lhca 3, and Lhca 4. These proteins are present in single copy per PS I and are organized in two adjacent dimers (Lhca 1/4 and Lhca 2/3) attached on one side of the core complex. The structure suggests that the strongest contact between the LHC Is and the core complex is due to the interaction between the Lhca 1 and the PsaG subunit (40). The rest of the peripheral antenna complexes interact only weakly with the core complex; Lhca 4 interacts with PsaF and Lhca 2 – with PsaJ. LHC Is share sequence and structural homology with the LHC II complexes of PS II. Each Lhca monomer is composed of two long and one short TMHs and binds ~14 Chl *a* and *b* molecules (40). The organization of the LHC I complexes is such that most of their Chls are arranged in a narrow belt with Mg-Mg distance to the closest Chls from the core complex of ~20-30 Å.

Similarly to cyanobacterial PS I, higher plant PS I also contains the peculiar **′red′ Chls**. However, in higher plants these Chls are shifted outside the PS I core complex to the LHC I complexes (Figure 1.9). In this respect, the spectral properties of the LHC Is are significantly influenced in comparison to LHC II. The strongest spectral ′red′ shift is observed for Lhca 4 and Lhca 3, while this shift is much weaker in Lhca 2 and Lhca 1 (87). Mutation analysis of the LHC I proteins (88-91) shows that the Chls involved in the formation of the ′red′ forms are always located in positions A5 and B5 (92,93) (or according to the new nomenclature 603 and 609 (94)).

′Gap′ chlorophylls. Nine Chl molecules, stuffing the cleft between the LHC Is and the core complex have been resolved in the latest higher plant PS I structure (40) (Figure 1.9). The ′gap′ Chls stabilize the interactions and increase the ET coupling between the LHC Is and between them and the core complex (95). Additionally, it has been suggested that the ′gap′ pigments may play certain role in the formation of the ′red′ Chls (96).

1.5 Light harvesting in Photosystem I

All known photosynthetic complexes are composed of relatively large antenna system, harvesting light and a small RC unit, where the primary CS reaction occurs. The reason for such an organization can easily be found in the low photon flux to which photosynthetic units are normally exposed. In fact, rough calculations show that under average day light conditions each Chl molecule can absorb ~10 photons per second (16). This would make the operation rate of a hypothetical system composed of one Chl and complete electron transfer chain very low and inefficient. In the photosynthetic systems, this problem is overcome by gathering the light energy in a large antenna and then transferring it to a highly active RC.

1.5.1 Trapping models of light harvesting kinetics – general concepts

The efficiency of light utilization in the photosynthetic complexes does not depend merely on the size of the antenna system but also on the coupling of the antenna to the RC and, furthermore, on the properties of the RC itself. Detailed kinetic studies are necessary to assign correctly the role of each of these factors in the excitation trapping kinetics. Quite generally the excited state lifetime of a photosynthetic complex can be presented as a sum of three contributions (*cf.* (29,97,98) for detailed description):

$$\tau_{avg} = \tau_{trap} + \tau_{mig} + \tau_{del} \tag{1.6}$$

where τ_{avg} is the average lifetime of the excited state, τ_{trap} (sometimes marked as τ_{CS}) is the lifetime of the trapping of the excitations located on the RC, τ_{mig} is the average first passage time for an excitation to approach the RC, τ_{del} is the additional time needed for the energy to be delivered to the RC. The sum of the last two contributions is sometimes represented as τ_{ET}.

Depending on which term dominates the latter expression (Eq. (1.6)) three extreme cases for the trapping kinetics in the photosynthetic complexes can be distinguished.

Diffusion-limited kinetics. This case is realized when the migration of the excitation energy in the antenna system is the slowest process, and hence τ_{mig} is the dominating term in Eq. (1.6). Currently, there is general agreement that this term has insignificant influence since the energy equilibration in the core antenna is completed on the time scale of ~1-2 ps (51,52,70,99,100); interesting exception are the ′red′ Chls in PS I (76,101). However, it is important to note here that although the energy equilibration in the antenna is very fast, the antenna enlargement is limited. This is due to the fact that the increase of the antenna size leads to an increase of the time the excitation spends outside the RC, and hence to an increase of the probability for other de-excitation pathways (*e.g.* fluorescence or radiationless decay).

Transfer-to-the-trap-limited kinetics. This model has been proposed (102-105) in relation to the relatively large distance between the core antenna and the RC cofactors (>16 Å in PS I (41) and ~20 Å in PS II (8)). Since the rate of ET is strongly dependent on the distance between the molecules (*cf.* Section 1.3.1) such a separation between the antenna and the RC is expected to increase the time necessary for the ET to the RC (τ_{del} in Eq. (1.6)) and make it the dominant process in the trapping kinetics.

Trap-limited kinetics. The last model describing the trapping kinetics is realized when both the energy migration (τ_{mig}) in the antenna and the energy delivery to the RC (τ_{del}) are much faster than the trapping of the excitation energy on the RC (τ_{trap} dominates in Eq. (1.6)). In this case, the probability that the excitation will escape from the RC before it is consumed is very high. If we assume identical excited state energy for the antenna and the RC, this probability is directly proportional to the

antenna size (98). A special case of the trap-limited kinetics is the so-called *exciton-radical-pair-equilibrium (ERPE) model* (106), which describes a situation where the primary photochemical reaction in the photosynthetic complexes is reversible, hence, the charge-separated state can recombine to an excited state and the excitation can move back to the antenna. The ERPE model is proposed to describe the kinetics in both PS I (52) and in PS II (100).

1.5.2 Trapping kinetics in Photosystem I

Despite the large number of theoretical and experimental works on PS I complexes from various organisms, currently there exist no agreement about the type of the kinetics that describes the light utilization in PS I. It appears, however, that the major discrepancies in the field are not primarily related to differences in the experimental data (52,75,76,107-110), but rather to differences in the used modeling approaches (52,76,107-109,111). Since the ET processes in the antenna are very fast (except for the ′red′ Chls) (51,52,70,99) the possibility for diffusion-limited kinetics in PS I is generally not supported, although there are some theoretical works which are in favor of such model (112). Based on the relatively large distance between the RC and the antenna system (*vide supra*) significant part of the experimental data are analyzed or discussed in the frame of the transfer-to-the-trap-limited model (76,107-109,111,113). The lifetimes describing the excited state kinetics of PS I found in these studies are usually split in two groups: *i)* several minor lifetimes bellow ~15 ps, which are assigned to energy equilibration in the antenna and between the antenna and the ′red′ Chls; and *ii)* one main lifetime of ~20-30 ps, which is assigned to the trapping process from the bulk antenna (depending on the model several other trapping lifetimes might be present reflecting the decay from some minor antenna compartments, like *e.g.* the ′red′ states). Although a bit confusing, in the description of the transfer-to-the-trap-limited model (*vide supra*) the last lifetime(s) is in fact related to τ_{del} in Eq. (1.6) and represents the arrival of the excitation to the RC (the process of CS in the RC is assumed to be much faster than the delivery of the excitation energy, and thus is not considered in the transfer-to-the-trap-limited representation (τ_{trap} is ignored)). Several experimental and theoretical works have proposed a more balanced description of the trapping kinetics in PS I in which the model is neither purely trap-limited nor purely transfer-to-the-trap-limited (49,59,75). Nevertheless, typical problem of all these studies appears to be a certain oversimplification of the kinetic picture of PS I. In most of the above-mentioned works *a priori* has been assumed that the RC and its kinetics cannot be experimentally resolved. However, there hardly exists any experimental evidence for such a justification. On the contrary, the strong coupling between the RC pigments (6,48-54) and their relatively distant position from the antenna (*vide supra*) imply that such a compartment should be present. In fact, recent studies on PS I core complexes isolated from *Chlamydomonas reinhardtii* (do not have ′red′ Chls which may obscure the RC signal), using the ERPE model, have resolved kinetically and spectroscopically the RC compartment (52). In this work for the first time has been resolved also the lifetime of the energy equilibration between the antenna and the RC (~2 ps). This lifetime (predominantly related to τ_{del}) appeared to be much shorter than the overall excited state decay lifetime (~13 ps) resulting in a trap-limited description of the PS I kinetics. An important question that remains after this study is whether the same kinetic description applies to PS I complexes that contain ′red′ Chls. These Chls are expected to have significant influence on the ET processes due to their slow equilibration kinetics.

1.5.3 The role of antenna size and ′red′ chlorophylls in the trapping kinetics of Photosystem I

The antenna system of PS I has two specific properties: *i)* it is relatively large; and *ii)* it often contains low energy Chls (′red′ Chls). Both features have an effect of slowing down the trapping kinetics (104); the large antenna size by increasing the energy equilibration time and the de-trapping probability from the RC, and the ′red′ Chls by acting as temporal energy traps in the antenna. Quantification of these effects is of major interest. On the one hand, the knowledge about the properties of large antenna systems, covering broad spectral range has significant application in the design of artificial light-harvesting systems. On the other hand, the information about the effect of the ′red′ Chls on the trapping kinetics of PS I can be used to better understand their physiological role – funneling excitations to the RC (114); photoprotection (61,114-119) or broadening the covered light energy range (115,120,121). However, the transfer-to-the-trap-limited model (*cf.* Section 1.5.2) which is widely used to describe the kinetics in PS I (76,104,108,109) has some weak points, which do not allow correct discussion of the role of the antenna size and the ′red′ Chls. In such models, direct trapping from the ′red′ compartments is allowed, although none of the proposed ′red′ Chls is located near the RC (*vide supra*). In addition, very high radiationless deactivation rate is used, which would severely reduce the quantum yield of CS in PS I. In respect to these problems a new kinetic description of the trapping processes in PS I complexes containing ′red′ Chls is necessary.

1.5.4 Electron transfer in the reaction center of Photosystem I

During the last decade the view about the electron transfer processes in PS I has been totally reshaped. Initially, it has been assumed that the primary CS reaction takes place between P_{700} and the ec3 Chl (A_0) and several attempts were made to resolve the lifetime of this process. However, the results were quite contradictory, yielding lifetimes ranging from ~2-4 ps (111,122), through ~13 ps (123) up to ~20-30 ps (70,76,108,124-126). The critical examination of these studies reveals problems in almost any of them. First, the ultrashort lifetime for the primary CS, found in (111,122), is highly unlikely for a one-step electron transfer, considering the large distance (>15 Å) between P_{700} and the ec3 Chl (*cf.* Section 1.3.2). Second, in some of these studies (111,122,122,126) an assumption that the excited state decay is the same in PS I with open (P_{700} is reduced) and closed (P_{700} is oxidized) RC has been made. However, it has been shown that this assumption is not correct (75). Third, all the attempts to model the experimental data were made with kinetic schemes, which did not include the excited RC compartment (70,76,108,124-126). Such models, however, are essentially unable to describe correctly the reactions that occur after the trapping of the excitation and thus the observed lifetimes can easily be a mixture of different energy and electron transfer components. The real breakthrough in the understanding of the early electron transfer reaction in PS I was made in a series of studies on *C. reinhardtii* PS I core complexes (6,52,127). Using the ERPE model, without any *a priori* assumptions and including the excited RC state, these studies demonstrated convincingly that the formation of the $P_{700}^{+}ec3^{-}$ state occurs in two electron transfer steps. Furthermore, they showed that, similarly to PS II (4,5), the primary CS in PS I occurs between the ec2 (Chl_{acc}) and the ec3 Chls, followed by a fast electron transfer from P_{700} to ec2. The apparent lifetime for the primary CS from the ec2, found in these studies, was ~8 ps, while the lifetime for the secondary electron transfer from P_{700} ~19 ps. The next electron transfer reaction in the RC of PS I is the re-oxidation of the ec3 Chl by the Q_K. The lifetime for this reaction is commonly accepted to be ~30 ps (52,128).

By analogy with PS II, the results from the studies on the electron transfer reactions in PS I were usually interpreted as a single branched electron transfer. Although such an interpretation has a reasonable explanation in the case of PS II, where the electrons are ultimately delivered to the mobile electron carrier Q_B, in the case of PS I it is no longer rational, since the quinone molecules are only intermediate electron transfer cofactors, which are permanently positioned in the structure of the complex. Moreover, the two cofactor branches in PS I share relatively high symmetry (*cf.* Section 1.4.1 and Figure 1.7), which makes the presence of an obsolete branch even more bizarre. Nevertheless, it should be noted here that there is a breakdown in the symmetry of the two branches found in P_{700} (*cf.* Section 1.4.1), which may support a single-branched electron transfer. However, since it was shown that not P_{700} but in fact an ec2 Chl functions as the primary donor in PS I (6), the asymmetry in P_{700} is more likely to be related to the reduction of P_{700}^+ by the mobile electron carriers PC and Cyt *c*$_6$ rather than to the directionality of the electron transfer towards the [4Fe4S] clusters.

For the first time experimental results were discussed in relation to a bi-branched electron transfer in PS I by Joliot and Joliot (129), who observed two phases ($\tau_{1/2}$ of 18 ns and 160 ns) in the absorption difference signal related to Q_K^- re-oxidation in *Chlorella sorokiniana* cells. Similar results were obtained also in other studies (130-134) but they were not always interpreted as bi-branched electron transfer. However, the direct evidence for the branching of the electron transfer has come from a study on *C. reinhardtii* mutants where the Trp residues in π-stacking contact with the Q_Ks were exchanged with Phe (135). This exchange had an immediate effect on the electron transfer rates of both phylloquinones. Furthermore, the results provided for the first time assignment of the two phases to particular cofactor branch, *i.e.* the fast phase to the B-branch and the slow phase to the A-branch. Even tough the above-mentioned works are extremely valuable; they describe only the final steps of the electron transfer along the cofactor branch(es), *i.e.* the redox state of Q_K. However, the important decision about the branch along which the electron will be transferred is taken already in the primary CS reaction. Consequently, in order to resolve categorically the branching problem and to understand the underlying mechanisms, ultrafast time-resolved studies have to be conducted. In this regard, Dashdorj and co-workers have studied the electron transfer kinetics in cyanobacterial PS I RC, where the axial ligand to the ec3 Chls (Met) has been modified in either of the branches (136). However, the authors concluded that the electron transfer in cyanobacteria is strongly asymmetric and proceeds predominantly along the A-branch. Nevertheless, the results from this study should be considered with caution because of two reasons. First, the data was analyzed with the help of a questionable approach, where a double difference signals from open and closed RC is used (based on the assumption that the excited state decay would be the same in both cases, *vide supra*). And second, which is partly a consequence of the used approach, the analysis could not resolve two important lifetime components present in other studies (6,52). The non-resolved components in fact represent the first two electron transfer reactions. In contrast, similar PS I mutants from *C. reinhardtii* were used to demonstrate bi-directional electron transfer with 1:1 ratio (137). Mutations of the axial Chl ligands, as used in the last two studies, are often harsh and bring about relatively large changes. A more elegant approach has been used by Li and co-workers (138), who studied *C. reinhardtii* PSI where the Tyr residues involved in H-bond formation to the ec3 Chls have been exchanged by Phe. These authors show several evidences, including EPR results, supporting the bi-directionality of the electron transfer in PSI. However, none of the above studies attempted a detailed kinetic analysis of the data; without such analysis, the mechanisms of the primary electron transfer processes in PS I remain unrevealed. In this respect we should note that the model used in (6,52,127) and discussed at the end of the previous paragraph is still valid even if the electron transfer kinetics in PS I is bi-branched; in

this case it simply represents the combined kinetics of the two branches. This model could be used as a basis for the development of a more complex kinetics scheme, which accounts for the electron transfer in each branch. Whether such a model will successfully describe the experimental data remains to be elucidated.

1.6 Goals and structure of this work

PS I is one of the main components of the oxygenic photosynthetic apparatus. Several specific features, like *e.g.* very high quantum yield, large antenna system, low energy Chls in the antenna, two electron transfer branches, make this complex an ideal model system for studying the mechanism of the early reactions of light energy utilization. However, the extensive introduction and discussion in this chapter demonstrate that many aspects of the operation of this complex are not clear yet (*vide supra*). In this respect, the current work aims at achieving better understanding of the operation principles of PS I. Of particular interest were the following questions:

i) What is the type of the trapping kinetics in PS I complexes with ′red′ Chls in their antenna system and can this kinetics be correctly described with the help of the previously proposed ERPE model (52)?

ii) What is the precise influence of the antenna size and the ′red′ Chls on the trapping kinetics of PS I and what could be their physiological role and practical application?

iii) What is the location of the ′red′ Chls in the antenna of PS I?

iv) Are both of the cofactor branches in the PS I RC competent in conducting electron transfer and if yes, what is the branching ratio?

v) What could be the reason for the presence of a second electron transport branch and what practical application it can have?

In order to answer these questions we have studied different PS I complexes – cyanobacterial PS I monomers and trimers, higher plant core and intact PS I complexes, and algae PS I core complexes (wild type and mutants). The advantage of using such a variety of systems is that each one has specific properties, which allowed us to test different features of the trapping kinetics in PS I. To accomplish our goals we have employed two ultrafast time-resolved optical methods – time-resolved fluorescence (single-photon counting and streak camera techniques) and transient absorption.

Structure of the thesis:

Chapter 1 introduces the main reactions occurring during the light-dependent phase of photosynthesis. Additionally, it gives an overview on the major issues in the light energy trapping kinetics (in particular of PS I) that still remain to be elucidated.

Chapter 2 summarizes the main experimental techniques and data analysis strategies used in the current work.

Chapter 3 represents a broad description of one of the methods used here – synchroscan streak camera – for time-resolved detection of fluorescence signals. Separate chapter has been dedicated to this method because the installation and development of the Synchroscan Streak Camera is a significant part of this work. The chapter covers the main tests that were performed during the installation of the set-up and improvements that were made during this work in order to obtain high quality data from this set-up.

Chapter 4 is a thorough investigation of the light energy trapping kinetics in higher plant PS I complexes. This work reveals the type of trapping kinetics in higher plant core and intact PS I

complexes. Additionally, it provides a complete description of the influence of bulk antenna enlargement and the presence of the ′red′ Chl on the trapping kinetics.

Chapter 5 is a study of the light energy trapping kinetics in cyanobacterial PS I complexes – monomers and trimers, addressing the same question as in the previous chapter. Appart from describing the type of trapping kinetics in this complexes and the impact of the ′red′ Chl on it, this chapter also delivers some qualitative information about the plausible location of the ′red′ Chls in the structure of PS I.

Chapter 6 describes a sub-ps time resolved study on intact PS I complexes isolated from *C. reinhardtii*. The sub-ps time-resolution of this work allows a more detailed description of the ET processes in the antenna system of this complex.

Chapter 7 deals with the branching of the electron transfer reactions in the RC of PS I. It describes for the first time the primary electron transfer reactions in both cofactor branches and provides additional evidence that the primary charge separation processes in PS I occurs between the ec2 and ec3 Chls in the RC. The results on this study are of great practical importance since they reveal the solution used by Nature to optimize the light trapping kinetics from large antenna systems.

Chapter 2

Materials and methods

2.1 Samples and their preparation for the experiments

2.1.1 Higher plant Photosystem I – core and intact* complexes

The higher plant PS I complexes used in this work were isolated from *Arabidopsis thaliana* thylakoids. The isolation and purification of the complexes was done by Matteo Ballottari in the group of Roberto Bassi at the department of Biotechnology, Verona University, Italy (for details see (50)).

For the time-resolved fluorescence measurements, the isolated core and intact PS I complexes were diluted in 30 mM Tricine buffer# (pH 7.8), containing 500 mM sucrose and 0.009% n-dodecyl-(α)-D-maltoside (α-DM) to an OD ~0.3 cm^{-1} at the Chl *a* Q_Y maximum.

2.1.2 Cyanobacterial Photosystem I – monomers and trimers

The cyanobacterial PS I complexes used in this work were isolated from the thermophilic bacterium *T. elongatus*. The isolation and purification of the complexes was done by Eithar El-Mohsnawy in the group of Mathias Rögner at the Plant Biochemistry department of Ruhr-University Bochum, Germany (for details see (139)).

For the time-resolved measurements the purified and concentrated PS I complexes were resuspended in 30 mM Hepes buffer# (pH 7.5), containing 10 mM $MgCl_2$, 10 mM $CaCl_2$, 200 mM Mannitol and 0.02% β-DM to an OD ~0.6 cm^{-1} at the Chl *a* Q_Y maximum.

2.1.3 Algae Photosystem I – core and intact complexes (wild type and mutants)

The algae PS I complexes used in this work were isolated from the *C. reinhardtii*. The isolation and purification of the complexes was done by Galina Gulis and Rajiv Luthra in the group of Kevin Redding at the Chemistry and Biochemistry department of Arizona State University, USA (for details see (138,140)).

For the time-resolved measurements the purified and concentrated PS I complexes were resuspended in 25 mM Hepes buffer# (pH 7.5), containing 100 mM NaCl, 5 mM $MgSO_4$, 200 mM Mannitol and 0.01% β-DM to an OD at the Chl *a* Q_Y maximum of ~0.8 cm^{-1} for the streak camera measurement and ~7-8 cm^{-1} for the transient absorption measurements. Alternatively, in some measurements the following buffer# was used: 25 mM Tricine (pH 7.5), 100 mM NaCl and 0.02% β-DM.

In order to study the electron transfer reaction in the cofactor branches two PS I mutants were used: PsaA-Y696F and PsaB-Y676F (the numbering of the residues is according to the cyanobacterial PS I structure (41)). In the mutants the Tyr residue, forming an H-bond to the ec3 Chl (primary electron acceptor, A_0, *cf.* Sections 1.4.1 and 1.5.4) in A- and B-branches is exchanged with Phe. This substitutions destroys the H-bond and consequently changes the redox properties of the ec3 cofactor and the electron transfer rates for the steps in which this Chl is involved.

---

* The expression *intact PS I* refers to a complex composed of the PS I core and the attached semi-belt of LHC I (*cf.* Section 1.4.2)

All buffers were prepared with filtered water (Millipore, Schwalbach, Germany); the buffers were additionally filtered (Millipore, 0.22 μm pore size) before the addition of the sample to remove any potential light scattering sources. Origin of the chemicals: Fluka Biochemika, Buchs, Switzerland – Mannitol, $MgSO_4$, Sucrose; Glycon, Luckenwalde, Germany - α(β)-DM; Merck, Darmstadt, Germany - $CaCl_2$; Roth, Karlsruhe, Germany – Hepes, $MgCl_2$, NaCl, Tricine.

2.1.4 Redox state of the Photosystem I complexes during the experiments

Of particular importance for the time-resolved studies of the energy trapping and electron transfer kinetics of PS I is the redox state of the complexes. It has been shown that trapping kinetics differs significantly between PS I with open (P_{700} reduced) and closed (P_{700} oxidized) RC (75). In order to prevent the accumulation of closed RC during the experiments, the redox agents sodium ascorbate (40 mM) and phenazine methosulfate (60 μM) were added to the buffer medium[◊] and the measurements were conducted in darkness.

2.1.5 Sample protection from reactive oxygen species (ROS)

During sample preparation special care was taken to prevent the formation of ROS: *i)* the buffer was bubbled with N_2 for a period of ~1 h under Ar atmosphere; *ii)* the sample preparation was made in oxygen free conditions; *iii)* the so-called oxygen-scavenging system (141), containing 8 mM glucose, 65 μl/ml glucose oxidase and 65 μl/ml catalase[◊], was added to completely eliminate the presence of oxygen throughout the experiment.

2.2 Calculation of the optimal excitation conditions for PS I complexes.

Generally, the kinetic description of the ultrafast processes in the photosynthetic systems is limited to the first order reactions and higher order processes such as singlet annihilation are not taken into account. In this respect, special care should be taken to assure single excitation of the studied sample and avoid higher order reactions.

Several factors should be taken into account in the estimation of the excitation intensity that can be used in the time-resolved measurements of PS I; namely the frequency and the wavelength of the available excitation source (usually pulsed laser) and the molar extinction coefficient (ε) of the excited chromophore (ε of Chl *a* is ~80000 $cm^{-1}M^{-1}$ at the Q_Y max). The extinction coefficient should be corrected for the total number of chromophores in the sample (*e.g.*, in the case of PS I core, the total number of chromophores (Chls) per particle (single PS I core complex) is ~100, hence $\varepsilon_{corr} = \varepsilon * 100$). If the value of ε at the excitation wavelength is not available, additional correction of ε is necessary. In this case, ε is multiplied by a factor taken from the ratio of the absorbance of the sample at the excitation wavelength (*e.g.* 660 nm) and at the wavelength at which ε is available (*e.g.* Chl Q_Y max of PS I (~680 nm)).

The total number of photons absorbed by a particle per laser pulse should be kept sufficiently low (in the range of 10^{-3}–10^{-4} photons per particle per laser pulse) to avoid higher order processes and can be calculated in the following way:

$$N_{abs} = N \cdot \sigma_{eff}(\lambda) \tag{2.1}$$

where N_{abs} is the number of photons absorbed by a particle per laser pulse, N is the number of photons in a laser pulse, and σ_{eff} is the effective absorption cross-section of a particle at the excitation wavelength (λ).

◊ Origin of the chemicals: Sigma-Aldrich, Germany – Catalase, Glucose, Glucose oxidase, Phenazine methosulphate; Fluka Biochemika, Buchs, Switzerland –Sodium ascorbate.

The effective absorption cross-section (σ_{eff}) in Eq. (2.1) can be calculated from the corrected molar extinction coefficient (ε_{corr}) (142):

$$\sigma_{eff}(\lambda) = ln\,10 \cdot \varepsilon_{corr}(\lambda)/N_A \tag{2.2}$$

where N_A is Avogadro's number and $\varepsilon_{corr}(\lambda)$ is the molar extinction coefficient corrected for the number of chromophores in a PS I complex and sometimes also for the difference between the excitation wavelength and the wavelength, at which ε is estimated (*vide supra*).

It follows from the above expressions that the number of photons in a laser pulse (N) is the only adjustable parameter, given that a particular excitation wavelength should be used. N depends according to Eq. (2.3) on the properties of the excitation source, which can be changed (within a certain range) to achieve optimal excitation intensity.

$$N = \frac{P}{f} \cdot \frac{\lambda}{hc} \cdot \frac{1}{\pi r_{lb}^2} \tag{2.3}$$

where P is the power of the laser train, f is the repetition frequency, λ is the excitation wavelength, r_{lb} is the radius of the laser beam on the sample, h is the Planck constant, and c is the velocity of light. P/f is the pulse energy, hc/λ is the photon energy, πr_{lb}^2 is the area of the laser spot.

The substitution of σ_{eff} from Eq. (2.2) and N from Eq. (2.3) in Eq. (2.1) results in a final expression, describing the number of photons absorbed per particle per laser pulse:

$$N_{abs} = \frac{ln\,10}{hc\pi N_A} \cdot \frac{P\lambda\varepsilon_{corr}(\lambda)}{f r_{lb}^2} \tag{2.4}$$

Another critical point in the time-resolved measurements of photosynthetic samples is the control of the redox state of the complexes. Even at low pulse intensities and appropriate redox conditions (*cf.* Section 2.1.4), prolonged excitation of the sample can lead to accumulation of long-lived species (like *e.g.* P_{700}^+), which significantly change the studied kinetics (*cf.* Section 1.5.2). In order to avoid such effects a special sample holder (*cf.* Section 2.3.1.1) has been used to exchange periodically the part of the sample that is excited. With the help of this holder, the cuvette compartment was both rotated and moved sideways, which assured that the excitation beam always hit fresh dark-adapted particles.

The optimal combination of rotation and sideways movement frequencies, at which the number of photons absorbed per particle during the time it spends in the laser beam (N_{abslb}) is sufficiently low (<0.1), was calculated in the following way:

$$N_{abslb} = N_{abs} \cdot n \tag{2.5}$$

where N_{abslb} is the number of photons absorbed by a particle during the time it spends in the laser beam and n is the number of laser pulses during this time.

n depends on the repetition frequency of the laser, f, and the frequency of the cuvette rotation, f_r:

$$n = f \cdot \frac{2r_{lb}}{2\pi f_r R} \tag{2.6}$$

where R is the distance from the center of the cuvette to the position of the laser beam on the cuvette.

The sideways movement frequency (f_{side}) necessary to assure that after every cuvette rotation cycle the laser hits fresh part of the sample was calculated with the help of Eq. (2.7)

$$f_{side} = \frac{2r_{lb} f_r}{s} \tag{2.7}$$

where $2r_{lb}$ is the diameter of the laser spot on the sample, s is the amplitude of the side movement.

Special care should be taken that the time after which the same part of the sample arrives at the laser beam is longer than the time necessary for the decay of the long-lived species. In particular, under the redox conditions used in this work (*cf.* Section 2.1.4), P_{700}^+ decays in <5 ms, while the rotation and sideways movement were adjusted such that re-excitation of the same sample spot was possible only after more than 500 ms.

2.3 Experimental methods

2.3.1 Time-resolved fluorescence

Fluorescence is the processes of spontaneous relaxation of a singlet excited state of a molecule to its ground state via emission of a photon and represents one of the possible competing decay pathways of the excited state (*cf.* Section 1.3 and Eq. (2.12) in Section 2.4). Thus the properties of the emitted fluorescence are directly influenced by the interactions of the excited molecule, which can either change the probability of the competing processes (IC, ISC) or introduce new relaxation pathways (ET, electron transfer, isomerization, *etc.*). Currently, fluorescence techniques are extensively used to study the excited state kinetics of different samples. The main advantages of the fluorescence techniques are their high sensitivity and selectivity, and particularly their non-destructive nature. In the current work are used two methods for detection of the time-resolved fluorescence signal from PS I – time-correlated single photon counting (143,144) and streak camera (145). Both methods use short excitation pulses to measure the δ-pulse response* of the studied sample convoluted with the instrument response function (*IRF*). Special data analysis techniques are used to obtain the deconvoluted signal (*cf.* Section 2.4)

2.3.1.1 Time-correlated single photon counting (TCSPC)

The method, sometimes also referred to as *single photon timing (SPT)*, is based on the fact that the probability of detecting single photon at time, t, after the excitation pulse is proportional to the intensity of the fluorescence at this time. Since the experiment concerns counting of single photon events, a large number of excitation cycles have to be recorded to reconstruct the fluorescence intensity decay curve of the measured sample. Each detected photon is timed and recorded, and the information about its time of arrival at the detector in respect to the excitation pulse is stored in a histogram. The method is characterized with the highest dynamic range (due to its inherently digital nature, *e.g.* counting photons), very high sensitivity (single photons) and moderately high time-resolution (in the order of 2-3 ps).

A schematic diagram of an SPT set-up is shown in Figure 2.1. In the conventional configuration, the ultrafast laser pulse is detected by a photodiode (PD) and routed to the *start* input of a time-to-amplitude converter (TAC), which initiates charging of a capacitor. In the meanwhile, the laser pulse excites the sample and the subsequent fluorescence is detected by a microchannel plate

* The response to an infinitely short pulse of light expressed as the Dirac function, δ.

photomultiplier (MCP). The signal from the detector then *stops* the charging ramp in the TAC. The so generated voltage from the TAC is a linear function of the time elapsed between the start and the stop events. An analog-to-digital converter (ADC) is used to assign a numerical value to the voltage level in the TAC, which is then converted into a time channel by the multi-channel analyzer (MCA) and stored in the form of histogram. This cycle has to be repeated millions of times in order to obtain a high signal to noise ration (S/N). The S/N ratio can be improved by passing both the start and the stops signals through a so-called constant fraction discriminator (CFD) before they reach the TAC. CFDs transmit only pulses reaching certain constant amplitude, and thus differentiate between the background noise and the real signal. It is noteworthy that the nature of the TAC operation is such that it registers only the first stop pulse. This means that the rate of the stop pulses should be low enough so that only one photon is detected per excitation; otherwise, the detected fluorescence signal will be distorted from the pile-up effects. In order to increase the counting efficiency, the SPT system can be operated in the so-called *reversed start-stop* configuration (in Figure 2.1 is shown exactly this configuration), where the signal from the MCP is used as a start input for the TAC, while the signal from the PD as a stop input. It is advisable in this configuration to adjust the delay unit in such way that both the start and the stop signals are related to the same excitation pulse.

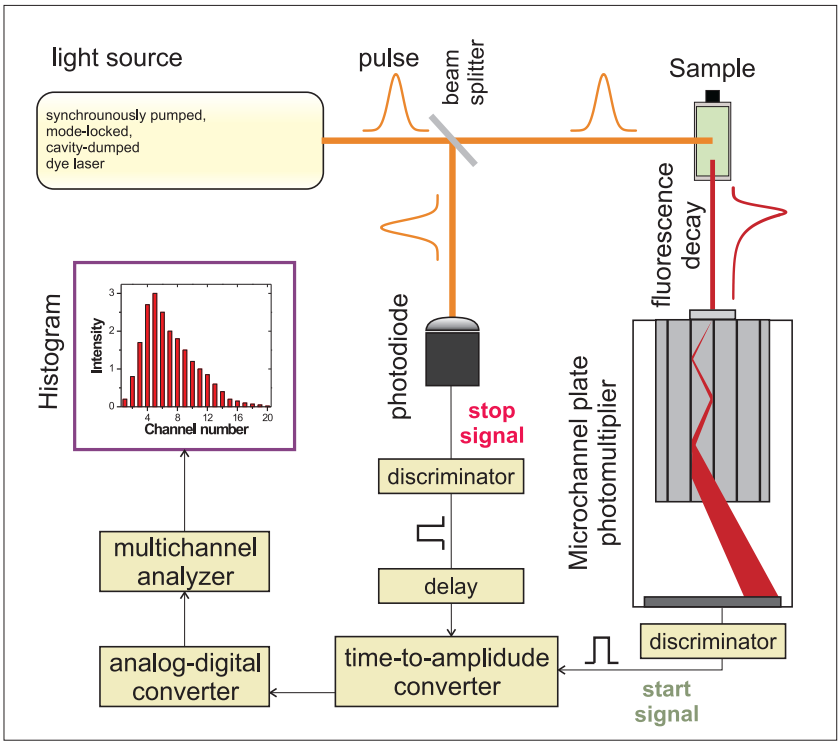

Figure 2.1
Block diagram of an SPT set-up with reversed start-stop configuration (see text for details).

Even when the laser pulse duration is much shorter than the detected fluorescence lifetimes, the large number of optical elements (*e.g.* lenses, monochromator, *etc.*) together with the delays in the detector and the electronics cause significant broadening of the *IRF* of the set-up. Consequently, in order to obtain the true δ-response of the studied sample the recorded signal has to be deconvoluted with the *IRF*. The *IRF* is measured under the same experimental conditions as the fluorescence emission (cuvette size and sample volume), using scattering medium, like *e.g.* colloidal silica (Ludox) or simply diluted milk.

The SPT set-up (reversed start-stop configuration) used in the current work is described in details previously (127,146,147).

Excitation source. The excitation of the sample was provided by a synchronously pumped, mode-locked, cavity-dumped dye laser (Spectra Physics) at a repetition rate of 800 kHz. 4-(dicyanomethylene)-2-methyl-6-(p-dimethylaminostyryl)-4H-pyran (DCM) (148) was used as a laser dye, which provides well-shaped and short excitation laser pulses (FWHM ~10 ps) in the 650-690 nm wavelength range. The dye laser was pumped by an argon ion laser (Spectra Physics), which was operated at the 514 nm line.

Instrument response function. The total IRF of the set-up was about 30 ps FWHM, which after deconvolution results in a time-resolution of ~2 ps. The IRF was determined with the help of diluted in distilled H_2O (1/1250) fresh milk (1.5 % fat) as a scattering solution.

Sample compartment. Special sample holder was developed, which allowed the excited sample to be periodically refreshed (*cf.* Section 2.2). Components of the sample compartment:

i) rotating cuvette – two glass windows* separated by a 1.5 mm thick silicon ring (the thickness of the spacer determines the optical path length in the sample). The two glass windows were hold together with the help of two metal rings. The effective diameter (determined by the silicon ring) of the cuvette was 10 cm. A special metal ring (diameter of 2.5 cm) was glued in the center of one of the glass windows and used to attach the cuvette to a motor for cuvette rotation.

ii) motor for cuvette rotation – the motor had a control unit which allowed adjustment of the cuvette rotation frequency between 0 and 5000 rpm.

iii) translation stage – the motor for cuvette rotation was attached to a special stage placed on a rail and connected to a second motor, which moved the stage sideways. The range of the side movement was limited to 2 cm to keep the excitation pulse always on the sample.

iv) motor for sideways movement – the motor had a control unit which allowed adjustment of the sideways movement frequency between 0 and 120 rpm.

Measurement conditions. The sample, prepared as described in Section 2.1, was placed in a rotating cuvette and the optimal excitation conditions for PS I were chosen as described in Section 2.2: laser intensity at the sample ~0.05 mW (spot diameter ~0.8 mm); cuvette rotation frequency 4200 rpm and cuvette side movement frequency 66 rpm. Under these conditions, less than 1% of the particles receive a second laser excitation during the time they spend in the laser beam. The excitation wavelength was 663 nm to selectively excite the bulk antenna Chls. Measurements were carried out at ambient temperature (21 ±2°C).

Fluorescence detection. Fluorescence signals were stored in 4096 channels of the computer memory, which together with the time-window used resulted in a time step of 2.61 ps per channel. The photon counting stop criteria used in the experiments were: *i)* fluorescence at particular wavelength – 30000 counts collected in the peak channel or 50 minutes passed; *ii)* IRF – 50000 counts collected in the peak channel.

2.3.1.2 Synchroscan streak camera system

In order to satisfy the demand for higher time-resolution of the fluorescence experiments a new streak camera system was assembled. Since the installation and the development of this set-up

* Cuvette windows were made from Borofloat®, by Hellma, Germany. Properties of the windows: diameter - 10.5 cm; thickness - 1.1 mm; flatness - λ/2; protection coating.

represent significant part of the current work, a separate chapter (*cf.* Chapter 3) is dedicated to their detailed description.

2.3.2 Ultrafast transient absorption

The excitation of a molecule and the subsequent reactions that can occur from the excited state (Section 1.3 and Figure 1.5) are associated with significant changes in the energy levels of a studied sample, and hence with changes of its absorption properties. Thus, a vast amount of information about the molecular reactions can be obtained by monitoring the ultrafast absorption changes. The *transient absorption* (TA) technique is essentially a pump-probe technique, where the difference in the absorbance, ΔA, of the studied sample after excitation with a relatively strong *pump* pulse is measured in time (Eq. (2.8)). The changes in the sample are monitored by a weaker *probe* pulse, which arrives at particular time intervals after the pump pulse. The time-resolution is achieved by sending the probe pulse through a motor-driven optical delay line.

$$\Delta A = A_{pump} - A_{nopump} = -\log \frac{I_{1,\,pump}}{I_0} + \log \frac{I_{1,\,nopump}}{I_0} = -\log \frac{I_{1,\,pump}}{I_{1,\,nopump}} \qquad (2.8)$$

ΔA is the difference between the measured absorbance before (A_{nopump}) and after (A_{pump}) the excitation with the pump pulse. It follows from the Lambert-Beer law that the ratio of the transmitted (I_1) to the incident (I_0) light depends exponentially on the absorption of the sample: $T = I_1 / I_0 = exp(-\varepsilon c l)$, where $A = \varepsilon c l$ is the absorbance of the sample (ε - molar extinction coefficient, c – concentration, l – sample thickness). It is apparent that the absorbance changes are directly associated with the dynamics of the population of the absorbing species.

The absorbance difference signal, ΔA, measured in a TA experiment represents the δ-pulse response of the studied sample convoluted with the *IRF* (similar to the time-resolved fluorescence, *vide supra*):

$$IRF(t) = \int_{-\infty}^{\infty} I_{pump}(t') \cdot I_{probe}(t + t')dt' \qquad (2.9)$$

Here the *IRF(t)* is the cross-correlation function of the pump and the probe pulses.

The changes in ΔA depend on the processes that occur in the studied system after the excitation. The chromophores absorbing at the wavelength of the pump pulse are promoted to an excited state, and thus lose their ground-state absorption (GSA), in effect a negative ΔA is observed (bleaching). Negative ΔA is observed also due to the process of stimulated emission (SE) from the excited state induced by the probe pulse. On the other hand, positive ΔA are observed at the wavelengths of the excited state absorption (ESA) of the excited molecule, or if formation of new species occurs (in result of some photophysical and photochemical reactions) at their absorption wavelengths.

In Figure 2.2 is shown a scheme of the basic elements of a TA set-up. The femtosecond TA set-up used in this work is described in detail elsewhere (52,149) with some recent modifications.

Excitation source. The measurements were performed with the help of a Ti:sapphire based amplifier system (Libra, Coherent). This system is a one-box integration of a seed laser (Vitesse, Coherent), pump laser (Evolution, Coherent), regenerative amplifier, and a stretcher/compressor unit. The seed laser is composed of a CW diode-pumped Nd:YVO_4 laser (second harmonic at 532 nm) and a mode-locked Ti:sapphire oscillator (~800 nm), and delivers ultrashort pulses (FWHM <50 fs) at 80 MHz repetition rate. The integrated stretcher/compressor and the regenerative amplifier are used for chirped pulse amplification of the Ti:sapphire pulses to ~5 mJ at 3kHz repetition rate, retaining pulse widths of ~50 fs. The pump laser for the regenerative amplifier is a

diode-pumped, second harmonic (527 nm) Q-switched Nd:YLF laser. The amplified pulses are used to generate the pump and the probe pulses necessary for a TA experiment.

i) pump pulse – the major part of the amplified pulse was used to pump an optical parametric amplifier (OPA) (Topas, Light Conversion) and produce color-adjustable pulses (for the PS I experiments pulses at ~670 nm and ~700 nm, with a pulse width of ~60 fs and a spectral width of ~8-9 nm were used).

ii) probe pulse – the white light continuum for the probe pulse was generated from a minor part of the amplified pulse (pulse width ~80 fs).

In order to avoid unwanted polarization effects, polarizers were placed in both the pump and the probe beams with an angle of 54.7° (magic angle) between the polarization directions.

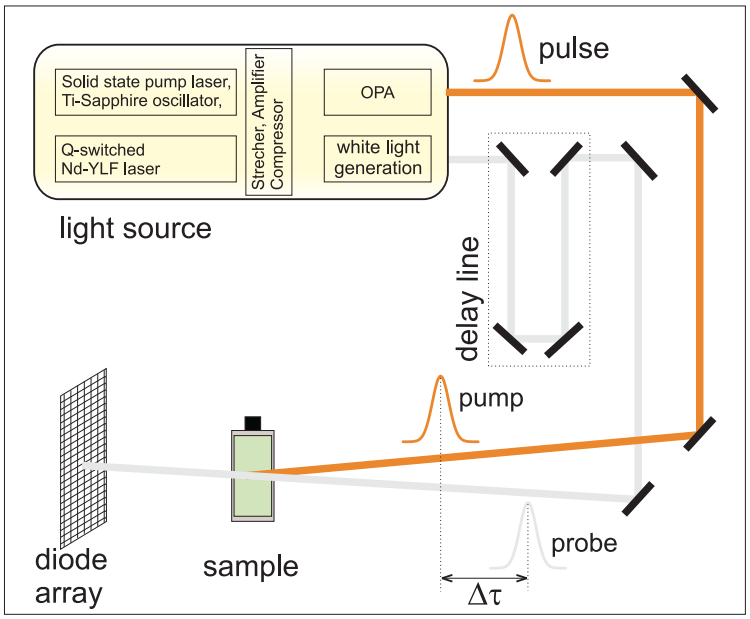

Figure 2.2
Schematic representation of a TA set-up (see text for details).

Detection system. A home-built diode array camera system (~250 wavelength channels) was used to detect the absorption changes. The system is able to measure 3000 spectra/s from at full resolution of ~0.5 nm per pixel (wavelength range of ~125 nm).

Measurements conditions. The sample, prepared as described in Section 2.1.3, was placed in a rotating cuvette (*cf.* Section 2.3.1.1) and the optimal excitation conditions for PS I were chosen as described in Section 2.2. Under the experimental conditions, less than 1% of the particles receive a second laser excitation during the time they spend in the laser beam. Measurements were carried out at ambient temperature (21 ±2°C).

2.4 Data analysis

The ultimate goal of all time-resolved experiments is revealing the detailed kinetics of the processes that occur in the studied sample. In the linear regime, the decay of the excited state of a molecule, *M*, is given by a first-order differential equation:

$$\frac{dM^*(t)}{dt} = -k_M M^*(t) \tag{2.10}$$

where M^* is the excited state of a molecule, k_M is the molecular decay constant, t is time.

After integration, Eq. (2.10) gives a mono-exponential decay of the excited state.

$$M^*(t) = M_0^* \exp(-k_M t) \tag{2.11}$$

where M^* and M_0^* is the excited state concentration at time t and $t = 0$, respectively.

The lifetime of the excited state is inversely related to the molecular decay rate constant, which is essentially a sum of the decay constants of all the processes that a molecule in excited state can undergo (*cf.* Section 1.3):

$$k_M = 1/\tau_M = k_r + k_{nr} + k_p + k_{ET} + k_Q[Q] \tag{2.12}$$

where k_r, k_{nr}, k_p, k_{ET}, and k_Q are the rate constants for the radiative and nonradiative decays, photochemistry, energy transfer and quenching by a quencher (Q).

Equation (with the exponent) can be used as a model function to directly describe only an ideal case where the experimental data is continuous in time, noise-free, the location of the $t = 0$ point is known, and the instrument response of the detection system is a δ-pulse. However, this is never the case, which means that during the data analysis all of the imperfections of the real experiment should be taken into account; the discontinuity of the data can be overcome by using a model function with time step as the one of the data channels, the noise statistics can be included in the fitting function (*cf.* Section 2.4.4) and the *IRF* of the system can be measured and convoluted* with the model function (Eq. (2.13)) before it is tested against the experimental data in the fitting routine. The latter correction also helps to localized the $t = 0$ point, since it is directly related to the position of the measured *IRF*.

$$S(t) = \sum_{j=1}^{n} A_j \exp\left(-t/\tau_j\right) \otimes IRF(t) \tag{2.13}$$

where S is the detected signal, A is fractional amplitude for each decay lifetime (τ), *IRF* is the instrument response function.

The excited state kinetics in complex systems, such as the photosynthetic system, which are composed of large number of chromophores with specific spectral and kinetic properties, can be disentangled only if the time-resolved experiments (*e.g.* fluorescence, absorption difference, *etc.*) are conducted over a broad spectral range and often under different conditions (*e.g.* different redox state of the complexes). However, these kinds of experiments deliver large multidimensional data sets, which require special data analysis techniques in order to unravel the underlying kinetic mechanisms. Bellow are summarized the data analysis techniques used throughout this work to study the light-

* Note that deconvolution of the experimental signal is an ill-posed problem (*i.e.* the solution is not unique, does not depend continuously on the data and is highly sensitive to errors in the data) and thus forward convolution of the model function with the IRF significantly simplifies the analysis. Usually the convolution is performed in the Fourier space where it is a simple multiplication of the two functions (220).

harvesting kinetics in PS I. Detailed description of these methods can be found in the literature (149-152).

2.4.1 Global analysis

The recorded time-resolved signal (*e.g.* fluorescence, absorption difference, *etc.*) from a system with n spectrally different components depends on both the excitation and the detection wavelengths. In the linear regime, such signal can be described with a system of n first-order differential equations (Eq. (2.10)), whose solution yields a n-exponential decay kinetics (Eq. (2.11)). If the decay traces at each of the m detection wavelengths, are analyzed separately with the help of Eq (2.13), the total number of parameters that have to be recovered from the fitting of the experimental data is the sum of $n*m$ lifetimes and $n*m$ amplitudes. Obviously, in such single trace analysis, the number of determined lifetimes is m times larger than the real one, which severely increases the number of fitting parameters. The solution to this problem is found in a special data analysis technique, commonly referred to as *Global analysis* (150). The power of this technique is that the complete multidimensional experimental data set is analyzed simultaneously, which allows to account for the parameters that are connected across the data set (like *e.g.* the lifetimes in the example above). Eq. (2.14) is a modified version of Eq. (2.13), which can be used in a Global fitting routine. Clearly, the only wavelength dependent parameters in Eq. (2.14) are the pre-exponential factors, A_j, while all decay traces are described with a single set of lifetimes, τ_j.

$$S(t, \lambda_{exc}, \lambda_i) = \sum_{j=1}^{n} A_j(\lambda_{exc}, \lambda_i) \exp\left(-t/\tau_j\right) \otimes IRF(t) \qquad (2.14)$$

where S is the recorder signal, λ_{exc} is the excitation wavelength, λ_j is the detection wavelength, A_j is the fractional amplitude for each decay lifetime τ_j, and IRF is the instrument response function.

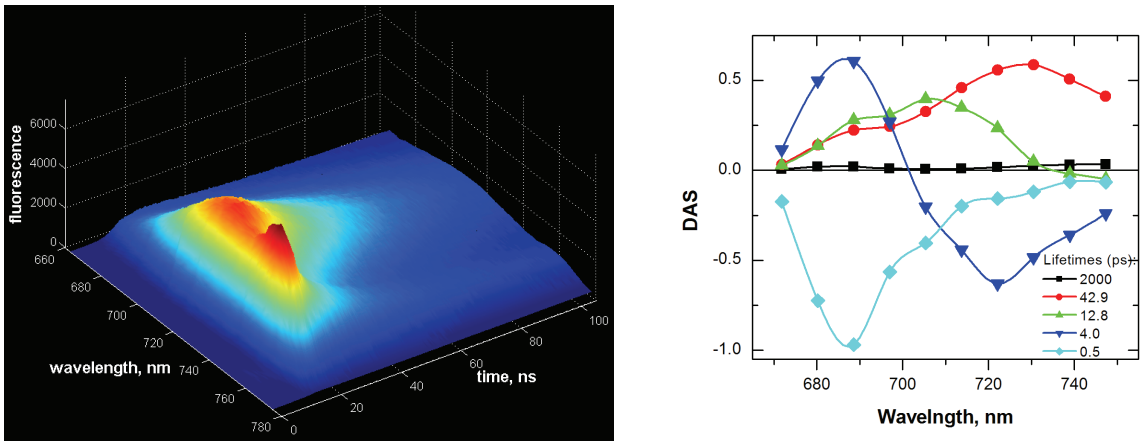

Figure 2.3
Wavelength and time dependence of fluorescence signal measured from cyanobacterial PS I complexes (A) and the DAS obtained from the Global analysis of the decay traces at several wavelengths (B).

The pre-exponential amplitudes, A_j, related to a particular lifetime, τ_j, extracted form the fitting of the time-resolved data, can be plotted against the detection wavelengths to generate the co-called *decay-associated spectra (DAS)* plots. These plots can be viewed as a compact representation of the kinetic information contained in the experimental data. In Figure 2.3 are shown the original time-

resolved fluorescence signal of cyanobacterial PS I complexes and the corresponding DAS obtained from the Global analysis of this signal.

It should be kept in mind during examination of the DAS that the dynamics of the studied signal is described with the help of multi-exponential **decay** kinetics (Eq. (2.14)). Hence, if part of the signal reflects a rise process (like, *e.g.* rise of the fluorescence of particular state due to ET from another state), the lifetime associated with this process will have negative amplitudes.

The time-resolved fluorescence kinetics of the different PS I complexes studied in this work was analyzed with a home-built program for Global analysis (147).

2.4.2 Lifetime density analysis

Although Global analysis has proved over the years to be a very powerful method for analysis of complex data sets, it has its limitations, which sometimes cannot be easily overcome. Often the time-resolved data contains large amount of kinetic components, which cannot be correctly resolved at most of the detection wavelength with the discreet set of lifetimes, normally used in Global analysis. In this respect, recently in our group has been developed a new method, called *Lifetime Density Analysis (LFD)* (149), which is suitable for analysis of time-resolved data that contains large amount of closely spaced kinetic components. In this analysis the amplitudes, A_j (Eq. (2.14)), in a sum of large number (n ~100) of exponential functions with fixed equally spaced lifetimes, τ_i, are determined for each detection wavelength, λ_i. LFD method combines the *Exponential Series Method (ESM)* (153,154) with a regularization procedure (155). In essence, the experimental time-resolved signal, S, can be approximated with a continuous distribution of individual decays, which represents a *Laplace transform* of the underlying lifetime distribution function, $\Phi(\tau)$:

$$S(t, \lambda_{exc}, \lambda_i) = \int_0^\infty \Phi(\tau, \lambda_{exc}, \lambda_i) \exp\left(-t/\tau\right) \qquad (2.15)$$

a discrete form of this expression, similar to Eq. (2.14), is used in the LFD analysis . In this case, the lifetime distribution functions, $\Phi(\tau)$, is approximated with a large number of pre-exponential amplitudes, A_j (n ~100). The so generated model function (discrete form of Eq. (2.15)) is convoluted with the IRF in the Fourier space, where the procedure is reduced to simple multiplication of the model function and the *IRF*; the inverse transform of this product is fitted to the experimental signal. Since the inverse Laplace transformation of the experimental signal (performed here by fitting the model function convoluted with the IRF to the experimental signal) is an ill-posed problem (*cf.* footnote on page 32), the use of a regularization procedure is necessary to avoid oscillations of the amplitudes of the closely spaced exponents.

The transient absorption kinetics of PS I studied in this work was analyzed with the LFD method, using a home built program (149).

It is comfortable to represent the results from the LFD analysis in the form of the so-called *LFD maps* (*cf.* Figure 7.3, Section 7.2.1 for examples), which show the amplitude, A_j, of particular lifetime component, τ_j, at particular detection wavelength λ_i.

2.4.3 Target analysis

The data analysis methods described above aim at correct mathematical description of the experimental results. The parameters that are obtained with the help of these methods, however, are

purely mathematical, and do not contain direct physical information. Therefore, these methods are mainly applied to obtain some preliminary information, which can be used later on to construct physical models (*e.g.* a kinetic model) of the studied system. Methods where a physical model is tested on the experimental data are often referred to as *Target analysis* (150-152).

Kinetic modeling of the light harvesting in the photosynthetic complexes. Often in the kinetic description of the photosynthetic complexes, the so-called *compartmentalization* approach is used (151). This approach is based on grouping certain chromophores in compartments* according to their spectral and kinetic properties (*e.g.* antenna compartments, RC compartment and RPs compartments). Such simplification of the kinetic picture in the photosynthetic systems is necessary due to the large number of chromophores (*e.g.* ~100 Chls per PS I core complex), which cannot be easily accounted for separately. In addition the equilibration of the excitation energy over the pigments in particular compartment is often bellow the time-resolution of the experimental set-ups, and thus these pigments are essentially indistinguishable. The number of compartments that is necessary to build a model that can describe the experimental data can be deduced from some previous knowledge, like *e.g.* Global analysis, low temperature steady state experiments, structural information, *etc.* In Figure 2.4 is shown an example of a kinetic scheme used to model the time-resolved data of the trapping kinetics in PS I. The processes occurring between the interacting compartments are described with specific rate constants (k_{ijk}). In addition, the decay of the excited state compartments to their ground state is also accounted for (k_{jj}).

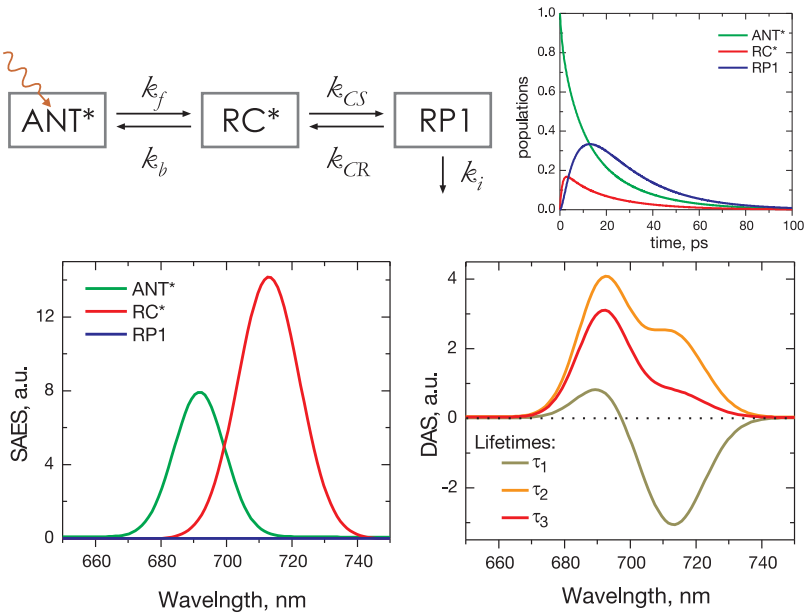

Figure 2.4
Kinetic scheme of a plausible model describing the kinetics in PS I. With the help of Target modeling the population dynamics, the SAES and DAS spectra of the states involved in the kinetics can be obtained.

The kinetics of the studied system can be expressed by a system of homogeneous first-order differential equations:

$$\frac{d}{dt}\mathbf{X}(t) = \mathbf{T} \cdot \mathbf{X}(t) + \varepsilon(\lambda_{exc}) \cdot IRF(t) \qquad (2.16)$$

where $\mathbf{X}(t)$ is the vector of time-dependent population of the species (compartments), $\mathbf{T}$ is the kinetic transfer matrix, $\boldsymbol{\varepsilon}$ is a vector of the initial absorbance of the species (can be viewed also as the vector of the initial concentrations of the species), and *IRF* is the instrument response function.

* When using a mathematical formalism the compartments may also be called *states*. If the states are characterized spectroscopically they may also be called *species*.

$$T_{jk} = k_{jk} - \delta_{jk}\left(k_{jj} + \sum_{m=1}^{n} k_{mk}\right), \qquad j, k = 1,..., n \tag{2.17}$$

where δ_{jk} is the Kronecker delta (1 for $j=k$ and 0 for $j \neq k$). The off-diagonal elements of the transfer matrix, T_{jk}, represent the transition rates (k_{ik}) between the compartments, while the diagonal elements, T_{jj}, describe the sum of all decay rates of a compartment.

Such system of differential equations can be solved analytically:

$$\mathbf{X}(t) = exp(\mathbf{T}t) \otimes \varepsilon(\lambda_{exc}) \cdot IRF(t) \tag{2.18}$$

The eigenvector-eigenvalue decomposition of the transfer matrix, **T**, yields $\mathbf{T} = \mathbf{U\Lambda U^{-1}}$, and hence $exp(\mathbf{T}t) = \mathbf{U}exp(\mathbf{\Lambda}t)\mathbf{U^{-1}}$ (where $\mathbf{\Lambda}$ is the vector with the eigenvalues and **U** is the eigenvector matrix of the transfer matrix, **T**). The eigenvalues, $\mathbf{\Lambda}$, are related to the measured lifetimes via $\Lambda_j = -1/\tau_j$, while the eigenvector matrix demonstrates the contribution of a particular compartment to specific processes and their lifetimes. A negative value in this matrix represents the rise of the population of a compartment, while a positive value corresponds to the depopulation of a compartment.

Finally, a complete expression for the time-dependence of the experimental signal (fluorescence or absorption difference) can be derived:

$$S(t, \lambda_{exc}, \lambda_i) = \sum_{k=1}^{n} SAS_k(\lambda_i)\left(\mathbf{U}^{-1} \cdot \varepsilon(\lambda_{exc})\right)_j U_{jk} \cdot \sum_{j=1}^{n} exp(\Lambda_j t) \otimes IRF(t) \tag{2.19}$$

where Λ_j is the j-th eigenvalue of the transfer matrix, **T**, SAS_k is the spectrum of k-th species, and **U** is the matrix of the eigenvectors of **T**.

It is apparent that this expression is similar to Eq. (2.14). The major difference between the two expressions is that in the case of Target analysis the lifetimes and the amplitudes of the model exponential function are no longer pure mathematical parameters but are now related to real physical parameters, like the rate constants of particular processes and the spectra of particular compartments, respectively. An important parameter that emerges from the kinetic description of the time-resolved data is the so-called *species-associated spectrum (SAS)*. Physically SAS represent the stationary spectra of the model compartments as if they were measured separately. SAS are directly related to DAS introduced in Section 2.4.1 through the first summation in Eq. (2.19), which is equal to the pre-exponential amplitude in Eq. (2.14). In effect, at given detection wavelength, the DAS of particular lifetime component are a linear combination of the SAS of the compartments.

$$DAS_j(\lambda_i) = \sum_{k=1}^{n} c_{jk} \cdot SAS_k(\lambda_i) \tag{2.20}$$

where c_{jk} for a given kinetic model is an array of coefficients, depending on the rate constants, k_{jk}, and the initial absorbance of the species $\varepsilon(\lambda_{exc})$ (*cf.* Eq. (2.19), the first summation).

At the end, similarly to the Global analysis, in Eq. (2.19) there is only one set of rate constants (hence lifetimes) that describes the kinetics at all detection wavelengths in a data set and thus can be used to fit the data in a global fashion (*e.g. Global target analysis*).

2.4.4 Quality of the fit

Independent of the type of the analysis that is used (Global or Target), the resulting model function is tested in a least-squares minimization routine against the experimental data. Several different criteria are used to measure the mismatch between the data and the model function.

Statistical fit quality criterion. The primary fitting criterion is the quantity *chi square* (χ^2), which is defined as the weighted sum of the squares of the deviations of the model function from the experimental data. In practice, it is often convenient to normalize χ^2, so that it is independent of the number of data points and fitted parameters (Eq. (2.21)). This expression is referred to as the *reduced chi square* and in the case of a good fit, the value of this parameter tends to 1.

$$\chi_r^2 = \frac{1}{(N - p)} \cdot \sum_{i=1}^{N} \left[\frac{R(t_i) - R_c(t_i)}{\sigma_i} \right]^2 \tag{2.21}$$

where $R(t_i)$ is the experimental data, $R_c(t_i)$ is the calculated function, N is the total number of data points, σ_i is the standard deviation of the i-th data point (in case of photon counting experiments, the statistics follows Poissonian distribution and the expected standard deviation is approximately equal to $[R(t_i)]^{1/2}$), p is the number of fitted parameters (*e.g.* p=3 for a bi-exponential kinetics with a constant term).

Graphical fit quality criterion. A very important and comfortable for visual inspection fit quality criterion is the plot of the *weighted residuals* (W), defined as:

$$W(t_i) = \frac{R(t_i) - R_c(t_i)}{\sigma_i} \tag{2.22}$$

see Eq. (2.21) for the meaning of the terms.

In case of a good fit, the weighted residuals are randomly distributed around zero (Figure 2.5).

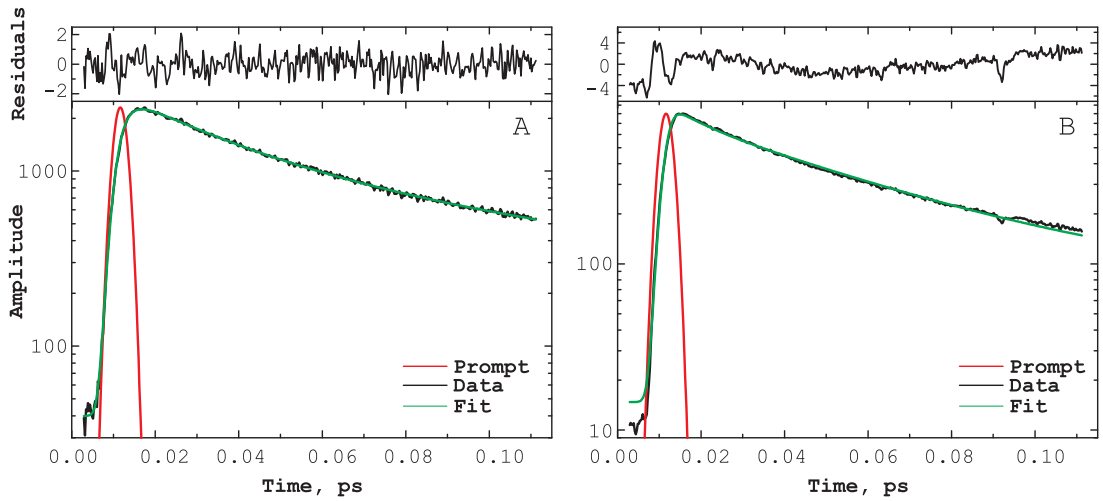

Figure 2.5
Examples of good (A, χ^2 = 1.03) and bad (B, χ^2 = 4.03) fits of experimental data. Data obtained with Streak camera from PS I complexes from *C. reinhardtii*.

Physical reasoning. Often during the analysis several mathematical solutions can describe the experimental data equally well in terms of the quality criteria discussed above. In such cases, additional reasoning has to be used to discriminate between the different solutions and select the most likely one. First, the resulting spectra (DAS and SAS), lifetimes, and rate constants should be carefully examined for specific problems, like *e.g.*: *i)* amplitude compensation between two lifetimes,

which normally gives a good mathematical fit, but has no physical meaning; *ii)* since the SAS represent the real absorption/fluorescence spectra of a particular compartment, they should be smooth and without sharp deviations; *iii)* the rate constants and the lifetimes should have realistic values. Second, apart from the latter purely practical considerations, the resulting mathematical descriptions should be examined for compatibility with previous knowledge about the studied system and more importantly with the known physical and chemical laws. The physical reasoning thus represents the most powerful tool for selecting the proper description of the experimental data.

2.4.5 Average lifetime of the excited state and scaling analysis

A useful parameter that can be calculated during the analysis of the time-resolved data is the *average excited state lifetime* (τ_{avg}, *cf.* Eq. (2.23)). This lifetime, together with the spectral properties is characteristic for each investigated sample and can be used to compare results obtained under different conditions or in different labs. Additionally, it can be used as a self-consistency test for the data analysis, since it should not differ between different analysis techniques (Global or Target) given that the same data sets are used. The average excited state lifetime at particular detection wavelength λ is defined as:

$$\tau_{avg} = \frac{\sum_{i=1}^{k} A_i \cdot \tau_i}{\sum_{i=1}^{k} A_i}, \qquad (2.23)$$

where τ_i are all the lifetime components found in the analysis of the data and A_i are their corresponding amplitudes at particular wavelength.

It should be noted here that in Target analysis, where a kinetic scheme is used to analyze the experimental data, one or few model compartments of this scheme may account for signal originating from contamination (like, *e.g.* free Chls) that is interacting with the studied sample neither physically nor chemically. In this case, the contribution from the contamination (its lifetime and amplitude) can be excluded from the calculation of the average excited state lifetime.

Scaling analysis. The average excited state lifetime is of major importance for the determination of the type of the trapping kinetics (diffusion-, transfer-to-the-trap- or trap-limited) in the photosynthetic samples (*cf.* Section 1.5.1, Eq. (1.6) and (29) for detailed derivation of the expression). Since the terms τ_{mig} and τ_{del} in Eq. (1.6) are related to ET processes in the antenna and from the antenna to the RC, these two terms can be replaced by a single one, τ_{ET}, and a simplified version of Eq. (1.6) can be used (Eq. (2.24)). The new equation will allow quantifying precisely the contribution of the CS process to the average lifetime of the excited state.

$$\tau_{avg} = \tau_{CS} + \tau_{ET} \qquad (2.24)$$

where τ_{avg} is the average lifetime of the excited state, τ_{CS} (τ_{trap}) is the lifetime of the trapping of the excitations located on the RC, τ_{ET} is the sum of τ_{mig} (the average first passage time for an excitation to approach the RC) and τ_{del} (the additional time needed for the energy to be delivered to the RC). Since the migration of the excitation in the antenna is very fast, the term τ_{mig} usually can be neglected.

The lifetimes resulting from the Target analysis are not related to a particular process but rather represent a complex mixture of contributions (the contribution of each process to a particular lifetime can be deduced from the weighted eigenvector matrix, *cf.* Section 2.4.3), therefore these lifetimes cannot be directly related to one of the terms in Eq. (2.24) - τ_{CS} or τ_{ET}. In this respect, specific

analysis, called *scaling*, is used to reveal the contribution of the different processes occurring in the studied system to the average excited state lifetime. In short, the rate constants obtained during the fitting of the experimental data can be used to simulate a hypothetical case where certain rates are scaled to infinity (like *e.g.* the ET rates), while others (like *e.g.* CS and electron transfer rates) are kept as the ones obtained from the fitting of the data (Figure 2.6). From the new set of rates, the lifetimes of the processes in the system can be recalculated (note that no fitting of the experimental data is involved in this recalculation). If the scaling is applied to the ET rates then these processes become ultrafast and their contribution to the average excited state lifetime negligible, *i.e.* $\tau_{ET} \rightarrow 0$. In effect, the recalculated τ_{avg}^{calc} is equal to τ_{CS} (Figure 2.6), which means that the overall decay of the excited state in the artificially created situation is governed completely by the CS process in the RC. The difference between the real τ_{avg} (obtained from the fitting of the experimental data) and the simulated τ_{avg}^{calc} (obtained from the scaling analysis) gives the contribution of the ET processes (migration in the antenna and delivery to the RC) in the overall decay of the excited state. The trap-limited case of the light utilization kinetics of photosynthetic complexes is realized when the ratio τ_{CS}/τ_{ET} is >1.

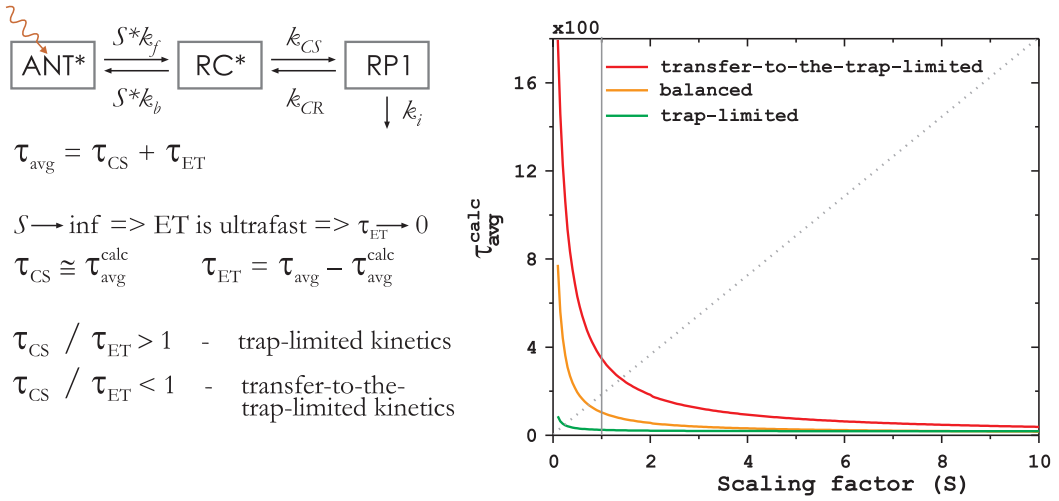

Figure 2.6
Scaling analysis. (left) Schematic representation of a kinetic model where the ET rates between the antenna compartment and the RC are scaled with a factor, S. (right) Dependence of the calculated τavg on the scaling factor (S) varied from 0 to 10 (at S=1, $\tau_{avgcalc} = \tau_{avg}$). Each color line shows the scaling analysis performed for three different models found in the literature (52,75,76). If τ_{avg} falls on the right side of the dotted line, the trap-limited case is realized, while if it is on the left side the transfer-to-the-trap-limited model is valid.

2.4.6 Calculation of the standard free energy

Another useful parameter that can be obtained from the results of the kinetic modeling of the experimental data is the free energy difference (ΔG) of the electron transfer steps. This parameter can be easily calculated using the rate constants of the corresponding processes and the Maxwell-Boltzmann distribution laws:

$$\Delta G = k_B T \ln \frac{k_b n_2}{k_f n_1} \qquad (2.25)$$

where ΔG is the free energy difference for a particular reaction step, k_B is the Boltzman constant, T is the absolute temperature, k_b is the rate constant for the backward reaction and k_f – for the forward one, n_2 and n_1 is the degeneracy of the corresponding state. Typically, ΔG values are given in the units of meV.

In order to study the dynamics of the ΔG changes along the time scale of the electron transfer reactions the time dependent ΔG can be calculated using the following formula:

$$\Delta G(t) = \frac{\sum_i \Delta G_i P_i(t)}{\sum_i P_i(t)} \tag{2.26}$$

where ΔG_i is the free energy difference for particular electron transfer reaction step as calculated from the previous equation, $P_i(t)$ is the population of each state (ANT*, RC*, RP1 *etc.*) at particular time.

Chapter 3

Installation and development of a synchroscan streak camera system for sub-ps time-resolved fluorescence measurements

Time-resolved fluorescence spectroscopy is one of the main methods for studying the ultrafast excited state (ES) dynamics of different chemical and biological samples. The major advantages of the fluorescence techniques are their high sensitivity and selectivity, and particularly their non-destructive nature. In addition, the time-resolved fluorescence traces are generally easier to interpret as compared to the transient absorption signals, where the partial overlap of the ground state bleaching with the stimulated emission and the presence of excited state absorption make the analysis of the data very difficult. Currently, there are three main pulse techniques used for time-resolved detection of fluorescence – single-photon timing (SPT), streak camera (SC), and fluorescence up-conversion (156). Each of these methods has certain advantages and disadvantages: *i)* the SPT, where single photons are being detected is by far the method with the highest dynamic range and sensitivity. However, due to the temporal jitter in the detectors (micro-channel plates photomultipliers) and the delays in the electronics, the instrument response function (IRF) of the SPT set-ups is limited to ~20-30 ps and thus the time-resolution can hardly be increased from ~2 ps (156); *ii)* the fluorescence up-conversion technique is an optical gating technique where the fluorescence signal and part of the excitation pulse (at variable delay times, Δt) – gating pulse – are mixed in a non-linear crystal, which opens an optical gate for detection of the fluorescence signal only at particular time instants after the excitation pulse (157-159). The time-resolution of this technique is independent of the response of the detector and the electronics and depends only on the cross-correlation of the excitation and the gating pulses and thus it has an ultrahigh time-resolution (~100 fs). However, the intensity of the detected signal is equal to the sum of the fluorescence signal and the gating pulse, and hence it requires high excitation energies, which makes the sensitivity of the methods relatively low.; *iii)* the other commonly used method for time-resolved fluorescence detection is the SC, where the time-resolution problem is translated into a spatial-resolution problem (*vide infra*) (145,160,161). The method retains relatively high sensitivity but already in the sub-ps time domain. In addition, the SC has the inherent ability for two-dimensional detection, which means that when used in combination with a spectrograph both the time-resolved and the spectral information from the studied sample can be recorded simultaneously.

The purpose of this chapter is to present the improvements and developments made in our group for the application of the SC technique.

3.1 General principles of SC operation

The basic operation principle is well reviewed in (145,161), the latter containing an extensive summary of the application of the SC technique in the photosynthesis research. Different SCs are developed to operate either in single-pulse mode (<10 Hz), used predominantly for detection of the occurrence of an event (like *e.g.* single shot lasers), or in high repetition, *synchroscan*, mode. Here is described the principle of operation of a Synchroscan SC (SSC), although there exists no difference in the basic mechanism of operation.

The principal of SSC operation is demonstrated in Figure 3.1. The ultrafast optical signal originating from the studied sample with its specific time-dependent intensity is focused on a photocathode and converted into a stream of photoelectrons, which are accelerated by accelerating electrodes and directed onto a phosphor screen. However, before the photoelectrons reach the phosphor screen they pass between a pair of deflection plates (sweep electrodes), whose voltage is rapidly modulated in *synchrony* with the repetition rate of the excitation source. In the high electric field of the sweep electrodes, the photoelectrons are deflected vertically at different angles depending on their time of arrival. The so-deflected electrons enter a micro-channel plate where they are

multiplied several thousands of times and then hit the phosphor screen in respect to their time of arrival – the earliest photoelectrons hit the phosphor screen in the upper part, while the rest are spread downwards, thus the vertical axis of the phosphor screen serves as the time axis. The intensity of the phosphor image depends on the intensity of the incident on the streak tube light. The horizontal axis of the phosphor screen corresponds to the horizontal position of the incident light, and in case a spectrograph is placed in front of the streak tube, this axis can be used for resolving spectral information from the studied sample. Finally, the image from the phosphor screen is recorded using a charge-coupled device (CCD). Relatively high S/N ratio of the detection of an optical phenomenon can be achieved by synchronizing (*phase locking*) the sweep frequency, so that streak images are accumulated on a fixed position of the phosphor screen.

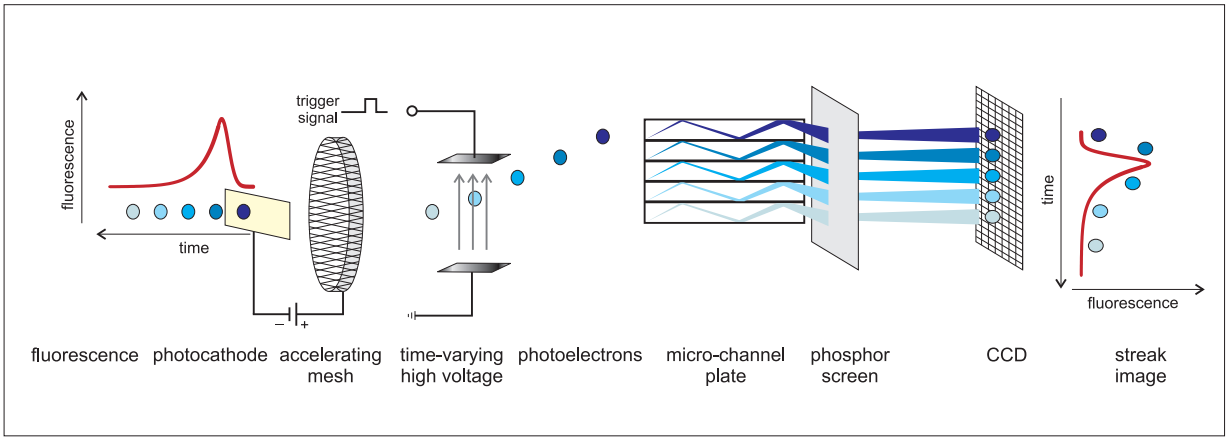

Figure 3.1
Basic principles of streak camera operation (*cf.* text for details).

3.2 Experimental set-up

The SSC set-up used in the current work is schematically illustrated in Figure 3.2.

3.2.1 Excitation source

A diode-pumped, continuously working (CW) Nd:YVO_4 (second harmonic at 532 nm) laser (Verdi 10, Coherent) operated at 9W was used to pump a mode-locked Ti:sapphire oscillator (Tsunami, Spectra-Physics). The Ti:sapphire oscillator supplied ~80 fs (full-width-at-half-maximum, FWHM) pulses (800 nm) with 1.7-1.8 W power at 81.47 MHz repetition rate. A small part of the Ti:sapphire beam (3-5 mW) was used to drive the triggering diode for the SSC (synchronization of the sweep voltage), while the major part was fed into an optical parametric oscillator (OPO PP Automatic, APE). The nonlinear periodically poled (PP, $LiNbO_3$) crystal in the OPO converts the pump pulse (800 nm) into a signal (1050-1600 nm) and an idler (in the range of 3.4 μm). The OPO used here had a highly efficient intracavity second-harmonic generation (ring OPO configuration with LBO (LiB_3O_5) crystal), which allowed transformation of the infrared OPO signal into ~200-300 fs pulses in the visible spectral range (effectively from ~520 nm to ~750 nm, 6-9 nm FWHM, vertical polarization) for sample excitation. A pulse picker (Model 3980, Spectra-Physics) was used to reduce the repetition rate from 81.47 MHz to 800 kHz or 4 MHz for the measurements. In addition, a neutral density filter was used to adjust the intensity of the excitation laser beam to an appropriate one for particular sample.

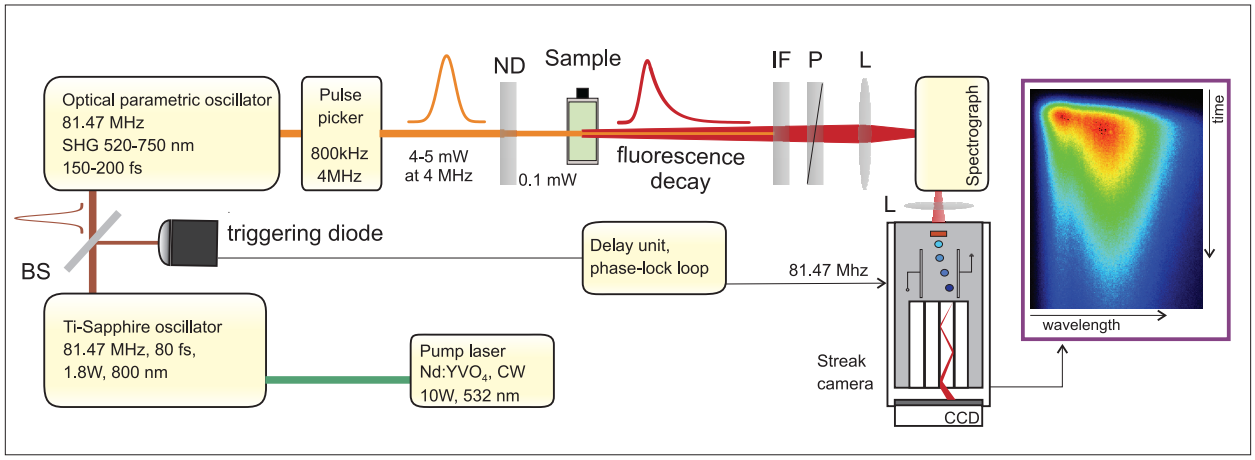

Figure 3.2
Scheme of the SSC set-up used in this work. CW –continuously working, SHG – second-harmonic generation, BS – beam splitter, ND – neutral density filter, IF – interference filter, P – polarizer, L – lens.

3.2.2 Optical pathway, sample box, sample holder

The so-generated train of laser pulses with particular wavelength, repetition rate and intensity was directed into a specially constructed for the experiments sample box. Under measurement conditions, this box has only one small opening; entrance for the excitation laser beam. Both the excitation of the studied sample and the collection of the emitted fluorescence were done inside the box, in complete darkness.

Home build holders for the cuvette containing the sample were used to position the sample into the excitation beam. For light sensitive samples or samples in which long-lived states can be accumulated under continuous illumination, a mobile holder designed for both rotation and sideways movement of the cuvette was used (*cf.* Section 2.3.1.1). Optimal excitation conditions, *e.g.* laser frequency and intensity, frequency of cuvette rotation and sideways movement, were chosen (*cf.* Section 2.2) for the experiments to avoid over excitation of the sample and to ensure its complete recovery prior to a next excitation cycle.

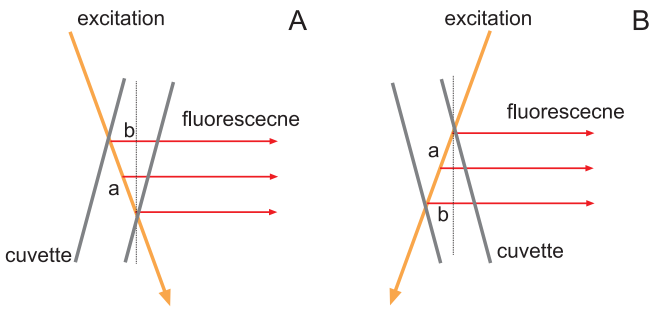

Figure 3.3
Time dispersion of the fluorescnece signal depending on the path of the excitation beam. A) front-face excitation - the time dispersion depneds on the difference between the pathways a and b (distance between the orange and the dashed line). B) back-face excitation - the time dispersion depends on the sum between the pathways a and b.

The optical pathway in the sample box was organized such that back-face excitation of the sample and front-face detection of the fluorescence was used. This organization reduces significantly the time dispersion of the emitted fluorescence signal in comparison to both front-face excitation and 90° emission detection (*cf.* Figure 3.3). This is extremely important especially if ultrahigh time-resolution of the set-up is desired. However, in such organization, the amount of scattering is relatively large and thus the cuvette position has to be carefully adjusted in order to keep the scattering low.

3.2.3 Fluorescence detection

The excitation laser beam was focused on the sample to a spot of 300 μm diameter, using a lens with focal length of 250 mm. The fluorescence emitted from this spot passes through an interference filter (to reduce the laser scattering) and a polarizer (set to magic angle (54.7º) for isotropic measurements) before it is collected by a lens system (Olympus F-Zuiko Auto-T, 85 mm focal length, f/#=2) corrected for optical aberrations. The lens systems focused the fluorescence on the entrance slit of a spectrograph (Chromex 250 IS, three holographic gratings (40, 50 and 150 grooves/mm, 250 nm spectral range), blazed at 600 nm) to a spot with a diameter corresponding to the slit width of the spectrograph. The light gathering power of an optical system is usually characterized by the so-called numerical aperture, which shows the size of the light cone that can be accepted by the system. This parameter is inversely related to the commonly used focal ratio (*f/#*). The *f/#* expresses the size of the entrance/exit pupil in terms of object/image distance*. The optimal light gathering of the spectrograph can be ensured by matching the *output f/#* of the imaging optics to the *input f/#* of the spectrograph.

In order to obtain high time-resolution in the SSC measurements several limitations have to be imposed on the collection of the emitted light; these were clearly summarized in a recent review (145). In short, any significant time dispersion of the photon flux entering the SSC and hitting the photocathode has to be restricted. In this respect, the first major limitation is the height of the horizontal entrance slit to the SSC. This slit determines the height of the photon flux that will be converted by the photocathode in a photoelectron flux, which will be then deflected by the sweep electrodes to recover the time information (*cf.* Section 3.1 and Figure 3.1). However, it is apparent that since the deflection of the electrons depending on their time of arrival is done in vertical direction, the time information within the height of the photon flux and hence within the height of the photoelectron flux cannot be recovered. Consequently, in order to maintain high time-resolution this height has to be kept low by closing down the horizontal entrance slit of the SSC (normally bellow 100 μm, but for achieving highest time-resolution - in the range of ~20 μm). Another major source of time dispersion of the emission signal is the time dispersion due to the diffraction grating in the spectrograph. The high-dispersion gratings introduce significant time dispersion between the different emission wavelengths and thus low-dispersion gratings (50 grooves/mm) should be used to minimize the effect (the problem is thoroughly treated in (145,161) and the references therein). However, to maintain a relatively high spectral resolution when using low-dispersion gratings (the linear spectral dispersion of a 50 groves/mm grating is ~60 nm/mm slit width) the vertical entrance slit of the spectrograph should be closed down. Taking into account the relatively broad fluorescence spectra of the different photosynthetic systems, this slit can be open up to ~200 μm to maintain reasonable spectral bandwidth of up to ~12 nm (FWHM). Under these conditions the largest spot that can be monitored by the SSC at relatively high time-resolution and maintaining reasonable spectral resolution is 20 μm in height and 200 μm in width. Due to the limited amount of light that can be detected, long data acquisition times are necessary in the SSC experiments.

* Attention should be paid to the usage of the *f/#*. As a specification for particular optical system, this number is normally expressed using the focal length of the optical system (lenses, mirrors, *etc.*). However, when the object/image is not positioned at the focal length the *f/#* is different and is expressed as the input/output *f/#* for the optical system, using the corresponding distances. In the optical configuration used in this study the output *f/#* of the imaging system was ~3.5, while the input *f/#* of the spectrograph was 4.

The SSC used for the time-resolved detection of the fluorescence emitted by the studied sample was purchased from Hamamatsu (C5680, M5675, Hamamatsu). The sweep voltage of the SSC was synchronized to the output laser train of the mode-locked Ti:sapphire oscillator running at 81.47 MHz (*cf.* Section 3.2.1). The SSC allowed selection between four adjustable detection time ranges (here 116 ps, 600 ps, 1000 ns and 1600 ps) depending on the amplitude of the high-voltage sine wave (frequency 81.48 MHz) applied on the deflection plates. The image produced by the streak tube on the phosphor screen (Figure 3.1) was recorded using a high-speed CCD camera (C9300-201). The highest acquisition rate* (150 Hz, or ~6.7 ms) of the CCD camera is achieved in the so-called dual tap mode, where a separate readout amplifier is used for each half of the CCD.

3.3 Data acquisition mode

3.3.1 Analog integration vs. photon counting

Normally, the SSC is operated in the so-called *analog integration* mode, in which the photons originating from the phosphor screen are recorded by a slow CCD camera. This mode is associated with relatively long exposition times and generation of images, which are integration of several thousands of photons. Major drawbacks of this mode of data acquisition are the relatively limited dynamic range and the high level of offset signal related to the dark currents in the CCD camera, which requires background correction of the recorded images. Another drawback can be considered the vulnerability of the analog integration mode towards second order noise processes related to different energy contribution of the detected photons, which may lead to an increase of the noise variance. However, despite these apparent disadvantages the analog integration mode is often preferred due to the relatively short duration of the measurements.

An alternative to the analog integration acquisition mode is the so-called *photon-counting* mode. The essence of the operation of the SSC in this mode is the use of a high-speed CCD camera (here 150), which is able to acquire images of the phosphor screen, containing spots formed only by single photon events. It is clear that this mode of operation of the SSC resembles in a certain way the single-photon counting technique, since both experiments are associated with counting photons. Typically, in the photon-counting mode, a certain threshold level is set for discrimination between electronic noise and real signal (Figure 3.4). Consequently, an inherent advantage of the photon-counting mode over the analog integration is the high signal to noise ratio, which makes the background correction of the images unnecessary. In addition, the collected data (images), likewise in other counting experiments, follow Poissonian distribution that can be easily accounted for in the data fitting algorithms. Nevertheless, when using the photon-counting mode special care should be taken to avoid recording of too high intensities of the phosphor screen, since they may be related to some multi-photon events (pile-up). The pile-up effects usually lead to serious distortion of the recorded data and in order to avoid them the intensities recorded by the CCD camera should be kept bellow certain threshold level (according to the specification for the SSC used here the threshold level should be at most 5-7%). The major drawback of the photon-counting mode is that due to the low intensities that have to be measured the signal is recorded after many excitation cycles, which leads to relatively prolonged measurements.

* This CCD camera allows also binning of several pixels (2x2, 4x4, and 8x8), in which case the readout of the CCD can reach ~700 Hz in dual tap mode.

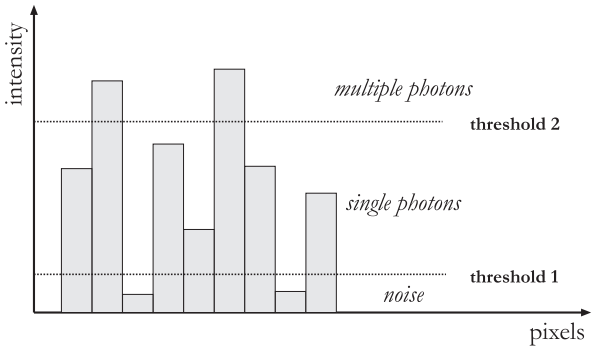

Figure 3.4
Threshold levels in photon-counting mode. Single photon events are detected only above certain intensity level (*threshold 1*) to discriminate the electronic noise. The threshold level should not exceed some particular intensity level (*threshold 2*) above which there is high probability that the images are formed by the overlap of two or more photons (multi-photon events leading to pile-up effects).

3.3.2 Photon counting and the Moiré effect

The implementation of the photon-counting mode in the SSC meets certain technical challenges related to some internal constrictions. The images generated on the phosphor screen and recorded by the CCD camera are usually large enough to cover several pixels of the CCD. However, in the photon-counting mode these images correspond to a single-photon event and hence should be located on a single pixel. The discrepancy is due to the large amplification of the photoelectrons in the micro-channel plate (*cf.* Section 3.1), which broadens the image on the phosphor screen. Several different image-processing methods accounting for this artifact are incorporated in the software of the SSC used here (HPD-TA, Hamamatsu). Here shortly will be summarized the properties of the offered methods (for a more detailed description the reader is referred to the user manual of the software). The simplest method that can be used is the so-called *slice* method. In this method all the pixels covered by the image spot will be allowed to count the event either as a complete event (the value of the frame-buffer will be increased with one) or as a fraction corresponding to the intensity in a particular pixel (the value of the frame-buffer will be increased with some fraction of one). In both cases the number of counts will not correspond to the number of photons, therefore the method is not recommended since it distorts the photon-counting statistics. The other two methods use different algorithms for assignment of the photon event to a certain pixel within the image spot and thus maintain the Poissonian statistics of the signal: *i) peak detection* – the photon event is assigned to the pixel with the highest intensity; *ii) center of gravity* – quite generally in this method the photon event is assigned to the pixel located in the center of the most intense signal within the image spot (not necessarily at the peak intensity).

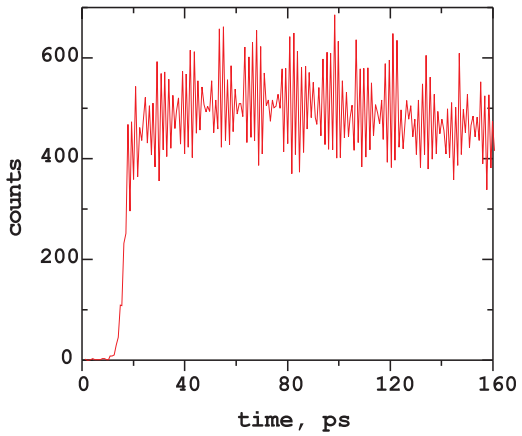

Figure 3.5
Specific Moiré pattern on the recorded signal in photon-couniting mode (peak detection or center of gravity methods) without using any Moiré reduction algorithms. The use of 'add free random value' algorithm removes this effect completely.

Our tests of the different photon-counting methods indicated that they introduced a specific pattern on the detected signal resembling the well-known Moiré effect in photography (Figure 3.5). Moiré effect is a specific interference pattern observed in the images, arising from the mismatch of overlaid grids. In the case of the SC, the pattern is related to the mismatch between the grid structures of the micro-channel plate and the CCD camera. Upon our request, the engineers in Hamamatsu have implemented in their software (HPD-TA, Hamamatsu) several Moiré reduction algorithms for the different photon-counting methods. The tests showed that the most efficient algorithm, which succeeded in suppressing the Moiré pattern without disturbing the photon counting statistics was the *´add free random value´* algorithm implemented for the peak detection photon-counting method (*vide supra*). For details about the algorithm the reader is referred to Hamamatsu, here we will just mention that in this algorithm, once the position of the peak intensity is determined, its coordinates are randomly modified. The modification, however, is minor; it does not lead to shifts in the images, and does not significantly influence the image resolution.

3.4 Time linearity and resolution of the synchroscan streak camera

In the SSC the time information carried by the photons arriving at different times at the photocathode is transformed into spatial information with the help of high voltage (~10 kV) sine wave applied on the sweep electrodes in the streak tube (*cf.* Section 3.1). This wave is produced by a combination of oscillator and amplifier. The oscillator is driven by the output of a mode-locked laser (here Ti:sapphire oscillator, 81.47 MHz), detected with the help of a PIN photodiode. The frequency of the deflection field is *locked* to the frequency of the laser, which allows many streak images to be accumulated on the same position of the CCD camera. From the electrons swept by the deflection field in the streak tube, only those who are located in a specific region around the inflection point of the sine wave of the applied voltage are being detected (Figure 3.6). This region corresponds to the part of the sine wave, in which the change in the voltage is nearly linear with time.

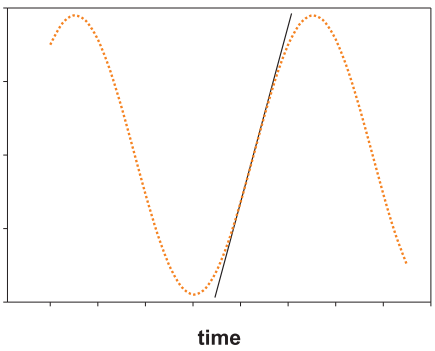

Figure 3.6
Quasi-linear part of a sine wave.

However, the non-linearity of the sweep voltage may be significant especially in the longest detection time ranges and thus has to be corrected for. Due to the non-linearity, the dependence of the position of the signal on the phosphor screen and hence on the CCD camera is not linear with time. This problem can be easily eliminated by measuring a train of pulses created with the help of a time etalon (161-163). The spacing between the pulses can be fitted with a polynomial function, which then can be used as a time calibration function (Figure 3.7), showing the time per pixel (signal position) dependence (this calibration is performed by Hamamatsu during the installation of the SSC). However, for our purposes we have developed an algorithm for linearization of the time scale in which the intensity in the non-equal time intervals is fractionalized on a linear time scale. The linear

time scales makes the analyses of the data easier because previously developed programs for data analysis with linear time scales can be readily used.

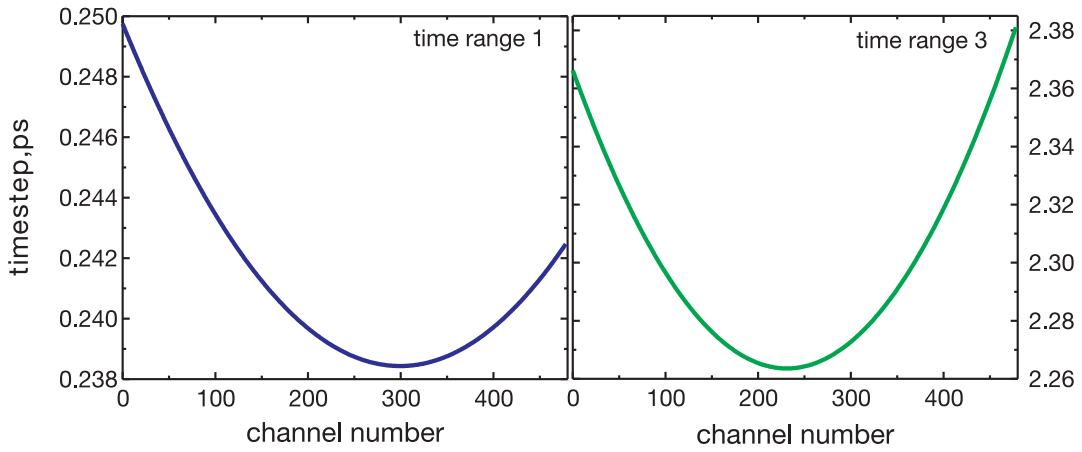

Figure 3.7
Time-calibration curves for two of the time ranges used.

The time-resolution of the SSC is perhaps the parameter that is of greatest interest since this is the major advantage of the method over the single-photon timing technique. The time-resolution depends on several factors and can be determined by simply evaluating the pulse width of a laser. The pulse should be measured under real experimental conditions and using a scattering solution instead of sample. The recorded signal is often referred to as either *instrument response function (IRF)* or *prompts response*. The major factors that contribute to the broadening of the IRF are (161): *i)* the response of the detector to a δ-pulse, $\Delta\tau_{DR}$; *ii)* the actual width of the used laser pulses, $\Delta\tau_P$; *iii)* the temporal dispersion due to the configuration of the excitation and due to the dispersion in the spectrograph (*cf.* Section 3.2.2 & Section 3.2.3), $\Delta\tau_D$; *iv)* the broadening of the *IRF* due to signal jitter and drift, $\Delta\tau_J$: If we assume that the various contributions to the time dispersion have Gaussian form then the time-resolution (FWHM), $\Delta\tau_S$, of the system can be expressed in the following way:

$$\Delta\tau_S = \sqrt{\Delta\tau_{DR}{}^2 + \Delta\tau_P{}^2 + \Delta\tau_D{}^2 + \Delta\tau_J{}^2} \tag{3.1}$$

Since we have already discussed the effect of the excitation geometry and the dispersion in the spectrograph (*vide supra*) and taking into account that the contemporary laser sources can provide ultrashort pulses, here we will concentrate on the other two factors. Every detector has specific response time, which in the case of SSC depends on two factors. The first factor is the so-called *transit time spread*, $\Delta\tau_{TS}$, which is determined by the statistical distribution of the velocities of the photoelectrons ejected from the photocathode (160,161,164). The effect is enhanced due to the difference in the energy (wavelength) of the photons striking the photocathode, since the difference in their energy is transformed in distribution of electron velocities that will broaden the response of the detector.

$$\Delta\tau_{TS} = (m\Delta v)/(eE) \tag{3.2}$$

where m is the mass of an electron and e is its charge, Δv is the difference in the velocity of the electrons, and E is the magnitude of the electric field near the photocathode.

The other limiting factor is the *technical time-resolution*, $\Delta\tau_T$, which is characterized by the time spread due to the finite minimum width of the image on the photocathode (*cf.* Section 3.2.3, horizontal slit width) and the finite sweep speed of the photoelectrons (160,161,164):

$$\Delta\tau_T = a/v_S \tag{3.3}$$

where a is the minimum resolvable distance and v_S is the sweep speed.

The minimum resolvable distance might be influenced by factors like imperfections in the focusing of the electron beam or electron repulsion in densely packed electron beams. The latter factor, however, has a small influence since in most case very low emission signals are detected with the SSC and thus the number of electrons in the beam is small. Combining Eq. (3.2) & (3.3) gives the detector response contribution to the time-resolution of the system:

$$\Delta\tau_{DR} = \sqrt{\Delta\tau_{TS}^2 + \Delta\tau_T^2} \tag{3.4}$$

The other factor that deserves great attention is the broadening of the *IRF* due to signal jitter and drift, $\Delta\tau_J$,. These two effects may have considerable impact on the time-resolution especially in the case of prolonged measurements of weakly emitting samples and thus here a separate subchapter is dedicated to this problem. The signal position stability is investigated elsewhere (164).

3.5 Sweep voltage stability – origin of the signal jitter and drift

The IRF of the SSC may become significantly broad under long signal acquisition times, which is due to the shift of the position of the detected signal. The origin of this shift is related to the stability of the sweep voltage in the streak tube. As described above the sine wave of this voltage is synchronized and phase-locked to a stable oscillator (here Ti:sapphire, 81.47 MHz). However, there is always a small random instability of the voltage phase, which makes the signal oscillating around particular detection position – *signal jitter*. Although in the current design of the SSCs the jitter is strongly reduced, it can still account for about 1-2 ps broadening of the *IRF* in the shortest detection time range. This component can be viewed as the lowest limit for the width of the *IRF* since there is no algorithm that can correct for it. If this was the only signal-shifting effect, the performance of the SSC will be highly satisfactory, delivering signals with IRF of 2-3 ps, which after deconvolution in the data analysis procedures could yield time-resolution of about ~200 fs. However, other effects play significant role and limit the time-resolution. We have investigated here thoroughly these effects and developed a new data correction algorithm for their elimination. We should mention that the software of the SSC used (HPD-TA, Hamamtsu) comes with an integrated correction algorithm. Nevertheless, this algorithm turned out to be inappropriate for our purposes since it depends on using the image of the laser pulse for the correction, which was not possible here.

3.5.1 Signal drift components

The time-resolution of the SSC depends on the spread of the photoelectrons by the electric field between the sweep electrodes. The highest time-resolution is achieved at the highest amplitude of the voltage sine wave applied on the electrodes (*vide supra*). However, the highest amplification is related to large thermal effects in the SSC, which inevitably lead to instabilities of the electronics. Our investigation on the thermal drifts concerns mainly the shortest time range (here 116 ps), where the amplification of the voltage is extremely high and the thermal effects are strongly manifested. The time-resolution in the rest of the time ranges is only slightly influenced by the thermal effects.

The tests that we have performed indicated that there are several components of the thermally induced signal drift. The first and shortest component is well known and is related to the initial warm-up, when the SSC is switched to the shortest detection time range. The initial warm-up time of the SSC used here is at least ~40-60 min. After this time, the phase-lock loop for the voltage sine wave can be activated. The locking of the phase allows images to be accumulated at particular position on the detector. Nevertheless, it appears that the thermal effects in the SSC need more time to be completely equilibrated. In Figure 3.8 is shown the kinetics of the thermal drift of the SSC after activating the phase-lock loop. The analysis of the dependence signal position *vs.* time showed that the drift kinetics of freshly turned on SSC (total system warm-up, including the lasers, of 4 h, initial warm-up in the shortest detection time range (*vide supra*) – 60 min) can be described with two components (Figure 3.8, trace A): *i)* a fast one of ~20 min lifetime; and *ii)* a slow one with ~800 min lifetime. The short component (20 min) appears to be related to the phase-lock loop, since such component is observed always after the activation of the loop and independently from the warm-up time of the SSC in the shortest time range. We have also tested the signal position drift after ~20 h warm up of the SSC in the shortest time range and the same warm-up time of the lasers (4h). In this case we allowed additional 60 min warm-up after the activation of the phase-lock loop (Figure 3.8, trace B). After this time, the system is very stable although there is a small drift that can be described with ~100 min lifetime. It is clear from the obtained results that the warm-up time of the SSC has a tremendous impact on the stability of the signal position drift; warm-up times of 20 h in the shortest time range can reduce the signal drift to less than 5 ps over more than 10 h of data collection. Exceedingly high stability is of crucial importance when very weak signals have to be measured or the measurements are performed in the photon-counting acquisition mode.

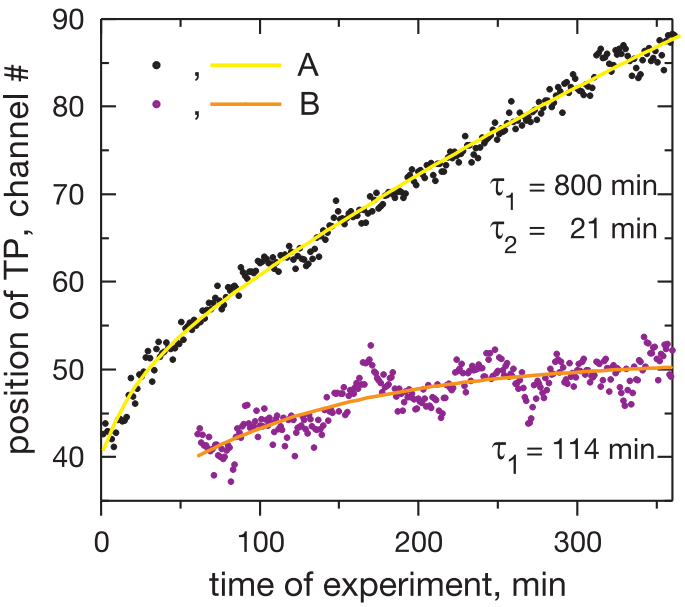

Figure 3.8
Signal position drift in the shortest time range (116 ps, time per channel – 0.2423 ps) of the SSC.
Trace A is recorded after 4 h warm-up time of the SSC, which includes also ~60 min initial warm-up in the shortest time range. The drift is recorded immediately after the activation of the phase-lock loop.
Trace B is recorded after ~20 h warm-up of the SSC in the shortest time range. The drift is recorded ~60 min after the activation of the phase-lock loop (note the difference with *trace* A).
The warm-up time of the lasers was the same as in both cases (4 h).
TP stands for turning point of the measured fluorescence signal originating from dye solution.

Independent of the temperature effects in the SSC there is another source of signal drift, which is related to the stability of the oscillator that is used for phase locking the SSC. The effect is well known and is pointed out in the user's manual of the SSC that we used. Without going in details, we will just mention that high stability of the signal position can be achieved by ensuring high stability of the oscillator to which the phase-lock loop is synchronized.

3.5.2 Correction procedures

Normally, the data from the SSC is recorded in the form of many sub-images, which are then averaged. This allows correction for the signal drift prior to the averaging of the images. The software provided with the SSC used here allowed correction of the time drift using the laser signal. The correction procedure searches for the center of gravity in this spot and aligns all sub-images to one position. We were not able to use this method since in our experiments the laser wavelength is very close to the detection wavelength and to avoid some distortions of the measured data we are filtering out the laser light. Although not applicable in our case, the method is highly effective. A possible development, which was offered by the engineers from Hamamtsu and used in (164) is introduction of a laser reference signal directly in the SSC. However, we have developed another algorithm for image correction, which makes such development for real measurements unnecessary.

In our approach, the signal drift correction is done directly using the measured signal; the approach can be applied even for very weak signals. The correction is performed as follows: *i)* in each recorded sub-image the available signal intensity in the different wavelengths is summed at each time instant, resulting in one decay curve composed of the decay curves of the studied sample at all wavelengths. In this way, we have gained significant intensity to perform further operations. *ii)* the next step is to fit the rise kinetics in the so-generated curve with a half Gaussian, which delivers parameters that can be used for aligning the sub-images. Namely, these are the inflection points of the half Gaussians, whose position can be precisely estimated from the fit. *iii*) the last step is to align the original sub-images using the position difference between the inflection points of the first sub-image and the rest of the sub-images. Using this procedure, we have obtained IRF in the shortest time range of ~3.5 ps for measurements with more than 10 h duration. Naturally, the result is sensitive to the amount of signal drift and thus it is recommended to allow reasonable warm-up of the SSC (*cf.* Section 3.5.1).

We have observed that for extremely low signals (high noise level), the half-Gaussian fit in some frames fails to correctly describe the rise kinetics in the summed up signal. In order to avoid such failures certain constrictions were implemented in the algorithm.

3.6 Long fluorescence decays and the back sweep problem

The sweep voltage of the SSC is a sine wave synchronized with the frequency of an oscillator (here Ti:sapphire, here 81.47 MHz); the period of the sine wave is equal to the inverse of the frequency of the oscillator, *e.g.* ~12.3 ns. It is apparent that every half period (~6.15 ns) the sweep wave will traverse the detection region in the streak tube; both in the direction of increasing voltage (forward sweep) and in the direction of decreasing voltage (*back sweep*). If the emission signal detected with the SSC has a lifetime longer than ~2 ns the tail of the emission decay will be brought again into the detection window by the back sweep and overlaid in opposite direction to the signal detected during the forward sweep. In case of very long lifetimes, several such forward backward cycles can be realized. This limitation can be overcome using two different approaches.

For measurements of relatively intense emission with long lifetime the so-called *blanking* unit provided with the SSC (M5678, Hamamatsu) can be used. The blanking unit uses additional, horizontal deflection plates, which shift the photoelectron beam in such a way that the back sweep photoelectrons related to the tail of the emission decay are not overlaid on the main signal. However, the horizontal shift of the photoelectrons by the blanking unit leads to generation of specific curvature on the detected signal, which has to be corrected for. The software provided with the SSC (HPDTA, Hamamatsu) has an implemented curvature correction option. The correction uses three

points on the signal arbitrarily selected by the user to straighten up the image. This correction is relatively simple and subjective, and thus in our view not reliable. In this respect, we have developed our own correction procedure. In essence, an intense image of a know sample (dye) with long lifetime is recorded for each detection time range using the blanking unit. In the next step the maximum position (channel number) of the fluorescence signal at every time instant is fitted with a polynomial function. The function can be used to straighten up any image recorded with the blanking unit. Additional advantage of our approach is the possibility to prove-test whether the algorithm works correctly. The data from the straighten image of the dye can be submitted to a data analysis program and the lifetime of the emission decay can be recovered. As long as the algorithm works properly, the recovered lifetime should not differ significantly from the known lifetime of the dye.

An alternative way to cope with the back sweep problem is to record the data with the back sweep signal overlaid on the main one and then account for this during the data analysis (145). This approach is appropriate when the long-lived emission signal has low intensity and is not of major interest, *e.g.* sample contaminations. We have implemented in our data analysis programs an additional step in the generation of the simulated data that is fitted to the experimental signal. In this step for every lifetime component longer than 1 ns the back sweep (or if necessary several forward-backward sweeps) is calculated and summed to the main forward sweep. The results from such analysis are shown in Figure 3.9.

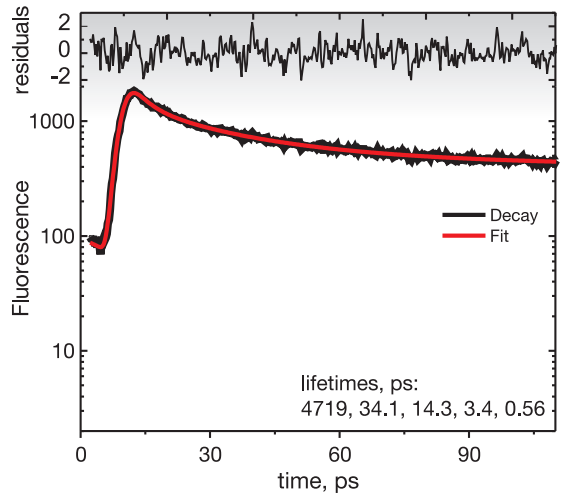

Figure 3.9
An example of SSC signal analysis of complex decay kinetics with a long lifetime contributing with back sweep intensity. The offset of the signal from 0 is due to intensity added from several forward-backward sweeps of a long decay lifetime (~5 ns). It is apparent that the data can be well fitted if the sweep is correctly accounted for. The signal is recorded from a PS I complex, and the long lifetime is well characterized in the literature (*e.g.* (101)).

3.7 Spectral sensitivity corrections

The sensitivity of the SSC detection is not uniform along the whole wavelength axis and in order to obtain the real spectra of the measured compounds a spectral sensitivity correction has to be performed. This correction can include also correction for the transmission of the filters used in the measurement (*e.g.* color glass filters or interference filters).

The correction function is obtained by recording a streak image of a continuous source of white light, like *e.g.* a halogen lamp. In the ideal case, the recorded image should match the real spectrum of the lamp. However, due to some imperfections of the detection the image is not precisely the same. Since the real spectrum of the lamp is usually provided with its specification the ratio of the recorded spectrum with the SSC and the real spectrum of the lamp can be used as the spectral sensitivity function of the system.

$$f_{spect.sens.} = L_{lamp.meas.} / \left(L_{lamp.real} \cdot f_{diff.transm.} \right) \quad (3.5)$$

$f_{spct.sens}$ – the spectral sensitivity function of the detection system; $L_{lamp.meas.}$– the recorded with the detection system lamp spectrum; $L_{lamp.real}$ – the real spectrum of the lamp; $f_{diff.transm.}$ – the transmission function of a diffuser in case such is used for recording the spectrum of the lamp (usually it is used to obtain uniform image from the lamp).

The spectral sensitivity function is then used to correct the emission spectra recorded in real measurements:

$$F_{real} = F_{meas.} / f_{spect.sens} \quad (3.6)$$

F_{real} – the real fluorescence spectrum of the studied sample; F_{meas} – the fluorescence spectrum of the sample measured with the detection system (contains sensitivity imperfections); $f_{spct.sens}$ – the spectral sensitivity function of the detection system as calculated in Eq. (3.5);

When a cut-off filter is used to eliminate certain part of the detected signal (*e.g.* laser scattering) additional correction should be performed for the transmission of the filter. This can be done either by directly recording the lamp image using the filter or by correcting the spectra for the filter transmission:

$$F_{real} = F_{meas.} / \left(f_{spect.sens} \cdot f_{filt.transm.} \right) \quad (3.7)$$

F_{real} – the real fluorescence spectrum of the studied sample; F_{meas} – the fluorescence spectrum of the sample measured with the detection system (contains sensitivity imperfections); $f_{spct.sens}$ – the spectral sensitivity function of the detection system as calculated in Eq. (3.5); $f_{filt.transm.}$ – the transmission of the filter used in the fluorescence measurement.

It is important to keep in mind that the transmission of the interference filters is strongly dependent on the incidence angle of the light. This means that the transmission function of the filter, which normally is recorded with collimated light in a spectrophotometer, should be corrected for this angle dependence. For this purpose, several transmission curves of the filter covering the range of angles at which the fluorescence emission passes through the filter in the real measurement should be recorded (Figure 3.10). The range of angles depends on the angle of view of the imaging optics used to focus the fluorescence emission on the entrance slit of the spectrograph. The recorded transmission curves are averaged to obtain the real transmission function of the interference filter. In the case of large angle ranges, a weighting factor can be used in the averaging to account for the difference in the illuminated area on the filter.

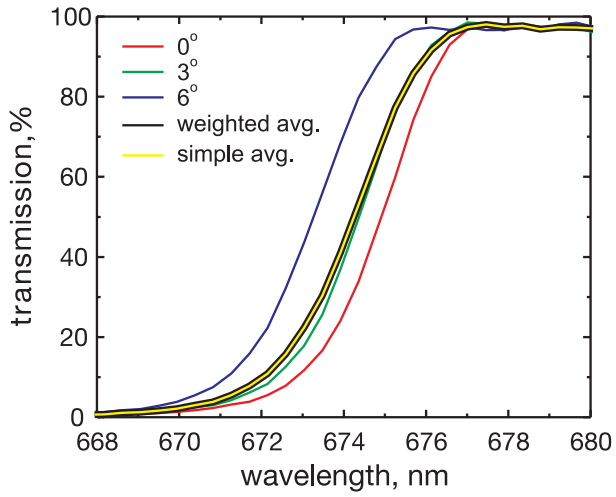

Figure 3.10
Transmission curves of an interference filter at three incident angles. In the case of small differneces in the area covered by the incident light the simple and the area weighted averaging of the transmission curves yields similar results.

3.8 Final remarks

The SSC method of fluorescence detection allows for a combination of relatively high sensitivity and time-resolution of the emission measurements. We have tested the possibilities to perform photon-counting experiments with the SSC and showed that such measurements of extremely weak signals can be performed without major distortions. The main challenge in this case is to achieve exceedingly high stability of the complete experimental set-up, starting from the output of the oscillator used to synchronize the sweep voltage in the SSC and finishing with allowing complete thermal equilibration of the SSC unit, especially in the shortest time range of detection. Provided that these conditions are achieved the broadening of the IRF in the shortest time range (most vulnerable) can be minimized to less than 5 ps over many hours of continuous measurement. In order to satisfy our requirements we have developed our own correction algorithms for both signal drift correction and for back sweep correction (both using and not the blanking unit). Our drift correction algorithm succeeds in compressing the drifted signal (for than 10 h detection) to the shortest possible *IRF* for our experimental organization, namely 3.5 ps.

The optical organization of our set-up (excitation and emission detection geometry, use of interference filters) allows for detection of the fluorescence signal very close to the excitation wavelengths (~6 ps), which is of significant importance in many experiments.

In our opinion, the SSC technique fulfills well its purpose to fill in the gap between the single-photon counting and the fluorescence up-conversion techniques, delivering data of high quality.

Chapter 4

Trap-limited charge separation kinetics in Photosystem I complexes from higher plant

This chapter is based on the publication:
Chavdar Slavov, Matteo Ballottari, Tomas Morosinotto, Roberto Bassi, and Alfred R. Holzwarth
Biophysical Journal 2008, 94:3601-12

4.1 Introduction

The process of photosynthesis in its early stages occurs in highly specialized membrane-bound pigment-protein complexes. These complexes are divided into two families, depending on the terminal electron transfer cofactors: *i)* the type II reaction centers (RCs), like PS II and some bacterial RCs; *ii)* and the family of the type I Fe-S RCs, to which PS I belongs. Higher plant PS I consists of a core complex of about 12 protein subunits and an outer antenna semi-ring of 4 units (40,165). The whole complex hosts approximately 200 cofactors amongst which six redox-active chlorophyll (Chl) molecules located in the RC, 97 Chls in the core antenna, 56 - in the outer antenna, and about 9 Chls fill the gap between the two antennae (for review see (166)). In addition, PS I carries further the redox-active cofactors on the acceptor side and a large number of carotenoid molecules (40) (for a high resolution structure of the cyanobacterial PS I which is to a large part conserved in the core of higher plant PS I see (41)). The six Chl molecules in the RC are strongly excitonically coupled between each other as predicted by theoretical calculations (48,49), thermodynamic analyses (50), and confirmed by experimental studies such as *e.g.*, ultrafast transient absorption (TA) (6,51,52), mutant studies (53), and Raman scattering (54). This strong coupling of the RC Chls and the ensuing widening of the covered energy spectrum might be of great significance for the efficient and fast energy transfer from the surrounding core antenna Chls to the RC (55).

Owing to its structure PS I possesses several specific properties distinguishing it from other photosynthetic complexes. The current study is concerned with two of these features. First, the inseparability of the core antenna and the RC of PS I, which together with the high Chl density render specific time-resolved studies of the electron transfer processes in the RC very difficult. The second characteristic is the presence of Chl forms with lower energy than the RC Chls ('red' Chls) (for a review see (61)). Apparently, these Chls have high importance for the overall function of PS I as they are conserved during evolution and even increased in higher plants with respect to algae. In order to reveal the function of these 'red' Chls, their role in the light trapping kinetics has to be characterized.

During the last few years great efforts were made by several research groups for analyzing the trapping kinetics in PS I, but no general agreement was reached. The 'red' Chls, supposedly located mainly at the periphery of the monomeric complex, play a decisive role in controlling the overall kinetics. In some of the recent ultrafast studies on cyanobacterial PS I the kinetics was discussed as balanced between trap- and transfer-to-trap-limited (75). In contrast, other authors proposed a purely transfer-to-trap-limited kinetics on the basis of a non-equilibrium trapping interpretation of the time-resolved fluorescence and transient absorption data (76,107-109,111), and theoretical modeling (49). In some early minimal models a purely trap-limited kinetics was also proposed (70,124) for cyanobacterial PS I. However, these studies lacked either sufficient time-resolution in the measurements (124) or did not attempt a detailed kinetic modeling (70). In addition some basic criticism may be applied to most of the above-mentioned studies since the analysis of the experimental data either did not account for some of the important features of the electron pathways such as *e.g.*, charge recombination (76,107-109), or used the highly questionable assumption of equality of the excited state quenching processes in open and closed PS I complexes (111). In fact an increase of about 12% in the fluorescence quantum yield after P_{700} oxidation was observed by Byrdin and co-workers (75), which implies a different trapping kinetics in PS I with closed RC.

Irrespective of the discrepancies between the models suggested by different groups, the underlying data themselves are often quite similar, with energy equilibration times ranging from a few

picoseconds to a few tens of picoseconds and a main trapping lifetime of about 20-25 ps (70,75,76,108,109,111,126) in PS I-cores and additional component(s) in intact higher plant PS I. However, the 20-25 ps component assigned to main trapping in many of these works is a complex component and most likely represents a mixture of more than one process. Recent TA and fluorescence decay studies on PS I-core particles from *C. reinhardtii* carried out in our laboratory (52,127) shed more light on the trapping kinetics of PS I-cores. One important conclusion of these studies was that a charge recombination step was required for the description of the energy and the charge transfer events in PS I. Furthermore, for the first time these studies resolved the excited equilibrated RC* (i.e. excited state of the group of the six RC Chls) of PS I as a separate compartment both spectrally and kinetically. According to these results energy trapping in the PS I-core is limited by the charge separation (CS) rather than the energy transfer (ET), i.e., the kinetics in PS I-cores that are devoid of 'red' Chls is purely trap-limited. Additionally, these studies for the first time provided an evidence for the accessory Chl – ec2 as a primary donor in PS I RC (52).

Recently, Ihalainen et al. have investigated the excited state dynamics in intact higher plant and algae PS I particles using time-resolved fluorescence with high resolution, and suggested a transfer-to-trap-limited kinetics (104). The authors used a model with two 'red' Chls compartments for the description of their data. However, the conclusions drawn from that modeling are subject to criticism since the internal conversion rate to the ground state for the LHC I bulk-red compartment is very high (6.81 ns^{-1}), which – if correct - would lead to high quantum yield losses for CS. So far there exists no convincing evidence, that radiationless deactivation to the ground state from excited 'red' Chls is so efficient that such a high deactivation rate is justified. Interestingly the 'red' PS I-core compartment in their model has a high transition rate directly to the trap (*i.e.*, the charge separated state), which – if this compartment is interpreted as a 'red' Chl located somewhere in the bulk antenna - implies that most of the energy reaching this 'red' Chl compartment does not pass through the core antenna before CS. Such a scenario has been ruled out, however, *e.g.*, by Jennings and co-workers (110). We will in fact show in this work that the compartment attributed by Ihalainen *et al.* to 'red' PS I-core in fact represents the RC itself. However in an alternative model Melkozernov *et al.* suggest a diffusion-limited step in the trapping kinetics of intact *C. reinhardtii* PS I particles, due to a bottleneck in the ET from the peripheral antenna (LHC I) to the PS I-core antenna due to the presence of regions of weak coupling (167). Additionally, the latter authors suggest slow energy equilibration amongst the LHC I complexes.

The functional and biological roles of the peculiar 'red' Chls represent a feature of the PS I antenna that still lacks understanding. Certainly, the presence of 'red' Chls does not impair the quantum efficiency of PS I substantially, if at all, since the lifetime of the excited state of a Chl in a protein is on the timescale of several ns, while the longest excited state decays of 'red' Chls in PS I are only up to ~100 ps. Some authors proposed that the 'red' Chl forms provide a physiological advantage for the plants in special light conditions (115,120,121). Others discussed their role in connection with the funnel model of ET to the RC (114) or suggested their participation in photoprotection (61,114-117,119).

Typically, the 'red' Chls have very broad 'red'-shifted spectra due to a high electron-phonon coupling (64-68). In cyanobacteria these 'red' Chls are located in the core of PS I. Low temperature studies reveal the presence of two to three main absorption bands at 708 nm and 719 nm (C708 and C719) (65,67) and possibly also at 715 nm (C715) (64) for *Thermosynechococcus sp.* Two 'red' Chl forms are found at low temperature also in *Synechocystis* at 708 nm and 714 nm (66). Unfortunately, the exact

position of the Chls responsible for the 'red'-shifted absorption and fluorescence in the structure is not known. According to Melkozernov et al. (73) they are located in the vicinity of the RC, contrary to the more distant position proposed by other authors (66,74-76). For cyanobacterial PS I a highly likely position is in the monomer-monomer interaction region of the trimer (41).

In contrast to cyanobacteria the 'red' Chls in higher plants appear to be located almost exclusively in the peripheral LHC I complexes (168) although Ihalainen *et al.* (104) assign one 'red' Chl state to the core antenna (*vide supra*). Several studies on preparations of PS I particles and LHC I complexes demonstrated convincingly that the main part of the 'red'-shifted fluorescence of intact PS I could be well explained by Chls situated in the peripheral LHC I complexes (110,169) and/or at the interface between the core complex and the peripheral antenna (167,170,171) possibly involving some of the so-called 'gap' Chls (96). A very small contribution of 'red'-shifted fluorescence from the PS I-core is supported by a site-selective and high-pressure spectroscopy study on PS I-200, PS I-core and LHC I, which suggests presence of three 'red' Chl states in the intact PS I complex. Two of them (C706 and C714) were proposed to be located in the core with extremely small emission yield (F722 nm), and one in the LHC I – absorbing around 710 nm (emission F730 nm) (68). The properties of the 'red' Chls differ strongly amongst the different LHC I complexes. In Lhca 1 and Lhca 2 the pigments responsible for the 'red' shift at low temperature emit at about 686 nm and 701 nm, respectively (172) and thus cannot be responsible for the 'red' Chls fluorescence observed in intact PS I. For Lhca 3 and Lhca 4 the 'red' emission maxima are however located at 725 nm and 735 nm, respectively (87) and are likely to be responsible for the 'red' emission in intact PS I. These spectral differences let us expect more than one 'red' Chl component arising from the peripheral LHC I complexes in time-resolved studies.

The energy exchange of the different 'red' Chls with the bulk antenna system (*i.e.*, the iso-energetic Chls of the PS I core complex, the 'gap' Chls and the LHC I complexes, excluding the 'red' Chls) was found to take place in the range of a few to tens of ps (75,76,104,173-177). Due to this relatively slow energy equilibration, and the related slowing down of the overall trapping kinetics it was concluded that the 'red' Chls in PS I can hardly increase the trapping efficiency in PS I (76) as had been discussed earlier. Their role should be a different one instead. Very clearly, they increase the absorption cross-section in a part of the solar spectrum that is not used efficiently otherwise (120,178). In addition they may have a photoprotective role (61,115-117,119). The shift of the 'red' Chls location in higher plant PS I towards the periphery of the complex might be attributed to differences in their function or/and to differences in the environmental conditions as compared to cyanobacteria.

Disagreement exists also about the influence of the bulk antenna enlargement and the presence of 'red' Chls on the overall trapping kinetics. According to the work of Jennings and co-workers (110) these two factors have an equal influence on the kinetics. The authors suggested that the ~30 ps and ~80 ps components in the fluorescence kinetics of PS I-intact particles are due to the dynamics of the outer antenna 'red' Chls. Alternatively, Ihalainen *et al.* proposed a dominant role for the 'red' Chls (104).

It follows from the discussion above that most aspects of the kinetics of higher plant PS I are not well understood yet. By comparing the ultrafast fluorescence data from PS I-cores with those of intact PS I the present work aims at characterizing in detail the ET and CS kinetics in higher plant PS I. We focus in particular at characterizing precisely the influence of the outer antenna and of the 'red' Chls on these processes, and to resolve also the RC* state kinetically and spectrally for higher

plant PS I. The discussion will address in detail the question of possible bottlenecks in the energy flow between the various antenna compartments. A further point concerns the possible role of detergents for the functional coupling of the peripheral LHC I complexes.

4.2 Materials and Methods

PS I-LHC I particles (PS I-intact particles) were isolated from *A thaliana* thylakoids by sucrose gradient ultracentrifugation after solubilization with 1% β-DM, using the protocol described in (50). Antenna and core moieties were dissociated by treating with 1% β-DM and 0.5% zwittergent -16. PS I-core particles and LHC I were isolated by sucrose gradient ultracentrifugation as in Croce *et al.* (50). Stroma membranes were purified by mechanical fractionation with a Yeda-press, followed by differential centrifugation according to previous reports (179).

For the time-resolved fluorescence measurements, the isolated core and intact PS I particles were diluted in 30 mM Tricine buffer (pH 7.8), containing 500 mM sucrose and 0.009% α-DM to an OD ~0.3 cm^{-1} at the Chl Q_Y maximum. The medium contained also 40 mM sodium ascorbate and 60 μM phenazine methosulfate as redox agents to keep the RCs open during the measurements.

The single-photon timing technique was used to perform picosecond time-resolved fluorescence measurements. The set-up consists of a synchronously-pumped, cavity-dumped, mode-locked dye laser at 800 kHz repetition frequency with a DCM as a laser dye (107,127). The pulse of the dye laser has a FWHM of 10 ps and the whole response of the system is about 30 ps FWHM, which after deconvolution results in a time-resolution of 1-2 ps. The sample was placed in a rotating cuvette (10 cm diameter, path-length of 1.5 mm) moving sideways at 66 rpm and rotating at 4200 rpm. The laser intensity at the sample was about 0.05 mW, ~0.8 mm spot diameter. Such experimental conditions ensure complete re-reduction of the RC before the next excitation occurs. Under these conditions, less than 1% of the particles receive a second laser excitation during the time they spend in the laser beam. The excitation wavelength was 663 nm to selectively excite the bulk antenna Chls. Measurements were carried out at ambient temperature (21 ±2°C).

Fluorescence decays were analyzed by means of global and target analyses (151,152). Global analysis is a combined mathematical fitting of the decay curves at different wavelengths done in a single fitting procedure. The analysis results in lifetimes and decay-associated spectra (DAS), describing the whole set of original data. In the more elaborate target analysis, kinetic models are fitted to the data in global fashion. Such an approach leads to a physically meaningful description (rate constants and spectra of the different compartments (species-associated emission spectrum (SAES)) and gives detailed information about rate constants of energy and electron the processes taking place in the investigated system. Several physically reasonable models are usually tested for their compatibility with the data.

4.3 Results

4.3.1 Global analysis

The fluorescence decay kinetics after 663 nm excitation of PS I- core and -intact particles and of purified stroma membranes (containing dominantly intact PS I complexes) were recorded with 1-2 ps time-resolution at different emission wavelengths. The excitation wavelength was chosen such to avoid direct excitation of the 'red' Chls and to ensure the start of the excited state dynamics to be in the bulk antenna. Global analysis was applied on the time-resolved data (see Figure 4.1).

At first glance the sets of lifetimes describing the fluorescence decays in the PS I-cores and PS I-intact particles look similar, in particular for the lifetime range below 20 ps. Significant differences can be observed in the amplitude of the 40 – 55 ps lifetime, which has nearly zero amplitude in the core particles but has a large amplitude in the intact PS I and in the stroma membranes. Due to the broad and 'red'-shifted spectrum of the 55 ps lifetime in the PS I-intact particles and in the stroma membranes this component can be clearly attributed to the dynamics of a 'red' Chl excited state. The lack of 'red'-shifted DAS components for higher plant PS I-cores is in agreement with other studies (110,169,170) and questions the assignment of the compartments in the modeling performed by Ihalainen et al. (104).

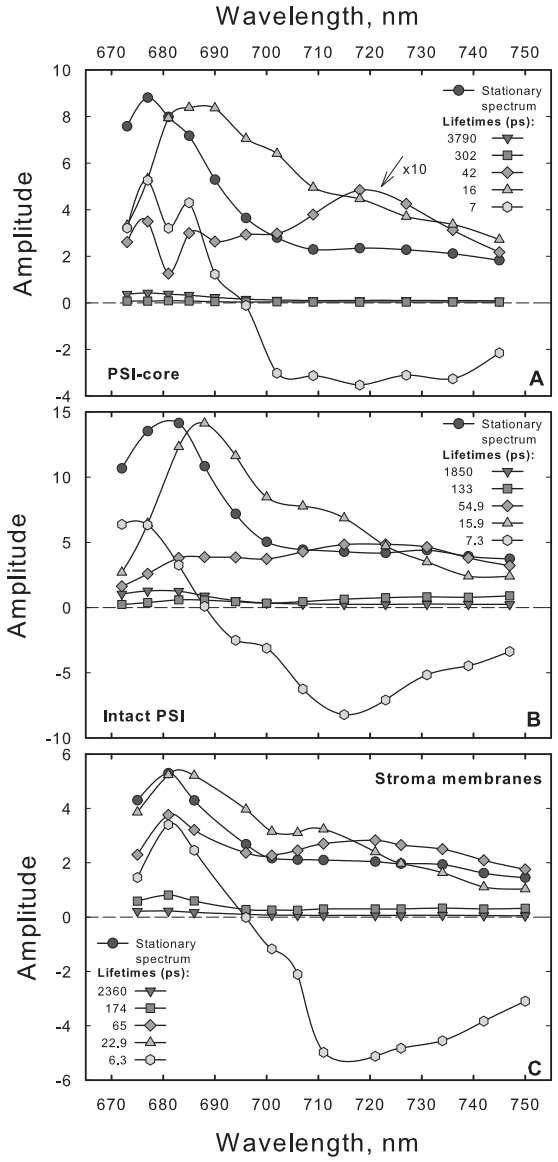

Figure 4.1
Steady state fluorescence spectra (black circles), and decay-associated spectra (DAS) and lifetimes of the fluorescence from A. thaliana PS I-core (A), PS I-intact (B) particles and stroma membranes (C) obtained through global analysis of the fluorescence decay data, λ_{exc} = 663 nm excitation. χ^2 = 1.032, χ^2 = 1.024 and χ^2 = 1.04 respectively.

The main fluorescence decay in both systems occurs with a lifetime of about 16-17 ps. This component has a relatively broad spectrum peaking in the 'blue' range (680-685 nm) and most likely reflects the energy trapping processes from at least partially equilibrated antenna, comprising also RC* fluorescence. However, unambiguous assignment of the lifetimes to a particular process at this stage of the analysis is not possible. Quite generally, the observed lifetimes and their DAS represent a weighted mixture of all the kinetic processes occurring in the system. Nevertheless, similar lifetime components were found in most of the recent studies of PS I energy trapping kinetics (51,104,110,127,167). Nonetheless, not all of the short-lived components were resolved in some of these works. The shortest lifetime component (~7 ps) possesses positive-negative amplitude with zero-crossing around 685 nm for intact PS I and 695 nm for PS I-core. This component thus represents the slowest part of the overall energy equilibration dynamics. The data from the intact PS I complexes are thus very similar to our previous data on intact PS I from maize (107) except that the fastest lifetime component is now resolved into two components. Additionally, we find a nearly negligible long-lived component in the ns time range, which can be assigned to a small amount of energetically decoupled Chls or antennae present in the sample. Our experience shows that the amplitude of this component is strongly dependent on the detergent concentration in the buffer used for the measurement. We observed that detergent concentrations right at the onset of the micelle formation (*i.e.*, the critical

micelle concentration) are the least disruptive for the complexes. A similar observation concerning the uncoupling of peripheral LHC I complex has been made earlier (180).

The comparison between the DAS of the stroma membranes and the detergent-isolated intact PS I particles (see Figure 4.1 B and C) reveals some slight spectral differences in the 'blue' part (around 680-690 nm) of the spectra of some of the decay components. These differences are presumably due to some lifetime overlap with a minor contamination by PS II in the stroma membranes, which is expected. Nevertheless, the set of lifetimes describing the fluorescence decay kinetics in stroma membranes is nearly identical with the one from detergent-isolated intact PS I. Importantly, the DAS in the 'red' spectral part are highly preserved (*cf.* Figure 4.1 B and C), which means that during the isolation of the intact PS I particles the 'red' Chl compartments were not disrupted by the detergent. For these reasons we will describe here in detail only the analysis on the purified intact PS I particles.

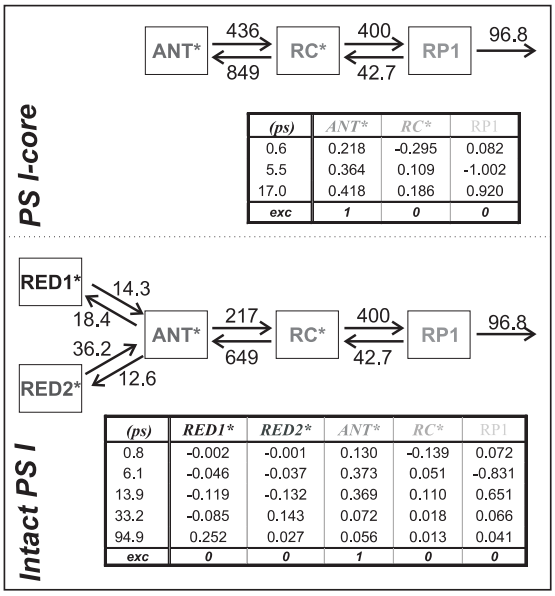

Figure 4.2
Compartment models with rate constants (ns^{-1}) (top), lifetimes and eigenvectors (bottom) for the PS I-core (top box) and PS I-intact (bottom box) particles. $\chi^2 = 1.1$ and $\chi^2 = 1.01$, respectively.

4.3.2 Target analysis

As mentioned above global analysis is a pure mathematical fitting and does not provide much physical insight and information. Principally, after obtaining some qualitative information from the former approach, kinetic modeling by target analysis was performed on the data to fully characterize the underlying processes within compartment models, which represent models of reduced complexity of the system (98). This reduction of complexity is required since the time-resolution and S/N ratio does not allow resolution of single ET steps. Thus for the purpose of kinetic modeling the investigated system is separated into physical domains with similar properties, *e.g.*, bulk antenna, 'red' Chls, *etc.* For each sample – PS I-core and PS I-intact particles several different kinetic models were tested on the data. Figure 4.2 and Figure 4.3 show the final results of the target analysis. The models yield the rate constants, the weighted eigenvector matrix and the time course of the relative populations of the involved states. For a detailed description of these terms see (52). Figure 4.4 illustrates the corresponding species-associated emission spectra (SAES). The models describing the trapping kinetics in PS I-core and in intact PS I particles differ in the presence of 'red' Chls. Since no significant 'red'-shifted fluorescence compartment was observed in the global analysis of the core

particles 'red' Chls compartments were not included in the model describing the kinetics of the core. In fact, such models were tested but they did not lead to satisfactory results. After performing the kinetic modeling we have recalculated the DAS for the studied complexes (see Figure 4.6). Besides the lifetime components directly associated with the model compartments, one (intact PS I) or two (PS I-core) additional components are present which are attributed to some minor content of detached LHC I and/or functionally decoupled Chls (*vide supra*).

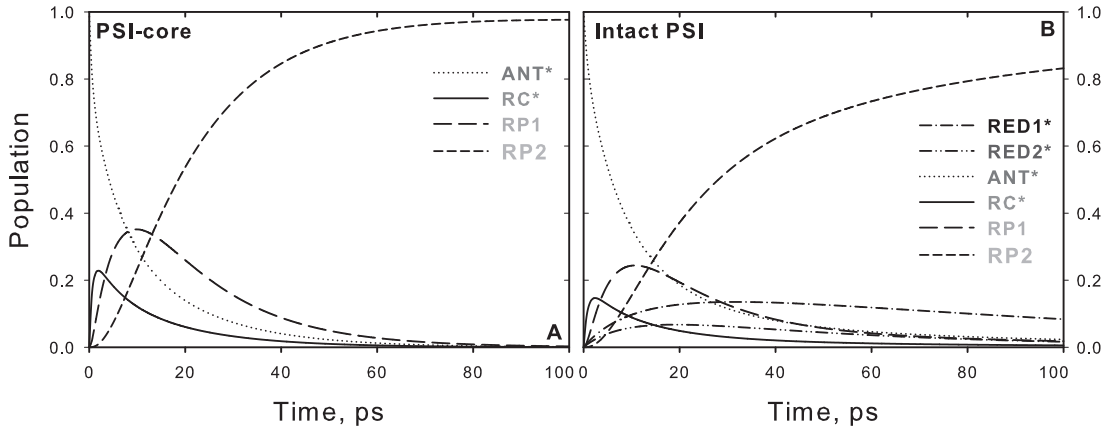

Figure 4.3
Time dependence of the relative populations for the different model compartments in Figure 4.2. A) PS I-core particles; B) PS I-intact particles.

4.4 Discussion

4.4.1 Reaction center kinetics

A key feature of the presented models is the presence of a fluorescing compartment representing the excited RC Chls (see Figure 4.2). Such a compartment was already resolved in our previous studies on green algae PS I (52,127) and has a solid theoretical and experimental base (48,50-54). Due to the strong excitonic coupling amongst the six RC Chls the physical properties of this group of pigments are significantly modified in comparison with the antenna Chls (49). Another reason is their spectral role as electron transfer cofactors and their relatively large distance from the core antenna Chls (40,41,165). Therefore the RC* kinetics should be separable and be described by an individual model compartment. Furthermore the proper rates of the first electron transfer steps can only be extracted if the RC* is resolved as a separate compartment. It was indeed possible to resolve the RC* kinetics in our data (see Figure 4.2 and Figure 4.3). The transient population of the RC* compartment reaches about 22% in the PS I-core and 15% in the intact PS I particles (see Figure 4.3). We also tested again whether a charge recombination step from the first radical pair (RP1) is required to describe our data (see Figure 4.2), following the recent studies of Holzwarth *et al.* (127). Clearly, any models that did not include such a process gave no reasonable description of the kinetics in agreement with our previous findings on green algae PS I-cores (52,127).

The electron transfer kinetics in the RC for both samples is the same within the error limits, which on the one hand is an expected result since this part of the PS I particle is not affected by the isolation procedures and should be independent of the antenna size. On the other hand, the fact that the kinetics in both particles is described by the same electron transfer rates, despite the largely different overall kinetics, provides very strong support for the validity of the presented models. The charge separation rate is ~400 ns^{-1} and is in the same range as the one obtained for green algae PS I-

cores (52,127). Additionally, we are also able to resolve the decay of RP1. In both of the studied complexes, this process occurs with a lifetime of ~14-17 ps, again in agreement with the above-mentioned data on green algae cores (rate constant of 97 ns^{-1}). As can be deduced from the table of the weighted eigenvector matrix in Figure 4.2 the apparent charge separation lifetime is 5-6 ps in accordance with our previous data (52,127). This lifetime is several times shorter than the apparent CS proposed by other authors (104,110,167). The discrepancy cannot be attributed to major real differences in the experimental data but rather to the fact that we include and resolve the RC* compartment in our data analysis. As was discussed above, excluding some inherent system properties from the model assumptions can easily lead to inconsistent interpretations of the results. In the kinetic models of other groups the 20-25 ps lifetime component was attributed to the apparent lifetime of the primary charge separation. Such an interpretation is in disagreement with our data. However both our earlier data (52,127) as well as the present data demonstrate that this lifetime reflects already the secondary electron transfer step.

4.4.2 Energy transfer dynamics

Our data analysis reveals that the main part of the energy equilibration between the bulk antenna (ANT*) and the RC (RC*) occurs on a sub-ps time scale (see Figure 4.2). The ratios of the corresponding forward and backward rates are ~0.5 for the PS I-core complex and ~0.3 for the intact PS I, in good agreement with the ones predicted from the detailed balance calculation:

$$k_b / k_f = N_{RC} / N_{ANT} \times exp\left(\left(E_{ANT} - E_{RC}\right) / k_B T\right) \qquad (4.1)$$

where k_f and k_b denote the forward and backward energy transfer rates; N_{RC} and N_{ANT} the degeneracy factors for the different compartments (N_{RC}=6, for intact PS I N_{ANT}=~160, for core PS I N_{ANT}=~97), and k_BT is the Boltzmann factor).

The increase of this ratio in the PS I-core complex correlates with the reduction of the bulk antenna size due to the removal of the LHC I complexes and possibly also some of the 'gap' Chls. The ultrafast energy equilibration of the bulk antenna with the RC proves that there is no rate-limiting step in the kinetics due to the ET between the peripheral and the core antennae and rules out the diffusion-limited model proposed by Melkozernov *et al.* (167). This result not only suggests that the 'gap' Chls are well coupled with the rest of the bulk antenna system, but it also shows that they serve as an efficient bridge for the ET from the peripheral LHCs of the intact PS I complex. We observe no evidence whatsoever for any bottleneck across the bulk Chls.

The ET kinetics of the 'red' Chls can be directly examined with the help of the weighted eigenvector matrix (see Figure 4.2). The energy equilibration between the bulk antenna and the 'red' compartments proceeds with a main equilibration time of ~14 ps in good agreement with studies on isolated LHC I complexes (176,177). In the latter study the main energy equilibration lifetime of the bulk antenna and the 'red' Chls in LHC I is not longer than ~8 ps. This lifetime is slightly shorter than the one detected here. However, an increase of the energy equilibration lifetime in the intact PS I complex is expected given that there is a general enlargement of the bulk antenna moiety. Nevertheless, this lifetime is much longer than the lifetime reflecting the energy equilibration between bulk antenna and RC, and also slower than the apparent CS lifetime. In addition some slower equilibration occurs for the RED1* compartment. It is evident from the eigenvector matrix that the two 'red' Chls states decay with distinct lifetimes, *i.e.*, RED1* decays with ~95 ps and RED2* - with ~33 ps lifetime. This result rules out the conclusion made by Engelmann *et al.* for a heterogeneity of the 'red' Chls kinetics (110). Their conclusion is based on a proposed mixing of the dynamics of the two 'red' Chl states, leading also to mixing of the spectra (*vide infra*). However, our data do not

support this hypothesis and we rather believe that their finding of a mixed kinetics is a direct consequence of the non-inclusion of a RC* compartment in their model, which also emits 'red' fluorescence. Addition of such a compartment clearly leads to better separation of the 'red'-shifted spectra. Another important observation is the relatively low transient populations of the two 'red' Chl compartments. RED1* reaches a maximum transient population of about 13.6% and RED2* ~6%. The low population of the 'red' states follows from the low ET rate constants and implies a low efficiency of the ET from the bulk antenna to these compartments. A direct consequence of the slow 'red' Chl ET rates is the fact that most of the excitation energy will be trapped from the bulk antenna before it ever reaches the 'red' Chls. The slow energy exchange between bulk Chls and the 'red' Chls in the peripheral LHC I complexes requires a special analysis. It must be caused either by poor spectral overlaps and/or by an unfavorable arrangement or distance of the 'red' Chls to the surrounding Chls.

4.4.3 Fluorescence spectra of the model compartments

One essential part of the modeling is the extraction of physically reasonable spectra (SAES) for each compartment. These spectra play a critical and decisive role when judging the adequacy of a model, in addition to the rates and the χ^2 fit quality criterion. The SAES reflect the fluorescence spectrum of each excited state compartment present in the model as if it was measured isolated from the whole entity (151). The corresponding SAES for PS I-core and intact PS I particles are presented in Figure 4.4. Since the number of the cofactors and the kinetics in the RC (*e.g.*, charge separation, charge recombination and secondary electron transfer rates) for both samples are preserved, the spectrum of RC* should be the same in both samples. In contrast the bulk ANT* spectrum may change to some extent since additional Chls are comprised in the bulk ANT* for the intact PS I. The spectrum of RC* is slightly broader for intact PS I than for PS I-cores. This may hint to some incomplete resolution of the ANT* and RC* equilibration.

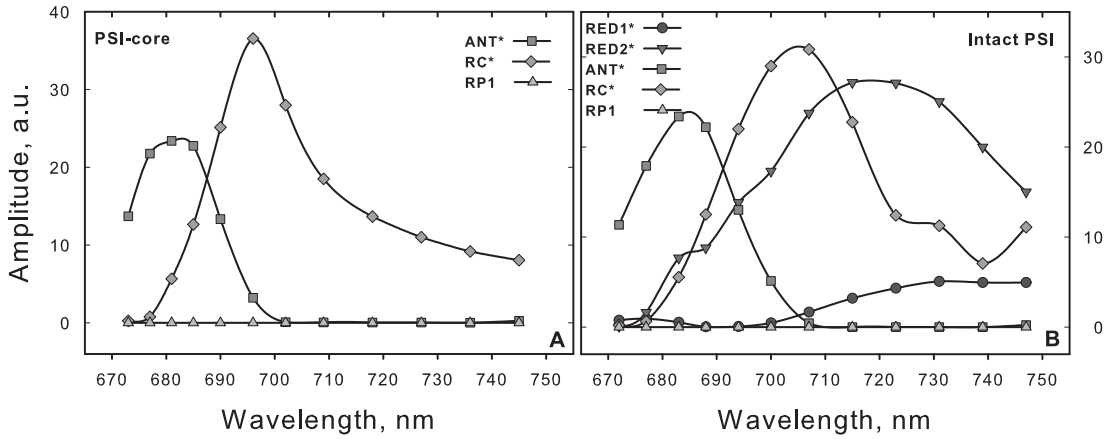

Figure 4.4
Species-associated emission spectra (SAES) from the modeling of the time resolved fluorescence data of core (A) and intact (B) PS I particles.

Additionally, for the PS I-intact complexes two 'red'-shifted spectra accounting for the presence of 'red' Chl forms are obtained. These spectra agree very well with our previous low temperature experiments on isolated LHC I complexes (87) In accordance to this study the spectrum of the compartment with a main 33 ps decay lifetime (RED2*), which peaks at about 721 nm should account for the fluorescence observed in Lhca 3 complexes (725 nm emission at low temperature)

(87). The other 'red' compartment (RED1*) with a lifetime of about 95 ps peaks at around 733 nm and should represent the 'red' Chl state in Lhca 4 (87). As a result, for the first time in this study we have assigned the 'red' kinetic components of intact PS I particles to the 'red' Chls located in the different isolated LHC I complexes (see Figure 4.5). Both spectra are very broad and strongly 'red'-shifted *vs.* the absorption, reflecting both exciton coupling and strong electron-phonon coupling as proposed by many authors (63-68), possibly caused by charge-transfer states.

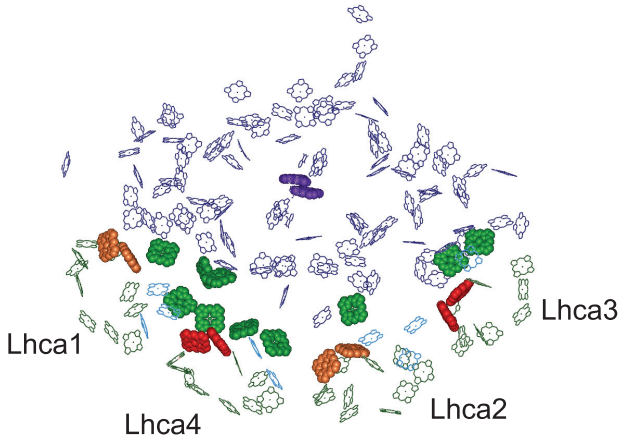

Figure 4.5
Structural picture exemplifying the role of 'gap' Chls in energy transfer to the PS I reaction center. Chl molecules of the structure from (165), deposited in the Protein Data Bank under accession number 1qzv, are shown. 'Gap' and linker chlorophylls are shown in light green and cyan, respectively, while the special pair P_{700} is in purple. Chls in sites A5 and B5 (603 and 609 according to (94) of antenna polypeptides are shown as well: they are in red in the case of Lhca 3 and Lhca 4, and in orange for Lhca 1 and Lhca 2, according to their fluorescence emission properties (87)

Provided that the SAES (see Figure 4.4) of the model compartments represent their fluorescence spectra (*vide supra*) one can calculate via the Kennard-Stepanov relation (181,182) the corresponding absorption spectra (see Supplementary materials for details of this calculation and analysis). These absorption spectra of ANT*, RC*, RED1* and RED2* are given in the Supplementary materials. Similar bands were found by Ihalainen *et al.* in Gaussian decomposition of the LHC I absorption spectrum (183). However, the calculated absorption spectrum of RED2* represents clearly an equilibrated state between a 'red' Chl compartment and a nearby pool of higher energy Chls rather than a pure 'red' Chls form. In contrast RED1* has a typical 'red' Chl absorption spectrum, peaking at ~710 nm. The RC* spectrum is in agreement with the spectrum found in our TA studies of PS I-cores (52). The relatively low transient population (see Figure 4.3) of the RED1* compartment can be explained by the minor spectral overlap with ANT*.

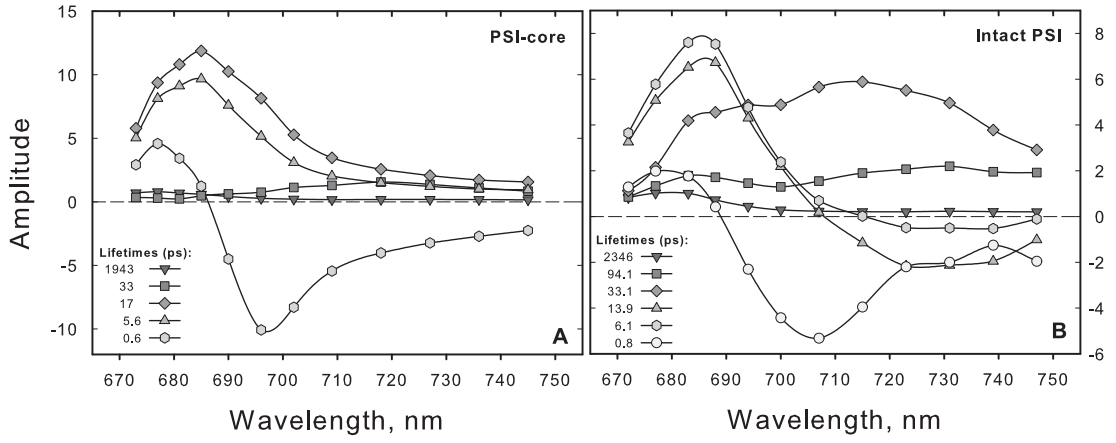

Figure 4.6
DAS of PS I-core (A) and PS I–intact (B) particles recalculated from the rates and SAES of the kinetic models. In PS I-core (A) the last two lifetimes (33 ps and ~1.9 ns) and the last one (2.3 ns) in intact PS I (B) reflect the additional components.

As a result of the kinetic modeling the DAS can be also presented with higher accuracy due to the better separation of the lifetimes describing the excitation dynamics in the system (see Figure 4.6). The shortest lifetime in the global analysis DAS (see Figure 4.1), which is apparently a mixture of two lifetimes, now is split into a sub-ps and ~6 ps lifetime. This leads to an additional slight adjustment of the other lifetimes. We should note that the sub-ps component resulting from the target analysis in principle is below the actual time-resolution of our apparatus. Nevertheless, this component follows implicitly from the kinetic models and is a global property of the overall kinetics and spectral shapes. It is common in target analysis that more and shorter lifetimes can be resolved than in simple global analysis (151). However, if such an additionally resolved lifetime falls below the resolution limit, it follows that the related errors for its spectral shape (DAS) and the rate constants that essentially contribute to this lifetime (in our case mostly ANT* and RC* transfer rates) have substantially larger errors than the other DAS and rates. This must be kept in mind when interpreting the data. Error analysis reveals that the ANT* and RC* ET rates could be off by up to 30%. However it is important to note here that all our femtosecond TA data on PS I particles (52,184) clearly demonstrate the presence of this sub-ps component. In fact, unpublished femtosecond TA data on the intact PS I complex also show this ultrashort ET component with large amplitude (Müller et al., 2006, unpublished). This component reflects to a large part the core antenna/RC equilibration. The spectral shapes of the DAS of the shortest lifetimes seem to indicate that part of the energy is still not completely equilibrated on the time scale of CS, because they are not conservative. This finding is in agreement with the results of other authors (104,167) who however used it as an argument to infer a transfer-to-trap or diffusion-limited type of trapping kinetics in PS I. Such an argumentation could well be misleading, since the decay of the fluorescence is a mixture of the decays due to all of the processes occurring in the system, like *e.g.*, ET and CS and additional analysis is in fact necessary to assign the actual limiting factor in the kinetics.

4.4.4 Trap-limited kinetics in higher plant PS I

According to theory the average lifetime for excited state decay in photosystems can be presented as a sum of two lifetimes: $\tau_{avg} = \tau_{ET} + \tau_{CS}$ (97,185). The first one is the energy transfer or migration lifetime (τ_{ET}) that represents the average lifetime for the energy migration through the antenna to the RC. In PS I core particles τ_{ET} is equivalent to the average lifetime of the energy equilibration between the bulk antenna (ANT*) and the RC*. However in intact PS I particles τ_{ET} has a significant or even dominant contribution from the equilibration with the 'red' Chls. The second one is the CS lifetime (τ_{CS}) representing the average trapping (CS) lifetime of excitations that are already located on the RC. This lifetime reveals the contribution of the CS to the total excited state decay and should not be confused with the apparent CS lifetime, which is the lifetime component describing the apparent rise of the primary RP. Both terms, *i.e.*, τ_{ET} and τ_{CS}, depend, *inter alia*, on the antenna size.

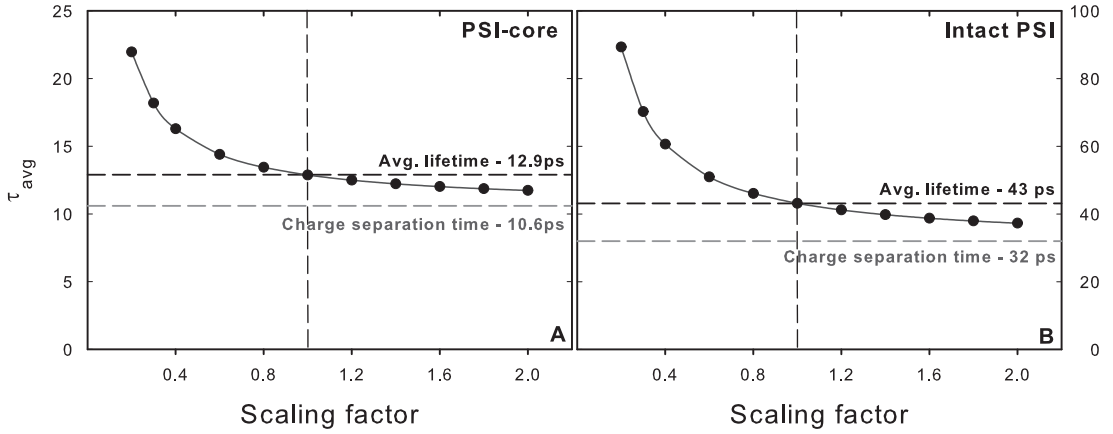

Figure 4.7
Dependence of the average fluorescence lifetime (τ_{avg}) on the scaling of the ET rates (ANT*-RC*) in the kinetic models (see Figure 4.2). Scaling factor 1 (vertical dashed line) corresponds to the experimental situation.

The trap-limited case is realized if τ_{avg} is determined mainly by τ_{CS}, *i.e.*, $\tau_{CS} / \tau_{ET} > 1$. The contributions of τ_{ET} and τ_{CS} can be calculated simply by scaling the ET rates (either ANT*-RC*, in case the excitation is placed on the ANT* compartment or RED*-ANT*, if the excitation is in the 'red') in the kinetic models (see Figure 4.2) to infinity (*i.e.* to ensure $\tau_{ET} << \tau_{CS}$). In this way, the overall decay of the fluorescence will be entirely due to CS and consequently the average lifetime will reflect exactly τ_{CS}. The same information can be obtained if in the kinetic model all excitations are created directly on the RC. The results are shown in Figure 4.7 and Table 4-1. According to this scaling analysis, the ratio between the CS lifetime (τ_{CS}) and the ET lifetime (τ_{ET}) in PS I-cores is ~4.6, implying a fully trap-limited kinetics. In the intact PS I particles this ratio is somewhat smaller (~2.7) but still substantially higher than 1 and the kinetics is still well on the trap-limited side. It is interesting to note that our results disagree with the theoretical modeling of Sener *et al.* (112). In that work the calculated so-called first usage lifetime (which corresponds to τ_{ET} in our description) is approximately 3 times larger than the one we observe (see Table 4-1). Thus the authors were led to suggest a diffusion-limited trapping kinetics in intact higher plant PS I. The decrease of the τ_{CS} / τ_{ET} ratio in intact PS I complexes in comparison to PS I-cores is primarily caused by the presence of the 'red' Chls and their relatively slow energy transfer with the other pigments and to a much smaller extent only by the larger bulk antenna system. The effect can be explained with the dependence of τ_{CS} not only on the CS rate but also on the equilibrium excited state population of the compartments. The RC population is lower in intact PS I particles in comparison to the PS I-cores, as can be seen from the population dynamics in Figure 4.3. Nevertheless, these substantial effects of the 'red' Chls do not suffice to change the type of the kinetics, which remains fully trap-limited also for the intact PS I complex.

	Excited compartment				
	ANT^*_{Core}	ANT^*_{Int}	$RED1^*_{Int}$	$RED2^*_{Int}$	$RED1/2^*_{Int}$
τ_{avg} (ps)	12.9	43.1	110	70	90
τ_{ET} (ps)	2.3	11.8	67	27	47
τ_{CS} (ps)	10.6	31.3	43	43	43
τ_{CS}/τ_{ET}	4.6	2.65	0.64	1.6	0.9

Table 4-1
Scaling analysis of the energy transfer rates (ANT* ↔ RC* and RED* ↔ ANT*) in the models (see Figure 4.2) depending on the excitation of different compartments in the core and intact (Int) PS I particles. See text for details about the meaning of the parameters.

4.4.5 Nature of the 'red' Chls energy transfer

In order to gain more insights into the properties of the system it is useful to perform further scaling analyses separately for the energy transfer rates of the 'red' Chl compartments in order to evaluate the type of their kinetics. The results of such analyses are summarized in Table 4-1. Interestingly, the two 'red' Chl sates differ largely in their kinetics. RED1*, which has a longer lifetime and the reddest spectrum shows a diffusion-limited kinetics if all the initial excitation is created on this 'red' Chl. In contrast, the ET dynamics of the other 'red' compartment (RED2*), whose ET kinetics is much faster than RED1* is not diffusion-limited. These results correlate with the Kennard-Stepanov calculations for the spectral overlap between ANT* fluorescence and 'red' compartments absorption (see supplementary materials). If the scaling analysis is done for equal excitation of both 'red' Chl compartments (see Table 4-1, RED1/2*) and zero bulk antenna excitation the overall kinetics turns out to be balanced between the two limiting cases. Such a difference in the kinetic properties between the 'red' Chls can be attributed to some differences in their function.

4.4.6 Influence of the 'red' Chls on the energy trapping process

The extension of the PS I-core antenna with the peripheral LHC I complexes, which contain the 'red' Chls, influences substantially the overall trapping kinetics. This effect is not merely due to the presence of 'red' Chls but also to the extension of the bulk antenna moiety. In order to quantify this effect, additional analysis of the data has to be carried out. Since the average decay of the excited state is a sum of two terms (τ_{ET} and τ_{CS}, *vide supra*) the contributions from the increased bulk antenna and the presence of 'red' Chls should be estimated separately, which is possible on the basis of the rate constants provided in Figure 4.2. We have thus performed the scaling analysis of the model describing the trapping kinetics for intact PS I particles without including the 'red' Chl compartments and keeping all other rates the same as in the model of Figure 4.2 (*i.e.,* ET rates between the bulk antenna and the RC* and the electron transfer rates). This allows us to evaluate the contribution of the bulk antenna enlargement alone on the increase of τ_{ET}, τ_{CS} and τ_{avg}. The results of this analysis are shown in Table 4-2. The extension of the bulk antenna of the PS I-core particles by the LHC I (~50 Chls, not including the 'red' Chls) and the 'gap' Chls (~10) contributes only about 24% (2.3 ps) to the total increase (9.5 ps) of the τ_{ET}, while the rest of the observed increase is due to the presence of the 'red' Chls. Likewise the bulk antenna enlargement in the intact PS I contributes only 3.7 ps to the total increase of 20.7 ps in τ_{CS}. Our results thus argue against the conclusion of Engelmann et al. (110) proposing an equal influence of the bulk antenna enlargement and of the presence of 'red' Chls on the total trapping. Our findings are, however, in relatively good agreement with the respective conclusion of Ihalainen *et al.* (104) suggesting a dominant effect of the 'red' Chls on the increased trapping, despite the fact that we disagree with their proposed overall transfer-to-trap-limited type of kinetics (*vide supra*). In conclusion, the presence of the 'red' Chls indeed substantially slows down the trapping kinetics in PS I. In this sense the 'red' Chls might well function as centers for a photoprotective mechanism. However, a photoprotective function of the singlet states has not been demonstrated yet to our knowledge. The 'red' Chls exert however a photoprotective function on the triplet states (117,119). On the other hand, the processes in the RC are slower than the total energy equilibration and rule the overall trap-limited kinetics. This allows the 'red' Chls easily to perform also the function of a spectral extension of the antenna system. Apparently, both functions can co-exist and can be modulated by the environmental conditions. The redox state of P_{700} may be the switch between these two functions.

Table 4-2
Contribution of the bulk antenna enlargement and the presence of 'red' Chls in PS I-intact particles in the slowing down of the overall trapping kinetics. Scaling was performed as described in Table 4-1 and in the text. For the ANT*$_{Int}$ (no REDs) case the calculation was performed without including the 'red' Chl compartments (for more details see text).

	Excited compartment			Differences		Contributions (%)	
	*ANT*Core*	*ANT*Int (No REDs)*	*ANT*Int*	*ANT*Int (no REDs) – ANT*Core*	*ANT*Int –ANT*Core*	*Antenna enlargement*	*'red' Chls*
τ_{avg} (ps)	12.9	18.9	43.1	6	30.2	20	80
τ_{ET} (ps)	2.3	4.6	11.8	2.3	9.5	24	76
τ_{CS} (ps)	10.6	14.3	31.3	3.7	20.7	18	82

4.5 Conclusions

In summary, we have described the trapping kinetics in higher plant PS I-core and PS I-intact particles, determined the rate constants and the lifetimes of the energy and electron transfer processes, and resolved the spectra and kinetics of RC*, ANT* and of the 'red' Chl compartments. In addition for the first time we have quantified the influence of the 'red' Chls and the effects of the enlargement of the bulk antenna in intact PS I on the overall trapping kinetics and described the effect separately for the ET and CS lifetimes.

Our results show that no 'red' Chls are present in the PS I-core particles from *A. thaliana*. The 'red'-shifted fluorescence (~700 nm) observed in the PS I-core preparations originates from the RC* itself. The trapping kinetics both in the core and in the intact particles from higher plant PS I falls into the trap-limited category, similarly to the one previously observed in algae PS I-cores (52,127). Due to the presence of 'red' Chls and the larger antenna system in the intact PS I complex the total trapping kinetics is slowed down ~3 times as compared to the core alone. Nevertheless, this effect is not large enough to switch the type of trapping to a diffusion- or transfer-to-trap-limited case. More than 80% of the slowing down of the trapping kinetics is caused by the 'red' Chls. The two 'red' Chl compartments differ in the type of their ET kinetics. Such difference may be linked to differences in the function(s), which these Chls perform in PS I. In this study, for the first time the two kinetically resolved 'red' states in the intact PS I complexes have been attributed to the 'red' states found in Lhca 3 and Lhca 4 (87). It is important here to comment on the general approach to describe and analyze the kinetics of such a complex system as the intact PS I particle by a compartment model with a small number of compartments. Clearly, these compartment models are 'minimal' in the sense that they provide only a description for the main components while leaving some details of the kinetics (and the associated spectra of the intermediate states) unexplained. However, in the absence of a precise and detailed X-ray structure there simply exists no better *a priori* possibility for resolving and describing the kinetics of such a complex system of about 200 pigments. Thus the question is not whether these compartments models are 'minimal' (they certainly are) but only whether they describe the actual situation well enough such that i) they allow us to resolve and assign the main components correctly, and that *ii)* the results of the analysis allow us to draw major conclusions as to the type and properties of the kinetics. While we are fully aware that such compartment models cannot provide a fully precise description of the kinetics (including the associated spectra), we do claim that these models and the resulting lifetimes describe the actual situation astonishingly well. Thus we claim – and this claim is supported both by the present results and their excellent general agreement with our previous published studies on the simpler PS I-core particles - that the 'simple'

compartment models not only do an excellent job in describing the overall kinetics but they also allow us to get important insights into the type of kinetics (diffusion- *vs.* trap-limit, resolution of the kinetics and spectra of the RC* *etc.*).

Finally, the studies of the light energy utilization kinetics in natural photosynthetic complexes and in particular the properties of the 'red' Chls, which both extend the spectral range and may also play a special role in photoprotection, provide valuable knowledge for the design and the development of artificial light-harvesting systems and systems for solar energy conversion.

4.6 Supplementary materials

Target analysis performed on the time-resolved fluorescence data provides the so-called SAES. These spectra correspond to the emission spectra of each of the model compartments. In this way we have obtained the emission spectra of ANT* (representing the whole bulk antenna of PS I), the six Chls in the RC (RC*), and the 'red' Chls (RED1* and RED2*). However, according to Kennard-Stepanov relation the fluorescence and the absorption spectra are interrelated:

$$A(\nu) = C(T) \times \nu^2 \times F(\nu) \times exp(h\nu / k_B T) \quad (4.2)$$

where (A(ν) is absorption spectrum, F(ν) the fluorescence spectrum, h the Planck constant; ν the radiation frequency, $k_B T$ the Boltzmann factor; C(T) a frequency independent term (181,182).

Based on this relation we have calculated the absorption spectra of the model compartments from the SAES. In Figure 4.8 these spectra are shown when fitted in their relative proportions to the experimental absorption spectra of the PS I-intact complex. One has to take into account that at the 'blue' edge of the spectra, where the intensity in the SAES is small, the error becomes relatively large, a common problem in Kennard-Stepanov calculations. Considering these error, the resulting absorption spectrum for the intact PS I particles agrees actually quite well with the experimental one. The calculated RC* absorption peaks at ~690 nm in good agreement with our previous TA data (52). RED1*, attributed to the 'red' state found in Lhca 4, posses the 'red' most spectrum (~710 nm). In contrast the spectrum of RED2* actually seems to reflect a small pool of equilibrated pigments that contain both 'blue' and 'red' absorption. The most likely interpretation is an excitonically coupled pigment pair.

In Figure 4.9 (A) are shown the spectral overlaps between the area normalized emission spectrum of the bulk antenna (ANT*) and the weighted absorption spectra of the other compartments (*i.e.*, RC*, RED1*, RED2*). The corresponding spectral overlaps of the ANT* absorption with the normalized fluorescence of RC*, RED1* and RED2* are shown in Figure 4.9 (B). The relative overlap integrals are summarized in Table 4-3. The spectral overlaps play crucial role in the energy transfer amongst the corresponding compartments (29). It is clear (see Table 4-3) that the diffusion-limited kinetics of RED1* is due to the poor spectral overlap between the spectrum of this compartment and the ANT* spectrum. The mixed 'red'/'blue' contribution to the absorption spectrum of RED2* makes the overlap with the ANT* large, resulting in a much faster equilibration for this pool of pigments than for RED1*. The large spectral overlap of RC* and ANT* are in perfect agreement with the observed ultrafast energy equilibration of these two compartments.

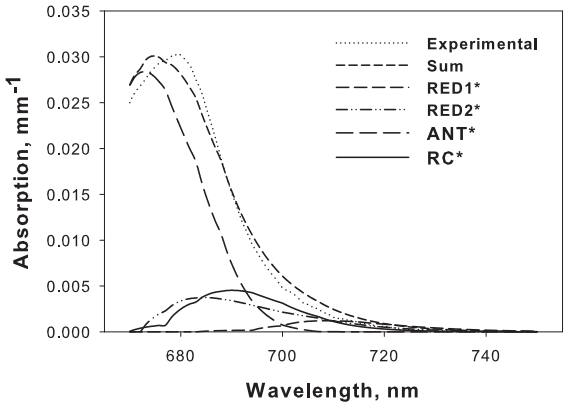

Figure 4.8
Absorption spectra of RED1*, RED2*, ANT* and RC* compartments as calculated by the Kennard-Stepanov relation from the corresponding SAES (Figure 4.4). The spectra of these compartments were then fitted to the experimental absorption spectrum of PS I-intact complexes in order to obtain their weighting factors. The sum of these spectra is presented for comparison with the experimental. The spectrum of RED1* is multiplied by 10 for better presentation.

Transfer step	Spectral overlap
*ANT** → *RED1**	0.025
*ANT** → *RED2**	0.87
*ANT** → *RC**	0.82
*RED1** → *ANT**	0.04
*RED2** → *ANT**	0.20
*RC** → *ANT**	0.34

Table 4-3
Relative overlap integrals of the corresponding normalized fluorescence and weighted absorption spectra.

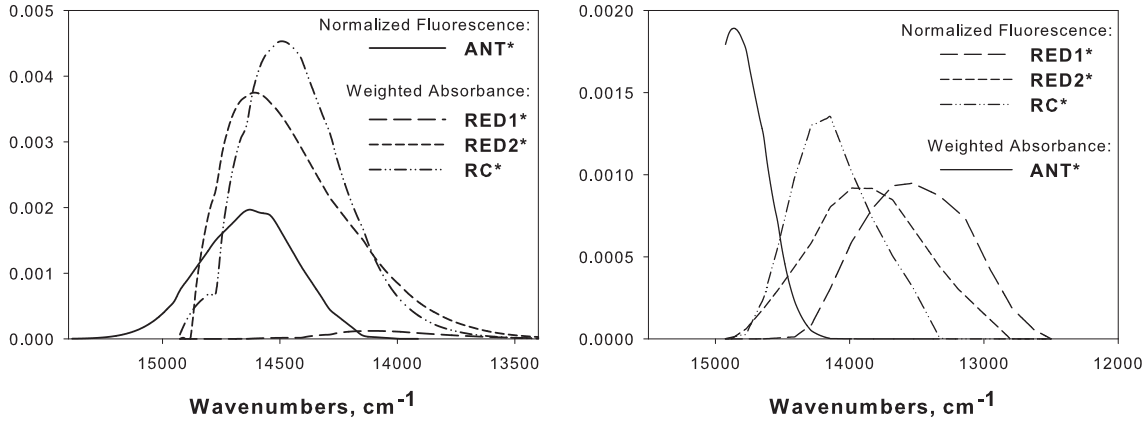

Figure 4.9
Spectral overlap between the area-normalized fluorescence spectra and weighted absorption spectra of the different compartments. A) Normalized fluorescence of ANT* with the weighted absorption spectra of RED1*, RED2* and RC*. B) Normalized fluorescence spectra of RED1*, RED2* and RC* and the weighted absorption spectrum of ANT*.

Chapter 5

Trapping kinetics in isolated cyanobacterial PS I complexes

This chapter is based on the publication:
Chavdar Slavov, Eithar El-Mohsnawy, Matthias Rögner, and Alfred R. Holzwarth
Chemical Physics 2009, 94:3601-12

5.1 Introduction

PS I is one of the largest membrane complexes, hosting 127 cofactors (41). It is involved, together with PS II, in conducting the light reactions of Photosynthesis. The structure of the cyanobacterial PS I complex is resolved to 2.5 Å resolution (41). It seems, that naturally most of the cyanobacterial PS I complexes are organized as trimers, as is evident both from electron micrographs of thylakoid membranes and from isolated PS I particles (42,43). However, it has also been shown that the monomer-trimer equilibrium in the membrane phase should be considered as a dynamic equilibrium which can be triggered by external parameters (186,187). Isolated trimeric complexes show an extraordinarily high density of pigment molecules in the core antenna (41). This antenna system is relatively well separated from the redox-active cofactors in the reaction center (RC) in order to be oxidation protected. The early electron transfer reactions in the RC involve six chlorophyll (Chl) molecules and two phylloquinones divided into two electron transfer branches. The six Chls of the RC are strongly coupled to each other (6,48-54), which leads to broadening of the covered energy spectrum and has high importance for the effective energy transfer from the different antenna compartments (55). In addition, this interaction renders specific spectroscopic properties of the RC and hence allows its experimental observation in spectrally resolved ultrafast experiments (6,52).

Most of the known PS I complexes exhibit an intriguing feature such as the presence of the so-called 'red' Chls (61,61,62). Normally, these Chls have very broad 'red'-shifted spectra. Their peculiar properties are explained by a strong excitonic interaction (63,64) and high electron-phonon coupling (64-68), likely combined with energetic shifts induced by the protein (69). In addition, mixing with a charge-transfer state was also proposed (64,66,68,70-72). In effect the 'red' Chls absorb light with longer wavelength than the RC Chls and, even though present only in a small number, have significant influence on the energy trapping kinetics of PS I.

However, despite the increasing knowledge of the properties of these pigments, their physiological role is not clear yet. Some authors connect their role to the funnel model of the energy transfer to the RC (114), while others proposed their participation in the photoprotection (61,114-119). Nevertheless, since the presence of the 'red' Chls does not impair the quantum efficiency of PS I their most apparent function is providing physiological advantage, through widening the spectral range of the light that can be utilized (115,120,121).

In *Thermosynechococcus elongatus* low temperature studies reveal the presence of two to three main absorption bands at 708 nm and 719 nm (C708 and C719) (65,67), and possibly also at 715 nm (C715) (64). Two 'red' Chls forms are found at low temperature also in *Synechocystis* at 708 nm and 714 nm (66). Currently, *Spirulina platensis* is the species with the 'red'-most absorption bands (C719 and C740) of its PS I (188). Interestingly, a single molecule study by Brecht and co-workers (77) demonstrates a striking spectroscopic difference between the 'red' Chls of C718 and C715/C719 in *T. elongatus*. The authors assigned the differences to the local environment and attempted to predict the position of the 'red' forms. Nonetheless, the precise location of these Chls in the core antenna system is still not identified. One of the possibilities is the monomer-monomer interaction region of the trimer (41). Another proposed location is the vicinity of the RC in relation to a funnel model of the energy trapping (73). In contrast, a more distant position for some or all of the 'red' pigments is suggested by other authors (66,71,74-76). At present, few pools of Chl molecules (the trimer B31/B32/B33, and the dimers - A38/A39, A32/B7 and B37/B38) have some experimental basis (41,77) to be the most likely candidates for the formation of the so-called 'red' Chls in cyanobacteria

and in particular in *T. elongatus*. However, several other Chl groups (the tetramer A31/A32/B7/B6, the trimers A2/A3/A4, A19/A20/A21 and the dimers A12/A14, A26/A27, A24/A35, A33/A34, B24/B25, B22/B34) were also proposed to contribute to the peculiar 'red' forms (59,69,71,78,79). It is apparent that the uncertainty in the assignment of the 'red' pigments is fairly large, since the different proposals involve over 20% of the Chls of PS I.

In order to clarify the physiological importance of the 'red' Chls, their role in the energy trapping kinetics of PS I has to be revealed first. This will also bring more information on the position of the pigments in the complex. A number of time-resolved studies attempted to characterize the trapping kinetics. However, there is a general disagreement on the type of trapping. Based on some time-resolved fluorescence studies, Byrdin *et al.* suggested that the kinetics in cyanobacteria is balanced between trap- and transfer-to-trap-limited (75). Other authors suggested a purely transfer-to-trap-limited kinetics on the basis of a non-equilibrium trapping interpretation of the time-resolved fluorescence and transient absorption data and an assumption of slow energy delivery to the RC from the antenna compartments due to the relatively large distance between them (~18 Å) (76,107-109,111). A weak point in part of the latter studies is that in the analysis of the data the charge recombination reaction was not included and the possibility of de-trapping of the excitation energy from the RC was underestimated (76,107-109). The charge recombination reaction, however, has been shown to play an important role in the trapping kinetics and cannot be omitted (52,127). On the other hand, the large number of Chl molecules belonging to the antenna system of PS I, which is intimately bound to the RC, increases tremendously the de-trapping probability. The results by Savikhin *et al.* (111) should also be considered with care given that the authors used in their analysis the highly questionable assumption of equality of the excited state quenching processes in open and closed PS I complexes. In fact, an increase of about 12% in the fluorescence quantum yield after P_{700} oxidation was observed by Byrdin and co-workers (75), which implies a different trapping kinetics in PS I with closed RC. In contrast, a purely trap-limited kinetics is observed in some early minimal models (70,124) in cyanobacterial PS I. However, these studies lacked either sufficient time-resolution (124) or did not attempt a detailed kinetic modeling (70). In some theoretical works (49) the trap-limited kinetics was excluded as a possibility, nevertheless, the authors discuss the relatively large probability for back energy transfer from the RC (49,72). The problem of these models is the neglect of the charge recombination reaction, which strongly influences the result for the rate-limiting step in the calculations. Other theoretical calculations are also in favor of the transfer-to-trap limited type of trapping kinetics (60,109). However, in these works the authors have assumed ultrafast CS in the RC, which has no solid experimental basis (52).

The large discrepancies in all these studies originate primarily from the differences in the attempts to describe the experimental data rather than the data themselves. Generally, only a few energy transfer (ET) lifetime components are resolved. A sub-ps lifetime component describing the bulk antenna energy equilibration and one or two picosecond ET components representing the energy equilibration between the bulk antenna moiety and the 'red' Chl pools (76,126,189). The latter components demonstrate significant non-equilibrium trapping. Finally, a 20-30 ps component is determined which is assumed to account for the main trapping (76,126,189).

A major difficulty in the spectroscopic investigation of the PS I complexes is the high pigment density, which together with the inseparability of the RC from the core antenna system, and the presence of the 'red' Chls make the experimental observation of the early electron transfer processes extremely hard. Thus the investigation of the PS I from different organisms has to be performed on the basis of the studies of the simplest possible PS I complex. Recently, such a study performed on

PS I-core particles from *C. reinhardtii*, which do not have any 'red' Chls has brought better understanding of the trapping kinetics in PS I (52,127). It was shown there that a charge recombination step is required for the description of the energy and the charge transfer events in PS I. Furthermore, for the first time these studies resolved the excited equilibrated RC* (*i.e.* excited state of the group of the six RC Chls) of PS I as a separate compartment both spectrally and kinetically. According to these results the kinetics in PS I-cores that are devoid of 'red' Chls is purely trap-limited (52).

In this work we present a time-resolved fluorescence investigation of the trapping kinetics of highly purified and intact PS I monomeric and trimeric complexes from *T. elongatus*. We demonstrate here that the energy trapping kinetics in these two complexes is identical and can be very well described with the help of the 'radical pair equilibrium' model (52). We have resolved an additional lifetime component and hence presented the existence of two separate lifetimes describing the fluorescence decay of the 'red' Chl pools. Furthermore, in accordance with our previous studies, we have estimated the rates of the primary and the secondary electron transfer reactions.

An important point for the decision on the correct trapping model is the consistency of the electron transfer reaction scheme and rates as well as the spectral properties of the RC across PS I from different species. This is important since the antenna properties and sizes vary widely for different PS I particles, while the RC properties should remain very similar. Thus, only kinetic descriptions that result in the consistency of the RC properties can be considered adequate.

5.2 Materials and Methods

T. elongatus was cultivated at 45°C in a 20 L photobioreactor using BG-11 medium (190) with air enriched in 5% CO_2 (191). Cell harvest and thylakoid membrane preparation was performed according to Rögner *et al.* (43) and Wenk & Kruip (192). Monomeric and trimeric PS I complexes have been purified according to Schlodder *et al.* (62). Enhancement of PS I monomers was achieved by preincubation of the thylakoid membrane in 0.6 M ammonium sulfate at 50°C. After extraction by 0.6% n-dodecyl-β-maltoside (β-DM) and ultracentrifugation (Ti70-Rotor, 60 min, 50000 rpm, 4°C, Beckman), monomeric and trimeric PS I were separated by hydrophobic interaction chromatography (POROS 50-OH, Applied Biosystem, Germany) followed by ion exchange chromatography (POROS 50 HQ/M, Applied Biosystem, Germany).

The purified PS I complexes, containing 108 Chls/P_{700} were used for the time-resolved fluorescence measurements. The isolated monomeric and trimeric PS I particles were diluted in 30 mM HEPES buffer (pH 7.5), containing 10 mM $MgCl_2$, 10 mM $CaCl_2$, 200 mM Mannitol and 0.01% β-DM to an OD ~0.6 cm^{-1} at the Chl Q_Y maximum. The medium contained also 40 mM sodium ascorbate and 60 μM phenazine methosulfate as redox agents to keep the RCs open during the measurements.

The single-photon timing technique was used to perform picosecond time-resolved fluorescence measurements. The set-up consists of a synchronously-pumped, cavity-dumped, mode-locked dye laser at 800 kHz repetition frequency with a DCM as a laser dye (107,127). The pulse of the dye laser has a FWHM of ~10 ps and the whole response of the system is about 30 ps FWHM, which after deconvolution results in a time-resolution of 1-2 ps. The sample was placed in a rotating cuvette (10 cm diameter, path-length of 1.5 mm) moving sideways at 66 rpm and rotating at 4200 rpm. The laser intensity at the sample was about 0.05 mW, ~0.7 mm spot diameter. Such experimental conditions ensure complete re-reduction of the RCs before the next excitation occurs. Under these

conditions, less than 1% of the particles receive a second laser excitation during the time they spend in the laser beam. The excitation wavelength used (663 nm) selectively excites the bulk antenna Chls. The fluorescence decays at different wavelengths were selected by a double monochromator (spectral bandwidth 4 nm). Measurements were carried out at ambient temperature (21 ±2°C).

Fluorescence decays were analyzed by means of global and target analyses as previously described in detail (151,152). Global analysis is a combined mathematical fitting of the decay curves at different wavelengths done in a single fitting procedure. The analysis results in lifetimes and decay-associated spectra (DAS), describing the whole set of original data. In the more elaborate target analysis, kinetic models are fitted to the data in global fashion. Such an approach leads to a physically meaningful description (rate constants and spectra of the different compartments (species-associated emission spectrum (SAES)) and gives detailed information about the rate constants of the energy and electron transfer processes taking place in the investigated system. Several physically reasonable models are usually tested for their compatibility with the data.

5.3 Results

Time-resolved fluorescence measurements were performed on monomeric and trimeric PS I complexes from *T. elongatus* in order to investigate their light energy trapping kinetics. To avoid uncertainties in the initial energy distribution the excitation wavelength was chosen such to interact only with the pigments of the bulk antenna system (663 nm). The kinetics of the different processes in PS I was monitored by detecting the emission decays at different wavelengths from 670 nm to 750 nm.

5.3.1 Global analysis

Initially, the decays were analyzed by means of global analysis (151,152), which results in characteristic lifetimes and amplitudes (Figure 5.1). For each of the two samples the minimal number of lifetime components necessary to fit the data was five. Nevertheless, the DAS demonstrate some interesting differences. First of all, in the case of the monomeric PS I there are two lifetime components possessing the typical positive-negative amplitude feature of an ET component (3 ps and 9.3 ps), while the trimers have only one such component (5.5 ps). However, this 5.5 ps component has an intermediate value compared with the shortest components of the monomers and possibly represents their mixture. Secondly, the longer 20-25 ps and 40-50 ps components also show dissimilarities. In the monomers the ~25 ps component peaks at 720 nm and the 48 ps one - at ~730 nm, while in the trimers the corresponding components are slightly 'blue'-shifted and even show some differences in the shape of their DAS. Additionally, the amplitude ratios of the two lifetime components are different for monomers and trimers. The origin of the differences can easily be explained with some internal differences of the studied complexes. Such a preliminary conclusion, however, may be easily misleading since the global analysis is a fitting procedure with a simple sum of exponentials and does not consider some important functional relations amongst the different components. In contrast, the use of Target analysis, which describes these inherent relationships correctly often, leads to resolution of lifetime components that are not fully resolved or represent mixtures in Global analysis. In addition to the already described components, we observe further two other longer lifetimes with small amplitude. The ns component is common for both samples and is usually encountered in all PS I studies. This lifetime is attributed to some functionally decoupled Chls. Besides that, in the trimers we observe a ~300 ps lifetime with small amplitude, whose origin is also

not clear at present. However, it is worth noting that the shape of its DAS is similar to the one of the longest lifetime component, which indicates that it is also related to the decoupled Chls.

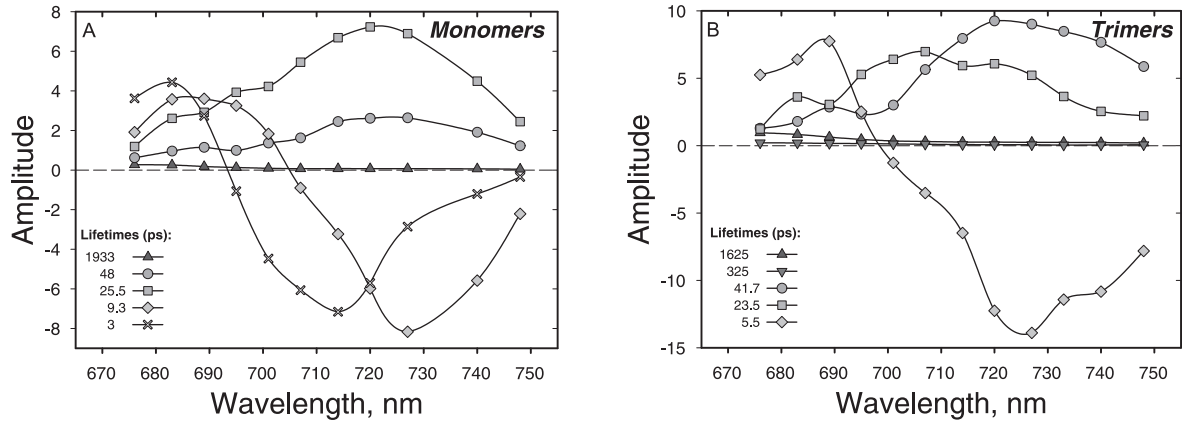

Figure 5.1
Decay-associated spectra (DAS) and lifetimes of the fluorescence from monomeric (A) and trimeric (B) PS I complexes from *T. elongatus* obtained through global analysis of the fluorescence decay data, λ_{exc} = 663 nm excitation. χ^2 = 1.04 and χ^2 = 1.03 for A) and B), respectively

In agreement with the earlier studies on cyanobacterial PS I (76,126,189), the ps lifetimes discussed above represent excitation energy equilibration between the bulk antenna Chls and the Chls from the 'red' pools. At this stage of the analysis it is not completely clear whether the ET to the 'red' Chls is not mixed with some electron transfer processes in the RC as suggested before (75,76). So far, on the longer time scale (20-60 ps) there has only been detected one decay component (75,76,126,189), assigned as the main trapping lifetime. In our work for the first time, both in monomers and in trimers, we resolve on the longer time scale two separate lifetimes (~25 ps and ~45 ps). These two components possess notably 'red'-shifted DAS and in our view represent the decay kinetics of two different 'red' Chl compartments. In regard to the three 'red' pools – C708, C715 and C719, revealed by the low temperature studies of PS I from *T. elongatus* (64) one would expect to observe three lifetimes, describing the 'red' Chls kinetics. The lack of such a third lifetime component, associated with the 'red' Chls however, can be simply explained either by the kinetic and spectroscopic inseparability of two of the 'red' pools at ambient temperature or by the formation of a new 'red' state at low temperatures, which is not present otherwise.

5.3.2 Target analysis

The initial knowledge about the samples, obtained through the global analysis together with the information from previous studies is used in a next step for the design of physical models. These models account for the specific features and relations between the different pigment pools in the complexes. We have tried many different kinetic models. We will however only discuss those that lead to both *i)* a good fit in a mathematical sense; and *ii)* physically reasonable SAES. In fact, the models that we found in this study could tolerate only minor changes in the rate constants (5-10%). Changes in the rate constants significantly larger than 5% bring severe deterioration of the SAES. In accordance to our earlier studies (52,127) we present here a model describing the trapping kinetics of cyanobacterial PS I monomers and trimers, which includes a fluorescing compartment representing the excited RC Chls (RC*) (see Figure 5.2). Additionally, analogous to green algae PS I (52,127) a charge recombination rate was needed to describe the time-resolved fluorescence data properly. Based on the result from the global analysis, where two separate decay components with 'red'-shifted

DAS were determined in both of the investigated complexes we included in the model schemes two 'red' Chl compartments. We have also tested a model with only one 'red' state, which however did not yield physically reasonable SAES. The resulting models and the rate constants obtained after fitting to the experimental data are presented in Figure 5.2. In this figure are presented also the so-called weighted eigenvector matrices, which give information for the contribution of each of the model compartments in the different decay lifetimes. In effect, by considering the physical properties of the studied complexes better resolution was achieved. The spectra of the different compartments are shown in Figure 5.4.

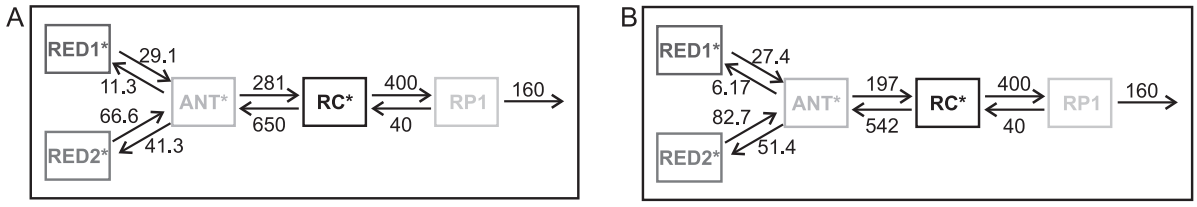

Monomers

τ (ps)	RED1*	RED2*	ANT*	RC*	RP1
0.8	-0.002	-0.006	0.173	-0.247	0.093
4.4	-0.017	-0.079	0.304	0.059	-0.912
7.9	-0.036	-0.215	0.308	0.122	0.660
23.4	-0.106	0.216	0.126	0.039	0.099
43.1	0.162	0.084	0.089	0.027	0.060
exc	0	0	1	0	0

Trimers

τ (ps)	RED1*	RED2*	ANT*	RC*	RP1
0.9	-0.001	-0.007	0.132	-0.202	0.091
4.6	-0.010	-0.118	0.311	0.039	-0.825
7.2	-0.013	-0.219	0.234	0.085	0.546
25.4	-0.112	0.248	0.210	0.052	0.128
44.2	0.136	0.096	0.112	0.027	0.060
exc	0	0	1	0	0

Figure 5.2

Compartment models with rate constants (ns^{-1}) (top), lifetimes and eigenvectors (bottom) for the monomeric (A) and trimeric (B) PS I particles. $\chi^2 = 1.06$ and $\chi^2 = 1.07$ for A) and B), respectively. The errors in the rate constants are in the range of 5% and the errors in resulting lifetimes in the range of about 10%. The fastest rate constants, contributing primarily to the fastest lifetime of 0.8-0.9 ps, do have significantly larger errors (up to 15%) because the fastest lifetime is at the resolution limit of our apparatus. Thus, the fastest lifetime may have an error in the range of 20%. The advantages of global target analysis nevertheless allow resolving of these components.

5.4 Discussion

5.4.1 Energy transfer

The kinetic modeling of the time-resolved data demonstrates that the main part of the energy equilibration between the bulk antenna (ANT*) and the RC (RC*) in PS I monomers and trimers occurs on a sub-ps time scale (see Figure 5.2). The different spectral properties of the model compartments together with the special kinetic relationships between them exert a constraint on the rates, which allows the estimation of lifetimes below the time-resolution of the set-up. The ratio of the corresponding forward and backward rates (~0.4) is in relatively good agreement with the one predicted by the detailed balance:

$$k_b / k_f = N_{RC} / N_{ANT} \times exp\left(\left(E_{ANT} - E_{RC}\right) / k_B T\right) \qquad (5.1)$$

where k_f and k_b denote the forward and backward energy transfer rates; N_{RC} and N_{ANT} the degeneracy factors for the different compartments (N_{RC}=6, and N_{ANT}=~90), and k_BT is the Boltzmann factor).

The observed ultrafast ANT*-RC* equilibration kinetics shows that there is no rate-limiting step in the energy delivery to the RC as proposed by others (76,108,109,111).The relatively high transient population of the RC* (~13-17%) is a good argument in favor of the possibility to observe this compartment (52)

In our analysis we have also estimated the lifetimes for the energy equilibration between ANT* and the two 'red' Chl compartments (RED*) (Figure 5.2). Apparently, for both of the 'red' compartments the process proceeds on all time scales up to ~20 ps. In agreement with previous studies (76,109,111,189) we found ~5 ps and ~7 ps components, which represent the main energy equilibration with the 'reds', however we observe also some additional equilibration on a later time scale for RED1*. RED1* and RED2* decay correspondingly with ~44 ps and ~25 ps. Interestingly, the differences in the kinetics of the 'red' Chls from monomeric and trimeric complexes are only minor. A plausible explanation of this effect is that the origin of the 'red' pools is the same for both complexes, *i.e.* that the 'red' Chls are in fact not influenced by the trimerization. In this case, some structural changes like *e.g.* detachment of Chls during previous isolation procedures can easily account for the differences with the earlier data.

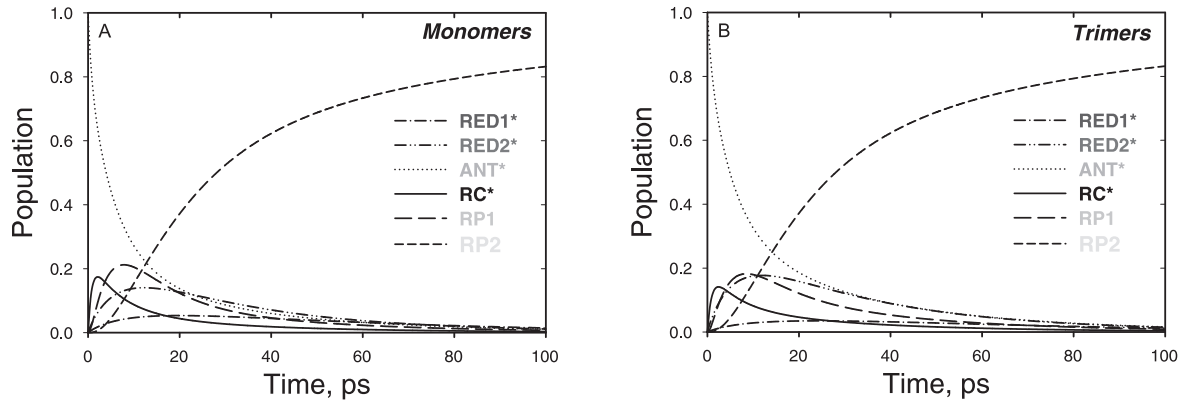

Figure 5.3
Time dependence of the relative populations for the compartments from the models shown in Figure 5.2. A) PS I-monomers, and B) PS I-trimers.

In Figure 5.3 is shown the population dynamics of the model compartments. The low transient population of RED1* is caused by a low ET efficiency from the bulk antenna system. Such a low efficiency of this process can be explained in the light of Förster theory either by a bad spectral overlap between the compartments or by a non-favorable spatial orientation. The other 'red' compartment (RED2*), however, obtains substantial transient population (~13-17%). We performed the Boltzmann calculation also for the 'red' Chls. Unfortunately, the number of the pigments in each pool is not known, and hence the comparison with the ratio of the experimental rates is difficult. However, one can make the calculation for the forward/backward rate constants ratio using different number of Chl molecules contributing to the 'red' compartments and then do the comparison with the ratio of the rates determined from the modeling. As a result, it turns out that within the given uncertainties either one or two Chl molecules can form each of the 'red' pools.

5.4.2 RC kinetics

One of the main elements of the presented models (Figure 5.2) is the presence of a fluorescing RC* compartment. The necessity of such a compartment emerges due to the specific properties of the six RC Chls (6,48-54) – *i)* strong excitonic coupling, which significantly modifies the physical properties of this pigments as compared to the antenna Chls; *ii)* relatively distant position from the core antenna; *iii)* and finally their role as electron transfer cofactors. The introduction of this compartment together with the introduction of a charge recombination rate allows the observation of the RC*, and correspondingly the initial electron transfer reactions. These features of our models are

supported also by the relatively high transient population of the RC* (~13-17% in both samples) (see Figure 5.3).

Within the error limits, the early electron transfer reactions in the RC of both monomers and trimers occur with the same rate constants. This means that during the isolation procedures the RC of PS I is not affected, which is reasonable. The *effective CS rate* from the equilibrated RC* Chls is ~400 ns^{-1} and is similar to the one resolved in green algae (350 ns^{-1} and 438 ns^{-1}) (52,127) and also to the one from higher plants (400 ns^{-1}) (101). However, this rate is not the so-called *intrinsic rate of CS* from a particular electron donor pigment. The latter rate is obtained by multiplying the *effective CS rate* by the number of the pigments amongst which the RC* excitation is equilibrated, *e.g.* 3-6, depending on the RC exciton model. The *intrinsic rate of CS* in cyanobacterial PS I may thus vary between 1.2 ps^{-1} and 2.4 ps^{-1} in agreement with our recent transient absorption data (52). From the eigenvector matrix (Figure 5.2) also the *apparent CS lifetime* can be obtained (**Note** that this is the main lifetime with which the first radical pair is formed, but it is **not** identical to the inverse of the above-mentioned *effective CS rate* from the RC, for detailed discussion see *e.g.* (52); the main difference is that the *apparent CS lifetime* also contains the effective antenna migration time and also reflects the statistical effects of the antenna size, *i.e.* in equilibrium the excited state population on the RC* is inversely proportional to the antenna size). In both of the studied PS I complexes this lifetime is ~4.5 ps, *i.e.* about 5-6 times shorter than the *apparent charge separation lifetime* estimated by other authors who did not resolve directly the RC* kinetics (73,76,109,111). The free energy drop in the first electron step is ~100 meV by far larger than the one observed in PS II core complexes (185). The decay of the first radical pair (RP1) occurs with a lifetime of ~7.5 ps. Interestingly, the secondary electron transfer reaction in cyanobacteria seems to be accelerated in comparison to algae (RP1 decay lifetime - 17 ps) (127) and higher plants (RP1 decay lifetime – 14-17 ps) (101). This effect is in a way unexpected given that the structure of the complexes from different organisms seemed to be highly preserved. However even minor changes in the orientation of the cofactors, not resolved in the structure of higher plants (40) may bring large differences.

5.4.3 Fluorescence spectra of the model compartments

The target modeling of the experimental data results also in the so-called species-associated emission spectra (SAES) or simply the fluorescence spectra of each of the model compartments. In fact, SAES are one of the basic criteria for the suitability of a given model. The spectra obtained from the modeling of the data from monomers and trimers are shown in Figure 5.4. The SAES of the bulk antenna (ANT*) both in monomeric and in trimeric PS I are relatively well conserved, peaking at about 685 nm. At first glance the RC* SAES of the two studied complexes look different; this is mainly due to two data points (707 nm and 727 nm), which impair the shape of the spectra. Nevertheless, the center position of the RC* spectra is the same in monomeric and in trimeric PS I - ~705 nm. We should note here, that the SAES of the RC* compartment is very sensitive to the determination of the shortest lifetime in the kinetics (ANT*-RC* energy equilibration, see Figure 5.2), which in fact is at the limit of the apparatus time-resolution. In this light the difference between the RC* SAES can be easily explained. The rest of the SAES represent the spectra of the 'red' Chls compartments. SAES of RED2* peaks at 720 nm and possesses a very broad shape, a sign for a large electron-phonon coupling, typical for the 'red' Chls (64-68). These spectra are very well conserved in both complexes, as is the kinetics of the corresponding compartments. However, this does not apply fully for the other 'red' pool – RED1*. Even though the peak wavelength and the shape remain the same, the relative intensity of this band is slightly diminished in the monomeric complexes as

compared to the trimers. This effect correlates with the small differences in the kinetics. Based on the latter result we suggest that the Chls involved in the formation of the RED2* pool are not situated in close proximity to the trimerization region. However, the Chls of the RED1* pool most probably are located somewhere near this region. Nevertheless, the preserved peak position and shape of the spectra of RED1*, indicate that this pool has one and the same origin in both complexes, meaning that there is no formation of a new 'red' form during the trimerization of the cyanobacterial PS I.

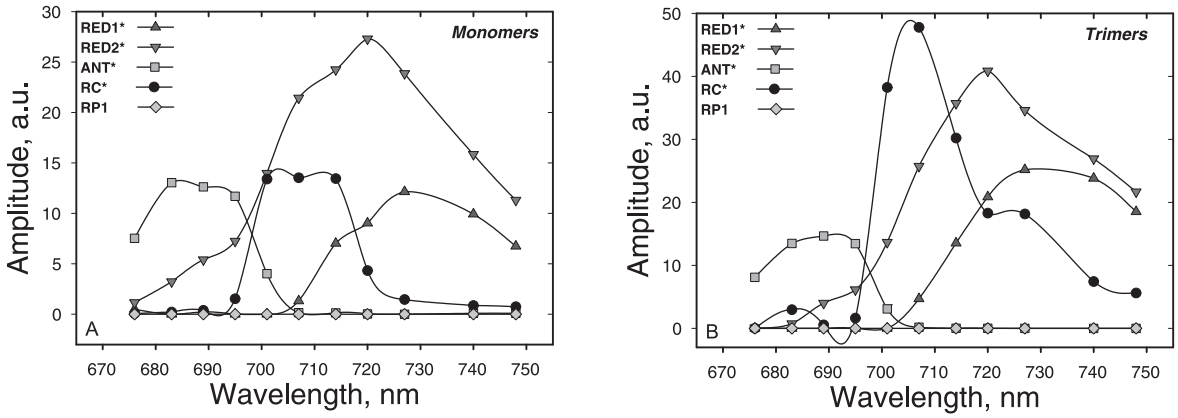

Figure 5.4
Species-associated emission spectra (SAES) resulting from the modeling of the time resolved fluorescence data of monomers (A) and trimers (B) PS I particles as shown in Figure 5.2. The errors in the species-associated spectra, in particular for the RC*, compartment are directly related to the errors in the rate constants (see comment Figure 5.2). Whereas the errors in the SAES for most compartments are in the range of 10%, the error for the RC* compartment could be up to 20%.

It is interesting to examine the changes in the DAS after analyzing the data with the help of a compartment model. These spectra for the monomeric and trimeric PS I complexes are shown in Figure 5.5. As discussed above, due to the consideration of the physical relationships between the different compartments the target analysis of the data is more precise and obtains more details. This effect is apparent in the DAS after the target analysis. The ~25 ps and the ~45 ps lifetime components have better resolved DAS in contrast to the ones resulting from the global analysis (Figure 5.1). In addition, higher resolution of the earlier kinetics in PS I is achieved, resolving a sub-ps component. The presence of such a lifetime component is confirmed by some transient absorption studies with higher time-resolution (70,126).

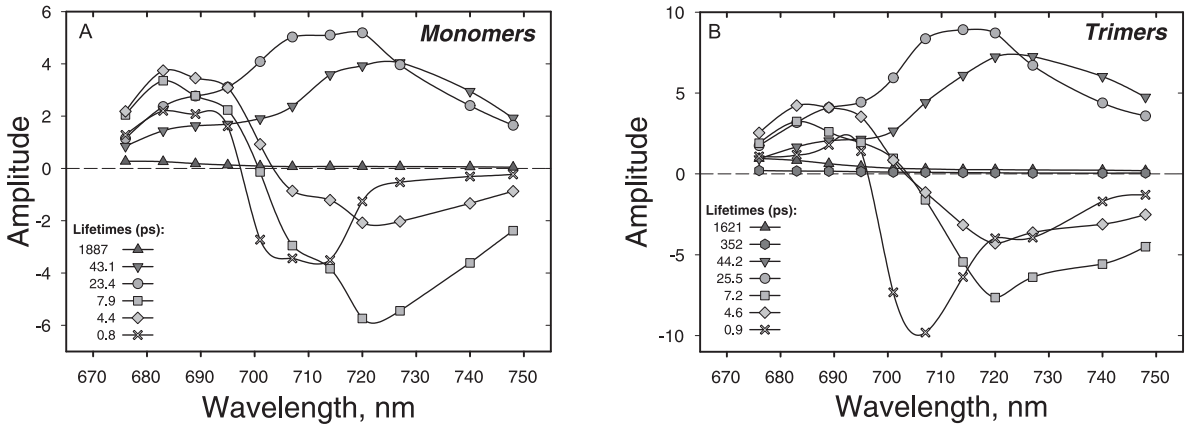

Figure 5.5
DAS of PS I monomers (A) and trimers (B) recalculated from the rates and SAES of the kinetic models shown in Figure 5.2. In PS I-monomers (A) the last lifetimes (~1.8 ns) and the last two (352 ps and ~1.6 ns) in trimers (B) reflect the additional components resulting from a small amount of unconnected Chls.

5.4.4 Nature of the trapping kinetics

The estimation of the rate-limiting step in the trapping kinetics is an important problem in the studies of the photosynthetic complexes, connected not only with their functionality but also with the design of artificial systems. We analyzed the results from our modeling further to gain more details about the energy trapping in cyanobacterial PS I. The average lifetime for the excited state decay in photosystems is basically the average lifetime of their fluorescence and can be presented as a sum of the lifetimes of two processes: $\tau_{avg} = \tau_{ET} + \tau_{CS}$ (97,101,185). The first one represents the average lifetime of the energy migration in the antenna system and its delivery to the RC (τ_{ET}). In cyanobacterial PS I complexes this lifetime is influenced by the presence of the so-called 'red' Chls. The second lifetime, the average CS lifetime (τ_{CS}), accounts for the trapping of the excitations that are already located on the RC. This lifetime reveals the contribution of the CS to the total excited state decay and should not be confused with the apparent CS lifetime, which is the lifetime component describing the apparent rise of the primary RP. By scaling (multiplying by a factor both the forward and the backward rate obtained from the modeling) the ET rates (ANT* ↔ RC*) in the kinetic models (see Figure 5.2) to infinity (*i.e.* to ensure $\tau_{ET} << \tau_{CS}$) the overall decay of the fluorescence will be entirely due to CS and consequently the newly calculated average lifetime will reflect exactly τ_{CS}. In this way the contributions of τ_{ET} and τ_{CS} can be calculated. The trap-limited case is realized if τ_{avg} is determined mainly by τ_{CS}, *i.e.*, $\tau_{CS} / \tau_{ET} > 1$. The results from this calculation are shown in Figure 5.6 and Table 5-1.

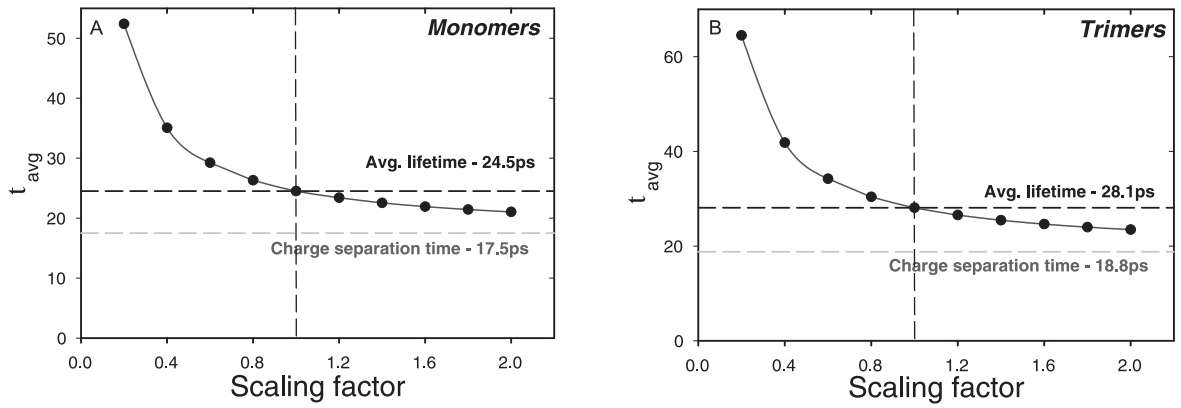

Figure 5.6
Dependence of the average fluorescence lifetime (τ_{avg}) on the scaling factor of the ET rates in the kinetic models (see Figure 5.2). Scaling factor 1 (vertical dashed line) corresponds to the actual situation. The scaling factor changes the ratio of the contribution of τ_{CS} and τ_{ET} to τ_{avg}. At very large scaling factors τ_{avg} approaches a limiting value (gray dashed line), which corresponds to τ_{CS}, unaffected by energy diffusion.

It is apparent from the ratio between the CS lifetime (τ_{CS}) and the ET lifetime (τ_{ET}) that in both monomeric and trimeric PS I-cores (2.5 and 2.04 correspondingly) the overall trapping kinetics is limited by the trap reactions, *i.e.* CS. Our results disagree with the theoretical modeling of Sener *et al.* (60) where the authors conclude that the trapping kinetics in PS I from cyanobacteria is diffusion-limited. In that work the calculated so-called first usage lifetime and the sojourn times, which in our description correspond to τ_{ET} and τ_{CS}, bear absolutely the opposite values, even though the average lifetimes are the same (see Table 5-1). It seems from the latter comparison that some of the initial conditions and assumptions in their calculation were not considered properly (especially the CS rate).

Table 5-1
Scaling analysis of the energy transfer rates (ANT* ↔ RC* and RED* ↔ ANT*) in the models (see Figure 5.2) depending on the excitation of different compartments in the monomeric and trimeric PS I complexes. For details of the meaning of the parameters see text.

	Monomers				**Trimers**			
	*ANT**	*RED1**	*RED1**	*RED1/2**	*ANT**	*RED1**	*RED1**	*RED1/2**
τ_{avg} (ps)	24.5	58.3	39.4	48.8	28.1	63.9	40	52
τ_{ET} (ps)	7	33.7	14.8	24.2	9.3	35.8	11.9	23.9
τ_{CS} (ps)	17.5	24.6	24.6	24.6	18.8	28.1	28.1	28.1
τ_{CS}/τ_{ET}	2.5	0.73	1.66	1.02	2.04	0.8	2.4	1.18

5.4.5 Influence of the 'red' Chls on the trapping kinetics

With the help of the above-mentioned approach, we performed a quantitative analysis of the impact of the 'red' Chls on the overall trapping kinetics in cyanobacterial PS I (see Table 5-1 and Table 5-2). At first we scaled the forward and backward rates of the ET of the different 'red' Chls (RED1*, RED2*) and then scaled also both of them together (RED1/2*), after placing the whole initial excitation into these compartments (see Table 5-1 and Table 5-2). From such a calculation the type of the kinetics of the 'red' Chls becomes apparent. It is important to understand that in case that only the ET rates of the 'red' pools are scaled, the original meaning of τ_{CS} and τ_{ET} (see above) is lost to some extent. Thus *e.g.* τ_{CS} will contain both ANT*-RC* energy equilibration and CS itself. However, in this case this is not a substantial disadvantage for the description since we are now interested in determining the type of the kinetics of the RED* compartments and not in determining the overall kinetics. Independent of the overall trap-limited charge separation kinetics in the whole complex, there exists a slight diffusion limitation with regard to the energy transfer to compartment RED1*. This diffusion-limitation is however a localized effect and does not shift the trapping kinetics of the whole complex into the diffusion-limited region. The reason is that in the whole complex the overall population of compartment RED1* is relatively small (*cf.* Figure 5.3). The kinetics of the two compartments is very similar in monomers and in trimers (Table 5-1). This similarity has already been discussed (*vide supra*). However, an interesting observation is that RED1* and RED2* differ between each other in their energy transfer kinetics. While RED1* introduces a minor diffusion-limited step, the RED2* does not limit the energy transfer processes. This difference in the basic properties of the two 'red' pools are in line with the ones observed in the single molecule studies by Brecht *et al.* (77).

Table 5-2
Effect of the 'red' Chls in PS I on the slowing down of the overall trapping kinetics. Scaling was performed as described in Table 5-1 and in the text. For the ANT (no REDs) case, the calculation was performed without including the 'red' Chl compartments (for more details see text).

	Monomers				**Trimers**			
	*ANT**	*ANT* (no REDs)*	*Difference*	*Effect (%)*	*ANT**	*ANT* (no REDs)*	*Difference*	*Effect (%)*
τ_{avg} (ps)	24.5	13.9	10.6	56.7	28.1	16.7	11.4	68.3
τ_{ET} (ps)	7	3.6	3.4	51.4	9.3	4	5.3	43
τ_{CS} (ps)	17.5	10.3	7.2	58.8	18.8	11.7	7.1	62.2

Since the 'red' Chls kinetics is now better understood, it is interesting to evaluate their total effect on the kinetics and in particular on its characteristic lifetimes (τ_{avg}, τ_{ET}, τ_{CS}). Using the scaling

procedures described above we calculated again the same parameters (τ_{avg}, τ_{ET}, τ_{CS}) based on the kinetic models shown in Figure 5.2 but without including the 'red' compartments. This calculation provides information about the trapping kinetics in a hypothetical case where there are no 'red' Chls present. The results are shown in Table 5-2. Clearly, the presence of the 'red' Chls introduces a deceleration of the overall trapping kinetics of ~60%. However, this overall significant effect on the total PS I kinetics not only does not impair the quantum efficiency of the complex but it also does not change the type of its kinetics.

5.5 Conclusions

We have described in detail the excitation energy trapping kinetics in cyanobacterial PS I monomers and trimers from *T. elongatus*. This work demonstrates the adequacy of the 'charge recombination' model in the analysis of the trapping kinetics of PS I complexes. With the help of this model the RC fluorescence spectra was resolved again as in other PS I complexes, and moreover information about the early electron transfer reactions was gained. We observe an acceleration in the secondary electron transfer reaction in this thermophilic cyanobacterium in comparison to mesophiles (101,127), while the first one remains unaltered. This may well be related to the large difference in the growth temperatures these organisms are adapted to. The kinetics in both of the studied complexes was shown to be trap-limited, even though a large slowing down effect (~60%) by the presence of the 'red' Chls was found. Our analysis revealed the presence of two separate kinetically different 'red' Chl pools both in monomers and in trimers. Some minor differences in one of the 'red' pools (RED1*) between the monomers and the trimers have been observed. However, the data strongly suggest that both of the 'red' compartments originate from the same groups of pigments in either of the two aggregation states. This precludes the location of these 'red' Chl pools immediately at the monomer-monomer interface. Thus such earlier assignments for the location of the 'red' Chls at the monomer-monomer interface, or even more extreme interpretations where the 'red' Chl pools are only created by the monomer-monomer interaction in the trimers, can be clearly excluded.

Chapter 6

Intra-antenna energy transfer and trapping processes in the intact Photosystem I complex of *Chlamydomonas reinhardtii*

This chapter is based on the publication:
Chavdar Slavov, Galina Gulis, Kevin Redding and Alfred R. Holzwarth
Submitted to Biochimica et Biophysica Acta, Bioenergetics 2009

6.1 Introduction

The process of photosynthesis, where light energy captured by extensive antenna systems is converted into and stored as chemical energy, provides the major energy supply for all living organisms on the planet. Photosystem I (PS I) is a main component participating in the early reactions of light energy transformation in oxygenic photosynthesis (2). PS I catalyzes the electron transfer from plastocyanin or cytochrome c_6, located on the lumenal side of the thylakoid membrane, to ferredoxin located on the stromal side. High resolution X-ray structures of PS I are available from the cyanobacterium *T. elongatus* (2.5 Å) (41) and from the higher plant *P. sativum* (3.4 Å) (40). The core antenna of PS I consists of ~100 densely packed chlorophyll (Chl) *a* molecules. These Chls are arranged in three domains – a central one, which surrounds the co-factors in the reaction center (RC) (at distance of ~16 Å) and spreads from the lumenal to the stromal side of the complex; and two peripheral domains (one on each side of the central domain) organized in two separate layers – stromal and lumenal. No spectral forms absorbing above 700 nm have been observed (51,101,127,167). However, most cyanobacterial PS I core complexes contain the so-called 'red' Chls (low energy Chls, absorbing well beyond 700 nm and up to 730 nm) which have a significant impact on the light energy trapping kinetics (61,76,193). Unlike cyanobacterial PS I, which in vivo is present in the form of trimers (42,43), higher plant and algae PS I are monomeric (80) and have a semi-belt of LHC I complexes attached at the periphery (40). It is worth noting that although the composition of the PS I core complex is the same in higher plants and algae (81), their macroorganization differs significantly. This is mainly due to the higher number of LHC I complexes attached to the PS I core complex in algae (82,83). The presence of some low energy Chls in the peripheral antenna of PS I form *C. reinhardtii* has been discussed in a number of studies ((104,167,171) and references therein). The amount of ′red′ pigments in the peripheral antenna of this complex (167,171) is significantly lower as compared to higher plants (101) and these red forms are much less red-shifted than in plant PS I. In fact, in most of the studies no ′red′ Chl pigments beyond 700 nm have been observed except in (104), where the authors have modeled a feature at ~705 nm in fluorescence as a ′red′ compartment. However, in the latter study the RC was not included as a separate compartment in the kinetic analysis of the data. Previous studies (101,127) clearly show that the RC spectrum carries pronounced amplitude in this spectral range. Thus, it appears possible that the reported ′red′ state (104) represented in fact the RC. Moreover the authors assigned the origin of the ′red′ compartment to the core complex, which contradicts other results (101,127,167) that do not find such a pool in the core complex.

The general organization of the electron transfer co-factors in the RC of PS I is preserved amongst all the complexes isolated from different organisms (2). The six Chls of the RC are strongly coupled (6,48-54), which leads to a ′red′ shift (~700 nm) of their absorption spectrum in comparison to the bulk antenna Chls (680 nm), and broadening of the covered absorption range. This change in the properties of the RC Chls has high importance for the effective excitation energy transfer (ET) from the different antenna compartments (55).

The mechanisms of the light trapping kinetics in PS I are widely discussed in the literature (51,52,76,101,104,109,111,167,193) (the reader is referred to references (52,193) and to recent reviews (194,195) for a discussion of the ET and trapping kinetics in the photosystems of oxygenic photosynthesis, as well as for definitions of the kinetics terms used throughout this work). For PS I the overall antenna to RC trapping kinetics and the charge separation (CS) kinetics in the RC have

been resolved only recently (52,127). It was shown that the energy equilibration between the bulk antenna system and the RC core in PS I in fact occurs on the time scale below 2-3 ps and the overall trapping is limited by the CS processes, *i.e.* a trap-limited kinetic model holds in contrast to the previously favored diffusion-limited trapping model (see (194) for a discussion). Slower fluorescence components in the few tens of ps time range that had previously been attributed to ET were shown to reflect charge recombination from the primary radical pair (RP) and forward electron transfer processes to the secondary RP. This new model was tested and further corroborated in a series of studies on PS I complexes isolated from various organisms (101,193). However, in all previous studies – with the exception of the kinetics to/from the ′red′ Chls – the antenna compartment was described in a simple manner and intra-antenna transfer was not taken into account. It is however clear that the overall ultrafast energy equilibration of the antenna with the RC on a time scale less than a few ps will be only possible if even faster intra-antenna energy transfer steps exist. The present study is thus aimed at a more detailed kinetic description of the intra-antenna EET processes occurring in the intact PS I complexes isolated from *C. reinhardtii*. Resolution of the intra-antenna EET steps will also provide further insight into the reasons of the ultrafast overall antenna/RC equilibration.

6.2 Materials and methods

6.2.1 Preparation of PS I samples

The preparation and isolation of the his-tagged PS I complexes form *C reinhardtii* is described in detail in (140). In short, six His residues were genetically added to the N-terminus of the PsaA core subunit of PS I. The His_6-tagged PS I was purified from detergent-solubilized thylakoid membranes in a single step using a Ni-nitrilotriacetic acid (Ni-NTA) column. The His_6-tagged PS I preparation was highly pure and extremely low in uncoupled pigments. The number of Chls per P_{700} was ~206 indicating that there are about seven LHC I complexes attached to the PS I core complex, *i.e.* substantially more than in higher plant PS I.

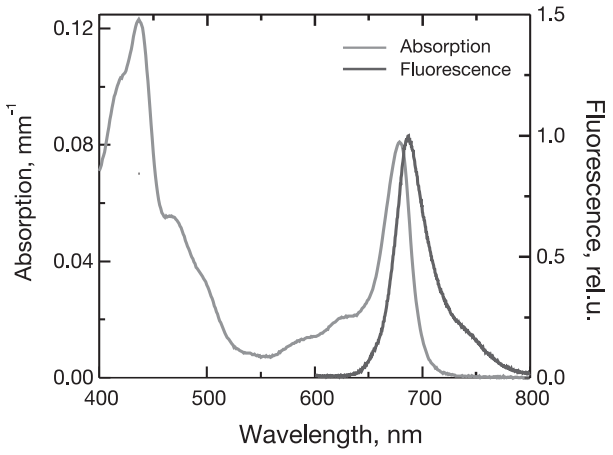

Figure 6.1
Room temperature absorption and fluorescence spectra of the His-tagged intact PS I particles isolated from *C. reinhardtii*.

For the time resolved measurements the intact PS I complexes were diluted in 25 mM Hepes buffer (pH 7.5), containing 100 mM NaCl, 5 mM $MgSO_4$. and 0.01% β-DM. In order to prevent the accumulation of closed RC during the experiments, the redox agents sodium ascorbate (40 mM) and phenazine methosulfate (60 μM) were added to the buffer medium. To avoid formation of reactive oxygen species during the measurements the buffer was purged with N_2 and the sample was added in

Ar atmosphere. Additionally, the so-called oxygen scavenging system (141), containing 8 mM glucose, 65 µl/ml glucose oxidase and 65 µl/ml catalase was used to completely eliminate the oxygen from the sample. The steady state absorption and fluorescence spectra of the sample are shown in Figure 6.1.

6.2.2 Sub-ps synchroscan streak camera fluorescence measurements

The time-resolved fluorescence measurements were performed with a streak camera set-up with sub-ps time resolution. The set-up consists of a CW frequency-doubled Nd:YVO_4 laser (Verdi V-10, Coherent), which pumps a Ti:Sapphire oscillator (Tsunami, Spectra Physics) to produce ultrashort pulses (~80 fs) at 800 nm (repetition rate of ~81.47 MHz). These pulses are fed into an optical parametric oscillator (OPO PP Automatic, APE, ring OPO configuration with second harmonic generation) to obtain ~200-300 fs pulses which are wavelength tunable (530 – 750 nm). For the excitation of the sample the repetition rate was reduced to 4 MHz using a pulse picker (Spectra Physics). The attenuated pulses were focused at the sample to a spot size of 300 µm in diameter. In order to minimize the time dispersion of the emission signal, front face fluorescence detection was used in the measurements. A steep cutoff filter is used to reduce potential excitation light scattering from the sample and a polarizer in the emission path was set at magic angle position (54.7°) to the excitation polarization for isotropic measurements. The fluorescence kinetics was detected by a synchroscan streak camera (C5680, M5675, Hamamatsu) working in photon counting mode. The streak camera was synchronized to the Ti:Sapphire oscillator and ran at 81.47 MHz (period of the sweep voltage – 12.3 ns). Since every half period of the sweep voltage in the streak camera the signal traverses the detection window, signals with lifetimes longer than 1-2 ns will cause the so-called secondary back and forth sweeps. These sweeps will give rise to additional intensity on top of the main detected signal from the forward sweep. If properly accounted for in the data analysis, as has been done here, this feature can be used to estimate long lifetimes quite well even on short sweep ranges (145). The spectral decomposition of the fluorescence emission was performed by an imaging spectrograph (Chromex 250IS). The overall instrument response function of the set-up after proper drift compensation is ~3.5-4 ps in the shortest scan range (here 115 ps), which allows sub-ps time-resolution after deconvolution. In effect, lifetimes down to about 300 fs can be resolved well if their amplitude reaches a significant percentage of the total amplitude (≥ 20%).

The time-resolved fluorescence measurements were conducted at room temperature (23 °C). The samples, diluted to OD_{680} 0.8 cm^{-1} and placed in a rotating cuvette to avoid multiple excitation and accumulation of long-lived species (10 cm diameter and path length of 1 mm, rotation frequency 70 Hz, sideway movement frequency 0.6 Hz), were excited with 200-300 fs pulses of 660 nm at the above-mentioned laser repetition rate. Careful tests showed that when a steep cutoff filter is used there is no scattered excitation light detected above 665 nm. The laser power at the sample was reduced to 100 µW. Under these excitation conditions both annihilation within a single pulse as well as consecutive double excitation of the same particle can be excluded.

Data analysis: The time-resolved fluorescence data was analyzed by means of global and target analysis procedures as described in detail previously (150-152). In short, global analysis is a simultaneous fitting of the decay traces at different emission wavelengths with a sum of exponentials function. However, the parameters (pre-exponential amplitudes as a function of emission wavelength and lifetimes) originating from this fitting are purely mathematical. In order to obtain physically meaningful parameters like e.g. the rate constants and the species-associated emission spectra (SAES) the so-called global target analysis of the original time-resolved fluorescence data has to be performed. In this analysis, various kinetic models are tested for their suitability to describe the

fluorescence kinetics over the whole detection wavelength range. The measurements were performed in two different times ranges of 115 ps and 600 ps and the results were analyzed simultaneously for both time scales.

6.3 Results

The time-resolved fluorescence kinetics of His-tagged PS I intact particles isolated from *C. reinhardtii* after 660 nm excitation were measured over the spectral range 665-750 nm. The decay-associated spectra (DAS) obtained from the combined global analysis of the fluorescence decays recorded in the two time ranges are shown in Figure 6.2. The longest lifetime component (~3 ns) is related to fluorescence signal originating from a small amount of uncoupled Chls, which are typically present in PS I preparations (101,104). The data analysis algorithms used here were modified to account for the secondary (return) sweeps in the streak camera, which carry information about the tail of the long-lived component and thus allow us to estimate its lifetime even in the short temporal ranges (145). The other lifetimes are below 50 ps and are all related to the EET and trapping kinetics in the intact core complex of PS I. Clearly, two EET components characterized by positive and negative amplitudes across the emission range can be directly seen in the DAS (one sub-ps and a ~2 ps component). These two EET components are in agreement with the ones found in previous femtosecond transient absorption results (52). Sub-ps components have been resolved also in other fluorescence studies (e.g. (109)). The other two lifetime components have only positive amplitude over the whole wavelength range. The ~9 ps component is related to excitation energy trapping in the RC by CS as found in our previous studies (101,127,193). Other groups (51,109) reported a somewhat shorter-lived component (~5 ps), which may reflect a mixture of the ~2 ps and the 7-9 ps components that are resolved here. The further component with all-positive amplitudes has a lifetime of ~40 ps and is the main decay component. A similar lifetime component was also observed in other works (104,167).

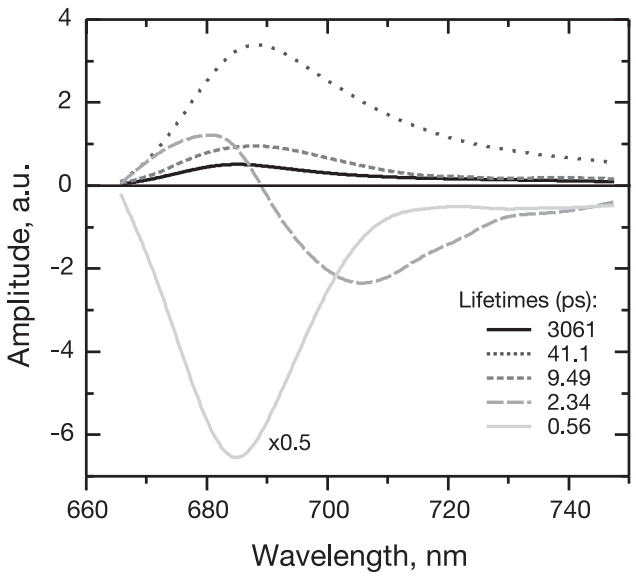

Figure 6.2
DAS obtained after Global analysis of the sub-ps time-resolved fluorescence data recorded from His-tagged intact PS I particles isolated from *C. reinhardtii*.

6.3.1 Kinetic modeling

Although global analysis gives invaluable information about the timescale on which the main processes in the studied sample occur, it contains no meaningful physical information since it is merely a fit of the experimental data with a mathematical function (here sum of exponentials). Thus,

additional analysis is necessary to gain detailed insight into the structure/function relationships of the kinetics and the mechanisms of the reactions proceeding in the system. Target analysis is an approach in which different kinetic models are tested to how well they describe the experimental data. For very complex systems as intact photosystems, the components in the kinetic modeling are reduced to several representative compartments. A compartment is generally defined as the part of a system (*e.g.* a group of pigments) that features similar kinetic and spectral properties and cannot be distinguished further at the given spectral and temporal resolution. We have tested several different kinetic models for compatibility with the time-resolved fluorescence data obtained here. These models are more complex in their antenna part as compared to previous models that were used *e.g.* to describe fluorescence kinetic data obtained by the lower time resolution provided by single-photon-counting methods (101,127). Our femtosecond transient absorption data on PS I core antenna of *C. reinhardtii* had already indicated the presence of at least two antenna compartments (52). Thus in the intact complex the antenna kinetics should be expected to be more complex. Nevertheless, we have first tested this minimal branched model on the present sub-ps fluorescence decays. Although the kinetic model with only two parallel ANT compartments gave relatively reasonable SAES and DAS spectra, the fitting of the experimental data was too poor in terms of χ^2 and residuals (*cf.* Supplementary Section 6.6, Figure 6.9, left). The failure of this simple parallel model in describing high-resolution data is not surprising taking into account that it does not describe any of the intra-antenna EET processes that most likely proceed in the more complex intact PS I. The DAS obtained from the global analysis of the time-resolved data (Figure 6.2) clearly indicates that the major part of the shortest lifetime component (<1 ps) is related to an intra-antenna ET. In order to account for the intra-antenna ET we tested several different models, which principally might account for these processes. At first, we have tested a single branch model with two sequential ANT compartments (*cf.* Supplementary Section 6.6, Figure 6.6B). This model improved significantly the quality of the fit and in addition delivered reasonable SAES. Nevertheless, we also had to keep in mind the results from the previous transient absorption measurements, which strongly suggested a parallel ANT model with two compartments reflecting essentially the antennae in the A- and B-sides, respectively (52). Based on the complexity of the intact PS I antenna structure (about seven LHC I complexes attached it is reasonable that there are more ANT pools within which intra-antenna ET can occur. On the one hand, the compartments could mechanistically reflect intra-antenna ET between 'blue' and 'red' ANT sub-pools on the A- and on the B-sides of the PS I complex. On the other hand, there could be intra-antenna ET between the stromal, lumenal domains of the whole antenna, including the LHC Is and the central domains of the core antenna. Therefore, several branches of sequential ANT compartments can be used to represent the ET kinetics. For that reason we have extended the parallel model used previously (52) to test a non-restrictive intra-antenna ET scheme. The kinetic scheme and the optimal rates obtained from the fitting of the sub-ps experimental data are shown in Figure 6.3 along with the information on resulting lifetimes and the weighted eigenvectors (for a definition of these terms see (52,151)). This model further improved the fitting of the time-resolved fluorescence data as compared to the uni-branched sequential antenna model (*cf.* Supplementary Section 6.6, Figure 6.9, right). Note that in addition to the presented model compartments a good fitting of the experimental data required at least one or occasionally two (*vide infra*) free lifetime components. One low amplitude component that is always present accounts some uncoupled Chls with a typical lifetime of ~3-4 ns. Furthermore, since in several other studies on intact PS I complexes isolated from *C. reinhardtii* (104,167) a ~70-100 ps compartment was used additionally we have tested our model for such a compartment by including a second free lifetime component in that range. Allowing for such an additional component, however, did not significantly increase the quality

of the fit. When allowed this state in our case carries at most ~8% of the total amplitude in the DAS at the maximum (*cf.* Supplementary Section 6.6, Figure 6.10), which is ~3-fold smaller than in the previous studies (104,167). Furthermore, the dependence of the amplitude of this component on the isolation procedure (here a mild isolation of His-tagged PS I vs. a more harsh detergent treatment), seems to indicate that this component originates from a small amount of partially disturbed complexes with more loosely attached LHC Is. For this reason, we do not include such a lifetime component in our actual model kinetics.

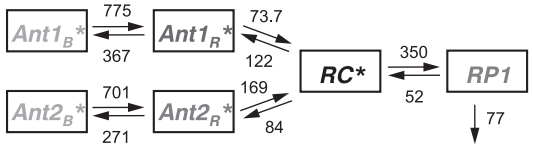

Lifetime (ps)	Ant1 $^{*}_{B}$	Ant1 $^{*}_{R}$	Ant2 $^{*}_{B}$	Ant2 $^{*}_{R}$	RC*	RP1	RP2
0.85	0.134	-0.145	0.003	-0.005	0.019	-0.006	0.0004
0.96	0.018	0.013	0.120	-0.148	0.052	-0.020	0.001
1.65	0.031	0.014	0.024	0.008	-0.214	0.157	-0.020
8.26	0.012	0.021	0.094	0.202	-0.019	-0.846	0.539
12.3	-0.055	-0.103	0.030	0.068	0.043	0.313	-0.297
39.2	0.196	0.401	0.030	0.075	0.119	0.402	-1.225
exc	***0.3***	***0.2***	***0.3***	***0.2***	***0***	***0***	***0***

Figure 6.3
Kinetic model describing the light-energy trapping kinetics in His-tagged intact PS I particles isolated from *C. reinhardtii*. The rates in the model are obtained from direct fitting of the sub-ps time-resolved fluorescence data recorded from the sample.

6.4 Discussion

6.4.1 Optimal number of antenna compartments and the excitation vector

Many previous ultrafast fluorescence studies on the trapping kinetics in PS I used excitation in the blue part (Soret band) of the absorption spectrum of the complexes(76,104). This represents a major disadvantage since this kind of excitation does not allow resolving of the short-lived intra-antenna ET components since there is significant mixing of the relaxation kinetics (internal conversion and vibrational relaxation) from the higher excited states (Soret to Q_Y) and the ultrafast ET. Reasons for using Soret excitation are mainly experimental problems that arise from scattering of excitation light causing mixing of excitation and fluorescence signals if the excitation and fluorescence detection are close in wavelength. Due to the use of a very steep cut-off filter in the emission path this problem was avoided in our measurements and thus allowed us to use direct excitation into the Q_Y band at 660 nm. Therefore, the shortest resolved lifetime component obtained in the global analysis (Figure 6.2) represents a pure EET component and is not influenced by scattered excitation light. It follows from Figure 6.2 that at least two spectrally different additional antenna compartments need to be included in the kinetic model in order to fit the experimental data. The presence of ′blue′ and ′red′ spectral pools in the antenna system of PS I complexes from *C. reinhardtii* has been previously suggested (52,167,171,196) and also follows from the width of the steady state absorption and fluorescence spectra (Figure 6.1). In addition, the clear high to low energy shift occurring on the fast time scales indicates that there occurs funneling of the energy towards the RC. Taking into account these observations we constructed a kinetic model (Figure 6.3) containing four ANT compartments separated into two branches. Alternatively, also a model with only two sequentially linked antenna compartments can be used (*cf.* Supplementary Section 6.6, Figure 6.6A). However, the fitting of the data with this model is slightly worse than with the four-antenna compartment model (*cf.* Supplementary Section 6.6, Figure 6.9). Thus in our view the model with only two sequential antenna compartments does not fully reflect the mixed kinetics of the A- and the B-side antenna branches.

6.4.2 Choice of excitation vector

A priori, it is not straightforward to deduct or estimate from the structure and the steady state spectra, which initial excitation vector (reflecting the total absorption cross-sections of the respective antenna compartments) should be used for the kinetic modeling in such a kinetic scheme. Since the spectral properties of the different sub-antenna compartments in the antenna of PS I should have a significant overlap, we have tested many different excitation vectors during the analysis of the data. The best results were achieved using the excitation vector shown in Figure 6.3, with ~30% of the excitation being absorbed by each of the ′blue′ ANT pools. Such excitation conditions were to a certain degree suggested by the amplitudes of the DAS from the global analysis (Figure 6.2).

6.4.3 The energy trapping kinetics

The rate constants describing the trapping kinetics in the optimal two-branch sequential model are shown in Figure 6.3. The ET between the ′blue′ and the ′red′ antenna pools of the PS I occurs on the time scale below 1 ps (Figure 6.3, weighted eigenvector matrix). After this ultrafast intra-antenna energy equilibration the excitation energy is transferred to the RC; the major ANT-RC energy equilibration takes place with a lifetime of <2 ps. ET components on these time scales have been detected previously (52,171).

After the main part of the energy equilibration over the antenna system and the RC the CS reaction occurs. The apparent lifetime of this process that we have found here is ~8 ps and is in agreement with our previous studies. The rate constants describing the electron transfer kinetics are in fact very close to the ones obtained from the transient absorption experiments (52). The charge recombination rate obtained from the fitting of the time-resolved fluorescence data is slightly higher than the one from transient absorption. However, this is in a way expected since the transient absorption is less sensitive to the charge recombination process. The last two lifetimes recovered from the kinetic analysis are ~12 ps and ~40 ps. The 12 ps component has a complex nature and is associated with both the decay of the first RP and certain energy transfer dynamics. The 40 ps component is mainly associated with the decay of the first RP.

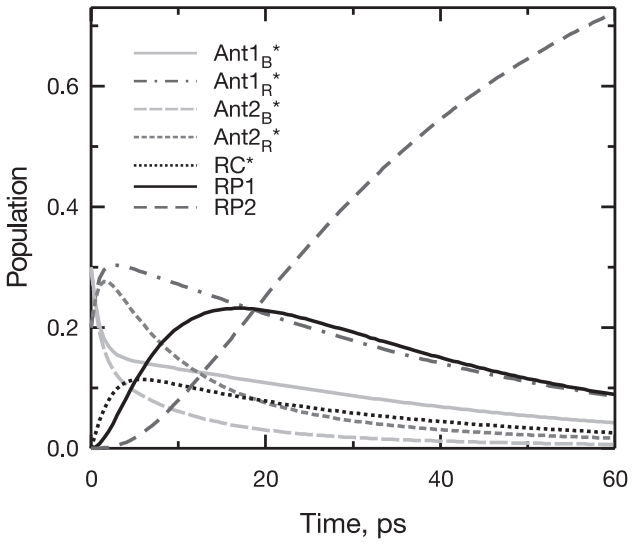

Figure 6.4
Population dynamics of the different model compartments used to describe the trapping kinetics of His-tagged intact PS I particles (*cf.* the kinetic scheme shown in Figure 6.3).

An important property of the model used here is the presence of a separate compartment representing the excited RC Chls. We have demonstrated in our previous studies (52,101,127,193) that such a compartment is necessary for the correct description of the trapping kinetics in PS I. Due to the strong excitonic coupling of the six RC Chls and their relatively large distance from the core antenna Chls the spectral and kinetic properties of this group of pigments are significantly different from the rest of the Chls (48-54,101,193). Here we further confirm that a separate compartment representing the RC can be resolved in the kinetic analysis. The maximum transient population of this compartment is ~12% (Figure 6.4).

In order to test the type of kinetics describing the energy trapping process in the studied complexes we have performed the so-called scaling analysis on the kinetic model (for details see (101,193) and the references therein). In this analysis the rate constants obtained from the fitting of the experimental data with a particular kinetic model (Figure 6.3) are used to calculate the average trapping lifetime in two different ways: first, using the actual ET rates between the ANT and the RC compartments and second, scaling these rates to infinity thus making the contribution of ET to the average trapping lifetime negligible. In the first case, the average trapping lifetime reflects both processes - ET and CS (called τ_{avg}), while in the second case this number reflects only the CS process (called τ_{CS}). The difference between these two terms gives the contribution of the ET (τ_{ET}) to the total trapping kinetics. Our calculations show that the τ_{avg} for the model shown in Figure 6.3 is ~34.3 ps, while τ_{CS} is ~19.7 ps (with τ_{ET} ~14.6 ps). Thus, the ratio τ_{CS} / τ_{ET} is 1.4. A ratio above 1 indicates an overall trap-limited kinetics type. The overall trapping time (τ_{avg} ~34 ps) is similar to the one in (104) and slightly shorter than in higher plant PS I containing ′red′ Chls (101,104). Since the τ_{avg} estimated in different PS I core complexes (101,127) is below 20 ps and there are no substantially ′red′ shifted Chls present in the intact complex studied here, the origin of the pronounced increase of the average trapping lifetime is clearly related to the much larger antenna system in the intact PS I (core antenna plus roughly seven LHC Is) of *C. reinhardtii*. Despite this lengthening of τ_{avg} due to the drastic increase in τ_{ET} from ~2.3 ps in the PS I core to ~14.6 ps in intact algae PS I, the trapping in *C. reinhardtii* is still on the trap-limited side (ratio τ_{CS} / τ_{ET} = 1.4 *vs.* 4.6 in PS I core and 2.6 in intact higher plant) but much less than for the PS I cores.

6.4.4 Spectral properties of the kinetic compartments

The SAES of the different kinetic compartments (Figure 6.3) are shown in Figure 6.5A. The spectra of the ′blue′ ANT compartments peak at ~673 nm, while the spectra of the ′red′ ANT compartments at ~686 nm. Interestingly, the amplitudes of the spectra of ANT1/2_B* are substantially smaller than the amplitudes of ANT1/2_R*. The origin of this effect is not entirely clear at present. One possible explanation could be the presence of still faster lifetimes contributing to the initial EET steps than what we have resolved here (our apparatus has a resolution in the ca. 500 fs range) for intra-antenna energy equilibration. In this case, the amplitude(s) associated with these faster processes will be missing in the SAES. In agreement with our previous studies on the trapping kinetics in PS I complexes from different organisms, the spectrum of the RC compartment peaks at ~705 nm (101,127,193). The SAES of the RC is very broad and has the largest amplitude of all spectra, accounting for the strong coupling between the RC Chls.

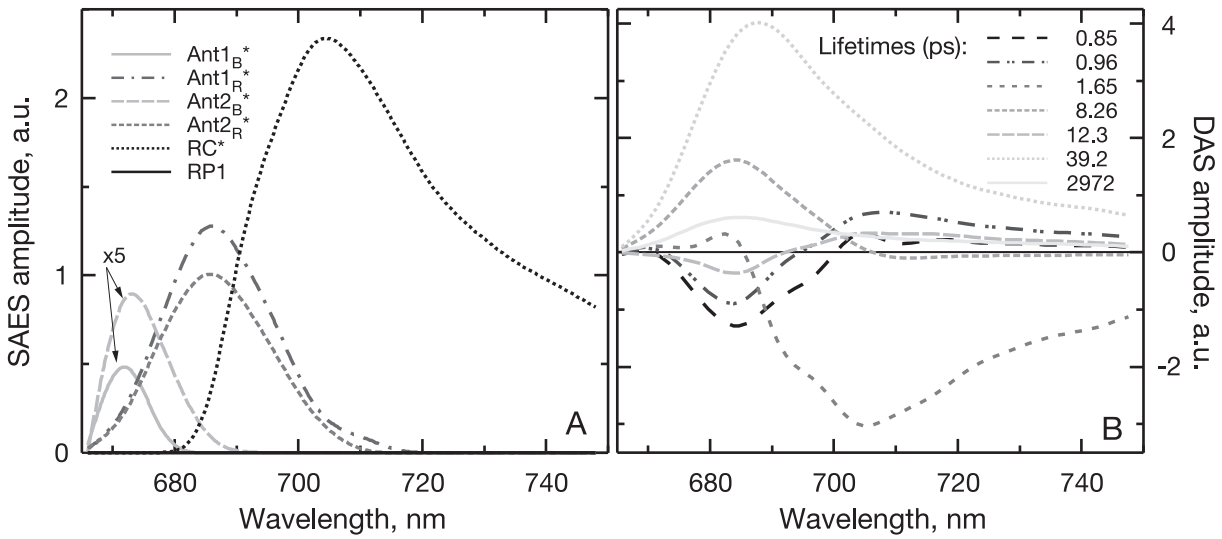

Figure 6.5
DAS and SAES obtained after target analysis of the sub-ps time-resolved fluorescence data recorded from His-tagged intact PS I particles isolated from *C. reinhardtii*.

Using the SAES (Figure 6.5A) and the weighted eigenvector matrix (Figure 6.3) obtained from the target analysis of the experimental data one can recalculate the DAS Figure 6.5B) as an internal consistency check. This DAS differs slightly from the DAS obtained from the Global analysis. However, this result is expected since the kinetics cannot be accounted for completely by the fit with a simple sum of exponents. The major differences are observed in the shortest components, where instead of one ~600 fs with very large amplitude (Figure 6.2) in the target analysis appear two (~800 and ~900 fs) components with smaller amplitudes. Since these components are associated with the EET from the ′blue′ ANT pools the smaller amplitudes is related to their relatively small SAES (*vide supra*). The other major difference is the appearance of a new component of ~12 ps in the target analysis. This component has a very complex kinetics and involves both ET and CS.

Due to the unknown structure and location of the peripheral LHC I complexes in the *C. reinhardtii* PS I antenna it is unfortunately not possible to discuss the ratio of the forward/backward energy transfer rates in terms of a Boltzmann thermodynamics model as has been discussed previously (101)

6.5 Conclusions

The analysis of the sub-ps time-resolved fluorescence signals recorded from His-tagged intact PS I complexes from *C. reinhardtii* clearly indicate the presence of intra-antenna ET processes occurring mainly on the time scale below 1 ps. In this respect, the simple kinetic model with two parallel antenna compartments used previously for the PS I core kinetics (52) is not sufficient to describe the full ET processes. However, extending this parallel model with two peripheral pools to include intra-antenna ET fits the present high-resolution data very well and gives physically reasonable spectra. Structural assignments of the four antenna pools used here, and in particular of the two peripheral ones remains somewhat speculative in view of the lacking structural data. However, after comparison of the present data for the intact PS I complex with those of the PS I core it appears reasonable at this point to identify the additional antenna pools with the peripheral LHC I complexes. Apart from achieving a detailed kinetic description of the ET process in the PS I antenna system the data confirmed again that the trap-limited 'charge recombination' model proposed earlier (52) successfully describes the total trapping kinetics in PS I.

6.6 Supporting materials

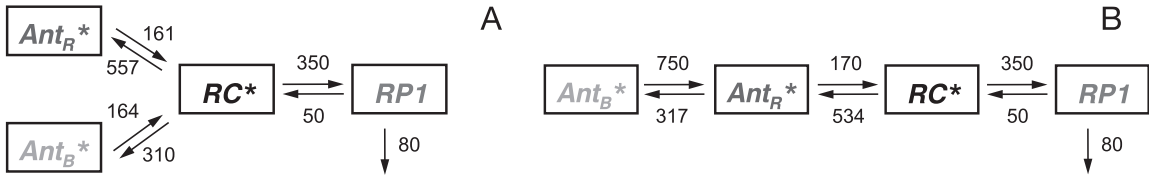

Lifetime (ps)	Ant_B^*	Ant_R^*	RC*	RP1	RP2
0.74	0.058	-0.032	-0.123	-0.035	-0.002
6.13	-0.049	0.050	0.0002	-0.002	-0.001
7.43	0.112	0.056	0.005	-0.426	0.254
39.6	0.481	0.262	0.117	0.392	-1.251
exc	***0.6***	***0.4***	***0***	***0***	***0***

Lifetime (ps)	Ant_B^*	Ant_R^*	RC*	RP1	RP2
0.82	0.134	-0.200	0.094	-0.030	0.002
1.18	0.172	-0.051	-0.217	0.106	-0.010
7.96	0.065	0.129	-0.006	-0.515	0.328
37.3	0.229	0.522	0.129	0.439	-1.319
exc	***0.7***	***0.3***	***0***	***0***	***0***

Figure 6.6
Kinetic schemes and weighted eigenvector matrices obtained after fitting the time-resolved fluorescence data with a parallel (A) and sequential (B) models with only two antenna compartments.

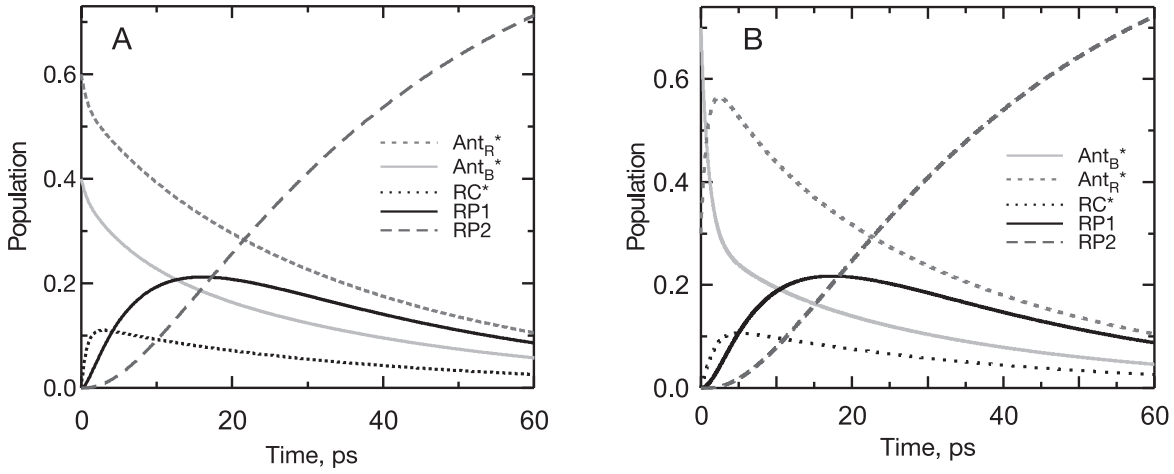

Figure 6.7
Population dynamics of the model compartments shown in Figure 6.6; A) parallel antenna model; B) sequential antenna model.

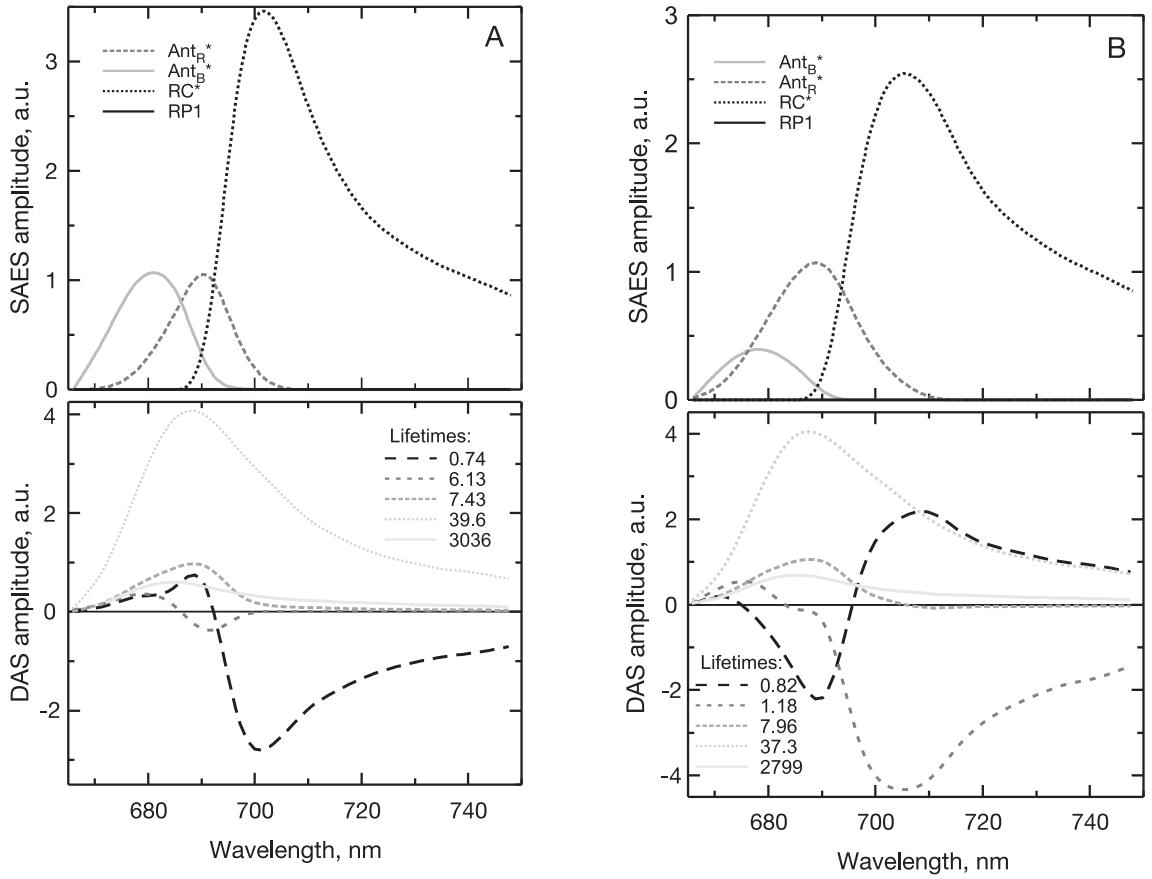

Figure 6.8
DAS and SAES obtained after target analysis (Figure 6.6) of the sub-ps time-resolved fluorescence data recorded from His-tagged intact PS I particles isolated from *C. reinhardtii*: A) parallel antenna model; B) sequential antenna model.

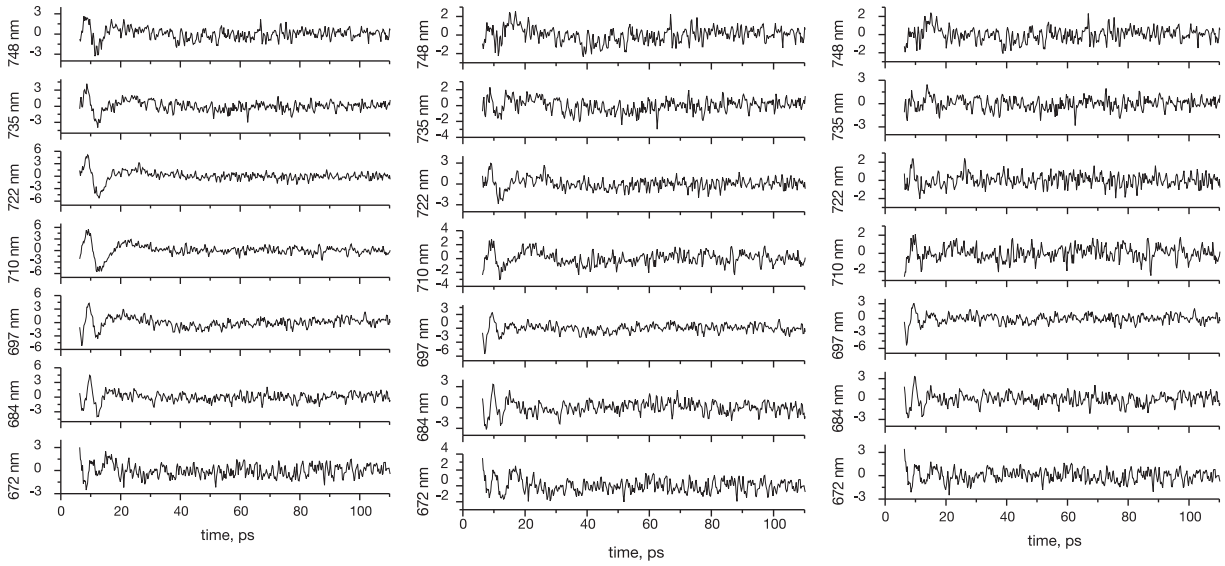

Figure 6.9
Residuals showing the quality of the fit at different detection wavelengths: *(left)* parallel antenna model (Figure 6.6A); *(middle)* sequential antenna model (Figure 6.6B); *(right)* combined model (*cf.* Figure 6.3)

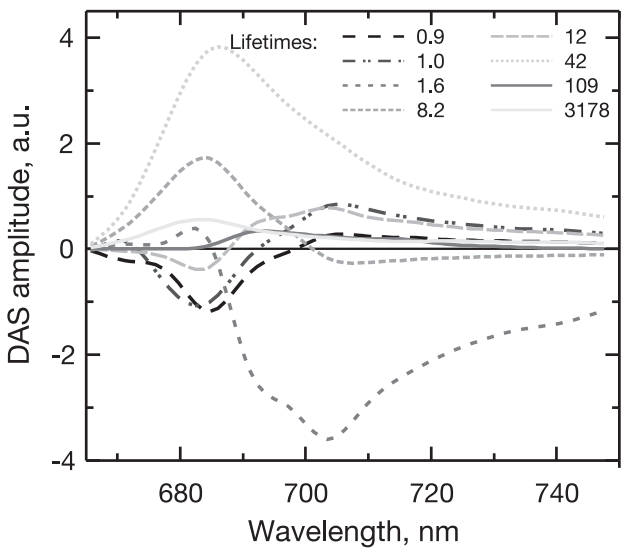

Figure 6.10
DAS obtained after target analysis of the sub-ps time-resolved fluorescence data recorded from His-tagged intact PS I particles isolated from *C. reinhardtii*. The kinetic model used here is analogous to the model presented in Figure 6.3 (*cf.* main part of the manuscript), but includes an additional free compartment giving rise to a ~100 ps lifetime.

Chapter 7

Primary electron transfer is initiated separately in two branches in the reaction center of Photosystem I

This chapter is based on the publication:
Marc G. Müller, Chavdar Slavov, Rajiv Luthra, Kevin Redding and Alfred R. Holzwarth
Submitted to Proc. Natl. Acad. Sci. USA, 2009

7.1 Introduction

In oxygenic photosynthesis the primary reactions of light utilization are driven by two multisubunit, pigment-protein complexes – PS II and PS I (2,194,195). The structure of PS I from the cyanobacterium *T. elongatus* is resolved to 2.5 Å (41) and from the higher plant *P. sativum* to 3.4 Å (40). Apart from the different macroorganization of cyanobacterial (forming trimers) and higher plant (monomers with LHC I attached) PS I (2), some differences are also observed in the organization of their core complexes. For example, there are some peripheral subunits that differ between cyanobacterial PS I and plant PS I, but most chlorophyll (Chl) molecules occupy conserved positions (84). The PS I core complex consists of an extensive antenna system of ~100 densely packed Chls and a relatively isolated group of redox active cofactors, called RC. As in all other RCs, the cofactors in the RC of PS I form two quasi-symmetric branches (Figure 7.1), diverging from a Chl *a*'/Chl *a* pair ($ec1_A$, $ec1_B$) traditionally called P_{700} (41). In each branch, there is a pair of Chl *a* molecules ($ec2_B/ec3_A$ or $ec2_A/ec3_B$) and a phylloquinone (Q_{KA} or Q_{KB},). Finally, the branches join again at the F_X iron-sulfur (FeS) cluster. The major break of the symmetry between the two branches is found in P_{700}, where the $ec1_A$ is actually a Chl *a*' (the 13^2 epimer of Chl *a*), which forms three H-bonds to the PsaA subunit, and a bound water molecule that is part of a H-bonding network. There is no such network near $ec1_B$, nor are there any H-bonds between $ec1_B$ and PsaB. In addition, small structural differences exist in the surroundings of the cofactors on the two sides. The symmetry of the cofactor branches is key to the discussion about the directionality of electron transfer in PS I. Originally, analogous to the type II RCs, it has been assumed that the electron transfer in PS I proceeded along only one of the cofactor branches, and that the other branch was not used. This idea would be supported by the structural asymmetry of P_{700}, if P_{700} were the primary electron donor in PS I. However it was shown recently that not P_{700} but in fact one or both of the ec2 Chls function as the primary donor (6). In this respect, the asymmetry of P_{700} is more likely related to the reduction of P_{700}^+ by the mobile electron carriers plastocyanin and cytochrome c6, rather than to the directionality of the electron transfer within the PS I RC.

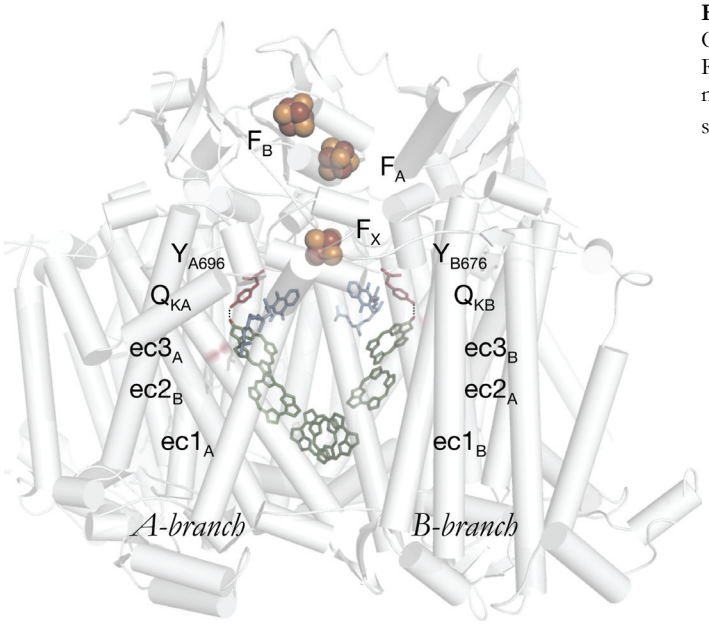

Figure 7.1
Organization of the electron transfer cofactors in the RC of PS I (41). Note that there exists an alternative nomenclature for the cofactors in PS I using the spectroscopic terms Chl_{acc}, A_0, and A_1 (58).

The first indication about bi-directional electron transfer in PS I can be found in the work of Sétif and co-workers on PS I particles from spinach (130) where bi-exponential decay kinetics of Q_K^- was been observed (with $\tau_{1/2}$ = 25 ns and 150 ns). Biphasic behavior of Q_K^- re-oxidation was later seen in cyanobacterial PS I (131,132). However, the authors (130) assigned the origin of the bi-exponential kinetics either to heterogeneity of the PS I complexes due to biochemical purification or to a complex establishment of redox equilibrium between Q_K and F_X along with forward electron transfer from F_X to F_A/F_B (132). However, the observation of bi-exponential kinetics in living algal cells ruled out the former hypothesis, and the lack of sensitivity to presence of a transmembrane electric field ruled out the latter (129). The authors observed two phases of Q_K^- oxidation with halftimes of 18 ns and 160 ns and similar amplitudes in *Chlorella sorokiniana* cells, and suggested that they be assigned to re-oxidation of the two Q_Ks within PS I. This hypothesis was tested directly by examination of the kinetics of Q_K^- re-oxidation in *C. reinhardtii* mutants where the Trp residues in π-stacking contact with the phylloquinones had been converted to Phe either singly or together (135). These results allowed for the first time assignment of the two phases to particular cofactor branches: the fast phase (13 ns) to re-oxidation of Q_{KB} and the slow phase (150 ns) to re-oxidation of Q_{KA}. Similar results were obtained in studies on cyanobacteria (133,134). Nevertheless, based on the interpretation of additional EPR results, the authors in (133) preferred the asymmetric model for electron transfer, in which the A-branch would be heavily favored.

It is important to note that the EPR studies are an essential part in solving the puzzle of the bi-directional electron transfer in PS I. Initially, there seemed to belittle support from the EPR experiments for participation of the two cofactor branches in CS (197-199),(197-199), especially in cyanobacterial PS I. On the one hand, the low time-resolution of this method does not allow direct detection of the fast phase of Q_K^- re-oxidation observed by optical spectroscopy (133,197). On the other hand, since the spin density of $P_{700}^{+\bullet}$ is localized on the $ec1_B$ Chl (46) one would expect to observe different geometries of the resulting RPs in case that both branches are active. This, indeed, has been achieved recently (200). Currently, the support for the bi-directional electron transfer model based on EPR techniques is growing (200-203).

Alternatively, in respect to the pronounced asymmetry of P_{700}, another model has been suggested to explain the bi-exponential kinetics of the Q_K^- optical signal (204). According to this model the electrons proceed only along the B-branch with a halftime of ~10 ns, followed by competing electron transfer from F_X^- to F_A and Q_{KA} (halftime of ~300 ns) (204). However, in the light of the evidence for a ec2 Chl acting as the primary electron donor in PS I (6), such a scenario becomes rather unlikely. Additionally, it does not agree with the above-mentioned EPR studies, independently of their support for the bi-directional electron transfer.

All of the above-mentioned works describe only the final steps of the electron transfer along the cofactor branch(es): electron transfer from Q_K to F_X. However, the decision about the branch along which the electron will travel is taken already in the primary CS step. Consequently, in order to categorically resolve the branching problem and to understand the underlying mechanisms and causes, ultrafast time-resolved studies have to be conducted. In the past, ultrafast studies on PS I were mainly concentrated on solving another major issue – the type of the energy trapping kinetics (52,76,101,109,111,193). Most of these studies either did not attempt to describe the electron transfer reactions in detail or used a single-branched and in most cases irreversible CS model. Most of these studies assumed a priori that the ET from the antenna to the RC of PS I is slower than the primary CS reaction, and no attempt had been made to resolve the RC* population kinetics. Thus the actual

rate of primary CS could not be determined (76,109). In case that ET to the RC would indeed represent the bottleneck of the overall trapping reaction, it would be extremely difficult to unravel the following faster electron transfer steps. Recent studies have demonstrated, however, that the RC* population kinetics and the rate of primary CS can in fact be resolved and trapping is limited by the electron transfer process rather than by the ET to the RC (6,52,101).

In this work, we aim to differentiate the early electron transfer steps in the two cofactor branches of the PS I RC in order to get insight into the origin of the bi-exponential kinetics previously observed at the Q_K/F_X level. Characterization of the activity of the two branches at early times is only possible with the help of mutants where important amino acid residues are selectively changed to modify the reaction in one of the branches. Dashdorj *et. al.* studied the electron transfer kinetics in the cyanobacterial PS I RC, where the axial ligand to the ec3 Chls (Met) had been modified in either of the branches (136). According to the authors, the electron transfer in cyanobacteria is strongly asymmetric and proceeds predominantly along the A-branch. This conclusion should be considered with caution because of two reasons. Firstly, the authors analyzed their data using a questionable approach where double difference signals of (reduced minus oxidized) RC kinetics were analyzed, which implies that the energy trapping is not changed by the presence of P_{700}^+. Secondly, the analysis could not resolve two important lifetime components present in other studies (6,52). These unresolved components in fact represent the first two electron transfer reactions. If these components were resolved, the authors might not have proposed the highly asymmetric A-side CS model. In contrast, similar PS I mutants from *C. reinhardtii* were used to demonstrate bi-directional electron transfer with a 1:1 branching ratio (137). However, mutations of the axial ligands are often harsh and bring about relatively large changes and possible side effects not limited to a pure redox change. A more elegant approach was taken by Li *et. al.* (138) who studied *C. reinhardtii* PS I in which the Tyr residues involved in H-bond formation to the ec3 Chls had been converted to Phe, with the predicted effect of destabilizing the ec3– Chl anion radical. They found that mutation of the A-side Tyr resulted in a decrease in the amplitude of the slower kinetic component (assigned to electron transfer from Q_{KA} to F_X) and an increase in the amplitude of the faster kinetic component (assigned to electron transfer from Q_{KB} to F_X); the opposite result was seen in the B-side Tyr mutant. Moreover, transient EPR data was consistent with the hypothesis that the amount of the faster kinetic component – which cannot be observed directly by this technique, but whose effect is manifested as an increase in the amount of the $P_{700}^+FeS^-$ RP at very early times – was decreased in the PsaA-Y696F mutant and decreased in the PsaB-Y676F mutant. Taken together, these data not only provided strong support for bi-directionality of electron transfer in PS I, they suggested that there was some sort of competition between the branches in terms of CS, and that the energetics of a state involving $ec3^-$ could affect this competition.

It is apparent from the above discussion that even though there exists a significant body of data supporting the electron transfer activity of both cofactor branches in PS I. What is lacking is a mechanistic model of CS within PS I that would naturally explain the observed directionality. In the current study, we used the same *C. reinhardtii* PS I mutants, PsaA-Y696 and PsaB-Y676, to probe the effects of loss of the H-bond to specific ec3 cofactors on the earliest electron transfer reactions in PS I. It has previously been shown that the primary CS reaction in PS I is not affected by mutations to P_{700} (6), strongly suggesting that the initial CS event is between ec2 and ec3. This study tests that hypothesis directly, as a clear prediction of it would be a significant effect on the CS rate in the branch in which the H-bond donor to ec3 had been removed.

7.2 Results

The femtosecond transient absorption kinetics of PS I upon preferential RC excitation at 700 nm are shown in Figure 7.2 as difference spectra at selected delay times (*cf.* Figure 7.6 in Section 7.5 for the complete hypersurfaces). The early blue shift of the initial absorption-bleaching band (690–695 nm) indicates that the major part of the RC/antenna ET is finished within ~2 ps. Hence, the difference spectra at later times reflect the overall trapping of excitation and the formation/decay of various RP states. The fast energy equilibration kinetics observed up to 1-2 ps are remarkably similar in both mutants and in the WT. Differences are observed only in the shape of the later spectra beyond ~10 ps. The kinetics in the spectral range above 720 nm, where there is virtually no ground state absorption, is crucial for a qualitative and quantitative understanding of the reaction steps. This range provides a window to selectively monitor the formation of the early RPs (205). For example, the appearance of the primary RP(s) from the excited state can be directly observed from the decay of the stimulated emission (SE) and the concomitant rise of the absorption of the RPs at 730 nm (52) (Figure 7.7, Section 7.5). The loss of the SE – negative signal – and the rise of the RP absorption occur by nearly a factor of two faster in the WT (~10 ps) than in the mutants (~20 ps), and are slightly slower in the A-side mutant than in the B-side mutant. This effect of the mutation on the primary CS process in both mutants, which can be seen without any further quantitative analysis, not only proves that both cofactor branches contribute to the primary CS reaction with substantial yield but also shows that the first CS step is slowed down by the mutation on both sides.

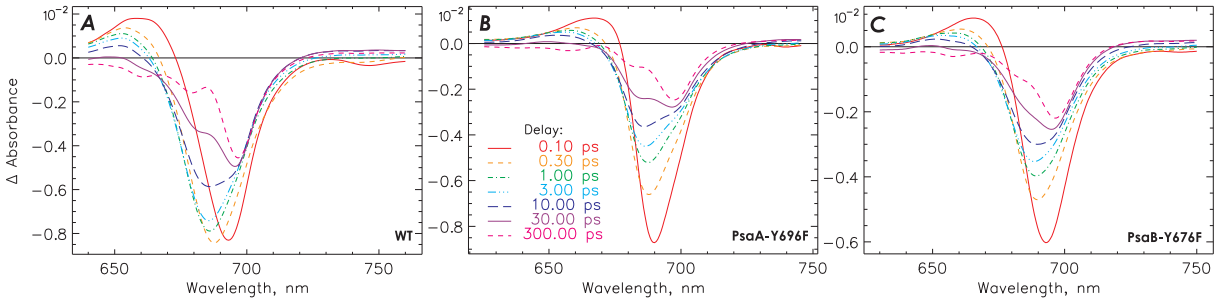

Figure 7.2
Transient absorption spectra at different delay times after excitation at 700 nm for the WT (A), PsaA-Y696F (B) and PsaB-Y676F (C) mutant PS I particles.

7.2.1 Lifetime density analysis

The data sets from both time ranges were submitted to a combined lifetime density (LFD) analysis. The LFD maps (Figure 7.3) reveal all of the relevant lifetime components. The correlated bright yellow-green and dark blue nodes (660-700 nm) represent the ~800 fs ET processes. The most important feature, describing excited state trapping and the rise of the primary RP(s) can be observed above 720 nm. This takes place with lifetimes of 7-20 ps in the mutants (*cf.* Figure 7.3). The broad dark blue feature (675-700 nm) with lifetimes of 15- 50 ps contains a complex mixture of RP kinetics that can be disentangled only by detailed kinetic modeling. This signal includes the loss of excited state absorption (ESA) below 670 nm (lifetimes from ~20-40 ps – bright yellow-green node). At the upper end of the LFD maps there is a long-lived non-decaying (ND) component that reflects directly the final P_{700}^{+}–P_{700} difference spectrum. The LFD map of the WT (*cf.* Figure 7.3A) shows the fast formation of the first RP(s) with lifetimes of 5-9 ps (blue band above 710 nm) indicating that the primary CS in the WT is much faster than in either of the mutants, in agreement with the transient decays (Figure 7.7).

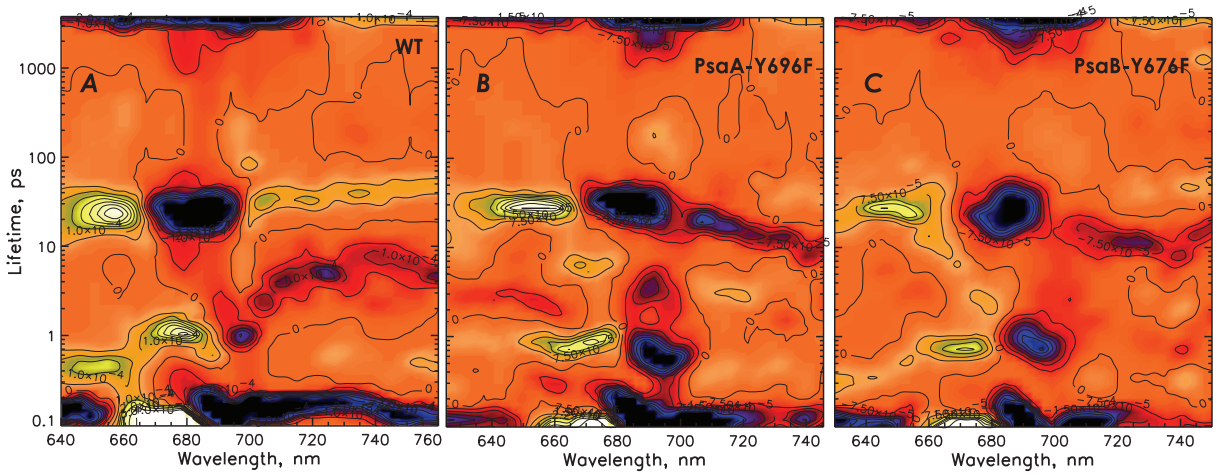

Figure 7.3
Lifetime density maps for WT, A-side and B-side mutant. The ordinate is a logarithmic lifetime axis and ranges from 100 fs to above 1 ns. On the abscissa are plotted the spectra calculated for each corresponding lifetime, using a color code for amplitude at each wavelength: orange corresponds to zero level, while negative amplitudes are blue to black, and positive amplitudes go from green to yellow to white. Thus, decay of a bleaching or rise of a new absorbance (*e.g.* at 8-20 ps above 710 nm) will appear as a dark feature, while a component with positive amplitude, indicating a loss in excited state absorption or a rise in a bleaching during an ET (*e.g.* the uphill ET results in a lifetime node at 0.8-1 ps between 660-680 nm) will appear as a bright feature.

7.2.2 Kinetic modeling

The next step in the data analysis is to build a physically meaningful kinetic model describing the underlying processes in a compartment model (98). Since we are focusing on the RC processes and are exciting the RC pigments preferentially at time zero (*cf.* Section 7.5.1) it is sufficient to describe the antenna by a very simple model – only one generalized antenna compartment (ANT) is considered, as has been described already earlier (6,52). The initial analysis of the present data was then performed using the earlier conventional uni-branched model (*cf.* Figure 7.8, Section 7.5) (52,101). The second and the third lifetime components reflect the primary and the secondary electron transfer steps, respectively. This simple model did however not provide a fully satisfactory and consistent description of all the data. It was neither suitable to provide a perfect fit in the 10-40 ps range, nor is it suitable to describe the effects of the mutations on either branch. Since the qualitative analysis of the data (*vide supra*) had already shown that mutations in the two branches influenced the CS kinetics independently, we extended the kinetic scheme to a bi-branched model to account for the ET reactions in both cofactor branches (Figure 7.4). Again one excited ANT compartment (ANT*) and one excited RC compartment (RC*) are used. The bi-branched model contains five additional rate constants to be determined (plus the new RP spectra) in comparison with the uni-branched model (*i.e.* a substantial increase in complexity). The challenges arising from such a complex kinetic model in terms of data quality, data analysis procedures used, and the accuracy of the extracted parameters are substantial. All the measures taken to overcome these problems and the type of test simulations performed to get an idea about the capabilities and limits of such an approach are described in detail in Section 7.5. In summary, it turned out that by using a minimal set of relatively unrestrictive boundary conditions, it is possible to solve the fitting problem for the bi-branched model and to determine all of the rate constants. The set of rate constants is shown in Figure 7.4 and the resulting species-associated absorption difference spectra (SADS) and the corresponding transient populations are shown in Figure 7.5. All results are collected in Table 7-1 (Section 7.5).

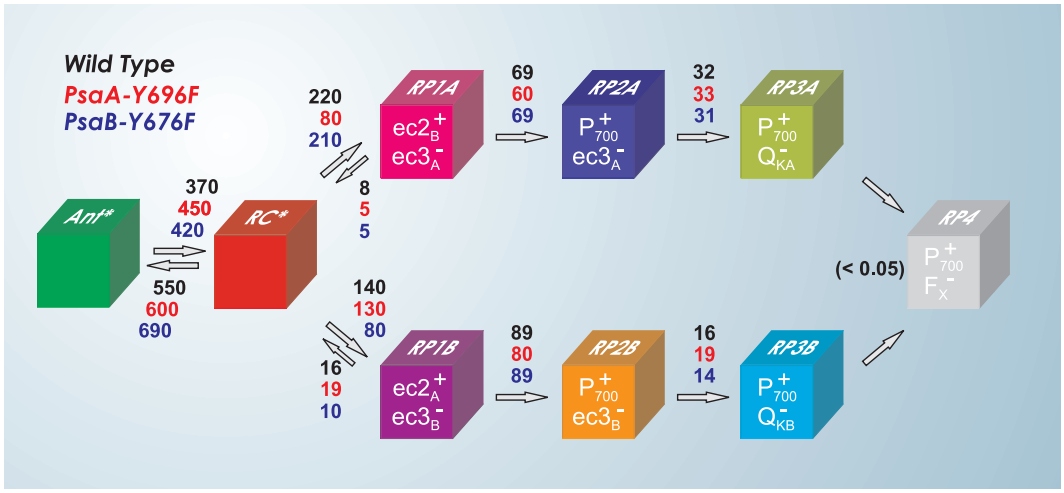

Figure 7.4
General kinetic scheme of the bi-branched kinetic model. The rate constants are given in units of ns^{-1} for the indicated energy and electron transfer steps in WT (black), PsaA-Y696F (red) and PsaB-Y696F (blue) PS I. (*cf.* Section 7.5 for the lifetimes and the weighted eigenvector matrices).

7.3 Discussion

7.3.1 The initial CS event

The fact that the PsaA-Y696F and PsaB-Y676F mutations preferentially affect primary CS demonstrates that the ec3 Chls must be part of the RP formed during this process. We had earlier found that three mutations near P_{700} (including an axial ligand and H-bond donor) had an effect upon the second electron transfer step (RP1 → RP2), but not on primary CS (6), which showed that P_{700} was not part of RP1. Taking together both the negative evidence (lack of effect of P_{700} mutations upon CS) and the positive evidence (observed effect of ec3 mutations upon CS), we can now unequivocally assign RP1 as $ec2^{+}ec3^{-}$, and state that primary CS occurs from the RC* to $ec2^{+}ec3^{-}$. The secondary step would then consist of electron transfer from P_{700} to re-reduce $ec2^{+}$ ($P_{700}ec2^{+}ec3^{-} \rightarrow P_{700}{}^{+}ec2ec3^{+}$). Furthermore, the fact that both Tyr mutations had quantitatively similar effects upon the primary CS rate demonstrates that RP1 can be formed on either branch, generating either $ec2_B{}^{+}ec3_A{}^{-}$ or $ec2_A{}^{+}ec3_B{}^{-}$. It should be noted that the effects of mutations upon primary CS is mirrored by their effects upon directionality, as manifested by the amplitudes of the nanosecond components assigned to re-oxidation of Q_{KA} and Q_{KB}. It had earlier been shown that loss of the H-bond donor to P_{700} had no effect upon directionality ((206)), and was later shown to have no effect upon primary CS. The ec3 mutations affected directionality ((138)), and now have been shown to inhibit primary CS. Thus, the directionality phenomenon observed in the nanosecond timescale is merely a manifestation of the primary CS mechanism, which has not been characterized so far.

7.3.2 Uni- vs. bi-branched kinetic models

Even with our previous analysis of the data from WT PS I, there were indications that the uni-branched models were inadequate. The fitting of such a model to the mutant data is shown in Figure 7.8 (Section 7.6) and the results confirm the qualitative and semiquantitative statements in Section 7.2. The average effective primary CS rates calculated from such a uni-branched model are

350 ns^{-1} (WT), 210 ns^{-1} (PsaA-Y696F) and 290 ns^{-1} (PsaB-Y676F). However, we had pointed out earlier that the electron transfer kinetics in the early steps in WT PS I appeared to be more complex than predicted from the uni-branched model (6,52), showing either distinct splitting of lifetime components or an unusual broadening in the LFD maps. The present mutant data go much further to corroborate the previous findings. For example, the broad distribution of lifetimes in the range of 10-40 ps for the mutant data (Figure 7.3) cannot be modeled properly with three lifetimes only. The present qualitative and quantitative results that mutation around either of the ec3 Chls, specifically changing its redox potential, selectively slows down substantially the first electron transfer step without substantially affecting the other rates (*cf.* Figure 7.8) now definitely excludes a uni-branched electron transfer model. Moreover, the fact that the two mutations have a quantitatively similar effect argues strongly that both ec3 Chls are involved in the CS event; it would be incoherent to claim that one mutation had a direct effect upon the cofactor in the active branch, while the other mutation (to a cofactor in the inactive branch) somehow had an indirect, yet quantitatively similar, effect upon the active branch. Thus, based on these mutant data an extension of the ET chain model to a two-branched model was mandated before even going into analyzing the details of the kinetics.

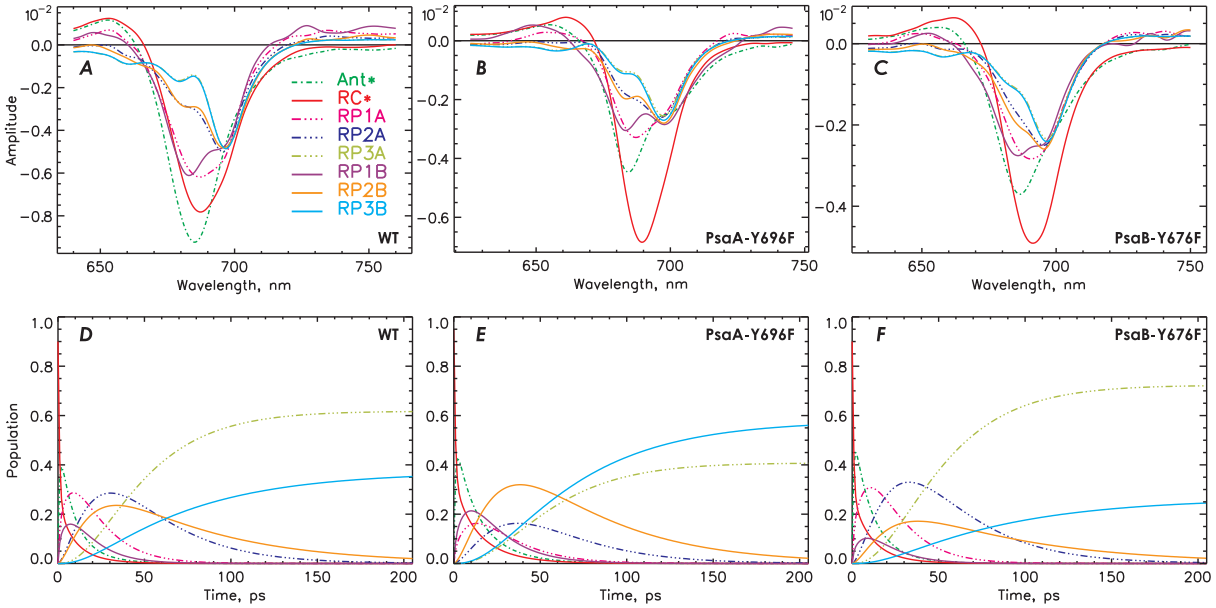

Figure 7.5
SADS (A, B, C) and transient populations (D, E, F) of the intermediates resulting from the bi-branched model shown in Figure 7.4.

All of these qualitative observations must be described satisfactorily by a meaningful and detailed kinetic model. We thus constructed the bi-branched model shown in Figure 7.4 and tested it on the data (cf. Section 7.5 for details). Each electron transfer chain starts from the same equilibrated RC* state and contains three potential intermediate RPs (6) leading up to a long-lived RP involving the Q_K (Figure 7.4). The resulting rate constants are also shown in Figure 7.4 and the resulting SADS in Figure 7.5. The modeling must answer the following questions: *i)* to what extent do the two branches differ in their electron transfer rates; *ii)* are there significant differences in the spectral properties of the two cofactor branches; and *iii)* which factors finally determine the branching ratio in terms of yields of the two $P_{700}^{+}Q_K^{-}$ RPs. While the electron transfer lifetime from either Q_K to F_X is well beyond our experimental time-scale (130,138) and thus cannot be resolved, the spectrum and yield of each $P_{700}^{+}Q_K^{-}$ RPs is contained in the long-lived ND component (Figure 7.4 and Figure 7.5). The

lifetimes associated with these models and the weighted eigenvectors are provided in Table 7-1 of Section 7.7.

Following excitation the energy equilibrates between the RC and the ANT compartment with τ_1 ~ 0.8-1 ps (Table 7-1) with an uphill transfer (k ~ 600-690 ns^{-1}) into the ANT that is somewhat faster than the downhill transfer (~420 ns^{-1}) towards the RC (Figure 7.4) in agreement with earlier findings (6) and these rates are unaffected by the mutations, as expected. In WT PS I, the primary CS reaction proceeds with an effective rate constant of 220 ns^{-1} in the A-branch and 140 ns^{-1} in the B-branch. The sum of these rates quite well agrees with the effective rate constant of the uni-branched model. The charge recombination is about twice slower in the A-branch (~8 ns^{-1}) than in the B-branch (~16 ns^{-1}). Comparison of the primary CS between the WT and the mutants reveals that the studied mutations have their direct effect specifically on the CS rate related to the branch in which they are introduced. The PsaA-Y696F mutation slows down the CS rate in the A-branch by a factor of about three to ~80 ns^{-1} (Figure 7.4). In addition, small effects of this mutation can also be observed on the corresponding charge recombination rate. However, no significant impact on the B-side electron transfer processes induced by this mutation is observed. Examination of the results from the PsaB-Y696F mutant indicates a substantial drop (by a factor of ~2) of the primary CS rate in the B-branch. Again, the other rates are unaffected within the error limits. These numbers also demonstrate that the effect of the mutations on the redox potential of the respective Chls is relatively mild, as expected, since neither of the mutations completely shuts off the initial electron transfer on that side. (Larger changes of redox potential, which could possibly be brought about by changes in the axial ligands of these Chls, would be required to achieve that effect and may be of interest for future work.) The rates for the secondary electron transfer are in the range of 60-70 ns^{-1} for the A-branch and 80-90 ns^{-1} for the B-branch. Interestingly, although unaffected by mutation, the tertiary electron transfer rates towards the Q_Ks differ significantly between the two branches, with ~32 ns^{-1} for the A-branch and ~14-19 ns^{-1} for the B-branch.

7.3.3 Assignment of the radical pairs and their spectra

As shown above, the first RP state on either branch is the $ec2^+ec3^-$ RP. Hence, on the A-branch it is the $ec2_B^+ec3_A^-$ RP, and on the B-branch the $ec2_A^+ec3_B^-$ RP. The SADS of both RP_3 states (Figure 7.5) resemble the difference spectrum found in transient spectroscopy studies in the nanosecond time scale, allowing us to assign it with confidence to $P_{700}^+Q_K^-$. Finally, the intermediate species (RP_2) must be attributed to the state $P_{700}^+ec3^-$, in agreement with the conclusions drawn earlier based on single-branch ET models (6).

Several specific spectral features can be used to discriminate between the SADS (Figure 7.5) of the compartments involving excited states (*e.g.* ANT* and RC*) from the ones involving RPs. The SADS of the ANT* and RC* compartments are typical for excited singlet states of Chls, showing a single bleaching band at about 683 nm and 690 nm, respectively, and SE up to 750 nm. In contrast, the RP SADS of both the A- and the B-branch feature a typical double band structure with a main band possessing a pronounced shoulder. Together with the positive absorption above 720 nm (52,205), these intermediates are clearly characterized as Chl RPs. These features play an important role in deciding whether a kinetic model is consistent with the experimental data in a physically meaningful way, beyond a mere perfect mathematical fit of the data.

Despite the pronounced similarity between the corresponding RP spectra in the two branches, the RPs involving the $ec3_B$ Chl (RP_{1B} and RP_{2B}) have SADS blue-shifted by about 2-3 nm relative to the corresponding RPs involving $ec3_A$ (RP_{1A} and RP_{2A}; *cf.* Figure 7.5). This finding is supported by the original transient absorption spectra (Figure 7.2) at delay times longer than 10 ps. These spectra in the WT have a well pronounced double band shape, which is indicative of bleaching of two Chls related to the formation of the RPs (*vide supra*). The mutations studied here introduce a noticeable modification of this double band structure. In the case of the PsaA-Y696F mutant, where the formation of the $ec2_B^+ec3_A^-$ RP is significantly reduced and therefore its spectral contribution, one can observe a pronounced increase of the short-wavelength part of the double band as compared to the WT and the PsaB-Y676F mutant (see Figure 7.2, transient absorption spectra in the range 10-30 ps). In contrast, in the PsaB-Y676F mutant, where the yield of $ec2_A^+ec3_B^-$ RP is reduced, the short-wavelength part of the double band has smaller amplitude than in the WT. It follows that the transient absorption spectra (mainly their short-wavelength shoulder) after ~10 ps in the PsaA-Y696F mutant resemble the SADS of the RPs involving $ec3_B$ Chl (Figure 7.5) and *vice versa* for the PsaB-Y676F mutant. These effects are in fact expected from the changes in the rate constants, since the suppression of one of the electron transfer pathways (A- or B-branch), leads to a stronger contribution of the RPs and their spectra from the other pathway in the overall decays (Figure 7.2).

7.3.4 Branching ratio

The transient populations (Figure 7.5) reveal that the first RPs (RP_{1A} and RP_{1B}) reach their maximal population at ~10 ps in all cases. At this early stage of the electron transfer kinetics, the population amplitudes of RP_{1A} and RP_{1B} can be used to estimate the initial branching ratio of the electrons passing through each branch. However, the rates of charge recombination and secondary electron transfer also influence substantially the overall amount of electrons transferred through the A-side and the B-side cofactor branches. Therefore, the precise value of the branching ratio (B/A) can only be determined at 300 ps after excitation, using the ratio of the population size of RP_{3B} and RP_{3A} (at this point they comprise >95% of the population). Taking into account all the rates in the system, we obtain a B/A ratio of 0.61 in WT, which increases to 1.43 in PsaA-Y696F and drops to 0.36 in PsaB-Y676F (*cf.* Table 7-2 in Section 7.7). Similar B/A branching ratios (WT - 0.67, PsaA-Y696F - 1.77, and PsaB-Y676F - 0.21) were estimated from the amplitudes of the kinetic components representing reduction of F_X by Q_{KA} or Q_{KB} (138). As noted previously, these latter values cannot be taken as exact values, since they assume that the extinction coefficients of the two Q_K species are identical, which may not be the case. Given all the caveats and the complexity of the present bi-branched model, the good agreement between the branching ratios resulting from these two independent techniques is very satisfying.

7.3.5 Free energy differences

The A-branch is the faster one in primary CS and in tertiary electron transfer. However, it is known from the nanosecond measurements (135,138) that the subsequent electron transfer step to the F_X cluster is about 10-fold slower in the A-branch ($\tau_{1/2}$ ~250 ns *vs.* ~25 ns) (138). Considering this difference, it becomes clear that the higher yield of CS in the A- branch in the WT can only be achieved if the primary CS process is faster than in the B-branch. The remarkable alternation of the orders of the rate constants across the two branches (*e.g.* the A-branch is faster for formation of RP_1, slower for formation of RP_2, and faster for formation of RP_3) implies a pronounced effect of the

relative energies of the corresponding RPs in the two branches. The relative energies of the RPs can be obtained from the ratio of forward and backward electron transfer rates. It is revealing to follow the development of the free energy difference (ΔG) changes on the time scale of the electron transfer reactions (*cf.* Figure 7.9 and Section 7.5.1.5 for details on the calculation of the time dependent ΔG). The total free energy loss from the RC* state to the $P_{700}^{+}F_X^{-}$ state must be the same for both branches, since the starting and ending states are the same. However, the intermediate electron transfer steps in the two branches are realized with observably different driving forces and free energy losses. This can then be related to the specific function of the final step for collecting the charges back on a single cofactor. In fact, a CS in the A-branch is more stable since the initial ΔG value is larger than in the B-branch, which implies that less driving force remains for this final step to F_X, which would lead to a slower electron transfer rate, as has been observed ((135,138)). Likewise, the smaller drop of ΔG for the primary CS in the B-branch implies a higher probability for charge recombination than in the A-branch, which could be tested in an ultrafast time-resolved fluorescence experiment.

7.3.6 The intrinsic CS rate as a universal property

Our results on the branching of the electron transfer in PS I reveal another interesting feature, concerning the primary CS process. When PS I trapping kinetics is modeled with a uni-branched model (Figure 7.8) the effective primary CS rate is about 360 ns^{-1}, which makes it about two times faster than in PS II (100). The same applies also for the intrinsic primary CS rate (*cf.* (52) for definitions of these terms), which is ~2.1-2.4 ps^{-1} in PS I (using the uni-branched model), assuming a 6-fold degeneracy of the RC, while in PS II it is ~1 ps^{-1} (6). Interestingly, not much attention has been paid to this significant difference between PS I and PS II. Based on the bi-branched model, however, both the effective and the intrinsic primary CS rates in each electron transfer branch of PS I are much closer to the ones in PS II. The intrinsic primary CS rate is ~1.5 ps^{-1} in the A-branch and ~0.8 ps^{-1} in the B-branch. This may imply that the electron transfer rates cannot be substantially faster than about 1 ps^{-1}. This upper limit may be imposed by protein relaxation dynamics (207,208), which has to provide the ultimate free energy difference that drives the energy trapping in the forward direction. It has been discussed earlier (207,208) that without a dynamic energy relaxation of the early RPs, caused by protein relaxation, efficient photosynthetic CS from a unit with a large antenna system would not be possible.

7.3.7 Evolutionary conservation of bi-directionality

These results have major importance for the understanding of the engineering solutions used by Nature for optimizing the ET and trapping in different photosynthetic RCs. It also helps to solve the mystery of why bidirectional CS was maintained in PS I. Although the PS I RC is now heterodimeric, it must have evolved from a homodimeric RC, and in fact the three other members of the type I RC family (Heliobacterial, Chlorobial, and Chloroacidobacterial) are all homodimeric (209-211). It is entirely reasonable to assume that the CS and electron transfer rates between the branches in a purely homodimeric RC would be indistinguishable, and that electron transfer would be perfectly bidirectional. However, if all the rates and SADS were the same, one could never assign branch-specific species. PS I is the one member of the type I RCs that became heterodimeric, presumably after a gene duplication event that gave rise to the *psaA* and *psaB* genes. The subsequent diversification of the PsaA and PsaB polypeptides could have led to an inactivation of one of the branches, as it did in all of the type II RCs. However, it did not – both branches remained active,

although there are quantitative differences between them. Why this should be so has not been obvious, but now we finally have an answer.

The answer has to do with the large core antenna of PS I. The bacterial type II RCs have essentially no core antenna, while that of PS II is ~35 Chls (8). Of the bacterial type I RCs, the heliobacterial RC has 22-35 pigments in its core antenna (212), while the chlorobial RC has ~16 (213). In contrast, the core antenna of PS I contains ~100 Chls, making it the largest by far. The increase in the antenna size tends to decrease the total rate and efficiency of CS and trapping. By keeping both branches active this undesirable effect can be minimized in PS I.

7.3.8 Implications for artificial photosynthetic systems

This knowledge has important consequences also for building artificial photosynthetic units. Using a RC construct with two active branches instead of one, and finally accumulating the charge on a single electron acceptor (F_X cluster in the case of PS I), significantly reduces the required driving force. New artificial photosynthetic systems could benefit from this concept using multi-branch RCs, allowing for an efficient energy trapping even from very large antenna systems using moderate ET rates for each branch. In turn, this also allows for a larger distance between donor and acceptor chromophores, which might be more favorable for artificial systems (214). Such concepts remain to be elucidated in future studies.

7.4 Materials and methods

Preparation of mutant PS I samples: Construction of the PsaA-Y696F and PsaB-Y676F mutants in *C. reinhardtii* has been previously described (138). PS I particles were purified from P71 FuD7 transformants, which lack PS II and have a low LHC content. The protocol used was based upon standard protocols but modified in order to minimize contamination by LHC (*cf.* Section 7.5.1 for details). Neither of the mutations caused any significant influence on the stationary absorption spectra (*cf.* Figure 7.10, Section 7.5).

Ultrafast spectroscopy: Femtosecond transient absorption data were recorded with a home-built camera detection system (149) at room temperature using an excitation wavelength of 700 nm with a narrow bandwidth (*ca.* 9-10 nm) to preferentially excite the RC and thus to enhance the RC signals. The polarization of pump and probe light was set at magic angle and recordings were taken with different time resolution over two times ranges in each case (8 ps and 300 ps ranges). The excitation intensity (pulses with a FWHM of about 70 fs) was kept sufficiently low (~$6x10^{12}$ photon cm^{-2} per pulse) to avoid annihilation. The combination of rotation speed and laser frequency also avoided consecutive double excitation and accumulation of closed RCs (P_{700} oxidized) and other long-lived intermediates (*cf.* Section 7.5 for further details).

Data analysis: Global lifetime analysis was performed employing lifetime density analysis to obtain the LFD maps as described previously (149). Detailed kinetic modeling was performed on the LFD maps with procedures described in detail in the SI.

Simulations: Extensive data analysis using simulated data from bi-branched models with realistic noise added was performed using the same analysis procedures to check the integrity and reliability of the approach (*cf.* SI for further details). These self-consistency checks confirmed that the kinetic modeling procedures are indeed capable of resolving the kinetics in two parallel electron transfer branches and also to extract the appropriate SADS of the intermediates.

7.5 Supporting Information

7.5.1 Materials and Methods

7.5.1.1 Thylakoid Membranes and PS I Complex Purification

A slightly modified version of the method in (215) was used on P71 FuD7 transformants, which lack PS II and have a low starting LHC content. After breaking the cells in a French press, the resulting lysate was spun for 10 minutes at 17000 × g, resuspended with 100 ml of 0.3 M sucrose/5 mM Hepes-KOH (pH 7.5)/10 mM EDTA and spun again for 15 minutes at 80000 × g. After discarding the supernatant, the pellet was very well homogenized using a large glass homogenizer. The homogenate was diluted to 50 ml in 1.8 M sucrose/5 mM Hepes-KOH (pH 7.5)/10 mM EDTA. At this stage, a rapid change of sucrose concentration was used to remove residual LHC, carotenes and xanthophylls. The homogenate was diluted with five times the volume of 5 mM Hepes-KOH (pH 7.5), 10 mM EDTA to reduce the sucrose concentration and spun down at 100000 × g. The resulting supernatant was clear with an orange film near the top. The sucrose shock was repeated twice to ensure complete removal of all contaminating pigments. The resultant pellet was resuspend with 1.8 M sucrose/5 mM Hepes-KOH (pH 7.5)/10 mM EDTA, and homogenized once again. A discontinuous gradient was formed by layering 12 ml of 1.4 M sucrose/5 mM Hepes-KOH (pH 7.5)/10 mM EDTA and then 10 ml 0.8 M sucrose/5 mM Hepes-KOH (pH 7.5)/10 mM EDTA and balancing with 0.5 M sucrose/5 mM Hepes-KOH (pH 7.5)/10 mM EDTA. The gradients were then spun for 3 hours at 12000 × g and the thylakoidmembranes were collected from the interfaces. These were diluted five times with 5 mM Hepes-KOH (pH 7.5), 10 mM EDTA and pelleted at 115000 × g. To obtain PS I particles, the pelleted thylakoid membranes were washed with 5 mM Tricine-KOH (pH 8.0) and then diluted to a final concentration of 0.2 mg/ml Chl in the same buffer. 10% (w/v) β-dodecyl maltoside was added to a final concentration of 0.9%, and solubilization allowed to take place for 30 minutes at 4°C in the dark with mild shaking. This was spun at 38000 × g to pellet any unsolubilized protein, and the cleared supernatant was loaded onto a continuous 0.9-1.7 M sucrose density gradient containing 0.05% β-dodecyl maltoside. The gradients were centrifuged at 170000 × g for 16 h. The lower bands containing the PS I particles were collected and diluted with 3 volumes of 5 mM Tricine-KOH (pH 8.0). The PS I particles were centrifuged at 250000 × g for 3 h, and the pellet was resuspended in the smallest possible volume of buffer.

7.5.1.2 Ultrafast spectroscopy

Femtosecond transient absorption data were recorded with a home-built camera detection system (149). The excitation pulses (70 fs FWHM) were provided by an optical parametric amplifier (TOPAS, Light Conversion, Lithuania) driven by a regenerative amplifier system (Libra, Coherent, USA). The pump and the probe pulses were polarized at magic angle to each other. In all measurements, an excitation wavelength of 700 nm with a narrow bandwidth (ca. 9-10 nm) was used to preferentially excite the RC and thus to enhance the RC signals. The excitation intensity was kept sufficiently low (~$6x10^{12}$ photon cm^{-2} per pulse) to avoid annihilation. All measurements were performed at room temperature using a rotating cuvette that is also periodically shifted horizontally. The conditions were chosen such that on the one hand each laser shot hits a fresh sample volume in which all RCs are in the open state (P_{700} reduced), and on the other, the accumulation of long-lived

intermediates is avoided. The samples were concentrated to an optical density of ~0.7 mm^{-1} in the Q_Y band maximum at 676 nm. The buffer was composed of 25 mM Tricine-NaOH (pH 7.5), 100 mM NaCl and 0.02% n-dodecyl-β-D-maltoside. The medium also contained 40 mM sodium ascorbate and 50 μM phenazine methosulfate as redox agents to keep the RCs open during the measurements (6,52).

7.5.1.3 Data analysis

Global lifetime analysis was performed employing lifetime density analysis to obtain the lifetime density (LFD) maps as described previously (149). Detailed kinetic analysis of the uni-branched model, analogous to the procedure used previously (6,52), can be achieved using straightforward fitting procedures (151). However, the analysis of more complex models like *e.g.* the bi-branched model often fails using conventional data fitting procedures. Typically, for such complex models several different solutions exist that from a mathematical point of view fit the data equally well (216). These solutions would differ *e.g.* in the set of rate constants and SADS. *A priori* they represent multiple mathematical solutions (minima of the cost function) located in different regions of the multi-dimensional data and solution space. Typically, only one of these mathematical solutions represents also a physically correct and meaningful solution. Thus, additional information is required to distinguish between the different mathematical solutions and to select the physically meaningful solution and model. This additional information can be provided by some qualitative knowledge about the studied system, *e.g.* qualitative properties of spectra, without requiring knowledge about their detailed shape, position, or size. This is equivalent to defining a suitable set of qualitative boundary conditions on the solution parameters; for example, the sign of a SADS spectrum at a particular wavelength or a certain wavelength range without knowing its size will be useful. We have previously discussed this problem extensively and have in particular provided qualitative criteria for distinguishing the SADS from Chl excited states from those of Chl RPs (6,52,100), *i.e.* exactly the problem that we are facing here.

Two types of methods are typically suitable to perform optimization under such side constraints: The first one are genetic algorithm based search methods (151,217,218) and the second one are grid optimization methods (219). We chose a grid optimization method since it requires less computing effort in our particular case to find the proper solutions and has the highest probability to actually find the minimum in the solution space. Analyses on simulated data of the complexity of the bi-branched model showed that such procedures are suitable to find the correct solution provided that the data quality (signal-to-noise ratio) is good enough.

The test analyses on simulated data showed that our experimental data quality is indeed high enough to perform successfully such an analysis (rms noise on the ΔA signals of about $1x10^{-5}$ units or less). The problem then boils down to define the suitable qualitative boundary conditions on the SADS. In our analyses of the experimental data the following boundary conditions were set (the qualitative side constraints suitable to distinguish between SADS of excited states and RP states have been discussed excessively before, *vide supra*): First, the signals of the SADS of excited states (ANT* and RC*) had to be negative above 720 nm to reflect the stimulated emission of Chl excited states in this range, and the SADS of RPs had to be positive in that range. Models (rate combinations) that did not fulfill these criteria were already discarded in the first fitting run together with all models that provided poor mathematical fitting. This set of conditions however still provided several different 'solutions'. In a second round, additional selection criteria were added. For example, the SADS of the excited states was required to be positive around 650 nm since this is a typical property of Chl excited

states. In addition, the areas under the different RP spectra should not differ by more than a factor of two. This assumption is not restrictive but helpful for a selection since all of these RPs consist of radical pairs being formed by two Chls which should thus lead to similar bleaching areas. Note that we do not restrict the spectral forms and not even the locations of the maxima in the spectra of neither the excited states nor the RPs; we just formulate some qualitative boundary conditions that these spectra have to obey. These restrictions turned out to be sufficient to extract the physically reasonable solution from the range of mathematical solutions in all cases.

7.5.1.4 Simulations

Various simulations were performed on the bi-branched kinetic analysis to check the integrity of the approach. One of these simulations is accomplished by taking the set of results for SADS and rate constants to simulate the lifetimes (inverse eigenvalues) and wavelength dependent amplitudes (decay-associated absorption difference spectra) and rebuild the transient absorption raw data hyper-surfaces with parameters as extracted from experiment, *e.g.* for the two time ranges and identical noise levels (Figure 7.7). This synthesized raw data set is then forwarded to the same kinetic analysis procedure as the experimental data. Various sets of boundary condition were applied to learn which kinds of boundary conditions are most useful and/or successful for extracting the correct physical solution. One set of such simulated results is shown for a set using parameters of the A-side mutant in Figure 7.11. The results should be compared with the input data for the simulation (*cf.* Figure 7.4 and Figure 7.5B). This self-consistency check confirms that the kinetic modeling is indeed capable of resolving the kinetics in two parallel branches with sufficient accuracy.

7.5.1.5 Calculation of time dependence of free energy differences

We have investigated the dynamics of the free energy difference (ΔG) changes along the time scale of the electron transfer reactions in PS I (Figure 7.9). For the calculation, we have used the rate constants in Figure 7.4. Since the time scale of our experiment does not cover the ns time range, where Q_K^- re-oxidation occurs, we have used in the calculation the rate constants for this process obtained in (138). It is apparent from Figure 7.9 that the total free energy loss for the electron transfer from the RC* state to the F_X is the same for both branches; however, the intermediate electron transfer steps in the two branches are realized with significantly different driving force.

The free energy differences for each electron transfer reaction step can be calculated from the rate constants of the corresponding process using the following equation:

$$\Delta G = k_B T \ln(k_{backward} n_2 / k_{forward} n_1) \tag{7.1}$$

where ΔG is the free energy difference for a particular reaction step, k_B is the Boltzman constant, T is the absolute temperature, $k_{backward}$ is the rate constant for the backward reaction and $k_{forward}$ – for the forward one, n_2 and n_1 is the degeneracy of the corresponding state.

The time-dependent ΔG(t) was calculated using the following formula:

$$\Delta G(t) = \frac{\sum_i \Delta G_i P_i(t)}{\sum_i P_i(t)} \tag{7.2}$$

where ΔG_i is the free energy difference for particular electron transfer reaction step as calculated from the previous equation, and $P_i(t)$ is the population of each state (ANT*, RC*, RP1A *etc.*) at the particular time.

7.6 Supporting figures

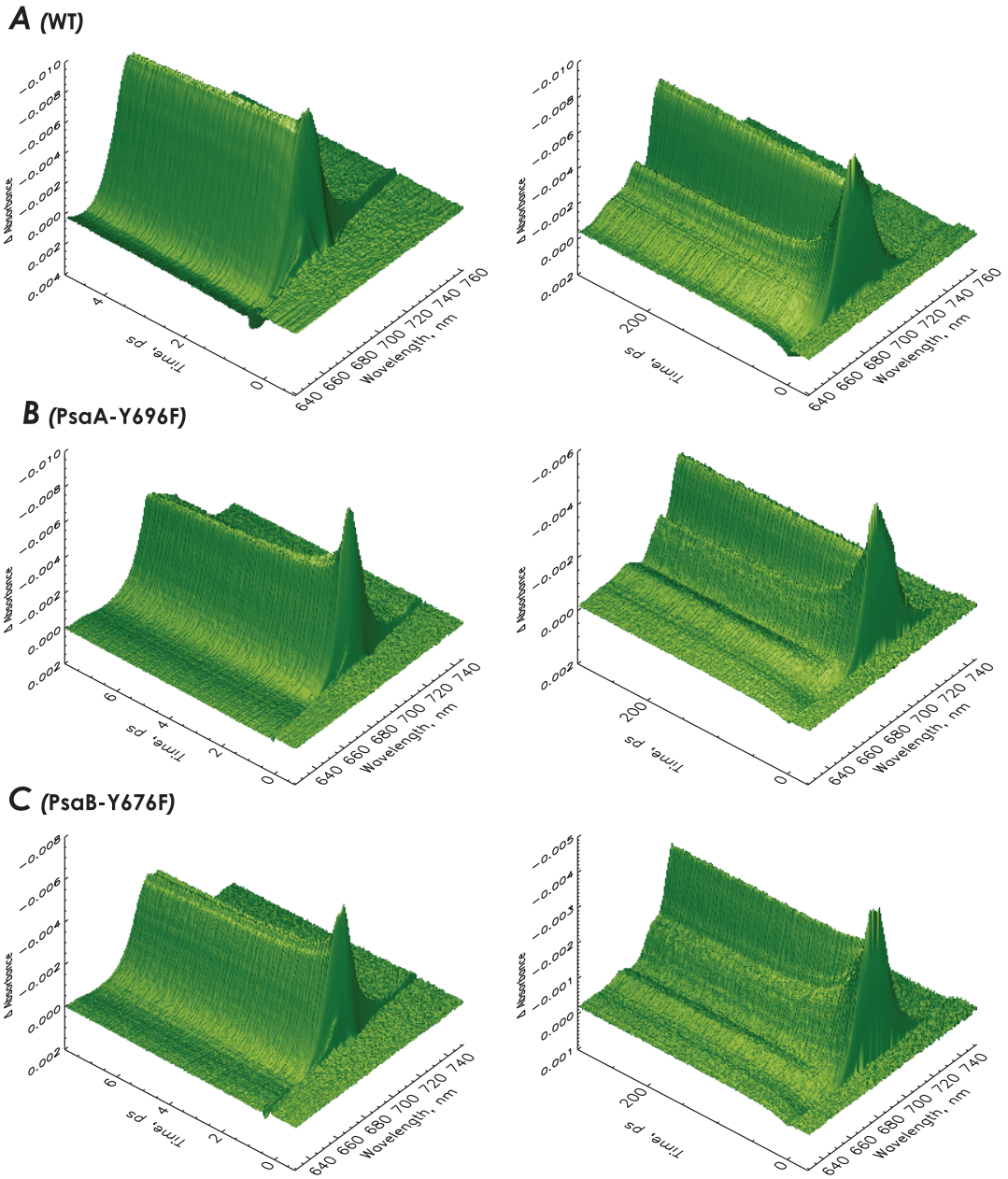

Figure 7.6
Original TA hypersurfaces for the WT (A), PsaA-Y696F (B) and PsaB-Y696F (C) PS I particles after excitation pulse at 700 nm. Two timescales (5-8 ps on the left and 300 ps on the right hand side) are shown, in order to allow visualization of early and late changes. (Note that the absorbance difference scale is inverted for clearer presentation.)

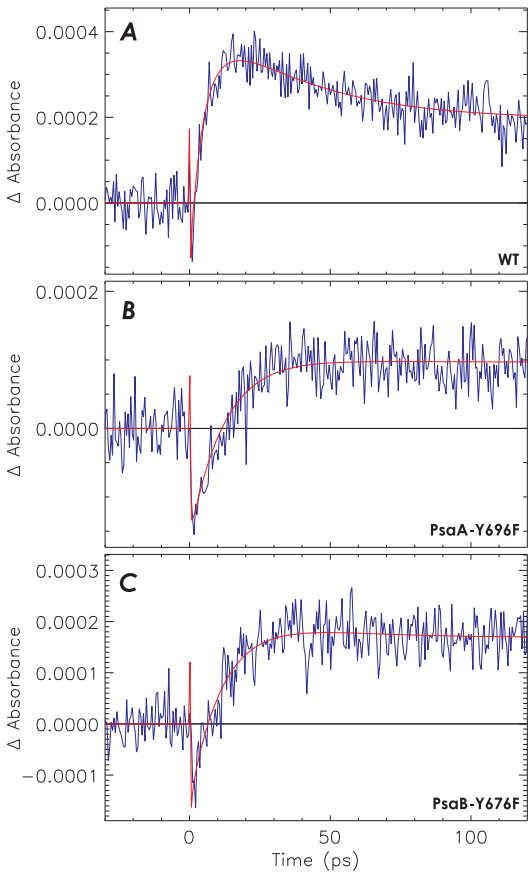

Figure 7.7
Transient absorption decays detected at 730 nm for the WT (A), PsaA-Y696F (B), and PsaB-Y676F (C) PS I particles after excitation at 700 nm. At this wavelength, the decay of the excited state of antenna and RC (giving rise to stimulated emission, *i.e.* a negative signal at time zero) and the subsequent rise of the positive signal due to charge separation forming RPs can be directly monitored.

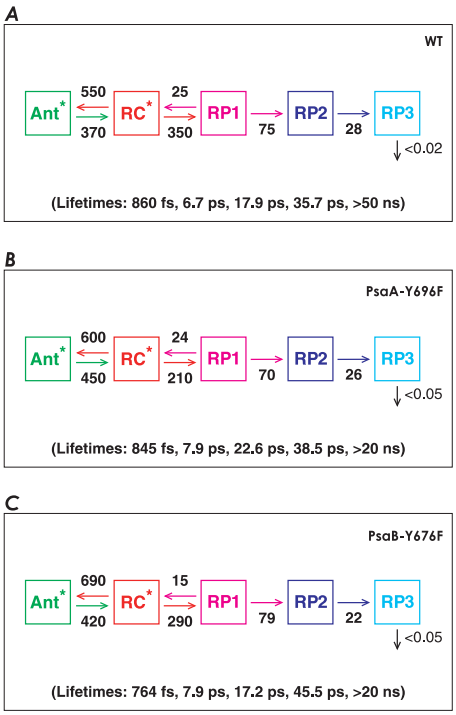

Figure 7.8
Results of the analysis of experimental data using the simple uni-branched kinetic model for WT (A), PsaA-Y696F (B) and PsaB-Y696F (C) PS I.

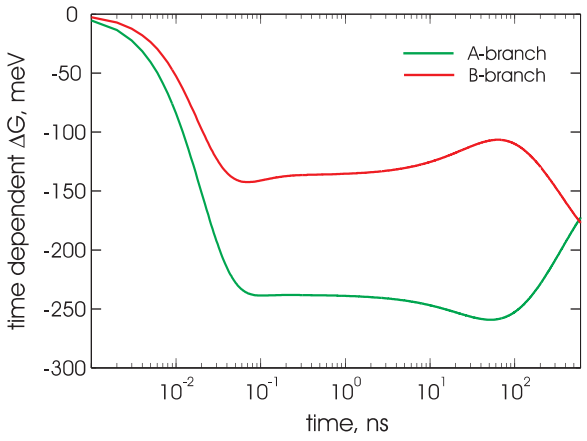

Figure 7.9
Time development of the free energy ΔG for the electron transfer reactions in WT PS I as calculated by F2 (see text).

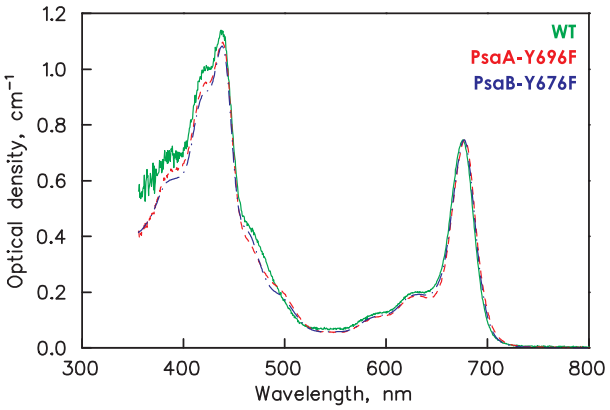

Figure 7.10
Stationary absorption spectra of WT (green), PsaA-Y696F (red) and PsaB-Y696F (blue) PS I particles. No significant differences are seen in the absorption spectra for these preparations in the Q_Y range.

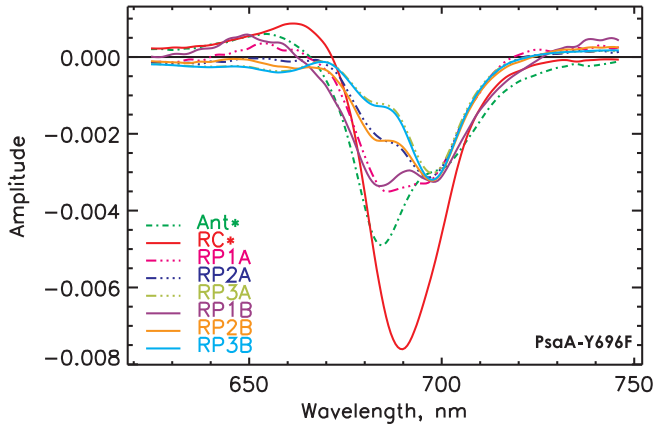

Figure 7.11
Resulting SADS of an analysis of simulated data using the rate constants and SADS of the bi-branched model for the A-side mutant (*cf.* Figure 7.4 and Figure 7.5B). The parameters for the simulation of the test data like *e.g.* noise added to the synthesized data and the amplitudes of the transient absorption signals were kept close to the ones in the real measurements (*cf.* Figure 7.7). This procedure yields insight into the spectral as well as kinetic resolution and accuracy of extracted parameters that can be achieved in the real measurements for this model system. The agreement of rates and lifetimes with the input data was within a 10% error limit, which we consider to be very good.

7.7 Supporting Tables

Table 7-1
Lifetimes and weighted eigenvector matrices for the bi-branched kinetic model and rate data presented in Fig. 4. The weighted eigenvector matrices provide the contribution of the kinetics of each state (ANT*, RC*, $RP1_A$ etc.) to a particular decay lifetime. Note, for simplification the eigenvectors of $RP3_A$ and $RP3_B$ were summed up and represented by RP3.

Lifetimes and the weighted eigenvector matrix for the **WT** PS I

	Excited states		A-branch		B-branch		
τ (ps)	**ANT***	**RC***	**RP1A**	**RP2A**	**RP1B**	**RP2B**	**RP3**
τ_1 0.9	-0.445	0.645	-0.130	0.008	-0.085	0.007	-0.000
τ_2 7.3	0.337	0.143	-0.523	0.344	-0.624	0.459	-0.134
τ_3 10.7	0.078	0.039	-0.527	0.593	0.464	-0.535	-0.112
τ_4 15.8	0.130	0.073	1.180	-2.590	0.245	-0.460	1.424
τ_5 31.3	0.000	0.000	0.000	1.645	0.000	0.000	-1.648
τ_6 62.5	0.000	0.000	0.000	0.000	0.000	0.529	-0.530
τ_7 >20 ns	0.000	0.000	0.000	0.000	0.000	0.000	1.000
exc	***0.1***	***0.9***	***0***	***0***	***0***	***0***	***0***

Lifetimes and the weighted eigenvector matrix for the **PsaA-Y696F** PS I

	Excited states		A-branch		B-branch		
τ (ps)	**ANT***	**RC***	**RP1A**	**RP2A**	**RP1B**	**RP2B**	**RP3**
τ_1 0.9	-0.456	0.557	-0.040	0.002	-0.067	0.005	-0.000
τ_2 8.4	0.201	0.111	-0.162	0.112	-0.695	0.552	-0.119
τ_3 14.0	0.101	0.064	-0.801	1.253	0.299	-0.457	-0.458
τ_4 19.4	0.254	0.169	1.003	-3.248	0.463	-1.138	2.502
τ_5 30.3	0.000	0.000	0.000	1.881	0.000	0.000	-1.884
τ_6 52.6	0.000	0.000	0.000	0.000	0.000	1.039	-1.041
τ_7>20 ns	0.000	0.000	0.000	0.000	0.000	0.000	0.999
exc	***0.1***	***0.9***	***0***	***0***	***0***	***0***	***0***

Lifetimes and the weighted eigenvector matrix for the **PsaB-Y676F** PS I

	Excited states		A-branch		B-branch		
τ (ps)	**ANT***	**RC***	**RP1A**	**RP2A**	**RP1B**	**RP2B**	**RP3**
τ_1 0.8	-0.484	0.623	-0.106	0.006	-0.041	0.003	-0.000
τ_2 8.8	0.281	0.125	-0.655	0.545	-0.667	0.593	-0.221
τ_3 11.2	0.128	0.061	-0.836	0.988	0.511	-0.603	-0.248
τ_4 16.1	0.175	0.091	1.597	-3.552	0.197	-0.365	1.859
τ_5 32.3	0.000	0.000	0.000	2.013	0.000	0.000	-2.017
τ_6 71.4	0.000	0.000	0.000	0.000	0.000	0.372	-0.373
τ_7 >20 ns	0.000	0.000	0.000	0.000	0.000	0.000	1.000
exc	***0.1***	***0.9***	***0***	***0***	***0***	***0***	***0***

Table 7-2
Percentage of electrons transferred through the two branches (errors are in the 10% range)

	A-branch (%)	*B-branch (%)*	*Ratio B/A*
WT	***62***	***38***	***0.62***
PsaA-Y696F	***41***	***59***	***1.4***
PsaB-Y676F	***74***	***26***	***0.35***

Summary

Photosynthesis is the primary process by which energy is fed into the biological world. In its course, complex machinery performs highly effective transformation of light energy. Quite generally, the process consists of two parts: *light-dependent*, including the reactions necessary for the conversion of light into chemical energy (ATP) and reducing power (NADPH), and *carbon-fixation*, where the latter compounds are used to incorporate CO_2 into simple sugars. The major part of the photosynthetic organisms utilizes water as a main electron source in a process called *oxygenic* Photosynthesis.

The significance and complexity of photosynthesis have been a matter of systematic research from the pure molecular mechanisms up to the physiological and even ecological aspects. The results from these studies find extensive application in fields like agronomy and environmental protection. Moreover, in the light of the global warming and the energy crisis faced by humanity, the detailed understanding of photosynthesis becomes crucial not only for the preservation of the vulnerable ecosystems, but also for the prevention of the world economy collapse. In this respect, a large field related to photosynthesis research deals with the design and development of eco-friendly light energy conversion systems mimicking the photosynthetic apparatus.

In order to precisely understand Nature's engineering approaches the working mechanism of each part of the photosynthetic apparatus has to be studied in detail. In this regard, the subject of the current work is one of the main participants in the light-dependent phase of oxygenic photosynthesis, Photosystem I (PS I). This complex carries an immense number of cofactors: chlorophylls (Chl), carotenoids, quinones, *etc*, which together with the protein entity exhibit several exceptional properties. First, PS I has an ultrafast light energy trapping kinetics with a nearly 100% quantum efficiency. Secondly, both of the electron transfer branches in the reaction center are suggested to be active. Thirdly, there are some so called *'red'* Chls in the antenna system of PS I, absorbing light with longer wavelengths than the reaction center. These 'red' Chls significantly modify the trapping kinetics of PS I.

The purpose of this thesis is to obtain better understanding of the above-mentioned, specific features of PS I. This will not merely cast more light on the mechanisms of energy and electron transfer in the complex, but also will contribute to the future developments of optimized artificial light-harvesting systems. In the current work, a number of PS I complexes isolated from different organisms (*Thermosynechococcus elongatus*, *Chlamydomonas reinhardtii*, *Arabidopsis thaliana*) and possessing distinctive features (different macroorganisation – monomers, trimers, monomers with a semibelt of peripheral antenna attached; presence of *'red'* Chls) is investigated. The studies are primarily focused on the electron transfer kinetics in each of the cofactor branches in the PS I reaction center, as well as on the effect of the antenna size and the presence of *'red'* Chls on the trapping kinetics of PS I. These aspects are explored with the help of several ultrafast optical spectroscopy methods: *i)* time-resolved fluorescence – single photon counting and synchroscan streak camera; and *ii)* ultrafast transient absorption. Physically meaningful information about the molecular mechanisms of the energy trapping in PS I is gained with the help of kinetic modeling.

Chapter 1 is a broad background introduction to the major issues in the light energy trapping kinetics (in particular of PS I) that still remain to be elucidated.

Chapter 2 summarizes the main experimental techniques and data analysis strategies used in the current work.

Chapter 3 represents a broad description of one of the methods used here – synchroscan streak camera – for time-resolved detection of fluorescence signals. The chapter covers the main tests that were performed during the installation of the set-up and improvements that were made during this work in order to obtain high quality data with.

Chapter 4 is a thorough investigation of the light energy trapping kinetics in higher plant core and intact PS I particles, and stroma membranes from *A thaliana*. The kinetic analysis of the experimental data confirms the previously proposed 'charge recombination' model for the trapping kinetics in PS I. No bottleneck in the energy flow from the bulk antenna compartments to the reaction center has been found. For both particles, a trap-limited kinetics is realized, with an apparent charge separation lifetime of about 6 ps. No 'red' Chls are found in the PS I-core complex from *A. thaliana*. Rather, the observed 'red'-shifted fluorescence (700-710 nm range) originates from the reaction center. In contrast, two 'red' Chls compartments, located in the peripheral light-harvesting complexes, are resolved in the intact PS I particles (decay lifetimes 33 and 95 ps, respectively). These two 'red' states have been attributed to the two 'red' states found in Lhca 3 and Lhca 4 respectively. The influence of the 'red' Chls on the slowing of the overall trapping kinetics in the intact PS I complex is estimated to be approximately four times larger than the effect of the bulk antenna enlargement.

Chapter 5 is a study of the light energy trapping kinetics in cyanobacterial PS I complexes – monomers and trimers isolated from *T. elongatus*, addressing the same questions as in the previous chapter. It demonstrates the adequacy of the 'charge recombination' model for describing the trapping kinetics. Based on this model the reaction center excited state can be resolved. The overall trapping kinetics in the studied complex is shown to be trap-limited even though the presence of the 'red' Chls induces a substantial slowing down (~60%). Two kinetically different 'red' Chl pools were resolved. Both of these 'red' pools originate from the same groups of pigments in either of the two aggregation states. This indicates that careful separation of the trimers into monomers does not disturb substantially the 'red' Chls and we can thus exclude their location at the monomer-monomer interface. Acceleration of the secondary electron transfer step in the studied complexes as compared to PS I from mesophilic organisms is observed.

Chapter 6 represents a sub-ps time-resolved fluorescence study performed on His-tagged intact PS I core complexes isolated from *C. reinhardtii*. The higher time-resolution of the experimental set-up used (<1 ps) allows indebt investigation of the intra-antenna excitation energy transfer. In order to account for these processes a new, branched model with two sequentially linked antenna compartments in each branch was used. The model successfully describes the experimental data and delivers valuable information about the spectral properties of the different PS I antenna pools. In addition, the data analysis further confirms the previously proposed 'charge recombination' model for the description of the trapping kinetics in PS I.

Chapter 7 deals with the branching of the electron transfer reactions in the RC of PS I. The RC is composed of two cofactor branches related by a pseudo-C_2 symmetry axis. The ultimate electron donor P_{700} (a pair of chlorophylls) and the tertiary acceptor F_X (FeS cluster), are both located on this axis, while each of the two branches is made up of a pair of chlorophylls (ec2 and ec3) and a phylloquinone. Based on the observed biphasic reduction of F_X it has been suggested that both branches in PS I are competent in electron transfer but the nature and rates of the initial electron transfer steps has not been characterized. This part of the current work reports an ultrafast transient

absorption study of *C. reinhardtii* mutants in which specific amino acids forming H-bonds with either $ec3_A$ (PsaA-Y696F) or $ec3_B$ (PsaB-Y676F) are exchanged. The analysis of the experimental data shows that the rate of primary CS is lowered independently in each of the mutant PS I complexes, providing direct evidence that the primary ET is initiated separately and independently in each branch. Furthermore, the data prove that the initial CS events occur within the ec2/ec3 pairs, generating $ec2^+$-$ec3^-$ radical pairs, followed by rapid reduction by P_{700}. The results on this study are of great practical importance since they reveal the solution used by Nature to optimize the light trapping kinetics from large antenna systems.

Zusammenfassung

Die Photosynthese stellt den primären Prozess zur Bereitstellung von Energie für die biologische Welt dar. In ihrem Verlauf wird die Lichtenergie durch komplexe Einheiten hocheffizient umgewandelt. Allgemein ausgedrückt besteht dieser Prozess aus zwei Teilen: dem lichtabhängigen Teil und der Kohlenstofffixierung. Der lichtabhängige Teil umfasst Reaktionen, die zur Umwandlung von Licht in chemische Energie (ATP) und zur Reduktion (NADPH) notwendig sind, während die Kohlenstofffixierung letztgenannte Komponenten zur Verbindung von CO_2 in einfache Zucker verwendet. Der Großteil photosynthetischer Organismen verwendet in diesem als oxygene Photosynthese bezeichneten Prozess hauptsächlich Wasser als Elektronenquelle.

Die Bedeutung und Komplexität der Photosynthese sind Bestandteil systematischer Forschung: beginnend von der Untersuchung der rein molekularen Mechanismen bis hin zur Betrachtung physiologischer und ökologischer Aspekte. Die Ergebnisse dieser Studien finden in Gebieten wie beispielsweise Agronomie und Umweltschutz breite Anwendung. Bezüglich der globalen Erwärmung sowie der Energiekrise, mit der die Menschheit konfrontiert ist, wird weiterhin das tiefere Verständnis der Photosynthese entscheidend sein: einerseits zur Erhaltung der empfindlichen Ökosysteme, andererseits zur Vermeidung eines Zusammenbruchs der Weltwirtschaft. In diesem Zusammenhang beschäftigt sich ein großes Gebiet der Photosyntheseforschung mit der Entwicklung ökologischer Umwandlungssysteme von Lichtenergie zur künstlichen Nachahmung des photosynthetischen Apparates.

Um hierbei die funktionellen Ansätze der Natur genau verstehen zu können, müssen die Mechanismen jedes einzelnen Teils des photosynthetischen Apparates detailliert untersucht werden. In der vorliegenden Arbeit steht das Photosystem I (PS I), das Hauptbestandteil des lichtabhängigen Teils der oxygenen Photosynthese ist, im Mittelpunkt. Dieser Komplex besitzt eine beträchtliche Anzahl an Kofaktoren: Chlorophylle (Chl), Carotenoide, Chinone *etc.*, welche in Verbindung mit der Proteineinheit einige außergewöhnliche Eigenschaften aufweisen. Charakteristisch für das PS I ist erstens eine ultraschnelle Kinetik des Lichteinfangs mit einer Quantenausbeute von nahezu 100%. Zweitens wird vermutet dass beide der Elektronentransferzweige im Reaktionszentrum aktiv sind. Drittens existieren im PS I - Antennensystem einige sogenannte '*rote*' Chls, die bei längeren Wellenlängen als das Reaktionszentrum absorbieren. Diese 'roten' Chls modifizieren die Kinetiken des Lichteinfangs in PS I beträchtlich.

Ziel der vorliegenden Arbeit ist das bessere Verständnis der oben erwähnten, besonderen Eigenschaften des PS I. Diese Untersuchungen werden nicht nur zum besseren Verständnis des Energie- und Elektronentransfers im PS I-Komplex beitragen, sondern auch zur zukünftigen Entwicklung von optimierten Lichtsammelkomplexen. In dieser Arbeit werden eine Reihe von PS I-Komplexen, die aus verschiedenen Organismen (*Thermosynechococcus elongatus*, *Chlamydomonas reinhardtii*, *Arabidopsis thaliana*) isoliert wurden und unterschiedliche Eigenschaften aufweisen (unterschiedliche Makroorganisation – Monomere, Trimere, und Monomere mit einen 'semibelt' von peripheren Antennen; Besitz von 'roten' Chls), untersucht. Der Schwerpunkt liegt auf den Kinetiken des Elektronentransfers in beiden Kofaktorästen im PS I Reaktionszentrum, sowie auf dem Effekt der Antennengrösse und den 'roten' Chls auf die Kinetiken des Lichteinfangs im PS I. Diese Aspekte wurden mittels mehrerer ultraschneller optischer Methoden erforscht: *i)* zeitaufgelöster Fluoreszenz – Single Photon Counting und Synchroscan Streak Kamera und *ii)* ultraschneller transienter

Absorption. Physikalisch bedeutsame Informationen zum molekularen Mechanismus der Energiesammlung im PS I werden mit Hilfe der kinetischen Modellierung gewonnen.

Kapitel 1 liefert eine breitgefächerte Einführung in die Hauptgebiete der Kinetik des Lichteinfangs (insbesondere von PS I), welche noch aufzuklären sind.

Kapitel 2 fasst die experimentellen Techniken und Methoden der Datenanalyse, die in der vorliegenden Arbeit verwendet wurden, zusammen.

Kapitel 3 beschreibt detailliert eine der in der vorliegenden Arbeit verwendeten Methode zur zeitaufgelösten Detektion von Fluoreszenzsignalen: die Synchroscan Streak-Kamera. In diesem Kapitel werden sowohl die Tests, die während des Aufbaus dieses Systems durchgeführt wurden, als auch die Verbesserungen, die im Rahmen dieser Arbeit zur Erzielung qualitativ hochwertiger Daten realisiert wurden, beschrieben.

In Kapitel 4 wird die Lichteinfangkinetik von Kernkomplexen und intakten PS I - Komplexen sowie der Stroma-Membran von *A. thaliana* detailliert untersucht. Die kinetische Analyse der experimentellen Daten bestätigt das zuvor vorgeschlagene 'Ladungsrekombinations'-Modell für die Einfangkinetik von PS I. Im Energiefluss von den Antenneneinheiten zum Reaktionszentrum wurde kein Engpass beobachtet. In beiden Komplexen liegt eine 'trap'-limitierte Kinetik mit einer Ladungstrennungslebensdauer von etwa 6 ps vor. Im PS I-Kernkomplex von *A. thaliana* wurden keine 'roten' Chls gefunden. Vielmehr stammt die beobachtete rotverschobene Fluoreszenz (700-710 nm Bereich) aus dem Reaktionszentrum. Im Gegensatz hierzu wurden in den intakten PS I - Teilchen zwei 'rote' Chl - Einheiten, die in den peripheren Lichtsammelkomplexen lokalisiert sind, aufgelöst (mit Zerfallslebensdauern von 33 bzw. 95 ps). Diese zwei 'roten' Zustände wurden zurückgeführt auf die zwei in Lhca 3 bzw. Lhca 4 gefundenen 'roten' Zustände. Der Einfluss der 'roten' Chls auf die Verlangsamung der Gesamt-Einfangkinetik im intakten PS I-Komplex ist schätzungsweise viermal größer als der Effekt der Antennenvergrößerung.

Kapitel 5 stellt eine Studie über die Lichteinfangkinetik in cyanobakteriellen PS I-Komplexen dar: betrachtet werden aus *T. elongatus* isolierte Monomere sowie Trimere, wobei hierbei denselben Fragestellungen wie im vorherigen Kapitel nachgegangen wird. Es wird gezeigt, dass das "Ladungsrekombinations"-Modell zur Beschreibung der Einfangkinetiken gültig ist. Auf der Grundlage dieses Modells konnte der angeregte Zustand des Reaktionszentrums aufgelöst werden. Es wird gezeigt, dass die Gesamt-Einfangkinetik im untersuchten Komplex trap-limitiert ist, obwohl die Gegenwart der 'roten' Chls eine beträchtliche Verlangsamung (~60%) verursachen. Zwei sich kinetisch unterscheidende 'rote' Chl-Einheiten wurden aufgelöst. Beide dieser 'roten' Einheiten stammen von derselben Pigmentgruppe in einem der zwei Aggregationszuständen. Dies zeigt, dass die 'roten' Chls durch eine sorgfältige Trennung der Trimere in Monomere nicht beträchtlich beeinflusst werden. Weiterhin kann ihre Position an der Monomer-Monomer Schnittstelle ausgeschlossen werden. In den untersuchten Komplexen wurde ein im Vergleich zu mesophilen PS I - Organismen beschleunigter sekundärer Elektronentransferschritt beobachtet.

Kapitel 6 stellt eine subpikosekunden zeitaufgelöste Fluoreszenzstudie an intakten 'his-tagged' PS I-Kernkomplexen, isoliert aus *C. reinhardtii,* dar. Die höhere Zeitauflösung des verwendeten experimentellen Aufbaus (<1 ps) gegenüber früheren Studien ermöglicht die Untersuchung der Anregungsenergieübertragung innerhalb der Antenne. Um diese Prozesse zu berücksichtigen, wurde ein neues verzweigtes Modell mit zwei sequentiell verbundenen Antenneneinheiten in jedem Zweig verwendet. Das Modell beschreibt erfolgreich die experimentellen Daten und liefert wertvolle Informationen über die spektralen Eigenschaften der unterschiedlichen PS I -

Kernantenneneinheiten. Außerdem bestätigt die Datenanalyse weiterhin das zuvor vorgeschlagene 'Ladungsrekombinations'-Modell zur Beschreibung der Kinetiken des Lichteinfangs in PS I.

Kapitel 7 behandelt die Verzweigung der Elektronentransferreaktionen im PS I - Reaktionszentrum. Das Reaktionszentrum ist aus zwei Kofaktorzweigen zusammengesetzt, die über eine Pseudo-C_2-Symmetrieachse miteinander in Verbindung stehen. Der endgültige Elektronendonor P_{700} (ein Chlorophyll-Paar) und der tertiäre Akzeptor F_X (FeS-Cluster) befinden sich beide auf dieser Achse, während jeder der zwei Zweige aus einem Chlorophyll-Paar (ec2 und ec3) sowie einem Phyllochinon besteht. Basierend auf der Grundlage der beobachteten zweiphasigen Reduktion von F_X wurde vorgeschlagen, dass beide Zweige in PS I zur Elektronenübertragung fähig sind, wobei die Natur und die Raten der ersten Elektronentransferschritte noch nicht charakterisiert worden sind. Dieser Teil der vorliegenden Arbeit stellt eine Ultrakurzzeit-Absorptionsstudie an PS I von *C. reinhardtii* Mutanten vor, in denen spezifische Aminosäuren, die entweder mit $ec3_A$ (PsaA-Y696F) oder $ec3_B$ (PsaB-Y676F) Wasserstoffbrücken eingehen, vertauscht sind. Die Analyse der experimentellen Daten zeigt, dass die Rate der primären Ladungstrennung unabhängig voneinander in jedem der mutierten PS I Komplexen verringert wird. Dies liefert den direkten Beweis dafür, dass der primäre Elektronentransfer separat und unabhängig voneinander in jedem Zweig initiiert wird. Weiterhin bestätigen die Daten, dass die ersten Ladungstrennungsschritte innerhalb der ec2/ec3 Paare auftreten. Diese bilden $ec2^+$ $ec3^-$ Radikalpaare gefolgt von einer schnellen Reduktion von $ec2^+$ durch P_{700}. Die Ergebnisse dieser Studie sind von großer praktischer Bedeutung, da sie die von der Natur in großen Antennensystemen realisierte Lichteinfangkinetiken verdeutlichen.

References

1. Szczepaniak M, Sander J, Nowaczyk M, Müller MG, Rögner M, Holzwarth AR (2008) Charge separation, stabilization, and protein relaxation in photosystem II core particles with closed reaction center. *Biophys.J.* **96**: 621-31.

2. Fromme P. Photosynthetic protein complexes A structural approach. 1, XXVI-360. 2008. Weinheim, Wiley-VCH.

3. Hanley J, Deligiannakis Y, Pascal A, Faller P, Rutherford AW (1999) Carotenoid oxidation in photosystem II. *Biochemistry* **38**: 8189-95.

4. Prokhorenko VI, Holzwarth AR (2000) Primary processes and structure of the photosystem II reaction center: A photon echo study. *J.Phys.Chem.B* **104**: 11563-78.

5. Diner BA, Schlodder E, Nixon PJ *et al.* (2001) Site-directed mutations at D1-His198 and D2-His 197 of photosystem II in *Synechocystis* PCC 6803: Sites of primary charge separation and cation and triplet stabilization. *Biochemistry* **40**: 9265-81.

6. Holzwarth AR, Müller MG, Niklas J, Lubitz W (2006) Ultrafast transient absorption studies on photosystem I reaction centers from *Chlamydomonas reinhardtii.* 2. Mutations around the P700 reaction center chlorophylls provide new insight into the nature of the primary electron donor. *Biophys.J.* **90**: 552-65.

7. Hill R, Bendall F (1960) Function of the two cytochrome components in chloroplasts: A working hypothesis. *Nature* **186**: 136-7.

8. Loll B, Kern J, Saenger W, Zouni A, Biesiadka J (2005) Towards complete cofactor arrangement in the 3.0 angstrom resolution structure of photosystem II. *Nature* **438**: 1040-4.

9. Kurisu G, Zhang HM, Smith JL, Cramer WA (2003) Structure of the cytochrome b(6)f complex of oxygenic photosynthesis: Tuning the cavity. *Science* **302**: 1009-14.

10. Stroebel D, Choquet Y, Popot J-L, Picot D (2003) An atypical haem in the cytochrome b_6f complex. *Nature* **426**: 413-8.

11. Redinbo MR, Cascio D, Choukair MK, Rice D, Merchant S, Yeates TO (1993) The 1.5-.ANG. crystal structure of plastocyanin from the green alga *Chlamydomonas reinhardtii. Biochemistry* **32**: 10560-7.

12. Kerfeld CA, Anwar HP, Interrante R, Merchant S, Yeates TO (1995) The structure of chloroplast cytochrome *c6* at 1.9 Å resolution: Evidence for functional oligomerization. *J.Mol.Biol.* **250**: 627-47.

13. Morales R, Charon MH, Hudry-Clergeon G *et al.* (1999) Refined X-ray structures of the oxidized, at 1.3 Å, and reduced, at 1.17 Å, [2Fe-2S] ferredoxin from the cyanobacterium *Anabaena* PCC7119 show redox-linked conformational changes. *Biochemistry* **38**: 15764-73.

14. Bruns CM, Karplus AP (1995) Refined crystal structure of spinach ferredoxin reductase at 1.7 Å resolution: Oxidized, reduced and 2'-Phospho-5'-AMP bound states. *J.Mol.Biol.* **247**: 125-45.

15. Carrilo N, Ceccarelli EA (2003) Open questions in ferredoxin-$NADP^+$ reductase catalytic mechanism. *Eur.J.Biochem.* **270**: 1900-15.

16. Blankenship RE Molecular mechanisms in photosynthesis. 1-321. 2002. Blackwell Publishing.

17. Boyer PD (1975) A model for conformational coupling of membrane potential and proton translocation to ATP synthesis and to active transport. *FEBS Lett.* **58**: 1-6.

18. Boyer PD (1999) Molecular motors: What makes ATP synthase spin? *Nature* **402**: 247-9.

19. Mitchell P, Moyle J (1967) Chemiosmotic hypothesis of oxidative phosphorylation. *Nature* **14**: 137-9.

20. Gouterman M (1961) Spectra of porphyrins. *Journal of Molecular Spectroscopy* **6**: 138-63.

21. Sundholm D (2000) Comparison of the electronic excitation spectra of chlorophyll a and pheophytin a calculated at density functional theory level. *Chem.Phys.Lett.* **317**: 545-52.

22. Parusel ABJ, Grimme S (2000) A theoretical study of the excited states of chlorophyll *a* and pheophytin *a. J.Phys.Chem.B* **104**: 5395-8.

23. Cogdell RJ, Frank HA (1987) How carotenoids function in photosynthetic bacteria. *Biochim.Biophys.Acta* **895**: 63-79.

24. Frank HA, Cogdell RJ (1993) Photochemistry and functions of carotenoids in photosynthesis. In: Young A, Britton G, eds. *Carotenoids in Photosynthesis.* London: Springer-Verlag, pp. 252-326.

25. Frank HA . The photochemistry of carotenoids. [8], 1-399. 1999. Dordrecht, Kluver Academic Publishers. Advances in Photosynthesis. Frank, H. A., Young, A. J., Britton, G., and Cogdell, B. J.

26. Niyogi KK (1999) Photoprotection revisited: Genetic and molecular approaches. *Annu.Rev.Plant Physiol.Plant Mol.Biol.* **50**: 333-59.

27. Plumley FG, Schmidt GW (1987) Reconstitution of chloroform *a/b* light-harvesting complexes: Xanthophyll-dependent assembly and energy transfer. *Proc.Natl.Acad.Sci.USA* **84**: 146-50.

28. Paulsen H, Finkenzeller B, Kühlein N (1993) Pigments induce folding of light-harvesting chlorophyll *a/b*-binding protein. *Eur.J.Biochem.* **215**: 809-16.

29. van Amerongen H, Valkunas L, van Grondelle R (2000) *Photosynthetic Excitons*. Singapore: World Scientific, p 1.

30. Krawczyk S (1989) The effects of hydrogen bonding and coordination interaction in visible absorption and vibrational spectra of chlorophyll *a*. *Biochim.Biophys.Acta* **976**: 140-9.

31. Förster T (1965) 1. Delocalized excitation and excitation transfer. In: Sinanoglu O, ed. *Modern Quantum Chemistry. Part III Action of Light and Organic Crystals*. New York: Academic Press, pp. 93-137.

32. Dexter DL (1953) A theory of sensitized luminescence in solids. *J.Chem.Phys.* **21**: 836-50.

33. Renger T, Holzwarth AR (2008) Theory of excitation energy transfer and optical spectra of photosynthetic systems. In: Aartsma TJ, Matysik J, eds. *Biophysical Techniques in Photosynthesis*. Dordrecht: Springer, pp. 421-443.

34. Marcus RA, Sutin N (1985) Electron transfer in chemistry and biology. *Biochim.Biophys.Acta* **811**: 265-322.

35. Hoff AJ, Deisenhofer J (1997) Photophysics of photosynthesis. Structure and spectroscopy of reaction centers of purple bacteria. *Phys.Reports* **287**: 1-247.

36. Moser CC, Keske JM, Warncke K, Farid RS, Dutton PL (1992) Nature of Biological Electron Transfer. *Nature* **355**: 796-802.

37. Moser CC, Page CC, Farid R, Dutton PL (1995) Biological electron transfer. *J.Bioenerg.Biomemb.* **27**: 263-74.

38. Moser CC, Page CC, Dutton PL (2005) Tunneling in PSII. *Photochem.Photobiol.Sci.* **4**: 933-9.

39. Jordan P . Röntgenstrukturanalyse des trimeren Photosystems I aus dem Cyanobakterium *Synechococcus elongatus* bei 2,5A Auflösung. 1-230. 2001. Freie Universität Berlin. Thesis/Dissertation

40. Amunts A, Drory O, Nelson N (2007) The structure of a plant photosystem I supercomplex at 3.4 Å resolution. *Nature* **447**: 58-63.

41. Jordan P, Fromme P, Witt HT, Klukas O, Saenger W, Krauβ N (2001) Three-dimensional structure of cyanobacterial photosystem I at 2.5Å resolution. *Nature* **411**: 909-17.

42. Boekema EJ, Dekker JP, van Heel MG *et al.* (1987) Evidence for a trimeric organization of the photosystem I complex from the thermophilic cyanobacterium Synechococcus sp. *FEBS Lett.* **217**: 283-6.

43. Rögner M, Mühlenhoff U, Boekema EJ, Witt HT (1990) Mono-,di- and trimeric PS I reaction center complexes isolated from the termophilic cyanobacterium Synechococcus sp. Size, shape and activity. *Biochim.Biophys.Acta* **1015**: 415-24.

44. Sun J, Xu W, Hervas M, Navarro JK, De la Rosa MA, Chitnis PR (1999) Oxidizing side of the cyanobacterial photosystem I - Evidence for interaction between the electron donor proteins and a luminal surface helix of the PsaB subunit. *J.Biol.Chem.* **274**: 19048-54.

45. Nield J, Morris EP, Bibby TS, Barber J (2003) Structural analysis of the photosystem I supercomplex of cyanobacteria induced by iron deficiency. *Biochemistry* **42**: 3180-8.

46. Krabben L, Schlodder E, Jordan R *et al.* (2000) Influence of the axial ligands on the spectral properties of P700 of photosystem I: A study of site-directed mutants. *Biochemistry* **39**: 13012-25.

47. Brettel K (1997) Electron transfer and arrangement of the redox cofactors in photosystem I. *Biochim.Biophys.Acta* **1318**: 322-73.

48. Beddard GS (1998) Excitations and excitons in photosystem I. *Phil.Trans.R.Soc.Lond.A* **356**: 421-48.

49. Yang M, Damjanovic A, Vaswani HM, Fleming GR (2003) Energy transfer in photosystem I of cyanobacteria Synechococcus elongatus: Model study with structure-based semi-empirical Hamiltonian and experimental spectral density. *Biophys.J.* **85**: 140-58.

50. Croce R, Zucchelli G, Garlaschi FM, Bassi R, Jennings RC (1996) Excited state equilibration in the photosystem I -light - harvesting I complex: P700 is almost isoenergetic with its antenna. *Biochemistry* **35**: 8572-9.

51. Gibasiewicz K, Ramesh VM, Melkozernov AN *et al.* (2001) Excitation dynamics in the core antenna of PS I from *Chlamydomonas reinhardtii* CC 2696 at room temperature. *J.Phys.Chem.B* **105**: 11498-506.

52. Müller MG, Niklas J, Lubitz W, Holzwarth AR (2003) Ultrafast transient absorption studies on photosystem I reaction centers from *Chlamydomonas reinhardtii*. 1. A new interpretation of the energy trapping and early electron transfer steps in photosystem I. *Biophys.J.* **85**: 3899-922.

53. Gibasiewicz K, Ramesh VM, Lin S, Redding K, Woodbury NW, Webber AN (2003) Excitonic interactions in wild-type and mutant PSI reaction centers. *Biophys.J.* **85**: 2547-59.

54. Stewart DH, Cua A, Bocian DF, Brudvig GW (1999) Selective raman scattering from the core chlorophylls in photosystem I via preresonant near-infrared excitation. *J.Phys.Chem.B* **103**: 3758-64.

55. Gibasiewicz K, Ramesh VM, Lin S, Woodbury NW, Webber AN (2002) Excitation dynamics in Eukaryotic PS I from *Chlamydomonas reinhardtii* CC 2696 at 10 K. Direct detection of the reaction center exciton states. *J.Phys.Chem.B* **106**: 6322-30.

56. O'Malley PJ (1999) Density functional calculated spin densities and hyperfine couplings for hydrogen bonded 1,4-naphthosemiquinone and phyllosemiquinone anion radicals: A model for the A1 free radical formed in photosystem I. *Biochim.Biophys.Acta* **1411**: 101-13.

57. Kaupp M (2002) The function of photosystem I. Quantum chemical insight into the role of tryptophan-quinone interactions. *Biochemistry* **41**: 2895-900.

58. Brettel K, Leibl W (2001) Electron transfer in photosystem I. *Biochim.Biophys.Acta* **1507**: 100-14.

59. Byrdin M, Jordan P, Krauss N, Fromme P, Stehlik D, Schlodder E (2002) Light harvesting in photosystem I: Modeling based on the 2.5Å-structure of photosystem I from *Synechococcus elongatus*. *Biophys.J.* **83**: 433-57.

60. Sener MK, Park S, Lu DY *et al.* (2004) Excitation migration in trimeric cyanobacterial photosystem I. *J.Chem.Phys.* **120**: 11183-95.

61. Karapetyan NV, Schlodder E, van Grondelle R, Dekker JP (2006) The long-wavelength chlorophylls of photosystem I. In: Golbeck JH, ed. *Photosystem I: The Light-Driven, Plastocyanin:Ferredoxin Oxydoreductase.*Blackwell Publishers, pp. 177-192.

62. Schlodder E, Shubin VV, El-Mohsnawy E, Roegner M, Karapetyan NV (2007) Steady-state and transient polarized absorption spectroscopy of photosystem I complexes from the cyanobacteria *Arthrospira platensis* and *Thermosynechococcus elongatus*. *Biochim.Biophys.Acta* **1767**: 732-41.

63. Gobets B, van Amerongen H, Monshouwer R *et al.* (1994) Polarized site-selected fluorescence spectroscopy of isolated Photosystem I particles. *Biochim.Biophys.Acta* **1188**: 75-85.

64. Zazubovich V, Matsuzaki S, Johnson TW, Hayes JM, Chitnis PR, Small GJ (2002) Red antenna states of photosystem I from cyanobacterium Synechococcus elongatus: a spectral hole burning study. *Chem.Phys.* **275**: 47-59.

65. Palsson L-O, Dekker JP, Schlodder E, Monshouwer R, van Grondelle R (1996) Polarized site-selective fluorescence spetroscopy of the long- wavelength emitting chlorophylls in isolated photosystem I particles of *Synechococcus elongatus*. *Photosynth.Res.* **48**: 239-46.

66. Rätsep M, Johnson TW, Chitnis PR, Small GJ (2000) The red-absorbing chlorophyll a antenna states of photosystem I: A hole-burning study of Synechocystis sp PCC 6803 and its mutants. *J.Phys.Chem.B* **104**: 836-47.

67. Jelezko F, Tietz C, Gerken U, Wrachtrup J, Bittl R (2000) Single-molecule spectroscopy on photosystem I pigment-protein complexes. *J.Phys.Chem.B* **104**: 8093-6.

68. Ihalainen JA, Rätsep M, Jensen PE *et al.* (2003) Red spectral forms of chlorophylls in green plant PSI - a site-selective and high-pressure spectroscopy study. *J.Phys.Chem.B* **107**: 9086-93.

69. Damjanovic A, Vaswani H, Fromme P, Fleming GR (2002) Chlorophyll excitations in photosystem I of *Synechococcus elongatus*. *J.Phys.Chem.B* **106**: 10251-62.

70. Melkozernov AN, Lin S, Blankenship RE (2000) Excitation dynamics and heterogeneity of energy equilibration in the core antenna of photosystem I from the cyanobacterium *Synechocystis sp.* PCC 6803. *Biochemistry* **39**: 1489-98.

71. Vaitekonis S, Trinkunas G, Valkunas L (2005) Red chlorophylls in the exciton model of photosystem I. *Photosynth.Res.* **86**: 185-201.

72. Vaswani HM, Stenger J, Fromme P, Fleming GR (2006) One- and two-color photon echo peak shift studies of photosystem I. *J.Phys.Chem.B* **110**: 26303-12.

73. Melkozernov AN, Lin S, Blankenship RE (2000) Femtosecond transient spectroscopy and excitonic interactions in Photosystem I. *J.Phys.Chem.B* **104**: 1651-6.

74. Palsson L-O, Flemming C, Gobets B, van Grondelle R, Dekker JP, Schlodder E (1998) Energy transfer and charge separation in photosystem I P700 oxidation upon selective excitation of the long-wavelength antenna chlorophylls of *Synechococcus elongatus*. *Biophys.J.* **74**: 2611-22.

75. Byrdin M, Rimke I, Schlodder E, Stehlik D, Roelofs TA (2000) Decay kinetics and quantum yields of fluorescence in photosystem I from Synechococcus elongatus with P700 in the reduced and oxidized state: Are the kinetics of excited state decay trap-limited or transfer-limited? *Biophys.J.* **79**: 992-1007.

76. Gobets B, van Stokkum IHM, Rögner M *et al.* (2001) Time-resolved fluorescence emission measurements of photosystem I particles of various cyanobacteria: A unified compartmental model. *Biophys.J.* **81**: 407-24.

77. Brecht M, Studier H, Elli AF, Jelezko F, Bittl R (2007) Assignment of red antenna states in photosystem I from *Thermosynechococcus elongatus* by single-molecule spectroscopy. *Biochemistry* **46**: 799-806.

78. Fromme P, Jordan P, Krauβ N (2001) Structure of photosystem I. Review. *Biochim.Biophys.Acta* **1507**: 5-31.

79. Sener MK, Lu DY, Ritz T, Park S, Fromme P, Schulten K (2002) Robustness and optimality of light harvesting in cyanobacterial photosystem I. *J.Phys.Chem.B* **106**: 7948-60.

80. Kouril R, van Oosterwijk N, Yakushevska AE, Boekema EJ (2005) Photosystem I: a search for green plant trimers. *Photochem.Photobiol.Sci.* **4**: 1091-4.

81. Wollman F-A, Minai L, Nechushtai R (1999) The biogenesis and assembly of photosynthetic proteins in thylakoid membranes. *Biochim.Biophys.Acta* **1411**: 21-85.

82. Kargul J, Turkina MV, Nield J, Benson S, Vener AV, Barber J (2005) Light-harvesting complex II protein CP29 binds to photosystem I of *Chlamydomonas reinhardtii* under State 2 conditions. *Febs Journal* **272**: 4797-806.

83. Dekker JP, Boekema EJ (2005) Supramolecular organization of thylakoid membrane proteins in green plants. *Biochim.Biophys.Acta* **1706**: 12-39.

84. Jolley C, Ben-Shem A, Nelson N, Fromme P (2005) Structure of plant photosystem I revealed by theoretical modeling. *J.Biol.Chem.* **280**: 33627-36.

85. Lunde C, Jensen PE, Haldrup A, Knoetzel J, Scheller HV (2000) The PSI-H subunit of photosystem I is essential for state transitions in plant photosynthesis. *Nature* **408**: 613-5.

86. Hippler M, Drepper F, Haehnel W, Rochaix J-D (1998) The N-terminal domain of PsaF: Precise recognition site for binding and fast electron transfer from cytochrome c(6) and plastocyanin to photosystem I of Chlamydomonas reinhardtii. *Proc.Natl.Acad.Sci.USA* **95**: 7339-44.

87. Morosinotto T, Breton J, Bassi R, Croce R (2003) The nature of a chlorophyll ligand in Lhca proteins determines the far red fluorescence emission typical of photosystem I. *J.Biol.Chem.* **278**: 49223-9.

88. Morosinotto T, Castelletti S, Breton J, Bassi R, Croce R (2002) Mutation analysis of Lhca1 antenna complex - Low energy absorption forms originate from pigment-pigment interactions. *J.Biol.Chem.* **277**: 36253-61.

89. Croce R, Morosinotto T, Ihalainen JA *et al.* (2004) Origin of the 701-nm fluorescence emission of the Lhca2 subunit of higher plant photosystem I. *J.Biol.Chem.* **279**: 48543-9.

90. Morosinotto T, Mozzo M, Bassi R, Croce R (2005) Pigment-pigment interactions in Lhca4 antenna complex of higher plants photosystem I. *J.Biol.Chem.* **280**: 20612-9.

91. Mozzo M, Morosinotto T, Bassi R, Croce R (2006) Probing the structure of Lhca3 by mutation analysis. *Biochim.Biophys.Acta* **1757**: 1607-13.

92. Kühlbrandt W, Wang DN, Fujiyoshi Y (1994) Atomic model of plant light-harvesting complex by electron crystallography. *Nature* **367**: 614-21.

93. Standfuss J, van Scheltinga ACT, Lamborghini M, Kühlbrandt W (2005) Mechanisms of photoprotection and nonphotochemical quenching in pea light-harvesting complex at 2.5Å resolution. *EMBO J.* **24**: 919-28.

94. Liu Z, Yan H, Wang K *et al.* (2004) Crystal structure of spinach major light-harvesting complex at 2.72 angstrom resolution. *Nature* **428**: 287-92.

95. Jensen PE, Bassi R, Boekema EJ *et al.* (2007) Structure, function and regulation of plant photosystem I. *Biochimica.Biophysica.Acta. - Bioenergetics* **1767**: 335-52.

96. Morosinotto T, Ballottari M, Klimmek F, Jansson S, Bassi R (2005) The association of the antenna system to photosystem I in higher plants. *J.Biol.Chem.* **280**: 31050-8.

97. van Grondelle R, Gobets B (2004) Transfer and trapping of excitations in plant photosystems. In: Papageorgiou GC, Govindjee, eds. *Chlorophyll a Fluorescence: A Signature of Photosynthesis*. Dordrecht: Springer, pp. 107-132.

98. Holzwarth AR (2004) Light absorption and harvesting. In: Archer MD, Barber J, eds. *Molecular to Global Photosynthesis*. London: Imperial College Press, pp. 43-115.

99. Kennis JTM, Gobets B, van Stokkum IHM, Dekker JP, van Grondelle R, Fleming GR (2001) Light harvesting by chlorophylls and carotenoids in the photosystem I core complex of *Synechococcus elongatus:* A fluorescence upconversion study. *J.Phys.Chem.B* **105**: 4485-94.

100. Holzwarth AR, Müller MG, Reus M, Nowaczyk M, Sander J, Rögner M (2006) Kinetics and mechanism of electron transfer in intact photosystem II and in the isolated reaction center: Pheophytin is the primary electron acceptor. *Proc.Natl.Acad.Sci.USA* **103**: 6895-900.

101. Slavov C, Ballottari M, Morosinotto T, Bassi R, Holzwarth AR (2008) Trap-limited charge separation kinetics in higher plant photosystem I complexes . *Biophys.J.* **94**: 3601-12.

102. Dekker JP, van Grondelle R (2000) Primary charge separation in Photosystem II. *Photosynth.Res.* **63**: 195-208.

103. Vassiliev S, Lee C-I, Brudvig GW, Bruce D (2002) Structure-based kinetic modeling of excited-state transfer and trapping in histidine-tagged photosystem II core complexes from *Synechocystis*. *Biochemistry* **41**: 12236-43.

104. Ihalainen JA, van Stokkum IHM, Gibasiewicz K, Germano M, van Grondelle R, Dekker JP (2005) Kinetics of excitation trapping in intact photosystem I of *Chlamydomonas reinhardtii* and *Arabidopsis thaliana*. *Biochim.Biophys.Acta* **1706**: 267-75.

105. Pawlowicz NP, Groot ML, van Stokkum IHM, Breton J, van Grondelle R (2007) Charge separation and energy transfer in the photosystem II core complex studied by femtosecond midinfrared spectroscopy. *Biophys.J.* **93**: 2732-42.

106. Schatz GH, Brock H, Holzwarth AR (1988) A kinetic and energetic model for the primary processes in photosystem II. *Biophys.J.* **54**: 397-405.

107. Croce R, Dorra D, Holzwarth AR, Jennings RC (2000) Fluorescence decay and spectral evolution in intact photosystem I of higher plants. *Biochemistry* **39**: 6341-8.

108. Gobets B, van Grondelle R (2001) Energy transfer and trapping in photosystem I. *Biochim.Biophys.Acta* **1507**: 80-99.

109. Gobets B, van Stokkum IHM, van Mourik F, Dekker JP, van Grondelle R (2003) Excitation wavelength dependence of the fluorescence kinetics in Photosystem I particles from Synechocystis PCC 6803 and Synechococcus elongatus. *Biophys.J.* **85**: 3883-98.

110. Engelmann E, Zucchelli G, Casazza AP, Brogioli D, Garlaschi FM, Jennings RC (2006) Influence of the photosystem I - Light harvesting complex I antenna domains on fluorescence decay. *Biochemistry* **45**: 6947-55.

111. Savikhin S, Xu W, Martinsson P, Chitnis PR, Struve WS (2001) Kinetics of charge separation and A_0^- -> A_1 electron transfer in photosystem I reaction centers. *Biochemistry* **40**: 9282-90.

112. Sener MK, Jolley C, Ben-Shem A *et al.* (2005) Comparison of the light-harvesting networks of plant and cyanobacterial Photosystem I. *Biophys.J.* **89**: 1630-42.

113. Melkozernov AN, Barber J, Blankenship RE (2006) Light harvesting in photosystem I supercomplexes. *Biochemistry* **45**: 331-45.

114. Melkozernov AN, Blankenship RE (2005) Structural and functional organization of the peripheral light-harvesting system in Photosystem I. *Photosynth.Res.* **85**: 33-50.

115. Karapetyan NV, Holzwarth AR, Rögner M (1999) The photosystem I trimer of cyanobacteria: Molecular organisation, excitation dynamics and physiological significance. *FEBS Lett.* **460**: 395-400.

116. Karapetyan NV (2004) The dynamics of excitation energy in photosystem I of cyanobacteria: Transfer in the antenna, capture by the reaction site, and dissipation. *Biophysics* **49**: 196-210.

117. Carbonera D, Agostini G, Morosinotto T, Bassi R (2005) Quenching of chlorophyll triplet states by carotenoids in reconstituted Lhca4 subunit of peripheral light-harvesting complex of photosystem I. *Biochemistry* **44**: 8337-46.

118. Elli AF, Jelezko F, Tietz C *et al.* (2006) Red pool chlorophylls of photosystem I of the cyanobacterium *Thermosynechococcus elongatus*: A single-molecule Study. *Biochemistry* **45**: 1454-8.

119. Croce R, Mozzo M, Morosinotto T, Romeo A, Hienerwadel R, Bassi R (2007) Singlet and triplet state transitions of carotenoids in the antenna complexes of higher-plant photosystem I. *Biochemistry* **46**: 3846-55.

120. Trissl H-W (1993) Long-wavelength absorbing antenna pigments and heterogeneous absorption bands concentrate excitons and increase absorption cross section. *Photosynth.Res.* **35**: 247-63.

121. Rivadossi A, Zucchelli G, Garlaschi FM, Jennings RC (1999) The importance of PSI chlorophyll red forms in light-harvesting by leaves. *Photosynth.Res.* **60**: 209-15.

122. Hastings G, Kleinherenbrink FAM, Lin S, Mchugh TJ, Blankenship RE (1994) Observation of the reduction and reoxidation of the primary electron acceptor in photosystem I. *Biochemistry* **33**: 3193-200.

123. Wasielewski MR, Fenton JM, Govindjee (1987) The rate of formation of $P700^+$ - A_0- in photosystem I particles from spinach as measured by picosecond transient absorption spectroscopy. *Photosynth.Res.* **12**: 181-90.

124. Holzwarth AR, Schatz GH, Brock H, Bittersmann E (1993) Energy transfer and charge separation kinetics in photosystem I: 1. Picosecond transient absorption and fluorescence study of cyanobacterial photosystem I particles. *Biophys.J.* **64**: 1813-26.

125. Turconi S, Schweitzer G, Holzwarth AR (1993) Temperature dependence of picosecond fluorescence kinetics of a cyanobacterial photosystem I particle. *Photochem.Photobiol.* **57**: 113-9.

126. Savikhin S, Xu W, Soukoulis V, Chitnis PR, Struve WS (1999) Ultrafast primary processes in photosystem I of the cyanobacterium *Synechocystis* sp PCC 6803. *Biophys.J.* **76**: 3278-88.

127. Holzwarth AR, Müller MG, Niklas J, Lubitz W (2005) Charge recombination fluorescence in photosystem I reaction centers from *Chlamydomonas reinhardtii*. *J.Phys.Chem.B* **109**: 5903-11.

128. Brettel K, Vos MH (1999) Spectroscopic resolution of the picosecond reduction kinetics of the secondary electron acceptor A_1 in photosystem I. *FEBS Lett.* **447**: 315-7.

129. Joliot P, Joliot A (1999) In vivo analysis of the electron transfer within Photosystem I: Are the two phylloquinones involved? *Biochemistry* **38**: 11130-6.

130. Setif P, Brettel K (1993) Forward electron transfer from phylloquinone A_1 to iron-sulfur centers in spinach photosystem I. *Biochemistry* **32**: 7846-54.

131. Brettel K, Golbeck JH (1995) Spectral and kinetic characterization of electron acceptor A(1) in a Photosystem I core devoid of iron- sulfur centers F-X, F-B and F-A. *Photosynth.Res.* **45**: 183-93.

132. Brettel K. Photosynthesis: Mechanisms and effects. [1], 611-614. 1999. Dordrecht, Kluwer Academic Publishers. Garab, G.

133. Xu W, Chitnis PR, Valieva A *et al.* (2003) Electron transfer in cyanobacterial photosystem I - II. Determination of forward electron transfer rates of site-directed mutants in a putative electron transfer pathway from A(0) through A(1) to F-x. *J.Biol.Chem.* **278**: 27876-87.

134. Bautista JA, Rappaport F, Guergova-Kuras M *et al.* (2005) Biochemical and biophysical characterization of photosystem I from phytoene desaturase and ξ-carotene desaturase deletion mutants of *Synechocystis sp* PCC 6803. *J.Biol.Chem.* **280**: 20030-41.

135. Guergova-Kuras M, Boudreaux B, Joliot A, Joliot P, Redding K (2001) Evidence for two active branches for electron transfer in photosystem I. *Proc.Natl.Acad.Sci.USA* **98**: 4437-42.

136. Dashdorj N, Wu X, Cohen RO, Golbeck JH, Savikhin S (2005) Asymmetric electron transfer in cyanobacterial photosystem I: Charge separation and secondary electron transfer dynamics of mutations near the primary electron acceptor A_0 . *Biophys.J.* **88**: 1238-49.

137. Ramesh VM, Gibasiewicz K, Lin S, Bingham SE, Webber AN (2004) Bidirectional electron transfer in photosystem I: Accumulation of A0 - in A- side or B- side mutants of the axial ligand to chlorophyll A0+. *Biochemistry* **43**: 1369-75.

138. Li Y, van der Est A, Lucas MG *et al.* (2006) Directing electron transfer within photosystem I by breaking H-bonds in the cofactor branches. *Proc.Natl.Acad.Sci.USA* **103**: 2144-9.

139. El-Mohsnawy EAR . Evaluierung von monomerem und trimerem Photosystem I in nativem Systemen sowie in semiartifiziellen Systemen zur Biowasserstofferzeugung. 1-143. 2007. Faklutät für Biologie und Biotechnologie an der Ruhr-Universität Bochum. Thesis/Dissertation.

140. Gulis G, Narasimhulu K, Fox L, Redding K (2008) Purification of His_6-tagged Photosystem I from *Chlamydomonas reinhardtii*. *Photosynth.Res.* **96**: 51-60.

141. Schelvis JPM, Germano M, Aartsma TJ, van Gorkom HJ (1995) Energy transfer and trapping in Photosystem II core particles with closed reaction centers. *Biochim.Biophys.Acta* **1230**: 165-9.

142. Braslavsky SE (2007) Glossary of terms used in photochemistry, 3rd edition (IUPAC Recommendations 2006). *Pure and Applied Chemistry* **79**: 293-465.

143. O'Connor DV, Phillips D (1984) *Time-correlated single photon counting.* London: Academic Press, p 1.

144. Birch DJS, Imhof RE (1991) Time-Domain Fluorescence Spectroscopy Using Time- Correlated Single-Photon Counting. In: Lakowicz JR, ed. *Topics in Fluorescence Spectroscopy. 1*. New York: Plenum Press, pp. 1-95.

145. van Stokkum IHM, van Oort B, van Mourik F, Gobets B, van Amerongen H (2008) (Sub)-picosecond spectral evolution of fluorescence studied with a synchroscan streak-camera system and target analysis. In: Aartsma TJ, Matysik J, eds. *Biophysical Techniques in Photosynthesis II*. Heidelberg: Springer, pp. 223-240.

146. Wendler CJ (1983) Untersuchung photochemischer und photophysikalischer Primaerprozesse von Gallenfarbstoffen. Picosekundenspektroskopie an Biliproteinen und Modellchromophoren. Thesis/Dissertation.

147. Müller MG Picosekundenuntersuchungen an Photosyntheseantennen. Schriftenreihe des MPI für Strahlenchemie Nr. 65. 1-190. 1992. ISSN 0932-5131. Thesis/Dissertation.

148. Meyer M, Mialocq J-C, Perly B (1990) Photoinduced intramolecular charge transfer and trans-cis isomerization of the DCM styrene dye. Picosecond and nanosecond laser spectroscopy, high-performance liquid chromatography, and nuclear magnetic resonance studies. *J.Phys.Chem.* **94**: 98-104.

149. Croce R, Müller MG, Bassi R, Holzwarth AR (2001) Carotenoid-to-chlorophyll energy transfer in recombinant major light-harvesting complex (LHC II) of higher plants. I. Femtosecond transient absorption measurements. *Biophys.J.* **80**: 901-15.

150. Beechem JM, Gratton E, Ameloot M, Knutson JR, Brand L (1991) The Global Analysis of Fluorescence Intensity and Anisotropy Decay Data - 2nd-Generation Theory and Programs. In: Lakowicz JR, ed. *Topics in Fluorescence Spectroscopy. 2*. New York: Plenum Press, pp. 241-305.

151. Holzwarth AR (1996) Data analysis of time-resolved measurements. In: Amesz J, Hoff AJ, eds. *Biophysical Techniques in Photosynthesis. Advances in Photosynthesis Research*. Dordrecht: Kluwer Academic Publishers, pp. 75-92.

152. van Stokkum IHM, Larsen DS, van Grondelle R (2004) Global and target analysis of time-resolved spectra. *Biochim.Biophys.Acta* **1657**: 82-104.

153. James DR, Ware WR (1986) Recovery of underlying distributions of lifetimes from fluorescence decay data. *Chem.Phys.Lett.* **126**: 7-11.

154. Siemiarczuk A, Wagner BD, Ware WR (1990) Comparison of the maximum entropy and exponential series methods for the recovery of distributions of lifetimes from fluorescence lifetime data. *J.Phys.Chem.* **94**: 1661-6.

155. Landl G, Langthaler T, Engl HW, Kauffmann HF (1991) Distribution of event times in time-resolved fluorescence: The exponential series approach - algorithm, regularization, analysis. *J.Comput.Phys.* **95**: 1-28.

156. Holzwarth AR (1995) Time-resolved fluorescence spectroscopy. In: Sauer K, ed. *Methods in Enzymology. Vol.246 Biochemical Spectroscopy*. San Diego: Academic Press, pp. 334-362.

157. Shah J (1988) Ultrafast luminescence spectroscopy using sum frequency generation. *IEEE J.Quantum Electron.* **24**: 276-88.

158. Schanz R, Kovalenko SA, Kharlanov V, Ernsting NP (2001) Broad-band fluorescence upconversion for femtosecond spectroscopy. *Appl.Phys.Lett.* **79**: 566-8.

159. Schanz HR . Femtosecond broadbandfluorescence upconversion. 2002. Humboldt Universität Berlin. 28-5-2002. Thesis/Dissertation.

160. Campillo AJ, Shapiro SL (1983) Picosecond streak camera fluorometry. A review. *IEEE J.Quantum Electron.* **19**: 585-603.

161. Nordlund TM (2002) Streak cameras for time-domain fluorescence. In: Geddes CD, Lakowicz JR, eds. *Topics in fluorescence spectroscopy, Vol.1 Techniques*. New York: Plenum Press, pp. 183-260.

162. Mitzkus R, Staerk H (1986) Sweep-nonlinearity correction procedures in picosecond streak camera measurements. *J.Phys.E:Sci.Instrum.* **19**: 679-81.

163. Wiessner A, Steark H (1993) Optical design considerations and performance of a spectro-streak apparatus for time-resolved fluorescence spectroscopy. *Rev.Sci.Instrum.* **64**: 3420-30.

164. Uhring W, Zint CV, Summ P, Cunin B (2003) Very high long-term stability synchroscan streak camera. *Rev.Sci.Instrum.* **74**: 2646-53.

165. Ben-Shem A, Frolow F, Nelson N (2003) Crystal structure of plant photosystem I. *Nature* **426**: 630-5.

166. Fromme P, Schlodder E, Jansson S (2003) Structure and function of the antenna system in photosystem I. In: Green BR, Parson WW, eds. *Light-Harvesting Antennas in Photosynthesis*. Dordrecht: Kluwer Academic Publishers, pp. 253-279.

167. Melkozernov AN, Kargul J, Lin S, Barber J, Blankenship RE (2004) Energy coupling in the PSI-LHCI supercomplex from the green alga *Chlamydomonas reinhardtii*. *J.Phys.Chem.B* **108**: 10547-55.

168. Mullet JE, Burke JJ, Arntzen CJ (1980) Chlorophyll proteins of photosystem I. *Plant Physiol.* **65**: 814-22.

169. Croce R, Zucchelli G, Garlaschi FM, Jennings RC (1998) A thermal broadening study of the antenna chlorophylls in PSI- 200, LHCI, and PSI core. *Biochemistry* **37**: 17355-60.

170. Jennings RC, Zucchelli G, Engelmann E, Garlaschi FM (2004) The long-wavelength chlorophyll states of plant LHCI at room temperature: A comparison with PSI-LHCI. *Biophys.J.* **87**: 488-97.

171. Melkozernov AN, Kargul J, Lin S, Barber J, Blankenship RE (2005) Spectral and kinetic analysis of the energy coupling in the PSI-LHC I supercomplex from the green alga *Chlamydomonas reinhardtii* at 77 K. *Photosynth.Res.* **86**: 203-15.

172. Castelletti S, Morosinotto T, Robert B, Caffarri S, Bassi R, Croce R (2003) Recombinant Lhca2 and Lhca3 subunits of the photosystem I antenna system. *Biochemistry* **42**: 4226-34.

173. Hastings G, Kleinherenbrink FAM, Lin S, Blankenship RE (1994) Time-resolved fluorescence and absorption spectroscopy of photosystem I. *Biochemistry* **33**: 3185-92.

174. Turconi S, Kruip J, Schweitzer G, Rögner M, Holzwarth AR (1996) A comparative fluorescence kinetics study of photosystem I monomers and trimers from *Synechocystis PCC 6803*. *Photosynth.Res.* **49**: 263-8.

175. Karapetyan NV, Dorra D, Schweitzer G, Bezsmertnaya IN, Holzwarth AR (1997) Fluorescence spectroscopy of the longwave chlorophylls in trimeric and monomeric photosystem I core complexes from the cyanobacterium *Spirulina platensis*. *Biochemistry* **36**: 13830-7.

176. Gobets B, Kennis JTM, Ihalainen JA *et al.* (2001) Excitation energy transfer in dimeric light harvesting complex I: A combined streak-camera/fluorescence upconversion study. *J.Phys.Chem.B* **105**: 10132-9.

177. Ihalainen JA, Croce R, Morosinotto T *et al.* (2005) Excitation decay pathways of Lhca proteins: A time-resolved fluorescence study. *J.Phys.Chem.B* **109**: 21150-8.

178. Koehne B, Trissl H-W (1998) The cyanobacterium *Spirulina platensis* contains a long wavelength absorbing pigment C738(F760/77K) at room temperature. *Biochemistry* **37**: 5494-500.

179. Bassi R, Giacometti GM, Simpson DJ (1988) Changes in the organization of stroma membranes induced by in vivo state 1-state 2 transition. *Biochim.Biophys.Acta* **935**: 152-65.

180. Turconi S, Weber N, Schweitzer G, Strotmann H, Holzwarth AR (1994) Energy transfer and charge separation kinetics in photosystem I. 2. Picosecond fluorescence study of various PSI particles and light-harvesting complex isolated from higher plants. *Biochim.Biophys.Acta* **1187**: 324-34.

181. Kennard EH (1918) On the thermodynamics of fluorescence. *Phys.Rev.* **11**: 29-38.

182. Stepanov BI (1957) A universal relation between the absorption and luminescence spectra of complex molecules. *Dokl.Akad.Nauk SSSR* **112**: 839-41.

183. Ihalainen JA, Gobets B, Sznee K *et al.* (2000) Evidence for two spectroscopically different dimers of light-harvesting complex I from green plants. *Biochemistry* **39**: 8625-31.

184. Holzwarth AR, Müller MG, Slavov C, Luthra R, Redding K (2007) Ultrafast energy and electron transfer in photosystem I. Direct evidence for two-branched electron transfer. In: Corkum PB, Jonas D, Miller RJD, Weiner AM, eds. *Ultrafast Phenomena XV*. pp. 471-473.

185. Miloslavina Y, Szczepaniak M, Müller MG *et al.* (2006) Charge separation kinetics in intact photosystem II core particles is trap-limited. A picosecond fluorescence study. *Biochemistry* **45**: 2436-42.

186. Bald D, Kruip J, Rögner M (1996) Supramolecular architecture of cyanobacterial thylakoid membranes: How is the phycobilisome connected with the photosystems? *Photosynth.Res.* **49**: 103-18.

187. Kruip J, Karapetyan NV, Terekhova IV, Rögner M (1999) In vitro oligomerization of a membrane protein complex - Liposome- based reconstitution of trimeric photosystem I from isolated monomers. *J.Biol.Chem.* **274**: 18181-8.

188. Karapetyan NV, Shubin VV, Vasiliev SS, Bezsmertnaya IN, Tusov VB, Pashchenko VZ (1992) P700-dependent variable fluorescence at 760nm in photosystem I complex of cyanobacteria at 77K. In: Murata N, ed. *Research in Photosynthesis*. Dordrecht: Kluwer, pp. 549-552.

189. Melkozernov AN, Schmid VHR, Lin S, Paulsen H, Blankenship RE (2002) Excitation energy transfer in the Lhca1 subunit of LHC I-730 peripheral antenna of photosystem I. *J.Phys.Chem.B* **106**: 4313-7.

190. Rippka R, Deruelles J, Waterbury JB, Herdman M, Stanier RY (1979) Generic Assignments, Strain Histories and Properties of Pure Cultures of Cyanobacteria. *J.Gen.Microbiol.* **111**: 1-61.

191. Kuhl H, Kruip J, Seidler A *et al.* (2000) Towards structural determination of the water-splitting enzyme-Purification, crystallization, and preliminary crystallographic studies of photosystem II from a thermophilic cyanobacterium. *J.Biol.Chem.* **275**: 20652-9.

192. Wenk S-O, Kruip J (2000) Novel, rapid purification of the membrane protein photosystem I by high-performance liquid chromatography on porous materials. *J.Chromatogr.B* **737**: 131-42.

193. Slavov C, El-Mohsnawy E, Rögner M, Holzwarth AR (2009) Trapping kinetics in isolated cyanobacterial PS I complexes. *Chemical Physics* **357**: 163-70.

194. Holzwarth AR (2008) Ultrafast primary reactions in the photosystems of oxygen evolving organisms. In: Braun M, Gilch P, Zinth W, eds. *Ultrashort laser pulses in biology and medicine*. Dordrecht: Springer, pp. 141-164.

195. Renger G, Holzwarth AR (2005) Primary Electron Transfer. In: Wydrzynski TJ, Satoh K, eds. *Photosystem II: The Light-Driven Water: Plastoquinone Oxidoreductase*. Berlin: Springer Netherland, pp. 139-175.

196. Gibasiewicz K, Ramesh V, Lin S, Redding K, Woodbury N, Webber A (2007) Two equilibration pools of chlorophylls in the Photosystem I core antenna of *Chlamydomonas reinhardtii*. *Photosynth.Res.* **92**: 55-63.

197. van der Est AJ (2001) Light-induced spin polarization in type I photosynthetic reaction centres. *Biochim.Biophys.Acta* **1507**: 212-25.

198. Boudreaux B, MacMillan F, Teutloff C *et al.* (2001) Mutations in both sides of the photosystem I reaction center identify the phylloquinone observed by electron paramagnetic resonance spectroscopy. *J.Biol.Chem.* **276**: 37299-306.

199. Cohen RO, Shen GZ, Golbeck JH *et al.* (2004) Evidence for asymmetric electron transfer in cyanobacterial photosystem I: Analysis of a methionine-to-leucine mutation of the ligand to the primary electron acceptor A_0. *Biochemistry* **43**: 4741-54.

200. Poluektov OG, Paschenko SV, Utschig LM, Lakshmi KV, Thurnauer MC (2005) Bidirectional electron transfer in photosystem I: Direct evidence from high-frequency time-resolved EPR spectroscopy. *J.Am.Chem.Soc.* **127**: 11910-1.

201. Muhiuddin IP, Heathcote P, Carter S, Purton S, Rigby SEJ, Evans MCW (2001) Evidence from time resolved studies of the $P700^{+}/A_1^{-}$ radical pair for photosynthetic electron transfer on both the PsaA and PsaB branches of the photosystem I reaction centre. *FEBS Lett.* **503**: 56-60.

202. Fairclough WV, Forsyth A, Evans MCW, Rigby SEJ, Purton S, Heathcote P (2003) Bidirectional electron transfer in photosystem I: electron transfer on the PsaA side is not essential for phototrophic growth in Chlamydomonas. *Biochim.Biophys.Acta* **1606**: 43-55.

203. Santabarbara S, Kuprov I, Hore PJ, Casal A, Heathcote P, Evans MCW (2006) Analysis of the spin-polarized electron spin echo of the $[P_{700}^{+}A_1^{-}]$ radical pair of photosystem I indicates that both reaction center Subunits are competent in electron transfer in cyanobacteria, green algae, and higher plants. *Biochemistry* **45**: 7389-403.

204. Agalarov R, Brettel K (2003) Temperature dependence of biphasic forward electron transfer from the phylloquinone(s) A(1) in photosystem I: only the slower phase is activated. *Biochim.Biophys.Acta* **1604**: 7-12.

205. Nuijs AM, Shuvalov VA, Smit HWJ, van Gorkom HJ, Duysens LNM (1987) Excited states and primary photochemical reactions in photosystem I. In: Biggens J, ed. *Progr. Photosyn. Res. 1*. Dordrecht: Nijhoff Publishers, pp. 229-232.

206. Li Y, Lucas MG, Konovalova T *et al.* (2004) Mutation of the Putative Hydrogen-Bond Donor to P_{700} of Photosystem I. *Biochemistry* **43**: 12634-47.

207. Holzwarth AR, Müller MG (1996) Energetics and kinetics of radical pairs in reaction centers from *Rhodobacter sphaeroides*. A femtosecond transient absorption study. *Biochemistry* **35**: 11820-31.

208. Wang HY, Lin S, Allen JP *et al.* (2007) Protein dynamics control the kinetics of initial electron transfer in photosynthesis. *Science* **316**: 747-50.

209. Büttner M, Xie D-L, Nelson H, Pinther W, Hauska G, Nelson N (1992) The Photosystem I-Like P840-Reaction Center of Green S-Bacteria Is a Homodimer. *Biochim.Biophys.Acta* **1101**: 154-6.

210. Bryant DA, Costas AMG, Maresca JA *et al.* (2007) *Candidatus* Chloracidobacterium thermophilum: An aerobic phototrophic acidobacterium. *Science* **317**: 523-6.

211. Liebl U, Mockensturm-Wilson M, Trost JT, Brune DC, Blankenship RE, Vermaas W (1993) Single core polypeptide in the reaction center of the photosynthetic bacterium *Heliobacillus mobilis*: structural implications and relations to other photosystems. *Proc.Natl Acad.Sci.USA* **90**: 7124-8.

212. Heinnickel M, Golbeck JH (2007) Heliobacterial photosynthesis. *Photosynth.Res.* **91**: 001-19.

213. Fyfe PK, Jones MR, Heathcote P (2002) Insights into the evolution of the antenna domains of Type-I and Type-II photosynthetic reaction centres through homology modelling. *FEBS Lett.* **530**: 117-23.

214. Noy D, Moser CC, Dutton PL (2006) Design and engineering of photosynthetic light-harvesting and electron transfer using length, time, and energy scales. *Biochim.Biophys.Acta* **1757** : 90-105.

215. Fischer N, Setif P, Rochaix JD (1999) Site-directed mutagenesis of the PsaC subunit of Photosystem I. F_B is the cluster interacting with soluble ferredoxin. *J.Biol.Chem.* **274**: 23333-40.

216. Krabs W (1979) *Optimization and approximation.* Chester-NewYork-Brisbane: John Wiley and Sons, p XII-220.

217. Trinkunas G, Holzwarth AR (1996) Kinetic modeling of exciton migration in photosynthetic systems: 3. Application of genetic algorithms to simulations of excitation dynamics in three-dimensional photosystem I core antenna/reaction center complexes. *Biophys.J.* **71**: 351-64.

218. Trinkunas G, Holzwarth AR (1994) Modelling of energy transfer in photosystem I using genetic algorithm. *Liet.Fiz.Zurn.* **34**: 287-92.

219. Kim J. Iterated grid search algorithm on unimodal criteria. 1-122. 1997. Thesis/Dissertation.

220. Andre JC, Vincent, L.M., O'Connor D, Ware WR (1979) Applications of fast Fourier transform to deconvolution in single photon counting. *J.Phys.Chem.* **83**: 2285-94.

List of activities

Publications:

Marc G. Müller, Chavdar Slavov, Rajiv Luthra, Kevin Redding and Alfred R. Holzwarth (2009) "Primary electron transfer is initiated separately in two branches in the reaction center of Photosystem I" submitted to Proc. Natl. Acad. Sci. USA

Chavdar Slavov, Galina Gulis, Kevin Redding and Alfred R. Holzwarth (2009) "Intra-antenna energy transfer and trapping processes in the Photosystem I core complexes of *Chlamydomonas reinhardtii*" submitted to BBA Bioenergetics

Chavdar Slavov, Madina Mansurova, Alfred R. Holzwarth, Wolfgang Gärtner (2009) "Excited state processes in 1-deazariboflavin studied by ultrafast fluorescence kinetics" submitted to Photochemistry and Photobiology

Chavdar Slavov, Eithar El-Mohsnawy, Matthias Rögner, Alfred R. Holzwarth (2009) "Trapping kinetics in isolated cyanobacterial PS I complexes" Chemical Physics, **357**: 163-170

Chavdar Slavov, Matteo Ballottari, Tomas Morosinotto, Roberto Bassi, Alfred R. Holzwarth (2008) "Trap-limited charge separation kinetics in higher plant photosystem I complexes" Biophysical Journal, **94**: 3601-3612

Conference proceedings:

Alfred R. Holzwarth, Marc G. Müller, Chavdar Slavov, Rajiv Luthra, Kevin Redding (2007) "Ultrafast energy and electron transfer in photosystem I. Direct evidence for two-branched electron transfer" in: *Ultrafast Phenomena XV*, 88: 471-473, Springer Berlin Heidelberg

Chavdar Slavov, Matteo Ballottari, Tomas Morosinotto, Marc G. Müller, Roberto Bassi, Alfred R. Holzwarth (2007) "Kinetic analysis of energy and electron transfer processes in PS I particles from *Arabidopsis thaliana*" in:. *14th International Congress of Photosynthesis*, Glasgow. Springer Netherlands

Alfred R. Holzwarth, Marc G. Müller, Chavdar Slavov, Rajiv Luthra, Kevin Redding (2007) "The dual-branched electron transfer in photosystem I" in: *14th International Congress of Photosynthesis*, Glasgow. Springer Netherlands

Oral presentations:

"Chasing The Excited States Of Photosynthetic Complexes: Time-resolved Spectroscopy with Sub-ps Resolution" *17. Photosynthese Workshop Nord-West*, 2008, Bochum, Germany

"Comparison of the Light Energy Utilization Kinetics in Cyanobacterial and Higher Plant Photosystem I" *Intro2 network symposium*, 2008, Lanzarote, Spain

"Energy Transfer and Charge Separation Events in Higher Plant PS I Monitored by Ultrafast Spectroscopy Techniques" *Photosynthesis in the Post-Genomic Era: Structure and Function of Photosystems*, International Meeting in Honor of Jim Barber, 2006, Pushchino, Russia (presentation on awarded poster)

"Energy and Charge Transfer Kinetics in PS I from *Arabidopsis thaliana*", *15. Photosynthese Workshop Nord-West*, 2006, Aachen, Germany

"Kinetic Description of Energy and Charge Transfer Processes in PS I from *Arabidopsis thaliana*", *Ultrafast Reaction Dynamic and Applications*, ESF Summer School, 2006, Algarve, Portugal

"Time Resolved Fluorescence Study on Higher Plant PS I – Core and Intact Particles. A Trapping Kinetics Comparison", *Photosystem I workshop*, PSICO network meeting, 2006, Fontevraud, France

Poster presentations:

"The Dual-Branched Electron Transfer in Photosystem I", *14th International Congress of Photosynthesis*, 2007, Glasgow, United Kingdom

"Kinetic Description of Energy and Charge Transfer Processes in PS I from *Arabidopsis thaliana*", *14th International Congress of Photosynthesis*, 2007, Glasgow, United Kingdom

"Comparison of the Light Energy Utilization Kinetics in Cyanobacterial and Higher Plant PS I", *Light-Harvesting Systems Workshop*, Satellite Meeting of the *14th International Congress of Photosynthesis*, 2007, Drymen, United Kingdom

"Location and Kinetic Properties of the Red Chlorophyll Forms in Higher Plant PS I", *16. Photosynthese Workshop Nord-West*, 2007, Mülheim, Germany

"Energy Transfer and Charge Separation Events in Higher Plant PS I Monitored by Ultrafast Spectroscopy Techniques" *Photosynthesis in the Post-Genomic Era: Structure and Function of Photosystems*, International Meeting in Honor of Jim Barber, 2006, Pushchino, Russia

Acknowledgments

This work is the result of the few years of research that I have performed at the Max Planck Institute for Bioinorganic Chemistry. I am deeply grateful to my supervisor Prof Alfred Holzwarth for giving me this opportunity and for his support during the years.

It would have been a tough way to go through if I did not have the support of my colleagues for which I am very thankful. In particular, I would like to acknowledge here Dr Marc Müller who guided me during my first steps in ultrafast spectroscopy, Michael Reus who always had good ideas for solving any technical issue and Dr Malwina Szczepaniak for the great cooperation in the everyday work and for all the interesting discussions.

A huge *Thank you!* goes to all of our collaborators, who were kindly supplying us with samples, even tough we were asking for giant amounts; Radjiv Luthra and Assoc Prof Kevin Redding from Arizona State University, who actually thought that we have a special diet which includes eating the sample, to Eithar El-Mohsnawy and Prof Mathias Rögner from Bochum University, to Prof Karapetyan from Bach Institute of Biochemistry, Moscow and to Matteo Ballottari and Prof Reberto Bassi from Verona University.

I wish to thank also my previous supervisors Assoc Prof Virjinia Doltchinkova and Assoc Prof Vasilij Goltsev for introducing me to the fields of biophysics and photosynthesis and giving me the flying start a young man needs.

I cannot miss to mention here all my friends who are spread around the world. Thank you guys for always being there for me. You turn the world into a cozy place to live.

Finally, here seems to be a right place to thank the ones whom I owe the most, my parents. There could not have been greater support than accepting and encouraging my most alternative decisions, believing that I will make the right choice.

Накрая, искам да изкажа най-дълбоките си благодарности към моите родители. Благодаря ви за всичко, което сте направили за мен, и особено много за това, че винаги сте приемали и окуражавали дори и най-необичайните ми решения, вярвайки, че ще направя най-правилния избор.

Thank you!